NUMERICAL SIMULATION OF WATER WAVES USING NAVIER-STOKES EQUATIONS

Ashish Raval

Submitted in accordance with the requirements for the degree of

Doctor of Philosophy

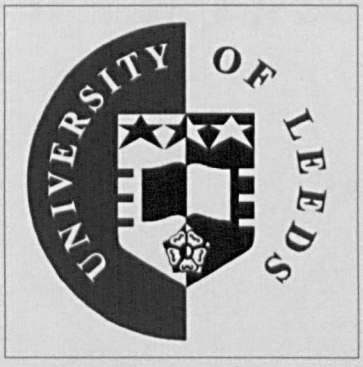

The University of Leeds

School of Earth and Environment

September 2008

To my loving wife Shruti

Abstract

The main purpose of this thesis is to use state of the art computational fluid dynamics techniques to solve the problem of water-wind waves which are related to air-sea interaction. In general, air-sea interaction is studied in a de-coupled manner where both air and water phases are separate and the water phase is either considered as a smooth or rough wall which is stationary or moving. However, in real ocean waves the air and water are coupled. Mass, momentum, heat and energy exchange takes place mostly on the surface waves and this process is culminated when the waves break. Numerical modelling to study these processes requires the solution of the full Navier-Stokes equations along with capturing the interface boundary of the wave with high accuracy, thereby helping us to understand the physical processes taking place on the air-water interface and improve current wave modelling techniques. Our primary motivation is two fold: (1) to investigate the accuracy and reliability of the state of the art numerical techniques available for simulating free surface flows and model air-water wave interaction and (2) to study various near surface physical processes taking place at the transient, viscous, rotational and nonlinear air-water wave interface and understand its effects on the momentum and energy exchange in wind waves.

The work presented in this thesis investigates a numerical model to solve the full Navier Stokes equations required to model transient, viscous, rotational and nonlinear water waves. The first step in the process is to model the water waves when the average wind speed is zero. Various other physical aspects related to wave dynamics are discussed for intermediate depth and deep water waves with different steepnesses. They are compared with earlier experimental and theoretical works available in order

to verify the accuracy of the model . The second step is to model these water waves in the presence of wind blowing at different speeds and analyze its effects on various near surface physical properties and its effect on the motions in the air and underlying water.

The other purpose of this thesis is to investigate some very interesting aspects related to wave dynamics such as vorticity and shear stress which are little studied due to complexities surrounding near surface flow measurements and the lack of an accurate analytical solution. The current work provides a tool for the application of CFD techniques to reliably predict wind-wave interaction by using numerical modelling techniques used in multi-phase flow environments.

The accuracy and convergence of the numerical technique used in this thesis is illustrated by comparing the numerical results with analytical and theoretical results available. The technique is demonstrated to be accurate in the simulation of two-dimensional flows where turbulent effects are negligible. At higher wind speeds, the use of suitable turbulence closure models is recommended.

The main conclusions drawn from the study are: (1) accurate simulation of two and three dimensional, unsteady, viscous and nonlinear water waves is possible with current CFD techniques; (2) The role played by shear stress and vorticity in the wind wave interaction is important and cannot be ignored; (3) the vertical velocity gradients observed inside the water in intermediate depth water waves are found to be stronger than deep water waves; and (4) the effect of the bottom boundary on the magnitude of free surface vorticity is not found to be high.

Publications

- Raval, A., Wen, X. and Smith, M. (2008). Numerical simulation of viscous, non-linear and progressive water waves, Journal of Fluid Mechanics (Submitted).
- Raval, A. and Wen, X. (2008). Energy exchange at the air-water interface, *Ocean Sciences Meeting*, Orlando, USA, 3-7 March 2008.
- Raval, A. and Wen, X. (In preparation). Wind shear stress over water waves. (Target journal, Journal of Fluid Mechanics).
- Mao, N., Raval, A., Wen, X. and Russell S.J. (2007). Controlled delivery of liquids from hydroentangled fabrics to targeted surfaces, *European Disposables and Nonwovens Association Conference*, Leeds, UK, 29-30 March 2007.

Acknowledgements

As for my supervisor, what can I say ? Dr. Xianyun Wen in School of Earth and Environment at the University of Leeds is the one who introduced me to the area of free surface flow and has ever since guided me with great enthusiasm and supportive attitude. I have a great debt to him for his faith in me and for giving me the opportunity to study at University of Leeds. I also thank the other members of my research support group in Institute for Climate and Atmospheric Science at School of Earth and Environment, the ever young, cheerful and inquisitive Professor Michael Smith and dynamic Dr. Andrew Ross for their support and encouragement to my work over the years, without their guidance this thesis would have been impossible. I am also thankful to Dr. Alan Burns of Ansys Europe for interactions related to multiphase flows.

I would also like to take this opportunity to thank all my colleagues and friends, a few of whom are Anil Agarwal, Kiran Bhagate, Gaurihar Kulkarni, Huiyi Yang, Ricardo, James Begg, Tom Breider, Zhihua and Shanmugam with whom I have shared many wonderful talks and thoughts over the dinners and will cherish their friendship over the years to come.

I owe a special thanks to my sponsor British Petroleum and National Environment Research Council, UK for sponsoring my research through Dorothy Hodgkin Post Graduate Awards. I also thank the computer support staff at School of Earth and Environment who promptly responded to any of my queries related to computer, software and networking. I would also extend my thanks to all the unmentioned people who have helped me along the way of completion of my work.

Finally, I could not have done this without my loving and caring wife, Shruti. She did a phenomenal job of handling a stressful job and a stressed out husband with a cheerful smile and lastly, I would also like to thank my parents for their continuous support, encouragement and blessings.

Contents

List of Tables

List of Figures

Nomenclature

a	Wave amplitude
c	Wave phase speed
h	Depth of water
h'	Depth of air
H	Free surface wave height measured in physical scale
L	Wavelength
k	Wavenumber
g	Gravitational acceleration
p	Pressure in the water
p'	Pressure in the air
t	Time
T	Wave period
V	Current velocity in water
V'	Current velocity in air
u	Water velocity component in x direction
u'	Air velocity component in x direction
v	Water velocity component in y direction
v'	Air velocity component in y direction
x	Cartesian horizontal coordinate
y	Cartesian vertical coordinate
f_w	Volume fraction of water or primary fluid
f_a	Volume fraction of air or secondary fluid

w	Holomorphic function
E_0	Total energy density in the water at inlet
E	Total energy density
R_w	Wave Reynolds number
A	Elemental surface area

Greek Symbols

η	Wave elevation
σ	Angular frequncy
ρ	Density of water
ρ'	Density of air
ϕ	Velocity potential in water
ϕ'	Velocity potential in air
Φ	Fluid flow quantity in general transport equation
ψ	Stream function
α	Energy density factor
β	Blend factor
γ	Temporal growth rate
ω	Vorticity
τ	Shear stress
μ	Dynamic viscosity
ν	Kinematic viscosity
Ω	Volume of control volume

Subscripts

i, j	Indices for Cartesian vectors
a	Quantity computed in air
w	Quantity computed in water
m	Mixture quantity
P, E	Cells adjacent to face
PE	Potential energy
KE	Kinetic energy
T	Total energy
ip	Integration point

Superscripts

$n-1, n, n+1$	Discrete time step
nb	Neighbouring points

Abbreviations

CFL	Courant Friedrich Levy Stability condition
DFSBC	Dynamic Free Surface Boundary Conditions
DNS	Direct Numerical Simulation
KFSBC	Kinematic Free Surface Boundary Conditions
VOF	Volume of Fluid
POM	Princeton Ocean Model
WAM	Wave Analysis Model
OPBL	Ocean Planetary Boundary Layer
ABLM	Atmospheric Boundary Layer Model

Chapter 1

General introduction

1.1 Introduction

The study of water-waves, wind-waves, swell and air-sea interactions is a subject area which interests a number of science and engineering disciplines. Structural engineers designing off-shore and floating platforms want to study the influence of water waves on the stability and wave impact forces on the platform. Naval engineers are interested in finding out the drag on their ships and enhancing the ship design. Aeronautical and mechanical engineers are interested in tracking the wake produced by the passing ships. Atmospheric scientists are interested in studying the lower boundary of their domain and the resulting effects of surface waves on marine boundary layers. Cloud physicists are interested in formulating droplet clouds produced by the wind on the ocean surface. Marine biologists are interested in finding out how the gas and mineral transfer takes place between two surfaces and its effects on marine life, scientists modeling air-sea interactions are more concerned about how the heat transfer, gas transfer and evaporation takes place at the surface and model its effect in various budgets. Most of these people are interested in the study of free-surface flows, which are complex and not yet fully understood or captured with very high accuracy by any field observation, prac-

Figure 1.1: Photograph of the open ocean with the wave breaking.

tical experimentation or numerical simulation. It is equally important to understand coupled wind-wave interaction as it affects the transfer of heat, mass and momentum near the surface. Many times theoretical studies rely upon the numerical simulations and their comparison with experimental observations since analytical solutions to such problems are not available unless simplified to the level of no merit practically while experimental observation are difficult or impossible at such scales of time and space. In the figure 1.1, a photograph from waves breaking in deep sea at Cape Reinga near NewZealand is shown. This project is aimed at the better understanding of near surface physical processes in water waves and wind waves by solving the full Navier-Stokes equations and increasing our knowledge about energy and momentum exchange taking place in a coupled nonlinear air-sea interaction. This research will provide an effective tool and methodology for future modeling of wave and coupled air-sea interactions. Results of this project will be important to clarify the understanding of important physical processes in a coupled nonlinear system.

1.2 Literature review

1.2.1 Historical perspective of water-waves

Before we proceed with the numerical solution of water and wind waves, a review on the origins of water-waves theory and work done up to the 20^{th} century is both relevant and insightful. A detailed review of the work done in the past is presented in Craik (2004).

The first attempt to device a theory of water waves was made by Sir Issac Newton (1687). His works were followed by Gravesande (1721) and Charles Bossut (1786), while the equations of hydrodynamics were derived by Euler (1757*a*, 1757*b*, 1761).

Laplace (1776) reexamined wave motion and posed the general initial value problem in Laplace (1799). Lagrange (1781, 1786) derived linearized governing equations for small-amplitude waves and obtained the solution in the limiting case of long plane waves in shallow water.

Gerstner (1802) gave the first exact nonlinear solution for waves of finite amplitude in deep water. Young (1821) wrote extensively on tides, but briefly on waves. The Cauchy-Poisson analysis was presented in 1827 and 1818 respectively and despite errors in the fundamental equations, as highlighted by Dalmedico (1988), it is acknowledged as an important milestone in the mathematical theory of initial-value problems.

Vince (1798) was one of the first British scientist to publish on Hydrodynamics. Pratt (1836) had brief section on the equations of inviscid flow.

Those who published on water waves in the next few years were Green, Kelland, Airy and Earnshaw. Kelland (1844) began his analysis by considering wave-motion in a fluid of finite depth, on the hypothesis of parallel sections considering long waves in shallow water. His formula correctly gives what is now commonly called the *Stokes frequency correction.* Kelland's work is mainly remembered for his study of waves in canals with nonrectangular cross sections. Earnshaw (1847) began with an interesting and well-written introduction for solitary waves and arrived at the results for horizontal velocity and water depth for the wave speed. Eventually, Rayleigh (1876) derived the

correct approximate solution, retaining both dispersion and nonlinearity and further observed that Earnshaw's solution is not irrotational. Although Airy's (1841, 1845) main focus of interest was tidal phenomena, he also wrote a substantial section on the *Theory of Waves in Canals* in 1841 and an *Account of Experiments on Waves* in 1845. Much of the work is original and concerned with modelling observed or observable phenomena. Airy gave the now-standard linear theory for plane waves and his theory gives very good approximate prediction of water waves but it is not applicable to predict steep waves and non-linear waves observed in the oceans.

1.2.2 Geophysical Fluid Dynamics in 20^{th} Century

Sir Horace Lamb (1930) is reputed to be the first person to put forward almost all the previous work in one place including his work describing linear mathematical models governing water waves and the analytical theory for wind-waves. Jeffreys (1924*b*, 1924*a*, 1925) suggested that separation of the airflow might occur at each wave crest and produce a region of low velocity and low pressure downwind of the crest. Thus there would be a difference in pressure between upwind and downwind faces of the wave able to transfer energy from the wind to the wind-waves. However, the generally observed rate of growth of wind-waves is lower than Jeffreys (1924*b*) calculation. John Miles (1957) presented seminal work on shear flow theory on the generation of surface waves by wind. There are certain assumptions in shear flow theory by Miles (1957) such as air flow is assumed to be inviscid, incompressible and has some specified mean shear flow in the absence of waves. The disturbances in the air flow induced by the surface waves are assumed to be two dimensional and small enough so that the equations of motion are linearized. The turbulent fluctuations which must be present to maintain the mean shear flow are neglected in the perturbation equations. The assumption is that the water is inviscid, incompressible, irrotational and has small surface slopes along with no mean drift currents. Furthermore, the wave speed is assumed to be unaltered by any push by the wind and the wind speed is considered low compared to the wave speed. All the above assumptions leads to inappropriate energy extraction and subsequently

underestimate the wave growth due to wind-wave interaction. The theory is found to under-predict the wave growth rate by a factor of 8 to 10 on comparing with fieldwork studies by Snyder & Cox (1966), Barnett & Wilkerson (1967) and laboratory studies by Bole & Hsu (1969). The resonance model of Phillips (1957) includes direct action of turbulent pressure fluctuations on the water surface but neglects any interactions between wave field and pressure field. It is an *uncoupled* model in the sense that the response is assumed to be independent from excitation and the wind profile over the waves is assumed to be logarithmic. Moreover, the theory by Phillips (1957) relies on turbulent pressure fluctuations to provide a random force acting onto the wave surface, ensuring wind-to-wave energy transfer and leading to a linear increase in wave amplitude in time. However, most of the researchers have found this assumption invalid in real ocean measurements. This proves that distribution of stress on the surface is a function of the pressure field and also the coupled instability mechanism. Kinsman (1965) has done detailed analysis about the effect of resonant wave and shear flow and has written extensively about the combined model (resonance and shear flow) and the nonlinear wind-wave model for surface waves.

1.2.3 Current knowledge in Water waves

Water waves can be studied by two broad ways: 1) Laboratory and ocean fieldwork studies and 2) Analytical and numerical study.

1.2.3.1 Laboratory and ocean fieldwork studies

In the past, laboratory and fieldwork studies on water-wind waves have been carried out for various parameters affecting momentum and energy exchange in the wind-waves. The notable fieldwork studies in the open ocean have been carried out by Ursell (1956) and he stated that "wind blowing over a water surface generates waves in the water by a physical process which cannot be regarded as known" and concluded that "the present state of our knowledge is profoundly unsatisfactory". Hasselmann *et al.* (1973) presented well known JONSWAP spectrum for ocean waves with an emphasis on third

order nonlinear interactions in wind waves, Snyder *et al.* (1981) carried out fieldwork to measure direct input of energy and momentum from wind by measuring air pressure fluctuations at finite heights above the surface waves and also compared it with previous work done by Dobson (1971), Priestley (1965) and Elliot (1972). The temporal growth rate of water waves estimated in that studies is given by

$$\gamma = \frac{\rho_w}{\rho_a} \frac{1}{\sigma E(\sigma)} \frac{\partial E(\sigma)}{\partial t} \tag{1.1}$$

where

$$\gamma = (0.2 - 0.3) \left(\frac{U_5}{c} - 1 \right), \tag{1.2}$$

$E(\sigma)$ is the radian frequency, σ spectrum of wave energy, ρ_w and ρ_a are the water and air density respectively, U_5 is the wind speed at 5-m height and c is the wave phase speed. Hasselmann & Bösenberg (1991) derived wave growth and decay rate from fieldwork studies including swell effects.

Bole & Hsu (1969) used a laboratory wind-wave channel to study the response of gravity waves in different wind speed conditions and compared it with Miles inviscid shear flow theory of gravity wave growth. Similarly, Kawai (1977, 1979) also studied wind-wave growth under various wind speeds in the wind-wave laboratory and confirmed the under-predictive nature of Miles theory on wind waves. Hsu *et al.* (1981) and Hsu & Hsu (1983) carried out a set of experiments studying the energy and momentum flux transfer from wind to mechanically generated water wave and concluded that the turbulent Reynolds stresses make negligible contribution to momentum transfer at the interface which can be considered aerodynamically smooth while emphasizing that Miles formula underpredicts the wave-supported stress by several factors. Plant (1982) compared several earlier laboratory, fieldwork and numerical studies and deduced a growth rate parameter for wind waves which was used to calculate the momentum flux from wind to wave which lies within a certain frequency range. Mitsuyasu & Honda (1982) studied the wave growth under turbulent wind on mechanically generated water waves and formulated a wave growth parameter. Cheung & Street (1988) developed the

data set on the momentum transfer under range of surface conditions and revealed that wind waves are not irrotational and the mean wave induced shear stress may contribute to direct energy input from wind to mean and wave fields in water. Hatori & Toba (1983) suggested two stages of transition of regular waves into wind waves starting from irregularization and breaking followed by mutual coalescence of individual waves through amplification of modulation. Papadimitrakis *et al.* (1986) found significant contribution of mean shear stress to the momentum and energy transfer directly into the currents and concluded that the momentum and energy transport processes are wind-field dependent. The wave-induced pressure dominates the wave-supported momentum and energy transfer rates, however, it does not always dominate the transfer of the corresponding total quantities to both waves and currents and may contribute significantly to the energy transferred into currents. Banner & Pierson (1998) used the PIV (Particle image velocimetry) technique to study tangential stress beneath a wind driven air-water interface and found it in significant magnitude while emphasizing the dominance of wave drag for longer time period. Thais & Magnaudet (1995*a*, 1995*b*) studied orbital rotational motion and turbulence below laboratory wind water waves and found that the rotational contribution plays a key role in the energy transfers between wave motion and shear flow. Mastenbroek *et al.* (1996) numerically calculated the growth rate in wind waves but their model underpredicts the observed rate significantly. Uz *et al.* (2002) found that the wind stress tends to be higher under decreasing wind than under increasing wind at a given wind speed, mainly because the response of short wind-wave spectra to varying wind forcing is delayed in time. Donelan(1999) and Pierson *et al.* (2003) carried out laboratory and fieldwork studies on wind wave growth and attenuation under the influence of wind forcing conditions from the opposite direction using direct measurement of surface elevation and more recently Donelan *et al.* (2006) measured the pressure growth term on waves and found that when the wave steepness and wind forcing reaches the combined threshold value, the airflow detaches from the wavy surface downstream of the crests, skips over the troughs, and reattaches on the windward face resulting in an increased shift of the phase of pressure and its

amplitude reduction.

1.2.3.2 Analytical and Numerical Study

The analytical and numerical studies in water waves is generally studied under three broad categories:

1. Potential flow,
2. Inviscid rotational flow and
3. Viscous flow

1.2.3.3 Potential flow

The main characteristics of the potential flow are inviscid, irrotational velocity field and exclusion of turbulence. In the case of Newtonian incompressible fluid, with volume V conservation of mass and momentum is given by:

$$\nabla.(\rho \mathbf{u}) = 0 \tag{1.3}$$

and

$$\rho\left(\frac{\partial \mathbf{u}}{\partial t} + \mathbf{u}.\nabla \mathbf{u}\right) = -\nabla p + \mu \nabla^2 \mathbf{u} - \rho g \tag{1.4}$$

Here, $\mathbf{u}$ stands for velocity vector, ρ is density of the fluid, p = pressure, μ stands for the dynamic viscosity of the fluid and g is acceleration due to gravity.

For an irrotational flow, a velocity potential ϕ exists such that $\mathbf{u}=\nabla\phi$. In an inviscid, potential flow, the continuity and momentum equations for the flow are replaced by the Laplace equation for the velocity potential

$$\nabla^2 \phi = 0 \tag{1.5}$$

and Bernoulli's equation for the pressure

$$-\frac{\partial \phi}{\partial t} + \frac{1}{2}\nabla\phi.\nabla\phi + \frac{p}{\rho} + g\eta = 0 \tag{1.6}$$

Some analytical solutions can be found under corresponding kinematic, dynamic, lateral and bottom boundary conditions, this is well documented in Lamb (1930), Milne-Thomson (1994) and is also elaborately explained in Dean & Dalrymple (1984). The boundary-discretization methods have been developed to numerically predict potential flows. The boundary integral equation methods which simulate an inviscid, irrotational overturning wave in two dimensions was utilized by Longuet-Higgins & Cockelet (1976) and later by Dommermuth & Yue (1987*a*) for axisymmetric three-dimensional problems. More recently Xu & Yue (1992) used the boundary integration equation method for calculating plunging breaking waves in three-dimensions. Other forms of the boundary discretization method involve the use of Cauchy's integral theorem to obtain an integral equation. It has been modified and used by Grosenbaugh & Yeung (1989) to study the unsteady bow wave generated by a forward moving two dimensional body. Tsai & Yue (1995) used this formulation to study the interaction between the free surface and the vortex-sheet shed by a surface piercing body. The primary drawback encountered in these methods is observation of "sawtooth instability", the cause of which is not precisely known and requires artificial smoothing or a re-gridding scheme. Recently, Zhang et al. (2006) have devised desingularized boundary integral equation method to simulate two-dimensional wave propagation in a numerical wave tank. However, little new information is revealed compared to earlier formulations and the other limitation of the boundary integral methods is its inability to deal with breaking waves. The high-order spectral method for nonlinear potential flow wave-wave interactions was independently developed by Dommermuth & Yue (1987*b*) and West et al. (1987). It analyses surface waves by modal and perturbation expansions, albeit with higher-order in wave steepness and a large number of modes using fast fourier technique in a pseudo-spectral treatment of nonlinear free-surface conditions.

It is however found to be limited by the maximum wave steepness one can obtain. The conventional mode-perturbation analysis is incapable of describing the wave-wave interaction between widely separated wavelengths i.e. long wave and short wave interactions. This raises doubt about the ability of higher order spectral methods to accurately model wave-wave interactions. Apart from this, research on this subject spans many years and is covered widely in several books and journals. A major hurdle to the above potential flow assumption is that it does not include all the characteristics of the flow. Hence, it is inaccurate for the flows with a boundary layer, which includes water waves.

1.2.3.4 Inviscid rotational flow

According to Saffman (1981), if vorticity, $\omega = 0$ everywhere in an incompressible fluid, then the fluid in reality ceases to be a fluid; it loses its infinite number of degrees of freedom, which makes the infinite variety of fluid motion possible. In the past, there had been several attempts to formulate vorticity in the inviscid solution for water waves. An analytical solution is outlined in Lamb (1930) for inviscid water waves with vorticity, as given by the exact solution of Gerstner's trochoidal wave theory (1802). Vanden-Broeck (1996) used a boundary integral equation method to numerically compute the periodic waves with constant vorticity. Teles da Silva & Peregrine (1988) used a boundary integral method for periodic and solitary waves with constant vorticity. However, these results are limited in application due to special vorticity distribution. More recently, Constantin (2001) and Constantin et al. (2006) have tried to formulate the solution for inviscid and rotational water waves, although few numerical results have been produced. For a viscous low Reynolds number flow, the convection terms in the full Navier-Stokes equations are dropped and original non-linear equations become linear, this allows an analytical solution to be found for the water wave with small amplitude. The solution for low Reynolds number viscous water waves is outlined in Kinsman (1965) and Lamb (1930).

1.2.3.5 Viscous flow

Although the above assumptions for water waves are valid under special circumstances, in order to study near surface flow processes and surface features it is not adequate. Hence, the most accurate way to study water waves is to discretize it as a viscous flow with a free surface. The study of viscous flow requires solution of the full Navier-Stokes equations.

The analytical study of viscous flow for water waves tries to formulate the viscous effects and incorporate it into the wave formulation. This has been done by Basset (1888), Boussinesq (1895) and Lamb (1930) in the past. The decay rate for finite amplitude water waves was derived by Lamb (1930) using linearized Navier-Stokes equations and is given by:

$$\frac{\partial a}{\partial t} = -2\nu k^2 a \tag{1.7}$$

where, a denotes wave amplitude, ν is the kinematic viscosity of the fluid and k denotes wave number. Viscous decay of wave amplitude is derived as $a \sim e^{(-2\nu k^2 t)}$. Several attempts are made to include vorticity in order to include dissipation effects in the potential flow solution. Ruvinsky *et al.* (1991) included a vortical component in the kinematic boundary condition. Longuet-Higgins (1992) added vorticity effects by time integrating the vortical component of the velocity. More recently, Joseph & Wang (2004) and Wang & Joseph (2006) took vorticity into account in Bernoulli's equation while using only the potential component of velocity in the kinematic condition.

The numerical study of viscous flow in the context of free surface flows is subdivided into four main types based on spatial discretization technique into 1) Boundary-fitted coordinate methods 2) Lagrangian methods with moving grids 3) Front-tracking methods and 4) Eulerian grid methods .

1.2.3.6 Boundary fitted methods

Boundary fitted methods are usually associated with high-resolution simulations of nonlinear free surface flows, where a complex physical domain is mapped on a regular domain on which the transformed equations are solved after discretization. It is often possible to write a boundary-fitted mapping in analytical form when complicated boundaries are not present. This has been done in the past by Dimas & Triantafyllou (1994) using algebraic grid discretization while attempting nonlinear interaction of a shear flow with a free surface in deep water. When the free surface becomes complex and steep algebraic grids are impossible and no longer robust, a curvilinear grid is used instead. Shanks & Thomson (1977) used elliptically generated boundary-fitted grids for solving viscous free-surface flows. Yeung & Ananthakrishnan (1992) used a more elaborate boundary-fitted method which is based on a variational formulation to study the viscous free-surface flow due to oscillations of a two-dimensional floating body. Boundary fitted methods become extremely complex for solving unsteady deforming phase boundaries as the field equations and boundary conditions become complicated and are best suited to relatively simple geometries.

1.2.3.7 Lagrangian methods with moving grids

The second class is Lagrangian methods where the moving grid follows the fluid. The Lagrangian moving grid method was applied for computations of the breakup of a drop by Oran and Boris (1987), simulations of unsteady two-dimensional motion of particles by Feng *et al.* (1994, 1995), Hu(1996) and study of the deformation of a buoyant bubble by Shopov *et al.* (1990). This method is fairly complex and computationally expensive which limits the size of the domain it can model and has not been applied to problems related to water waves. Another Lagrangian formulation technique is Smoothed Particle Hydrodynamics (SPH) method which is a relatively new development. This technique was developed by Lucy (1977) and Gingold & Monaghan (1977) to simulate non-axisymmetric phenomena in astrophysics. Several works pertaining its applica-

tions in free surface flows are outlined by Monaghan (1994), Monaghan & Kos (1999) and Dalrymple & Rogers (2005).

1.2.3.8 Front tracking methods

The third class is the front tracking technique using a fixed grid which is modified near the front making a grid line to follow the interface which is marked by a separate front. Glimm *et al.* (2001) developed this method. A specialized front tracking method was developed by Trygvasson *et al.* (2001) for the computations of multiphase flows. It uses a hybrid grid between front capturing and front tracking technique. While a stationary regular grid is used for the fluid flow the interface is tracked by a separate grid of lower dimension. However, unlike front tracking methods, where each phase is treated separately, here all the phases are treated together by solving a single set of governing equations for the whole flow field. The original version of this technique was published by Unverdi & Tryggvason (1992). While this method gives qualitatively similar results to VOF (Volume of Fluid), Marker and Cell and phase field method, its use of explicit front tracking makes it generally more complex than other methods. Moreover, there are relatively few attempts to apply this method in three dimensional flows.

1.2.3.9 Eulerian grid methods

Several eulerian methods have been developed for capturing free surface. The earliest of them is MAC (marker & cell) method by Harlow & Welch (1965) followed by the volume of fluid (VOF) method by Hirt & Nicolas (1981). More recent developments include the phase field method developed by Jacqmin (1999), the second gradient method from Jamet *et al.* (2001) and the level set method by Sethian (1999). The marker and cell was first developed by Harlow & Welch (1965) for interface tracking. Here, the fluid is represented by a set of marker particles and their motion is determined by a weighted

average of the velocity components through which these marker particles move and hence enable the interface to be tracked automatically. The major constraints in MAC are that it requires large number of marker particles, small grid size and very small time step to accurately track the free surface. More recently MAC has been modified and presented by Aulisa *et al.* (2004). It involves area conservation by redistribution of marker particles by adding or removing them locally when required by interface evolution. Since the simulation using MAC requires large number of particles for higher resolution, the time steps required will often be very small. This limits its suitability to model large domains.

The level set method was originally presented by Osher & Sethian (1988) and extended by Sussman *et al.* (1994) combining the projection method with the level set technique for application in bubble dynamics. The basic premise is to consider interface ζ as zero level set of function ϕ, defined as $\phi(\mathbf{x}, t = 0) = D$, where D is signed normal distance from the interface to $\zeta(t = 0)$. It is either positive or negative if $\mathbf{x}$ is outside or inside the initial $\zeta(t = 0)$. If the zero level set coincides with $\zeta(t = 0)$, then a equation for function $\phi(\mathbf{x}, t)$ that contains the motion of interface $\zeta(t)$ as level set $\phi = 0$

$$\frac{\partial \phi}{\partial t} + U \mid \nabla \phi \mid = 0 \tag{1.8}$$

where U is the speed of the interface ζ in the outward normal direction and it is the sum of interface propagation speed, the speed due to curvature and velocity normal to the interface, i.e. $\mathbf{u}.\hat{\mathbf{n}}$, where $\hat{\mathbf{n}} = \nabla\phi/\mid \nabla\phi \mid$ is the unit vector normal to the interface. The equation (1.8), for most free surface flows is similar to

$$\frac{\partial F}{\partial t} + (\mathbf{u}.\nabla)F = 0 \tag{1.9}$$

here, $\mathbf{u}$ is velocity at the interface and F is discontinuous heaviside function which takes values such as $F = F_1$ in fluid 1, $F = F_2$ in fluid 2 and $F_1 < F < F_2$ at the interface. Since ϕ is a smooth function the above equation is easily solved numerically. As the function ϕ is not a discrete representation of a Heaviside function H, it is not

directly integrated forward in time, hence it is reconstructed at each time step from the distance function ϕ. This method tends to loose the mass and has to be reinitialized as suggested by Sussman *et al.* (1994). The conventional routines for reinitializing a distance function are to find the contour $\phi = 0$ and reset ϕ at all points close to the front. This can distort the front leading to mass conservation errors. If we use local geometric information to fix the level set position for reinitialization it becomes similar to VOF method. More recently, Price & Chen (2006) used an improved level set method to simulate the free surface for incompressible two-phase flows for various cases like oscillating flow in a two-dimensional square tank, a breaking dam problem, sloshing in a two-dimensional rectangular tank and a Wigley ship hull travelling in calm water. Though the results are encouraging the authors have emphasized further validation to be done. Losasso *et al.* (2006) comprehensively reviewed spatially adaptive techniques for level set methods. They concluded that the original level set methods suffers from numerical dissipation, but, higher order, hybrid and adaptive techniques have increased the accuracy of the method.

Volume of fluid (VOF) was made popular by Hirt & Nicholas (1981) and is the most widely used method for interface tracking to date. It has been developed and applied for both incompressible fluid and compressible flows. The simplest type of VOF method is simple line interface calculation (SLIC) by Noh & Woodward (1976). However, the original VOF methods are obsolete nowadays as substantial development has been carried out for improving its spatial and temporal accuracy to higher orders. Rider and Kothe (1998) presented the historical and recent development in Volume of Fluid Methods and developed a new more accurate piecewise linear interface construction(PLIC) method which is second-order accurate for the volume tracking of material interfaces in two dimensions. The other notable earlier works in interface tracking are those from Debar (1974), Chorin (1980), Barr & Ashurst (1984), Ashgriz & Poo (1991), Parker & Youngs (1992), Li (1995), Rider & Kothe (1995), Pilliod & Puckett (2004), Rudman (1997, 1998). Scardovelli & Zaleaski (1999) has reviewed the volume of fluid methods in detail. Nielsen (2003) used VOF to predict green water loads on ships

along with several case studies related to free surface modeling. Lopez *et al.* (2005) presented an improved PLIC-VOF method for tracking thin fluid structures in two-phase flows which was extended from the previous work by Lopez *et al.* (2004). The method is based on using markers that are placed every time step at the mid-points of cell interface segments in order to improve the accuracy of the interface reconstruction, although it can essentially be considered as a VOF-type method. More recently, Schlottke & Weigand (2008) used VOF for Direct Numerical Simulation of evaporating droplets using PLIC algorithm for interface reconstruction.

Basic features of Volume of Fluid methods. In the VOF method, at the beginning a specified interface geometry is used to initialize the volume of fluid in each computational cell which requires computing fluid volume containing fluids and interface. This volume data is stored as volume fractions f which takes value of 0 or 1 for cells without interface and $0 < f < 1$ for the cell containing the interface or free surface. Since volume fraction is the only data containing interface information, the interface needs to be reconstructed in order to extract the exact interface information. This is done by forcing local volume conservation constraint. The interfaces are tracked by evolving fluid volumes forward in time with solutions of momentum equations. The interfacial geometry is determined from volume data, followed by interface reconstruction. The reconstructed interface is used to calculate volume fluxes required to integrate volume evolution equations. The current work uses Volume of Fluid Method developed by Zwart *et al.* (2002, 2007). In this method the reconstruction of interface is not necessary. More detailed description on the topic is presented in Chapter 3.

1.2.3.10 Ocean surface waves

Baker (2001) carried out an extensive literature review on all the major work in the area of wind-wave coupling. Accordingly, a standard assumption used by oceanographers studying mathematical aspects of wave turbulence is that the air and wave fields can be decoupled, allowing standard hydrodynamic models using approximate wind forcing terms to be used for wave predictions. The state of the art terms for forcing of

waves by winds use a simple exponential growth parameter obtained empirically from wave-tank measurements during the initial growth period of waves as in Plant (1982) and Komen (1994). Some approximate models based on a perturbational solution of the air flow equations by Miles (1957, 1993, 1996), Belcher (1993, 1994), Harris (1996), Cohen (1999) typically underproduce even these measurements by significant factors. Belcher (1998) has proposed the logarithmic relation for mean flow over hills and waves. It includes the modeling of turbulent stresses based on a *truncated mixing-length model* which leads to small, but non-zero stress perturbations above the hills, however, not satisfying the boundary conditions. In his paper, Belcher (1998) does not include the effects of viscosity, moreover a linear wave assumption with logarithmic wave growth is not applicable to coupled wind-wave in a two-phase free surface flow. The effects of a propagating wave on the turbulence in the air flow can be estimated using an extension of the scale analysis developed for flow over hills. This model however, leads to under prediction of the wave growth.

Although the oceanographic measurements with a satellite or airborne microwave remote sensing are improving the scale and size of sea wave observations as noted by Ulaby (1982), a comparison of sensor data with approximate hydrodynamic theories using wind forcing models shows poor agreement as noted by Hara (1994). Several recent models of the ocean surface wave spectrum based on both empirical data and "decoupled" models for wind forcing effects such as Apel (1994), Durden (1985), Elfouhaily (1997), Donelan (1987) show poor agreement in general. Recent work by Gent (1976, 1977), Al-Zanaidi (1984), Maat (1992), Meirink (2000), Mastenbroek (1996), Li (2000) and in recent past Sullivan (2000) has begun to address the problem by using the improved models for wind-wave interactions through the use of numerical methods for air flow over a "water wave" boundary. The water wave considered in these studies is a simple two-component Stoke's wave approximation, assumed to propagate at a constant velocity without evolving under the action of wind forcing. Although these studies have improved the understanding of air-flow effects, a means to extrapolate these results in coupled wind-wave system evolving due to reaction on

each other cannot be derived.

A commonly accepted view on geophysical flows over land surfaces assumes that the surface roughness is sufficiently large that the fluid dynamics is independent of Reynolds number. But Kitaigorodskii & Donelan (1984) and Harris *et al.* (1996) pointed out that the Reynolds number is likely to be important since oceanic conditions are often either transitional or even smooth rather than fully rough, thus further adding to the complexity of wind-wave interaction. In the past few years, studies using DNS (Direct Numerical Simulation) as well as LES (large-eddy simulation) are performed to study turbulent flows over wavy surfaces. Henn and Sykes (1999), Cherukat *et al.* (1998), De Angelis *et al.* (1997) and Maass & Schumann (1994) considered turbulent flow over sinusoidal surfaces driven by a pressure gradient. The use of pressure gradient to drive the fluid has the potential of creating an error in the solution which will be discussed later in the chapter 3. Maass & Schumann (1994) utilized finite-difference DNS to study air flow structure over stationary sinusoidal waves and reported large separation regions downstream of the wave crest. De Angelis *et al.* (1997) used pseudo-spectral DNS to study the effect of wave boundary on the turbulence statistics and the mean flow in the air. Cherukat *et al.* (1998) used spectral-element DNS to study the flow over stationary sinusoidal waves with high wave slope. Gong (1996) used LES to simulate turbulent flow developing over sinusoidal waves in a wind tunnel, Choi (1992) employed DNS to study turbulent flow over streamwise oriented riblets. It is worthwhile to note that in all the above cases, the wavy boundary is stationary and hence not applicable to flow over the evolving water waves. Some of the salient features in their observations were in momentum flux where a difference of about 40 percent was observed of square of friction velocity and hence it can be inferred that the presence of moving wavy surface significantly alters the near-surface turbulent flux. In proximity of the surface, the presence of moving waves leads to a more negative average turbulent flux irrespective of the wave age. This indicates a complex wave-turbulence interaction near the surface and that the wave-correlated flux is significant. It is noted that the turbulent flux enhancement that occurs near the surface is greater

than what might be inferred by the form stress. Also the near-surface winds accelerate on the windward side of the wave because of a favorable pressure gradient and reach a maximum speed in the vicinity of wave crest and finally decelerate on the leeward side under the action of an adverse pressure gradient. For the small wave slope, the flow remains attached and there are no separation points along the wave. The contours of wave-correlated velocity and the flux field are also strongly dependent on the variation of the critical layer height and the surface orbital velocities. The results also show that the waves significantly influence mean flow, vertical momentum fluxes, velocity variances, pressure and form stress depending on wave age and wave slope. However, the important limitation of these works is that the waves do not evolve under the action of the wind and hence the means to extrapolate the results to air-water wave interaction should be treated with caution. According to Sullivan (2000), some other questions which still persists are the influence of ocean waves on the height of the wave-induced boundary layer, partitioning of vertical momentum flux between turbulent and wave-induced components, modification of Monin-Obukhov similarity theory, role of wave age in determination of surface drag and parameterizations of wave effects for large-scale numerical models.

As per Jones (2001), since the air-sea interface is a sharp boundary between two fluids we can model momentum from one of the fluids to the other as a drag force per unit area at the sea surface. This is surface shear stress. The ocean waves that propagate on this sharp boundary can transport momentum horizontally. Hence, it becomes paramount to determine the interphase location accurately. Moreover, the drag coefficient is not constant over the ocean. Since the real ocean waves are high Reynolds number flows turbulent instabilities set in and physical viscosity is replaced by turbulent viscosity. When the waves are forced by the wind, they can no longer be accurately modeled as irrotational. The air flow does not have to remain attached to the water surface and separation of the air flow has often been observed over wind-waves. The surface displacement can be thought of as the sum of many fourier components or sine waves and can be locally steep enough to induce separation without any of the

individual fourier components being very steep. The power spectral descriptions of wind-waves make the prediction of breaking difficult. The surface friction and pressure gradients slow the air near the surface while momentum transported down the slope speeds up the fluid. The flow separation occurs when the momentum flux towards the wall is not sufficient to keep the fluid near the wall flowing in the same direction as the free stream. With the flow separation or just acceleration and deceleration of flow over the roughness elements, the horizontal component of the normal pressure on the surface does not have to average to zero. To estimate the momentum flux we turn to the experiments on the growth of the wind-waves. For short wind-waves such results can be obtained in wind wave tanks because in the ocean the complexity of making the measurements allows estimates of growth rate to be made only for longer wind-waves. In his book, Jones (2001) has discussed elaborately about the causes and effects of *Unsteady* turbulent boundary layer in oceans. His work provides a significant input to current understanding in wind-wave coupling.

1.2.3.11 Mechanism of generation of wind-water waves

The generation of sea surface waves by the wind is one of the fundamental air-sea interaction process which affects the global climate. As the wind starts blowing over the calm ocean surface, we observe small eddies being generated and convected across the ocean surface by the mean motion of wind. These eddies induce the pressure fluctuations disturbing the water surface and eddies produced in the air enhance its strength. Apart from this, shear stress is also exerted by the wind which leads to nonlinear growth of wave. As it continues to grow in the open ocean, a quasi-balanced stage is reached where energy obtained from the wind is lost by waves in the form of wave-break. This stage is reached only when there is constant speed wind blowing over a large portion of sea known as fetch. In a tropical cyclonic conditions, this stage is not reached and due to the high variability of the wind, the sea is in a partially developed state leading to constant changes in sea state. The vorticity produced as a result of momentum exchange between wind and wave is equally important for analysis

and can hold the key to separation in oceans producing nonlinear effects. Extensive studies, physical modelling and experimental measurements have resulted in limited understanding of the physics related to this nonlinear phenomena implicit in air flow and sea surface wave evolution.

As mentioned earlier, nonlinear hydrodynamic codes have been tested previously, but the air-forcing effects are modeled with empirical estimates without considering the effects of the wave profile on wind forcing. The linear wave theory results in wave growth estimations which are constant in time which is incorrect if an equilibrium between wind and waves is to be obtained.

1.3 Motivation and objectives

Geophysical flows have a very big domain and complex operating mechanism and due to its sheer size and complexity, the modelling assumptions are generally kept simple. However, the basic nature of processes at the water surface is nonlinear and small scale. In order to unravel the physics governing these small scale mechanism, we have to model the wind-water waves very similar to that observed in real world which means reducing the number of assumptions to absolute minimum. The advanced numerical techniques and computing power available currently can be used to address the problem with high accuracy and thereby improve our understanding of these complex interactions taking place on the surface resulting in transient nonlinear growth of waves. The other interesting aspects such as breaking waves and sea-spray transport over the ocean are under investigation by several experts worldwide but it is not the subject of interest in the current work. Instead we are interested in understanding the effect of viscosity and rotational behavior in the air and water on the structures of vorticity and shear stress observed near the free surface in a non-breaking wind-water wave system. Moreover, the study of momentum and energy transfer between air and water requires knowing exact water wave structure which requires study of wave's temporal and spatial characteristics. Hence, we are motivated by the problem of understanding the com-

plex interactions taking place on the free surface when the wind blows over nonlinear transient progressive waves. To summarize the brief review on the wind-waves, we can conclude that there is a lack of any consistent theory on generation of wave by the wind. The currently available theories needs further elaborations and validations. Moreover, the available experimental data do not provide the accurate information on momentum and energy transfer and subsequent growth rate terms leading to many different growth estimates. These motivates us to present a more clear picture on important mechanisms governing the small scale processes at wind-water wave boundary. The main objectives of current research is to

- Simulate viscous, transient and non-linear water waves using Navier-Stokes equations.
- Numerically investigate the wave decay and the wave growth parameters based on different wind speed conditions and compare them with experimental and analytical methods.
- Estimate the total energy exchange in wind-water waves by investigating the change in potential and kinetic energy densities in water which requires instantaneous tracking of the interface with high accuracy.
- In depth study of various physical parameters such as shear stress, vorticity, energy dissipation, pressure etc. in wind-wave environment.
- Investigate the effect of evolving wind-water wave on the velocity observed in air and viceversa.
- Present a numerical model which can be utilized to simulate different types of waves and its evolution under different wind speed regime to investigate other complex mechanisms observed in wind-water wave.
- Investigate the limitations and challenges facing the current free surface numerical techniques.

1.4 Approach

It is appropriate to give a brief overview of the use of computational fluid dynamics in the free surface flow conditions and its scope in the present work. The computational fluid dynamics is primarily a branch of science and engineering which operates on the fundamental physical laws such as conservation of mass, momentum and energy along with the solution of transport equations. Earlier its main applications were limited to supersonic and jet flows. It has constantly undergone improvement and is now applied to almost all disciplines of science and engineering varying from medical engineering to ocean science. CFD methods were confined to the bounds earlier due to its intensive computational requirements, but rapid growth in computing both in terms of capacity of computers and numerical techniques has ensured its application from supercomputing to desktop computing. Water waves are still one of the most intriguing processes of nature. Oceans cover 70 % of the Earth surface and therefore have a significant impact on the weather and climate in general. Most of the waves we observe in the oceans are wind generated surface waves. The current ocean models like WAM, POM, OPBL, ABLM, OCCAM (recent-yet to get comprehensive data) have not been able to accurately model the boundary layer process occurring near the free surface in ocean waves. It is highly desirable to model coupled wind-wave behavior observed in open ocean in order to improve the accuracy of future air-sea interactions ocean models. The fieldwork investigations in open oceans are very difficult and have no scope to repeat after failure. However it is possible to model the wave-trains with similar attributes in the laboratory wave tank using a wave-maker to create paddle waves of the required frequency. The wind forcing from the wave maker side or the opposite side can be modelled and this can give new insight into the transient wave growth and micro-scale turbulence generated due to instability created by shear flows and pressure fluctuations on the surface. The laboratory experiments face the same problem of difficulty in measuring the near surface physical processes due to experimental limitations. However, numerical modelling of these laboratory waves with wind forcing is

possible using widely used industrial CFD codes such as ANSYS-CFX, ANSYS-Fluent, Star-CD, Flow-3d etc. Highly accurate interface tracking of free surface flows is still a daunting challenge and subject to research in its own right. However, the recent progress in numerical methods coupled with the use of higher order schemes and grid generation have propelled the interest in simulation of multiphase free surface flows. This study of water-waves uses the Navier-Stokes equations with kinematic, dynamic and bottom boundary conditions to simulate wind-water waves. The advanced computational fluid dynamics techniques are applied to obtain high-accuracy while keeping computational requirements to a minimum. The VOF (Volume of Fluid) method is used to simulate the presence of fluid in each cell. The conservation of mass and momentum equations are used to capture the water waves initially without any forced air flow over the waves. This is the first case of our project which subsequently studies behavior of water waves under various wind speeds and depth of water. The initial and boundary conditions in air and water in the progressive waves are determined from calculation of "complex potential" in air and water based on theory by Milne-Thomson (1994). A detailed study of the mathematical model, numerical method and discretization is presented in subsequent chapters.

1.4.1 Research tools

ANSYS-Fluent and ANSYS-CFX are two widely used 3-D Navier-stokes solvers in CFD. ANSYS-Fluent has both segregated and coupled solvers incorporated using an iterative finite volume method to solve the Navier-stokes equations. ANSYS-CFX is a coupled finite element control volume solver and can be used with implicit scheme of discretization. Both the solvers were tested earlier in the research to compare the numerical results for transient free surface problem, dam-break problem and problem dealing with the wave breaking. On comparing both solvers in various aspects such as speed, accuracy, robustness and stability, ANSYS-CFX was found more suitable for the free surface problem . Therefore, we decided to use ANSYS-CFX solver in the current research.

1.4.2 Limitations of previous works

The free surface methods discussed earlier in the literature have several limitations which includes maximum steepnesses that these methods can model, assuming fixed or moving wavy boundary while imposing special conditions on the free surface or outlet boundary conditions, considering the flow inviscid or irrotational, while some methods requires higher computational power restricting the size of the domain it can model. More recently several fixed grid methods have demonstrated the ability to model viscous, rotational and nonlinear free surface flows with high-resolution and good mass and momentum conservation properties which includes Zwart *et al.* (2007), Ubbink and Issa (1999) and several others. For inviscid flows, boundary integral method developed by Longuet-Higgins and Cokelet (1976) have been widely used in the past but it is constrained by inviscid flow assumption and its inability to capture breaking waves. Similarly, the limitations of other numerical methods are also discussed earlier.

A major interest for most researchers is slow waves and most of the experimental, fieldwork and numerical modeling work have been concentrated in modeling these types of waves. It is relatively easier to observe the energy exchange in slow waves and to quantify it but it is also paramount to investigate energy exchange taking place in *fast waves* as critical layer mechanisms are either observed or observable under these waves. A stepwise increase in wind speed blowing over the water waves also enables us to determine the approximate wind speed related to wave steepness when air overcomes the energy dissipation in the water and start growing. The ability of numerical methods to fully capture the turbulence is still under research and hence the results from the study of turbulent flow over the waves should be treated with caution. Moreover, oversimplification of the flow properties in the past have also lead to incorrect estimates in the wind-wave environment.

1.5 Outline of thesis

The remaining thesis is structured as follows:

Chapter 2: The mathematical formulation

In this chapter, the initial and boundary conditions used in the calculation are explained. The concept of governing equations for the two-fluid system are given in a conservation form. These equations together with initial and boundary conditions are used to describe the problem of two fluid water waves completely.

Chapter 3: Numerical method, its implementation and simulation setup

A conservative finite element control volume scheme used for spatial and temporal discretization of the governing equations for the water waves is explained. The setup of simulation involving domain and grid creation is also presented.

Chapter 4: Interactions of water waves with zero average wind velocities

The numerical results obtained from solution algorithm are presented and interpreted. Three set of problems are solved, two deep water wave problems and one intermediate depth water wave problem are solved when the average wind speed is zero. Upon validation of results, two problems, one for deep water and one for intermediate depth water wave are solved with three sets of wind speed conditions. The first set of results for air-water interactions of water waves in intermediate depth and deep water waves when the average wind velocity is zero is presented. Several different types of waves with different wave steepnesses and water depth are also modelled and will be produced in suitable technical publications.

Chapter 5: Interaction of deep water waves with air blowing at different velocities

The second set of results for the air-water interactions of deep water waves with air moving at different wind speed is presented. Various phenomenons affecting air-sea interactions are discussed and many lesser known physical parameters are plotted and analyzed in detail.

Chapter 6: Interaction of intermediate depth water waves with air blowing at different velocities

The third set of results for air-water interactions of intermediate depth water waves with air moving at different wind speed is presented. Various phenomenons affecting air-sea interactions are discussed and compared with deep water wave cases and no-wind cases.

Chapter 7: Conclusions and future work

Thesis is summarized and the main conclusions and suggestions for future research are given.

Chapter 2

Mathematical formulation

2.1 Introduction

As mentioned in the first chapter, the main aim of this research is to capture the wind-water waves and analyze the related physics governing the growth and dissipation of water waves under different wind speed regimes which are separated by a well defined interface. A mathematical formulation describing the initial and boundary conditions applied to the solution domain along with a description of general transport equation and governing equations is the subject matter of this chapter.

The mathematical formulation of free surface flow problem is based on fundamental conservation laws. It consists of equations which are valid in the domain and equations which are valid on the boundary. The fluids are modelled as an homogeneous mixture having, at the interface, a jump in properties such as density, viscosity etc. An indicator function is used to mark each fluid and the region where this function undergoes a step change is marked as interface. The purpose of the current work is to develop a methodology to simulate progressive water waves under different low wind speed regimes where turbulent effects play negligible role in the energy exchange. The water waves studied

in this research are dominated by inertial, pressure and gravitational forces and small scale processes are resolved by using very small grid size. The approach used in this study is general and applicable to both laminar and turbulent flows with high Reynolds number, however for flows where turbulent effects are dominant, a suitable turbulence model to capture turbulence is advised. In order to minimize the computational effort required to simulate wind-water waves, we assume the presence of progressive water wave train and presence of air over it depending upon average wind speed considered for solution. The derivation of required initial and boundary conditions is done by considering the *waves at an interface* approach using complex potential as described in Milne-Thomson (1994). Section 2.2 describes the mathematical model for potential flow solution in water and air expanded from Milne-Thomson (1994). Section 2.3 briefly describes the general transport and governing equations for the water waves. Section 2.4 details the boundary conditions applied to the problem.

2.2 Waves at an interface approach

A potential flow approach based on the theory of complex potential by Milne-Thomson's (1994) *waves at an interface* is used to formulate the initial and boundary conditions for coupled wind-wave flows similar to laboratory wind waves experiment described by Mitsuyasu & Honda (1982).

2.2.1 The complex potential

Let ϕ, ψ be the velocity potential and stream function of the irrotational two-dimensional motion of an inviscid liquid. The velocity components are then given by,

$$u = \frac{\partial \phi}{\partial x} = \frac{\partial \psi}{\partial y}, \quad v = \frac{\partial \phi}{\partial y} = -\frac{\partial \psi}{\partial x} \tag{2.1}$$

The *complex potential* is given by,

$$w = \phi + i\psi \tag{2.2}$$

Here, w is a holomorphic function of the complex variable $z = x + iy$.

2.2.1.1 Definition of a holomorphic function of z.

If $\phi = \phi(x, y)$, $\psi = \psi(x, y)$ are any functions of x and y, the combination of $\phi + i\psi$ is a function of the complex variable $z = x + iy$, in the sense that given z, there must correspond to this value of z, one or more values of $\phi + i\psi$.

Hence, if we assume for w any holomorphic function of z, the corresponding real and imaginary parts give the velocity potential and stream function of a possible two-dimensional irrotational motion, and they satisfy the Laplace's equation. The mathematical analysis is simplified by working with the complex potential instead of ϕ and ψ separately.

2.2.2 The complex velocity

From the complex potential $w = \phi + i\psi$ we get

$$\frac{\partial \phi}{\partial x} + i\frac{\partial \psi}{\partial x} = \frac{\partial w}{\partial x} = \frac{dw}{dz}\frac{\partial z}{\partial x} = \frac{dw}{dz}. \tag{2.3}$$

Now,

$$u = -\frac{\partial \phi}{\partial x}, \quad v = \frac{\partial \psi}{\partial x} \tag{2.4}$$

and therefore

$$-\frac{dw}{dz} = u - iv \tag{2.5}$$

2.2.3 Initial and boundary conditions in the potential flow

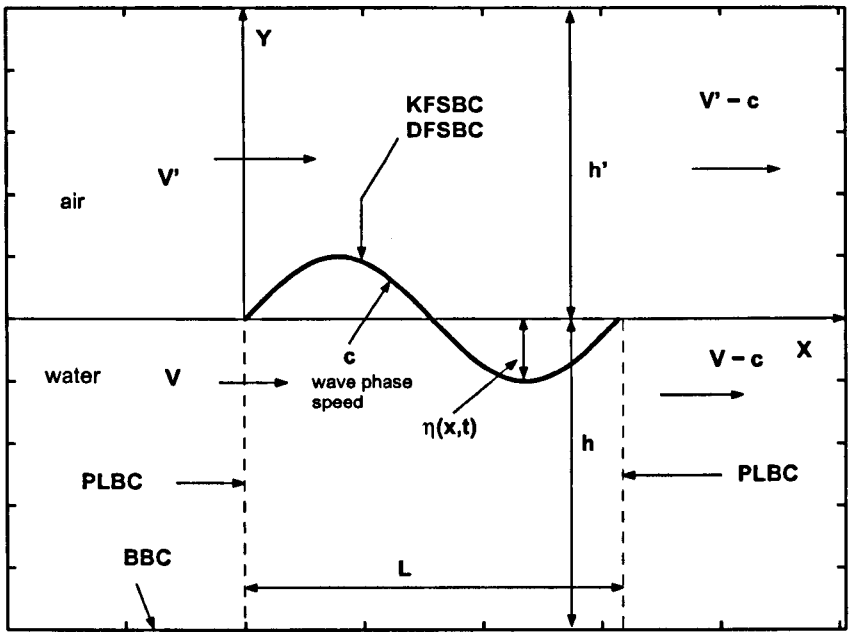

Figure 2.1: Boundary value problem for periodic water wave with air flowing over the wave

2.2.3.1 Kinematic condition at the free surface.

Consider a propagating water wave of depth h as shown in figure 2.1 in which the wave elevation is $\eta = \eta(x,t)$. The axis of x is taken along the bottom in the direction of propagation and elevation is measured from the undisturbed level.

The equation of the free surface is then $y - \eta - h = 0$, and as the surface moves with the fluid $d(y - \eta - h)/dt = 0$, so that

$$\frac{\partial \eta}{\partial t} + u\frac{\partial \eta}{\partial x} = v. \tag{2.6}$$

For the waves of small height and slope, upon linearisation, we can neglect $\frac{\partial \eta}{\partial x}$, which measures the slope of the wave profile, hence, from the above equation, the *kinematical surface condition* for the waves at the free surfaces takes the form

$$\frac{\partial \eta}{\partial t} = \frac{\partial \psi}{\partial x} \tag{2.7}$$

here, $v = \frac{\partial \psi}{\partial x}$. In the case of *irrotational* flow the profile of a progressive wave is given by

$$\eta = a\sin(kx - \sigma t). \tag{2.8}$$

where, a is wave amplitude, k is wave number, $k = \frac{2\pi}{L}$, L is wavelength, σ is angular frequency, $\sigma = \frac{2\pi}{T}$, T is wave period and t is time. An elucidated description on the elemental notions of a progressive wave can be found in Mei (1989), Kinsman (1965). From (2.7), when $y = h$, the stream function ψ is proportional to $\sin(kx - \sigma t)$. This can be proven by mathematical simplification. Hence, to satisfy (2.7), by the complex potential function, we get $w = b\ \cos(kz - \sigma t)$, giving $\psi = -b\sin(kx - \sigma t)\ \mathrm{sinh}kh$ at the free surface. Substitution in (2.7) gives $bk\mathrm{sinh}kh = a\sigma$, hence

$$w = \frac{ac}{\mathrm{sinh}kh}\cos(kz - \sigma t). \tag{2.9}$$

where $c = \sigma/k$ is the speed of propagation.

The complex potential for a simple sine wave moving forward is given by considering the axes of reference moving with the wave, the complex potential is deduced by writing $z' + ct$ for z and therefore the complex potential becomes

$$w = \frac{ac\ \mathrm{cos}kz'}{\mathrm{sinh}kh} \tag{2.10}$$

If we superpose on the whole system a velocity c in the direction of the negative axis of x, from right to left, the complex potential becomes,

$$w = cz' + \frac{ac\ \mathrm{cos}kz'}{\mathrm{sinh}kh}. \tag{2.11}$$

This system of equation represents a steady motion in which the force on any particle is unaltered, for the addition of a constant velocity has no dynamical effect. For applications taking origin in the undisturbed surface, which means $z' = z + ih$, dropping

a constant cih, we get

$$w = cz + ac\,\frac{\cosh k(z+ih)}{\sinh kh}. \tag{2.12}$$

Now we consider a liquid of density ρ' and depth h' flowing with current velocity V' over a layer of liquid of density ρ and depth h which flows with current velocity V and take the axis of x in the interface which separates the fluids and which constitutes a vortex sheet. In the initial model the fluids are bounded above and below by horizontal planes, see figure 2.1.

To investigate the condition that a wave of specific elevation $\eta = a\sin(kx - \sigma t)$ is propagating at the interface with velocity $c = \sigma/k$, we impose the mass of fluid with a velocity c in opposite direction which leads to a change in the velocities of the streams to $V' - c$ and $V - c$. From (2.12) the complex potential of the lower fluid(water) is

$$w = -(V-c)z - a(V-c)\frac{\cosh k(z+ih)}{\sinh kh}. \tag{2.13}$$

The complex potential for air is given by,

$$w' = -(V'-c)z + a(V'-c)\frac{\cosh k(z-ih')}{\sinh kh'}. \tag{2.14}$$

From the above set of equations 2.13 and 2.14 describing the complex potential in the water and air, we can derive the boundary conditions in the water and air with current in presence of wave. It is carried out as follows: Substituting the complex potential $z = x + iy$ into the equation 2.13 we get,

$$w = -(V-c)(x+iy) - a(V-c)\frac{\cosh k(x+iy+ih)}{\sinh kh}. \tag{2.15}$$

upon expansion, simplification and comparison with $\phi + i\psi$ we get,

$$\phi = -(V-c)x - a(V-c)\frac{\cos kx \cosh k(y+h)}{\sinh kh}. \tag{2.16}$$

Since we are in the fixed frame of reference, the above equations are modified to fixed

frame of reference. In moving frame of reference,

$$-\frac{\partial \phi}{\partial x} = U \tag{2.17}$$

In the fixed frame of reference, it becomes

$$\frac{\partial \bar{\phi}}{\partial x} = -u \tag{2.18}$$

Since, $u = U + c$, we get

$$-\frac{\partial \bar{\phi}}{\partial x} = -\frac{\partial \phi}{\partial x} + c \tag{2.19}$$

therefore,

$$\bar{\phi} = \phi - cx \tag{2.20}$$

Replacing, $\phi = \bar{\phi} + cx$, in the fixed reference frame, we get the velocity potential $\bar{\phi}$ in the flow as,

$$\bar{\phi} = (-Vx) - a(V-c)\frac{\cos(kx).\cosh k(y+h)}{\sinh kh}. \tag{2.21}$$

Hence, velocity potential $\bar{\phi}$, horizontal velocity component u, vertical velocity component v and pressure distribution p for progressive wave with $x = x - ct$ is given by,

$$\bar{\phi} = -V(x-ct) - a(V-c)\frac{\cos k(x-ct).\cosh k(y+h)}{\sinh kh}. \tag{2.22}$$

Now, current in the water $V = 0$ gives,

$$u = -\frac{\partial \bar{\phi}}{\partial x} = ak(c)\frac{\sin k(x-ct)\cosh k(y+h)}{\sinh kh}. \tag{2.23}$$

$$v = \frac{\partial \bar{\phi}}{\partial y} = -ak(c)\frac{\cos k(x-ct)\sinh k(y+h)}{\sinh kh}. \tag{2.24}$$

$$p = \rho\left(\frac{\partial \bar{\phi}}{\partial t}\right) - \rho(u^2+v^2) - \rho g y. \tag{2.25}$$

The corresponding velocity potential $\bar{\phi}'$, horizontal velocity component u', vertical velocity v' and pressure distribution p' in the air is given by,

$$\bar{\phi}' = -V'(x-ct) + a(V'-c)\frac{\cos k(x-ct)\cosh k(y-h')}{\sinh kh'}. \tag{2.26}$$

Now, with forced current in the air, we get

$$u' = -\frac{\partial \bar{\phi}'}{\partial x} = V' + ak(V'-c)\frac{\sin k(x-ct)\cosh k(y-h')}{\sinh kh'}. \tag{2.27}$$

$$v' = \frac{\partial \bar{\phi}'}{\partial y} = -ak(V'-c)\frac{\cos k(x-ct)\sinh k(y-h')}{\sinh kh'}. \tag{2.28}$$

$$p' = \rho'\left(\frac{\partial \bar{\phi}'}{\partial t}\right) - \rho'(u'^2 + v'^2) - \rho' gy. \tag{2.29}$$

When there is no forced wind, $V' = 0$ and the corresponding initial and boundary conditions can be derived. We use these equations to calculate initial velocity, pressure and volume fraction distributions in the domain alongside the boundary conditions for the volume fractions and velocity. These combined initial and boundary value problems constitute a general model which is applicable to two fluid laboratory wind-water waves..

2.3 General transport equation

The fluid flow in the water waves can be described by three conservative equations, namely, conservation of mass, momentum and energy. These laws hold true for any fluid independent of their physical properties such as density, viscosity, compressibility etc. The general form of the conservation equation for the time-dependent, fluid flow

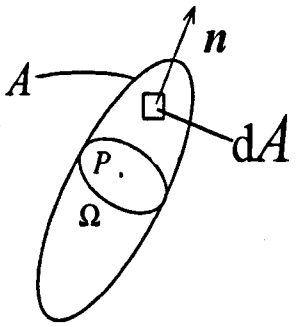

Figure 2.2: Volume of fluid

quantity Φ having control volume Ω and surface area A shown in figure 2.2, is :

$$\int_{\Delta t} \frac{\partial}{\partial t} \left(\int_{\Omega} \rho \Phi \mathrm{d}\Omega \right) \mathrm{d}t + \int_{\Delta t} \int_{A} \boldsymbol{n}.(\rho \Phi \mathbf{u}) \mathrm{d}A \mathrm{d}t$$

$$= \int_{\Delta t} \int_{A} \boldsymbol{n}.(\Gamma \nabla \Phi) \mathrm{d}A \mathrm{d}t + \int_{\Delta t} \int_{\Omega} S_{\Phi} \mathrm{d}\Omega \mathrm{d}t. \qquad (2.30)$$

If we consider infinitesimal volume, then equation (2.30) gives general conservative differential equation in vector form:

$$\frac{\partial(\rho \Phi)}{\partial t} + \nabla.(\rho \mathbf{u} \Phi) = \nabla.(\Gamma \nabla \Phi) + S_{\Phi} \qquad (2.31)$$

where, $\mathbf{u} = u, v$ or w, Φ can stand for: temperature, chemical species, a turbulent quantity or a velocity component in fixed cartesian coordinate system. Each Φ implies corresponding Γ, the diffusion coefficient and S_{Φ} is the source term which include pressure and body forces. It is clear from equation (2.30) that boundary conditions of domain are important for the conservation of flow quantity and these boundary conditions are discussed in Section 2.4.

2.3.1 Governing equations of fluid flow

The governing equation for conservation of mass is obtained by substituting $\Phi = 1$, in the equation (2.31). Since there is no chemical reactions or phase changes in the water waves, this equation gives:

$$\frac{\partial \rho}{\partial t} + \nabla.(\rho \mathbf{u}) = 0 \tag{2.32}$$

where, $\mathbf{u} = \mathbf{ui} + \mathbf{vj}$. The transport equations for the conservation of momentum are obtained on substituting $\Phi = u$ and $\Phi = v$ in equation 2.31. The expanded general momentum equation in x and y direction is given by:

$$\frac{\partial}{\partial t}(\rho u) + \frac{\partial}{\partial x}(\rho u u) + \frac{\partial}{\partial y}(\rho v u)$$

$$= -\frac{\partial p}{\partial x} + \frac{\partial}{\partial x}\left(\mu \frac{\partial u}{\partial x}\right) + \frac{\partial}{\partial y}\left(\mu \frac{\partial u}{\partial y}\right) \tag{2.33}$$

$$\frac{\partial}{\partial t}(\rho v) + \frac{\partial}{\partial x}(\rho u v) + \frac{\partial}{\partial y}(\rho v v)$$

$$= -\rho g - \frac{\partial p}{\partial y} + \frac{\partial}{\partial x}\left(\mu \frac{\partial v}{\partial x}\right) + \frac{\partial}{\partial y}\left(\mu \frac{\partial v}{\partial y}\right) \tag{2.34}$$

here, g is the acceleration due to gravity and μ is the coefficient of dynamic viscosity. The water waves is a incompressible, two-fluid system satisfying mass and momentum conservation equations. According to Unverdi & Tryggvason(1992) and Sussman *et al.*(1994), modeling two fluids as a continuum requires ρ to be continuous and differentiable over the domain while across the water surface ρ is discontinuous and differentiable. Hence, according to Zwart *et al.*(2007), let the velocity components be given by u and v at each point in space, f_w, ρ_w and μ_w represent the volume fraction, density and viscosity of water respectively and f_a, ρ_a and μ_a represent the volume fraction, density and viscosity of the air respectively. Therefore, in air $f_a = 1$, $f_w = 0$, in water $f_a = 0$, $f_w = 1$ and in the cell which contains free surface $0 < f_a < 1, 0 < f_w < 1$. Then for the 2-D unsteady flow, the full Navier-Stokes equations are given by

the continuity equation for water

$$\frac{\partial}{\partial t}(\rho_w f_w) + \frac{\partial}{\partial x}(\rho_w f_w u) + \frac{\partial}{\partial y}(\rho_w f_w v) = 0 \tag{2.35}$$

the continuity equation for air

$$\frac{\partial}{\partial t}(\rho_a f_a) + \frac{\partial}{\partial x}(\rho_a f_a u) + \frac{\partial}{\partial y}(\rho_a f_a v) = 0 \tag{2.36}$$

the momentum equation in the x direction

$$\frac{\partial}{\partial t}(\rho_m u) + \frac{\partial}{\partial x}(\rho_m uu) + \frac{\partial}{\partial y}(\rho_m vu) = -\frac{\partial p}{\partial x} + \frac{\partial}{\partial x}\left(\mu_m \frac{\partial u}{\partial x}\right) + \frac{\partial}{\partial y}\left(\mu_m \frac{\partial u}{\partial y}\right) \tag{2.37}$$

and in the y direction

$$\frac{\partial}{\partial t}(\rho_m v) + \frac{\partial}{\partial x}(\rho_m uv) + \frac{\partial}{\partial y}(\rho_m vv) = -\frac{\partial p}{\partial y} + \frac{\partial}{\partial x}\left(\mu_m \frac{\partial v}{\partial x}\right) + \frac{\partial}{\partial y}\left(\mu_m \frac{\partial v}{\partial y}\right) - \rho_m g \tag{2.38}$$

where g is acceleration due to gravity. Mixture density ρ_m and mixture viscosity μ_m are calculated by

$$\rho_m = \rho_w f_w + \rho_a f_a \tag{2.39}$$

$$\mu_m = \mu_w f_w + \mu_a f_a \tag{2.40}$$

The volume continuity constraint requires that the volume fractions of air and water must sum to unity, hence

$$f_w + f_a = 1 \tag{2.41}$$

The interface between the water and air is tracked by the solution of the volume of fluid f_w and f_a. To summerise, the above mass and momentum conservation equations are solved simultaneously along with the volume continuity constraint and the relations for the density and dynamic viscosity given by equations 2.39 and 2.40 respectively. The surface tension source term in the momentum equation is neglected in this study.

2.4 Initial and boundary conditions

To complete the mathematical model, it is necessary to specify the initial and boundary conditions in the domain. An elaborate discussion on various types of boundary conditions is found in Versteeg & Malalasekera(2007) and Patankar(1980).

- **Inlet:** The inlet boundary is a boundary where either velocity or pressure distribution is specified. We can also define mass flow rate at the inlet. The magnitude of the velocity is usually known and is either applied normal to the boundary or if velocity components in x, y and z directions are known, they are applied accordingly. In order to simulate water wave, the inlet boundary condition is specified from equations 2.23, 2.24, 2.25, 2.27, 2.28 and 2.29 and we can simulate different wind speed conditions by changing the wind velocity.

- **Outlet:** The outflow boundary conditions are better applied on the locations where the flow is relatively uniform and have small effect on the flow inside of the domain. The outlet boundary conditions are given by pressure, velocity or mass flow rate. The outlet boundary conditions also allow fluid to flow inside the domain which is sometimes very essential for mass conservation in coupled solvers.

- **Wall boundary condition:** The velocity of fluid on the non-moving and no slip wall boundary condition is set to be zero. Hence, $u, v = 0$. For a free slip wall boundary condition, the normal wall velocity and shear stress τ are equal to zero. In the free slip wall boundary condition, the parallel velocity is computed and

finite. We use no slip wall boundary condition in the current research domain.

- **Symmetry plane:** The symmetry plane boundary condition imposes the constraint which 'mirrors' the flow on either side of the boundary. The velocity component in normal direction is set to zero, i.e. $u_n = 0$. The scalar variable gradient normal to the boundary is also fixed at zero, i.e. $\frac{\partial \Phi}{\partial n} = 0$.

- **Initial conditions:** For transient problems such as water waves, the initial conditions are very important to achieve the faster convergence for the solution. The initial pressure and velocity conditions are important as they are used by solver code for subsequent time steps. Better initial conditions of pressure, velocity and density reduces the computational effort.

2.5 Chapter summery

This chapter presented a mathematical model for the prediction of interfacial wind-water waves. These differential equations are in a conservative form and discretized with help of finite-element control volume technique applied in ANSYS-CFX solution algorithm. This model combined with suitable initial and boundary conditions is used to simulate time-dependent, viscous water waves, study the interaction taking place in wind-water waves and analyse various physical quantities affecting the flow. The numerical solution is inevitable to study such complex phenomenon as the analytical solution available is not satisfactory.

Chapter 3

Numerical method, its implementation and simulation setup

3.1 Introduction

The numerical method used to solve the set of full Navier-Stokes equations described in the previous chapter requires solution to partial differential equations representing wind-wave domain in the form of mesh of nodes. This construction leads to a set of coupled algebraic equations which are solved by a solution algorithm.

The discretization method in these study is an element based finite volume method as described by Schneider & Raw (1987*a*) and Zwart *et al.* (2007). The earlier work includes Schneider & Raw (1985*a*) and Prakash (1986). The major advantage of this method is that it is designed to combine the strict conservation properties of finite volume method with the geometric flexibility of finite element method, Baliga & Patankar

(1983). It can work with tetrahedral, prism or hexahedral elements. In this method a polyhedral control volume is constructed around each mesh point, as shown in figure 3.1. The subface between two control volume within each element is known as *integration*

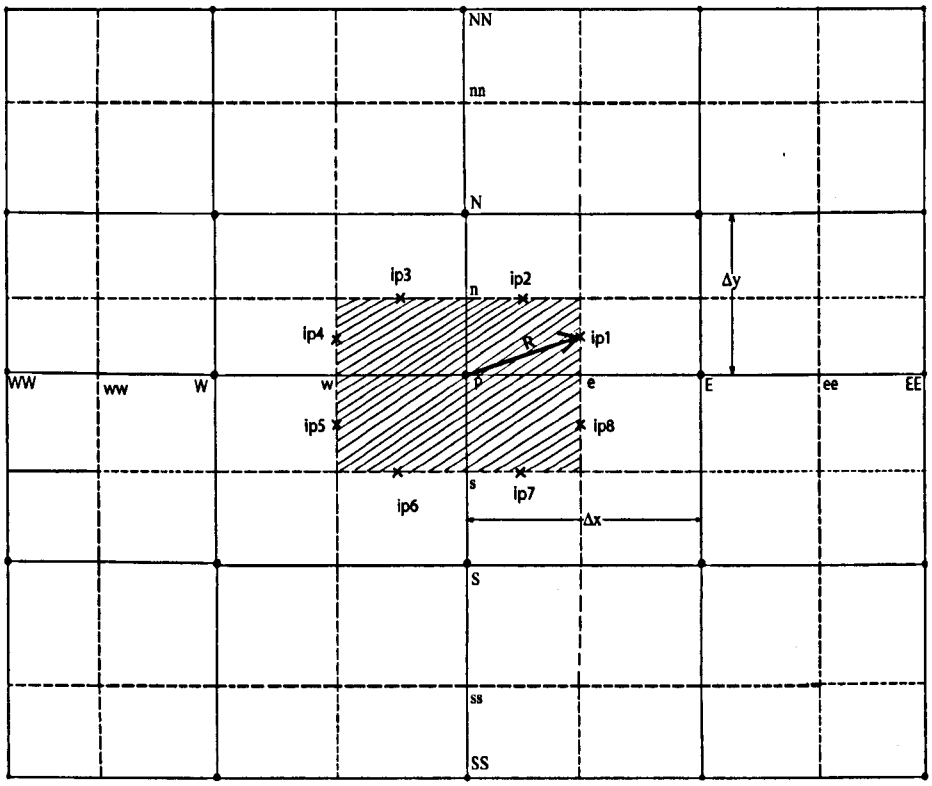

Figure 3.1: Element based finite volume discretization. Solid lines are element boundaries and dashed lines divide the elements into parts. Black dots(•) represent solution unknowns at the vertices and cross(×) represents integration points where surface fluxes are evaluated. Shaded region is control volume around each vertex.

point (ip) where fluxes are discretized. The finite element shape function determines the pressure and velocity gradients from the nodal values while the advected variables are calculated using an upwind-biased discretization method. The overall conservation of flow properties with this treatment is found highly accurate for all flow conditions, Schneider & Raw (1987*b*).

This chapter describes the discretization technique and treatment at the boundaries for solution of coupled algebraic equations used by ANSYS-CFX solver. A second order

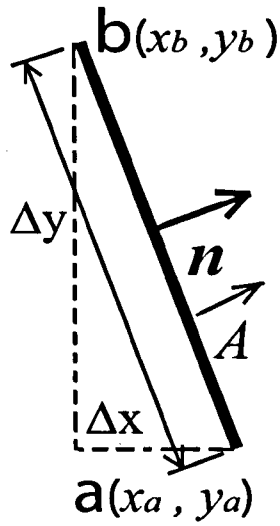

Figure 3.2: An example of a face of a control volume and the normal unit vector.

scheme is used for time derivative and second order upwind-biased scheme is used for advection variables. More details are included in section (3.3) related to equation discretization.

3.2 Spatial discretization

A finite element control volume technique which uses interpolated nodal solution to calculate the flux and integration point values is used to study the wind-wave interaction. It uses a collocated variable interpolation while avoiding checker-board oscillations found when the variables are collocated. This approach also simplifies computer programming and is equally applicable to both structured and unstructured grids. As seen from figure 3.1, let P be the upwind point and E and W denote the nodes located on east and west to it. Then a polyhedral control volume is constructed around each node as union of all the element sectors touching it. i.e. shaded region. The integration points can be easily determined using shape functions. Consider the equation (2.30), in order to evaluate control surface integration we need geometric quantities $\boldsymbol{n}$ and A along with expressions for flux vectors ($\rho\Phi\mathbf{u}$) and ($\Gamma\nabla\Phi$). The outward normal vector

$\boldsymbol{n}$ and elemental surface area A is calculated using simple trigonometry and vector algebra from the nodal coordinates of the grid. The required geometry parameters $\boldsymbol{n}$ and A are calculated as follows. Consider the control volume face shown in figure 3.2 which describes the face for unstructured grid. The parameters for structured grid can be calculated based on same formula. The face area is given by

$$A = \sqrt{(\Delta x)^2 + (\Delta y)^2}$$

here, $\Delta x = x_b - x_a$ and $\Delta y = y_b - y_a$. The normal unit vector to the surface is given by $\mathbf{n} = \frac{\Delta y}{A}\mathbf{i} - \frac{\Delta x}{A}\mathbf{j}$. The spatial discretization is complete and the discretized finite volume equations are constructed over this discrete space.

3.3 Equation discretization

We now consider the discretization of conservation equations (2.35)-(2.38). The conservative equations are integrated over each control volume and these volume integrals are converted to surface integrals by Gauss' divergence theorem. The surface fluxes at each integration points are evaluated in same manner for each control volumes adjacent to it.

3.3.1 Continuity equation

When the implicit second-order backward Euler scheme is used for the time derivative, the discrete representations of equation (2.35) and equation (2.36) in the water and air are:

$$\frac{\Omega}{\delta t}\left(\frac{3}{2}(\rho_w f_w)^{n+1} - 2(\rho_w f_w)^n + \frac{1}{2}(\rho_w f_w)^{n-1}\right) + \sum_{ip}(\rho_w u^i A^i)_{ip}^{n+1}(f_{w,ip})^{n+1} = 0 \quad (3.1a)$$

$$\frac{\Omega}{\delta t}\left(\frac{3}{2}(\rho_a f_a)^{n+1} - 2(\rho_a f_a)^n + \frac{1}{2}(\rho_a f_a)^{n-1}\right) + \sum_{ip}(\rho_a u^i A^i)_{ip}^{n+1}(f_{a,ip})^{n+1} = 0 \quad (3.1b)$$

here, Ω represents the volume of a control volume, A^i_{ip} is the i component of area vector $\mathbf{A}$ of a subface corresponding to integration point which is calculated as $\mathbf{A} = A^j\mathbf{e}_j = A^1\mathbf{e}_1 + A^2\mathbf{e}_2$, u^i_{ip} is the i component of velocity vector $\mathbf{V}$ which is equal to $u\mathbf{i} + v\mathbf{j}$, δt is the time step, $n+1$, n and $n-1$ represents new and old time steps of the evaluated quantity. We now have two unknown terms at integration points to be evaluated in the above equations. i.e. mass flux, $(\rho_w u^i A^i)^{n+1}_{ip}$and $(\rho_a u^i A^i)^{n+1}_{ip}$ and scalar quantity, volume fraction, $f^{n+1}_{w,ip}$ and $f^{n+1}_{a,ip}$.

The advection scheme used to evaluate $f_{w,ip}$ and $f_{a,ip}$ in term of neighbouring vertex values is written in the form:

$$\phi_{ip} = \phi_{up} + \beta\nabla\phi \cdot \mathbf{R} \tag{3.2}$$

where ϕ_{up} is the upwind vertex value and $\mathbf{R}$ is the vector from the upwind vertex to the integration point, ip, $\nabla\phi$ is calculated by averaging the adjacent nodal gradients. The $\mathbf{R}$ is calculated as:

$$\mathbf{R} = (x_{ip} - x_P)\mathbf{i} + (y_{ip} - y_P)\mathbf{j}$$

and $\nabla\phi$ is given by:

$$\nabla\phi = \frac{1}{2}\left[\left(\frac{\partial\phi}{\partial x}\mathbf{i} + \frac{\partial\phi}{\partial y}\mathbf{j}\right)_P + \left(\frac{\partial\phi}{\partial x}\mathbf{i} + \frac{\partial\phi}{\partial y}\mathbf{j}\right)_E\right] \tag{3.3}$$

here,

$$\left(\frac{\partial\phi}{\partial x}\right)_P = \frac{\phi_E - \phi_W}{2\Delta x} \quad \left(\frac{\partial\phi}{\partial y}\right)_P = \frac{\phi_N - \phi_S}{2\Delta y}$$

$$\left(\frac{\partial\phi}{\partial x}\right)_E = \frac{\phi_{EE} - \phi_P}{2\Delta x} \quad \left(\frac{\partial\phi}{\partial y}\right)_E = \frac{\phi_{NN} - \phi_P}{2\Delta y}$$

If $\beta = 0$ in equation 3.2, this scheme is bounded first-order upwind scheme which can be excessively diffusive. If $\beta = 1$, this scheme is a second-order upwind-biased scheme, but unbounded. For the continuity equations (3.1a) and (3.1b), a TVD scheme is used to get β and ϕ_{ip} is bounded by the maximum and minimum values of ϕ among the vertex's neighbours. It is similar to the method described by Barth and Jesperson

(1989). An important advantage of this scheme as compared with other compressive schemes based on controlled downwinding is that its compressiveness does not rely on small timesteps. As a result, bigger time-step size can be used without affecting the quality of interface representation. The mass flow flux in equation (3.1a) and (3.1b) is calculated using pressure smoothing technique for flux through the face of control volume developed by Rhie & Chow (1983). The advection velocity in (3.1a) and (3.1b) is evaluated in the following manner. Let **V** and **A** represent velocity and area vector which gives

$$\mathbf{V} = u^1\mathbf{i} + u^2\mathbf{j} \tag{3.4}$$

where $u^1 = u$ and $u^2 = v$ and

$$\mathbf{A} = A^1\mathbf{i} + A^2\mathbf{j} \tag{3.5}$$

hence we get

$$\mathbf{V}\cdot\mathbf{A} = u^1A^1 + u^2A^2 = uA^1 + vA^2 = u^iA^i \tag{3.6}$$

To calculate the fluid velocity on the face of the control volume, Rhie & Chow (1983) method is applied to the momentum equation. Let a represent coefficient of corresponding velocity. For the control volume seen in figure 3.1, we can calculate it as follows: at point P, E and *ip*,

$$a_p\mathbf{V}_P = \left(\sum a_{nb}\mathbf{V}_{nb} - \nabla P\,\Omega + \rho_m\mathbf{g}\,\Omega\right)_P \tag{3.7}$$

gives

$$a_P\mathbf{V}_P + (\nabla P\,\Omega)_P = \left(\sum a_{nb}\mathbf{V}_{nb} + \rho_m\mathbf{g}\,\Omega\right)_P \tag{3.8}$$

$$a_E\mathbf{V}_E = \left(\sum a_{nb}\mathbf{V}_{nb} - \nabla P\,\Omega + \rho_m\mathbf{g}\,\Omega\right)_E \tag{3.9}$$

gives

$$a_E\mathbf{V}_E + (\nabla P\,\Omega)_E = \left(\sum a_{nb}\mathbf{V}_{nb} + \rho_m\mathbf{g}\,\Omega\right)_E \tag{3.10}$$

$$a_P \mathbf{V}_{ip} = \left(\sum a_{nb} \mathbf{V}_{nb} - \nabla P \, \Omega + \rho_m \mathbf{g} \, \Omega \right)_{ip} \tag{3.11}$$

gives

$$a_P \mathbf{V}_{ip} + (\nabla P \, \Omega)_{ip} = \left(\sum a_{nb} \mathbf{V}_{nb} + \rho_m \mathbf{g} \, \Omega \right)_{ip} \tag{3.12}$$

Assuming that the terms on the right-hand side of equation (3.12) may be approximated by the weighted linear interpolation of the corresponding terms in the equations (3.8) and (3.10), then we obtain,

$$a_P \mathbf{V}_{ip} + (\nabla P \, \Omega)_{ip} = \left(\overline{\sum a_{nb} \mathbf{V}_{nb}} \right)_{ip} + (\overline{\nabla P} \, \Omega)_{ip} + (\rho_m \mathbf{g} \, \Omega)_{ip} \tag{3.13}$$

hence,

$$a_P \mathbf{V}_{ip} = \left(\overline{\sum a_{nb} \mathbf{V}_{nb}} \right)_{ip} + (\overline{\nabla P} \, \Omega - \nabla P \, \Omega)_{ip} + (\rho_m \mathbf{g} \, \Omega)_{ip} \tag{3.14}$$

Thus, the advection velocity is calculated as

$$\mathbf{V}_{ip} = \frac{1}{(a_P)_{ip}} \left(\overline{\sum a_{nb} \mathbf{V}_{nb}} \right)_{ip} + \frac{\Omega}{(a_P)_{ip}} (\overline{\nabla P} - \nabla P)_{ip} + \frac{(\rho_m \mathbf{g} \, \Omega)_{ip}}{(a_P)_{ip}} \tag{3.15}$$

and ∇P is calculated as

$$\nabla P = \frac{\partial P}{\partial x} \mathbf{i} + \frac{\partial P}{\partial x} \mathbf{j} \tag{3.16}$$

Therefore, the velocity components in x and y direction are given by,

$$u_{ip} = \frac{1}{(a_P)_{ip}} \left(\overline{\sum a_{nb} \mathbf{V}_{nb}} \right)^1 + \frac{\Omega}{(a_P)_{ip}} (\overline{\nabla P} - \nabla P)^1 + \frac{\rho_m g^1 \Omega}{(a_P)_{ip}} \tag{3.17}$$

$$v_{ip} = \frac{1}{(a_P)_{ip}} \left(\overline{\sum a_{nb} \mathbf{V}_{nb}} \right)^2 + \frac{\Omega}{(a_P)_{ip}} (\overline{\nabla P} - \nabla P)^2 + \frac{\rho_m g^2 \Omega}{(a_P)_{ip}} \tag{3.18}$$

Hence when $i = 1, 2$, we can write,

$$\mathbf{V}^i_{ip} = \frac{1}{(a_P)_{ip}} \left(\overline{\sum a_{nb} \mathbf{V}_{nb}} \right)^i + \frac{\Omega}{(a_P)_{ip}} (\overline{\nabla P} - \nabla P)^i + \frac{\rho_m g^i \Omega}{(a_P)_{ip}} \tag{3.19}$$

The pressure gradients at integration points calculated using the discretized continuity equations are fully implicit, and therefore involves the product of implicit variables $\mathbf{V}^i$ and f_w and f_a at time level $n+1$. By using Newton linearisation we get:

$$(\mathbf{V}^i f_w)^{n+1} \approx (\mathbf{V}^i)^{n+1} f_w^n + (\mathbf{V}^i)^n f_w^{n+1} - (\mathbf{V}^i)^n f_w^n$$

and

$$(\mathbf{V}^i f_a)^{n+1} \approx (\mathbf{V}^i)^{n+1} f_a^n + (\mathbf{V}^i)^n f_a^{n+1} - (\mathbf{V}^i)^n f_a^n$$

Hence, the continuity equations (3.1a) and (3.1b) are given by:

$$\frac{\Omega}{\delta t}\left(\frac{3}{2}(\rho_w f_w)^{n+1} - 2(\rho_w f_w)^n + \frac{1}{2}(\rho_w f_w)^{n-1}\right) + \sum_{ip}\left(\rho_w \mathbf{V}_{ip}^{n+1} \cdot \mathbf{A}_{ip}^{n+1}\right) f_{(w,ip)}^{n+1} = 0 \tag{3.20a}$$

and

$$\frac{\Omega}{\delta t}\left(\frac{3}{2}(\rho_a f_a)^{n+1} - 2(\rho_a f_a)^n + \frac{1}{2}(\rho_a f_a)^{n-1}\right) + \sum_{ip}\left(\rho_w \mathbf{V}_{ip}^{n+1} \cdot \mathbf{A}_{ip}^{n+1}\right) f_{(a,ip)}^{n+1} = 0 \tag{3.20b}$$

3.3.2 Momentum equation

The discreet representation of momentum equations (2.37) and (2.38) is:

$$\frac{(\rho_m)^n \Omega}{\delta t}\left(\frac{3}{2}(\mathbf{u})^{n+1} - 2(\mathbf{u})^n + \frac{1}{2}(\mathbf{u})^{n-1}\right) + \sum_{ip}(\rho_m \mathbf{u}^j A^j)^{n+1}(\mathbf{u})^{n+1}$$

$$= -\sum_{ip}(P_{ip}^{n+1} A_{ip}^1) + \sum_{ip}((\tau_m^{j1})^{n+1} A^j)_{ip}. \tag{3.21a}$$

$$\frac{\rho_m \Omega}{\delta t}\left(\frac{3}{2}(\mathbf{v})^{n+1} - 2(\mathbf{v})^n + \frac{1}{2}(\mathbf{v})^{n-1}\right) + \sum_{ip}(\rho_m \mathbf{v}^j A^j)^{n+1}(\mathbf{v})^{n+1}$$

$$= -\sum_{ip}(P_{ip}^{n+1} A_{ip}^2) - \rho_m^{n+1} g^i \Omega + \sum_{ip}((\tau_m^{j2})^{n+1} A^j)_{ip}. \tag{3.21b}$$

here, τ_m^{ji} is the mixture stress tensor given by:

$$\tau_m^{ji} = \mu_m \left(\frac{\partial u^i}{\partial x^j} + \frac{\partial u^j}{\partial x^i} \right) \tag{3.22}$$

in the x-direction is equal to

$$\tau_m^{j1} = \mu_m \left(\left(\frac{\partial u}{\partial x^j} \right) + \left(\frac{\partial u^j}{\partial x} \right) \right) \tag{3.23}$$

and in the y-direction it is equal to

$$\tau_m^{j2} = \mu_m \left(\left(\frac{\partial v}{\partial x^j} \right) + \left(\frac{\partial v^j}{\partial y} \right) \right) \tag{3.24}$$

The viscous forces and the pressure term in momentum equation (3.21a) and (3.21b) can be evaluated at the actual location of each integration point pressure values and velocity gradients respectively using true tri-linear interpolation, or at the location where each *ip* surface intersects the element edge using linear-linear interpolation. The finite element shape functions used for the above purpose are calculated as follows:

Shape Functions

Consider a variable ϕ varying within an element as:

$$\phi = \sum_{i=1}^{N_{node}} N_i \phi_i \tag{3.25}$$

here, N_i is the shape function for node i and ϕ_i is the value of ϕ at node i. The summation is over all nodes of the element. The main properties of shape functions include:

$$\sum_{i=1}^{N_{node}} N_i = 1 \tag{3.26}$$

at node j,

$$N_i = 1 \text{ when } i = j, \quad N_i = 0 \text{ when } i \neq j \tag{3.27}$$

Hence, the value of P_{ip} in the momentum equations is evaluated as:

$$P_{ip} = \sum_n N_n P_n \tag{3.28}$$

The velocity $(\mathbf{u}_{ip}^j)^{n+1}$ and $(\mathbf{v}_{ip}^j)^{n+1}$in the momentum flux term in (3.21a) and (3.22b) is calculated using gradient reconstruction method shown in equation (3.2). The buoyancy term is fully implicit. The set of equations (3.20a), (3.20b), (3.21a), (3.21b) and (2.41) represents equations for volume fraction, velocity and pressure fields along with two phases forming a coupled system of equations at each control volume. Assembled into the global system, these coupled system of equations are solved simultaneously by using an algebraic multigrid method developed by Hutchinson & Raithby (1986) and Raw (1996).

3.4 Boundary conditions

The discrete representation of the boundary conditions defined in section (2.4) is shown in this section. It is assumed that the specified boundary condition is valid along the whole face. Consider a boundary surface for fluid flow boundary as shown in figure 3.3. There are 3 types of boundary conditions in the current problem namely: 1) fixed value boundary conditions, 2) fixed gradient boundary conditions and 3) wall boundary conditions. While considering the discretization of the equations in the fixed value boundary conditions, the value of flow properties on the boundary face is calculated and used directly in the implicit implementation. They are determined as follows:

3.4.0.1 Fixed value boundary condition

- **Pressure equation:** The pressure term in the boundary condition is calculated directly. The momentum contributions from the surface pressure are given by

$$M_b^{up} = -\int_b p dy \qquad M_b^{vp} = +\int_b p dx \tag{3.29}$$

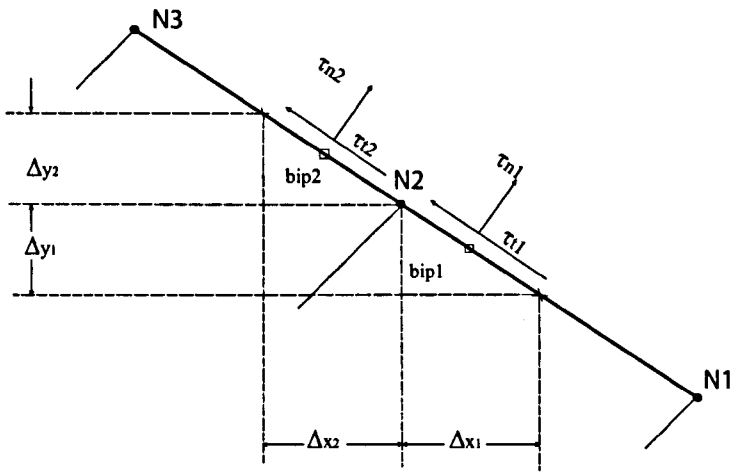

Figure 3.3: Typical boundary surface for fluid flow boundary.

by using the midpoint approximation, we obtain

$$M_b^{up} \approx -p_{bip1}\Delta y_1 - p_{bip2}\Delta y_2 \tag{3.30a}$$

$$M_b^{vp} \approx p_{bip1}\Delta x_1 + p_{bip2}\Delta x_2 \tag{3.30b}$$

here, M_b^{up} and M_b^{vp} represent the momentum contribution in x and y directions respectively. For a structured mesh, the face is vertical, hence $\Delta x_1 = \Delta x_2 = 0$ and $\Delta y_1 = \Delta y_2 = \Delta y$. The integration point pressures in equations (3.21a) and (3.21b) are calculated by interpolation of nodal values.

- **Diffusion term:** The contribution of viscous or diffusive terms to the momentum equation includes both the tangential and normal viscous stresses. The use of midpoint approximation gives

$$M_b^{ud} \approx \tau_{n1}\Delta y_1 + \tau_{n2}\Delta y_2 - \tau_{t1}\Delta x_1 - \tau_{t2}\Delta x_2 \tag{3.31a}$$

$$M_b^{vd} \approx -\tau_{n1}\Delta x_1 - \tau_{n2}\Delta x_2 + \tau_{t1}\Delta y_1 + \tau_{t2}\Delta y_2 \tag{3.31b}$$

where, τ_{n1}, τ_{n2} and τ_{t1}, τ_{t2} represent normal and tangential stress components on each subface as illustrated in Figure 3.3. Now there are two unknowns at

two integration points τ_n and τ_t at two respective integration points requiring two boundary conditions. According to Schneider & Raw (1987*a*), a general boundary condition in order to treat all the expected boundary conditions is given by normal and tangential boundary condition equations which are given by

$$a\tau_n + bu_n + cp = d \tag{3.32a}$$

$$e\tau_t + f(u_t + gu_n) = h \tag{3.32b}$$

where, the coefficients *a, b, c, d, e, f, g* and *h* are user defined constants according to the boundary conditions and can be used for to simulate various boundary conditions such as: (1) specified velocity, (2) pressure and velocity direction specified, (3) zero tangential velocity with zero normal stress and (4) zero tangential stress with zero normal velocity. The equations specified in (3.20) are decomposed in their x and y components in order to comply with use of (u, v) as unknown velocity fields. A more detailed reference on the boundary conditions can be found in Raw (1985) and Schneider & Raw (1985*b*).

- **Convection term:**

Both the continuity and momentum equations contain a convection term. A boundary control volume where two subcontrol volumes coincides are shown in the figure 3.4. Let the boundary integration points be given by *bip1* and *bip2* as observed. The convective flow of ϕ into the control volume is given by

$$M_b^c = \int_b \rho\phi \mathbf{u}^i.\mathbf{dA} \tag{3.33}$$

where M_b^c is the contribution due to convective flux in the momentum equation, **dA** is the surface vector directed out of the domain. In the continuity equation the value of $\phi = 1$ and in momentum equation $\phi = \mathbf{u}^j$ which is calculated through the advection scheme as shown in equation (3.2) and $\mathbf{u}^i$ is calculated through Rhie-Chow (1983) interpolation scheme. Hence the midpoint approximation to

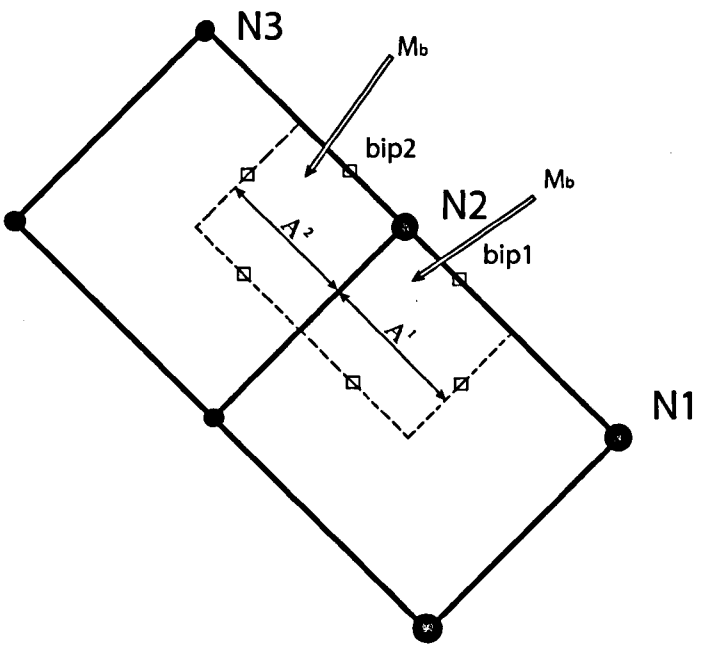

Figure 3.4: Control volume boundary for convection term.

this integral is given by

$$M_b^c \approx F_{bip1}\phi_{bip1} + F_{bip2}\phi_{bip2} \tag{3.34}$$

where F is the mass flows into the domain.

3.4.0.2 Fixed gradient boundary conditions

In the case of a fixed gradient boundary condition the gradient of the flow property over the face is specified, hence

$$(\nabla\phi)_f = (\nabla\phi)_b \tag{3.35}$$

where $(\nabla\phi)_b$ is specified gradient on the boundary. If the boundary condition is zero gradient boundary condition it gives $\nabla\phi = 0$. Similar to the fixed value boundary conditions, the fixed gradient boundary conditions also contributes to the convective and diffusive flux which are added in the source term.

3.4.0.3 Wall boundary conditions

In the non-moving wall boundary conditions as described in section 2.4 have u and v velocity of wall and fluid attached to it is set to zero. The volume fraction function at the boundary has the value as specified for each fluid and is commonly the cell center value of the cell, i.e. $f_{\alpha b} = f_{\alpha P}$, where α stands for volume fraction of water and air respectively, b is boundary and P is cell center value of the cell.

A brief description of the solution strategy is presented below.

3.5 Solution Strategy

The equations of motion in two-fluid water waves are coupled and the ideal way is to solve them simultaneously for the whole domain. Although this approach takes up a higher amount of memory because the solution matrix will be much bigger for larger numbers of computational points, the advantages such as robustness, efficiency, generality and simplicity outweighs the memory requirement. The system of equations for solution is described below.

3.5.1 Coupled System of Equations

The set of discrete conservation equations can be written in the form:

$$\sum_{nb_i} a_i^{nb} \phi_i^{nb} = b_i \tag{3.36}$$

where, ϕ is the solution, b is the right hand side, a is the coefficients of the equation, i is the number of nodes or finite volumes in the domain, nb is the neighbour, but also includes the central coefficient multiplying the solution at ith location. For the

coupled, 3D mass-momentum equation set, they can be expressed as:

$$a_i^{nb} = \begin{bmatrix} a_{uu} & a_{uv} & a_{uw} & a_{up} & a_{uW} & a_{uA} \\ a_{vu} & a_{vv} & a_{vw} & a_{vp} & a_{vW} & a_{vA} \\ a_{wu} & a_{wv} & a_{ww} & a_{wp} & a_{wW} & a_{wA} \\ a_{pu} & a_{pv} & a_{pw} & a_{pp} & a_{pW} & a_{pA} \\ a_{Wu} & a_{Wv} & a_{Ww} & a_{Wp} & a_{WW} & a_{WA} \\ a_{Au} & a_{Av} & a_{Aw} & a_{Ap} & a_{AW} & a_{AA} \end{bmatrix}_i^{nb} \tag{3.37}$$

and

$$\phi_i^{nb} = \begin{bmatrix} u \\ v \\ w \\ p \\ f_W \\ f_A \end{bmatrix}_i^{nb} \tag{3.38}$$

$$b_i = \begin{bmatrix} b_u \\ b_v \\ b_w \\ b_p \\ b_W \\ b_A \end{bmatrix}_i \tag{3.39}$$

3.5.2 The Coupled Solver

Segregated solvers by using the guessed pressure solves the momentum equation first and obtains the equation for pressure correction. This procedure requires a large number of iterations and a careful selection of relaxation parameters for the variables. ANSYS CFX is a coupled solver which uses a fully implicit discretization of the equations at any time step solving the Navier Stokes equations simultaneously.

The solution procedure for the unsteady, two-fluid system is given by:

1. Initialise the solution fields and advance in time.
2. Solve the coupled system equations.
3. Check if the coefficient loop criterion is satisfied, if not iterate within the timestep and go to step 2.
4. Check if the maximum time has been reached. If not advance in time and go to step 2.
5. Stop

3.5.3 Linear Equation Solution

The current solver uses a Multigrid (MG) accelerated Incomplete Lower Upper (ILU) factorisation technique for solving the discrete system of linearised equations. The general matrix form of the linearised system of discrete equations described above is written as:

$$[A][\phi] = [b] \tag{3.40}$$

where, $[A]$ is the coefficient matrix, ϕ the solution vector and $[b]$ is the right hand side. The equation (3.38) is solved iteratively by starting from an approximate solution ϕ^n, improved by a correction ϕ' to give a better solution ϕ^{n+1}, i.e.

$$\phi^{n+1} = \phi^n + \phi' \tag{3.41}$$

where ϕ' is a solution of

$$A\phi' = r^n \tag{3.42}$$

and r^n is the residual obtained from

$$r^n = b - A\phi^n \tag{3.43}$$

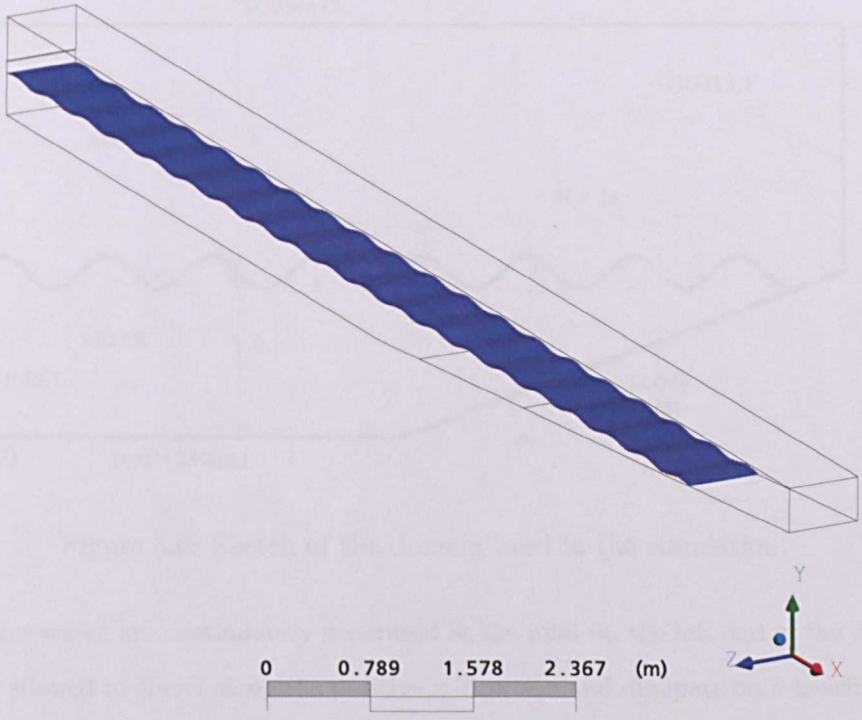

Figure 3.5: Sketch of the domain used in the simulation.

A desired accuracy is achieved by its repeated application. The efficiency of ILU solver is improved by use of multigrid technique by Raw (1996).

3.6 Simulation Setup

The domain modeled in the numerical solution is similar to the one used in the experimental study by Mitsuyasu & Honda (1982). A 3-D and a 2-D representation of the domain is shown in figure 3.5 and figure 3.6 respectively. The size of the domain is 12 m long and 0.8 m high, the mean depth of the water is $h = 0.335$ m and the depth of the air is $h' = 0.465$m. The slope of the beach is 1/15 which has been used in the experimental investigation in the past by Peirson *et al.* (2003) to minimize the reflection from the right end of the domain. The frame of reference for our computations and analysis is a fixed cartesian coordinate system and is aligned to the bottom of the solution domain near the inlet specified as (x,y) = (0,0) as shown in figure 3.6.

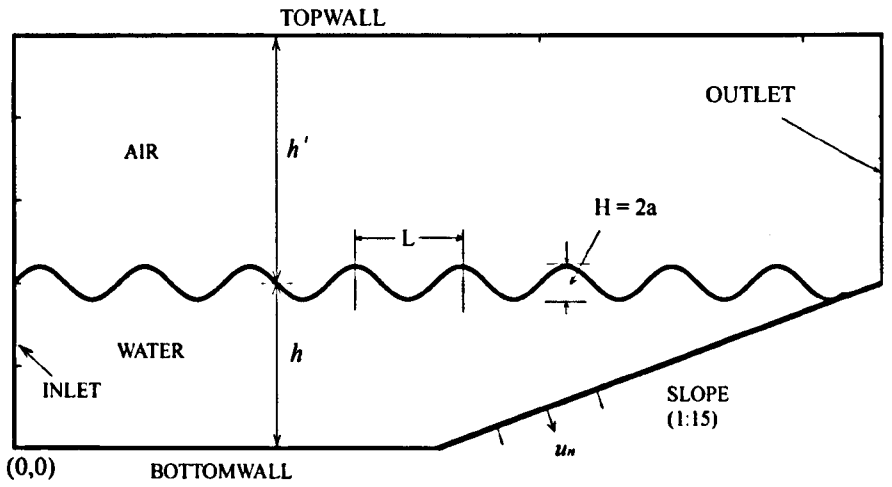

Figure 3.6: Sketch of the domain used in the simulation.

The water waves are continuously generated at the inlet on the left end of the domain and are allowed to travel along the positive x direction and dissipate on a beach at the far right end of the domain. The wavelength for the water wave is calculated using a dispersion relation given by $\sigma^2 = gk\tanh(kh)$. The numerical beach was modeled as we found the evidence that the use of periodic boundary condition creates stronger reflections from the end opposite to wavemaker and after some finite time period it starts affecting the progressive wave and significantly alters the flow parameters inside the solution domain. The other type of geometry using partial opening on the top in the experimental setup used by Peirson *et al.* (2003) was found to alter the air pressure in the domain which can lead to incorrect pressure distribution in the air domain and affect the flow conditions. Since, we are using the boundary conditions derived from the potential flow at the inlet, it is essential to allow the flow to develop into natural wave state which it gains after travelling about one and half wavelength in +x direction and the results presented here are calculated after that length and after several time periods. Due to the asymmetry of velocity resulting in more fluid moving in the wave direction under the wave crest than moving out under the trough region, there is a

mean transport of water from the inlet and it is calculated by

$$Q = \frac{1}{T}\int_t^{t+T}\int_0^{h+\eta} u\,dy\,dt = \frac{ac}{T\sinh(kh)}\int_t^{t+T}\sinh[kh + ak\sin(-\sigma t)]\sin(-\sigma t)dt \quad (3.44)$$

and it is taken out by setting an outflow u_n boundary condition on the slope, as seen in figure 3.6. While calculating the energy density in the numerical solution, the attenuation of wave due to no-slip wall observed in the experiment is taken out from the numerical result as per the analytical expression mentioned in Mitsuyasu & Honda (1982) as the numerical solution have symmetry boundary condition instead of no-slip wall in the front and back.

3.6.1 Numerical Implementation

The implementation of grid which includes finite volumes and nodes is a very important aspect in determining the accuracy of the numerical results. In order to accurately capture the water waves which is a transient free surface flow with small amplitude change, we require very small grid spacing. The alternative to this is the use of moving-grid methods which are not considered in the project due to much higher computational requirements and possibility of wave breaking on the beach. We started the analysis using fine unstructured grid in the near interface region and gradually inflating in the y-direction in the the air and water domain. The results for interface tracking with unstructured grids are comparable to that obtained from structured grid while the results for vorticity and shear stress distribution were found coarse in its distribution. In order to make these results comparable to structured grid results, the grid size in the unstructured grid has to be reduced in the y-direction in air and water which increases the computational effort by a factor of 4 which is expensive compared to structured grid results. Ansys ICEM CFD 5.1 is used to generate structured 1 cell thick volume meshes. The structured mesh has some inherent advantages over unstructured mesh with regard to number of computational points required being less, better mass conservation, higher spatial resolution and having better mesh aspect ratio which are

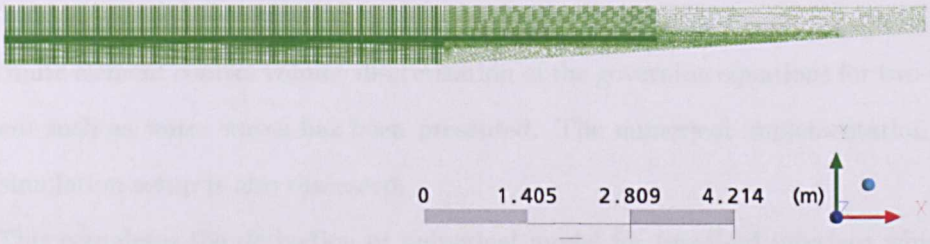

Figure 3.7: The overall grid view of the domain.

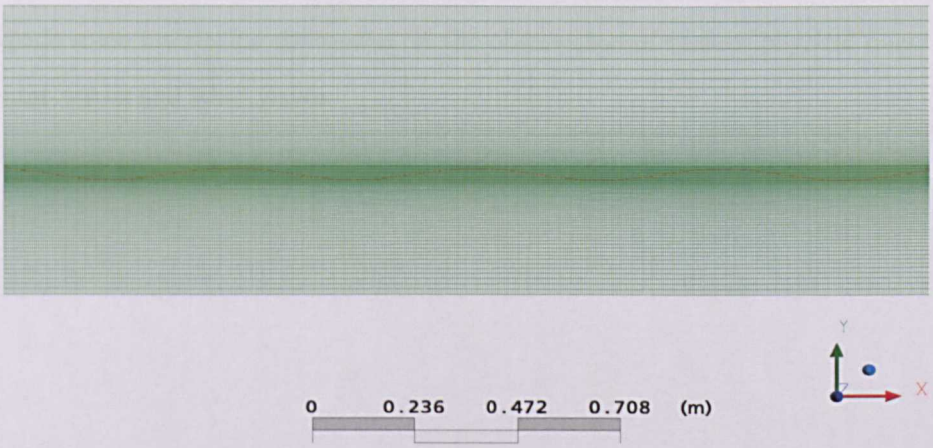

Figure 3.8: The detailed grid view of the domain.

important factor contributing towards accuracy of simulation. Hence, an structured mesh is used for grid generation and near the free surface 16 grid points are distributed in vertical direction in the wave height. In the air and under the water a non-uniform mesh is used. One hundred grid points are uniformly distributed in the x direction per wavelength which produces mesh independent results. The grid structure in the domain is shown in the figure 3.7. A detailed grid structure can be seen in the figure 3.8. The maximum number of iterations per time step is kept 40 for the simulation to quickly converge to required accuracy and conservation target. After it the required accuracy is achieved within 15 iterations per time step for most of the simulation time period.

3.7 Conclusions

The finite element control volume discretisation of the governing equations for two-fluid system such as water waves has been presented. The numerical implementation and the simulation setup is also discussed.

This completes the derivation of numerical model for two-fluid interface which is implemented for solving the full navier-stokes equations for water waves and wind waves. The next chapter evaluates the model with analytical and experimental data alongside some interesting discussion on the observation of various physical quantities in water waves and wind waves.

Chapter 4

Interactions of water waves with zero average wind velocities

4.1 Introduction

In the earlier chapters, a CFD methodology for capturing the interface between two fluids and the associated flow fields was presented. We use these methodology for capturing the free surface in wind-water waves and compare the results with analytical and experimental data available.

The cases selected for the studies in this chapter are from well referenced paper of Mitsuyasu & Honda (1982) on wind induced growth of water waves. The experimental observations in these paper are also compared with analytical solution and will be included in our comparison. The first case study in these category is the study of interaction of water waves when the average wind velocity is zero i.e. air is present but follows the water wave motion without forced convection.

We consider three most investigated cases in the work of Mitsuyasu & Honda (1982) for the purpose of comparison. Case 1 is the intermediate depth water wave (*hereinafter*

as C1) in which the wave steepness is $2a/L = 0.06$, $h/L = 0.44$, T = 0.7s. Case 2 is the deep water wave (*hereinafter as* C2) in which the wave steepness is 0.06, $h/L = 0.6$, and T = 0.6s. Case 3 (*hereinafter as* C3) is the deep water wave with a wave steepness of 0.04, $h/L = 0.6$ and T = 0.6 s. Various physical aspects observed in the water waves are discussed below.

4.2 Energy density

The energy in the water waves is of two types: the potential energy, as a result of free surface displacement, and the kinetic energy, due to the orbital movement of water particles. The total energy in the water waves and its propagation are important in determining the total power available to be extracted from the water waves. Hence it is important to study the effect of viscosity on the decay rate of the water wave. The calculation of the potential energy density and kinetic energy density separately in the water waves can provide valuable insight into the effects of viscosity on the wave amplitude attenuation and orbital velocity in the water wave. Since the input wave at the inlet is a potential flow, analytically, the total energy density at the inlet is given by $E_0 = \frac{1}{2}\rho_w g a^2$, Dean & Dalrymple(1984). The potential energy of a wave depends on the free surface elevation and the "potential energy density" for a progressive wave is given by

$$\overline{PE} = \frac{1}{L}\int_x^{x+L} \frac{\rho_w g \eta^2}{2} dx \tag{4.1}$$

At the inlet, the potential energy density is given by

$$\overline{PE_0} = \frac{1}{4}\rho_w g a^2 \tag{4.2}$$

A nondimensional potential energy density factor α_{PE} is defined using the ratio of the potential energy density and the total energy density at the inlet and it is given by

$$\alpha_{PE} = \frac{\overline{PE}}{E_0} \tag{4.3}$$

The kinetic energy density in the waves is given by

$$\overline{KE} = \frac{1}{L}\int_{x}^{x+L}\int_{-h}^{\eta}\rho_w\left(\frac{u^2+v^2}{2}\right)dx\,dy \tag{4.4}$$

At the inlet it is given by

$$\overline{KE_0} = \frac{1}{4}\rho_w g a^2 \tag{4.5}$$

This is equal to the magnitude of the potential energy of the potential flow. However, the kinetic energy density obtained numerically by the use of equation (4.4) in the solution domain is different from the analytical expression given by equation (4.5) as a result of the dissipation caused by viscosity. The kinetic energy density factor in the water waves is also calculated using the kinetic energy density and total energy density at the inlet and it is given by

$$\alpha_{KE} = \frac{\overline{KE}}{E_0} \tag{4.6}$$

The total energy density, E, in the water wave is the sum of the potential and the kinetic energy densities, hence

$$E = \overline{PE} + \overline{KE} \tag{4.7}$$

The total energy density factor is the sum of the potential energy density factor and the kinetic energy density factor and is given by

$$\alpha_T = \alpha_{PE} + \alpha_{KE} \tag{4.8}$$

The time averaged results for the total, potential and kinetic energy density factors are calculated by

$$\overline{\alpha}_T = \frac{1}{T}\int_0^T \alpha_T dt \tag{4.9}$$

$$\overline{\alpha}_{PE} = \frac{1}{T}\int_0^T \alpha_{PE} dt \tag{4.10}$$

$$\overline{\alpha}_{KE} = \frac{1}{T}\int_0^T \alpha_{KE} dt \tag{4.11}$$

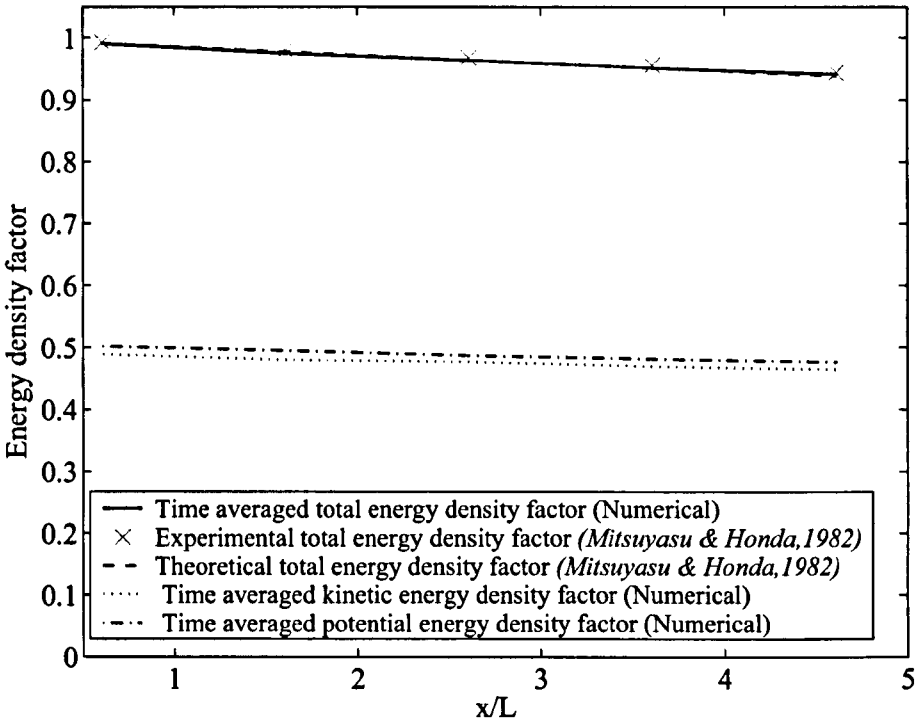

Figure 4.1: Time averaged energy density factor vs x. Case C1.

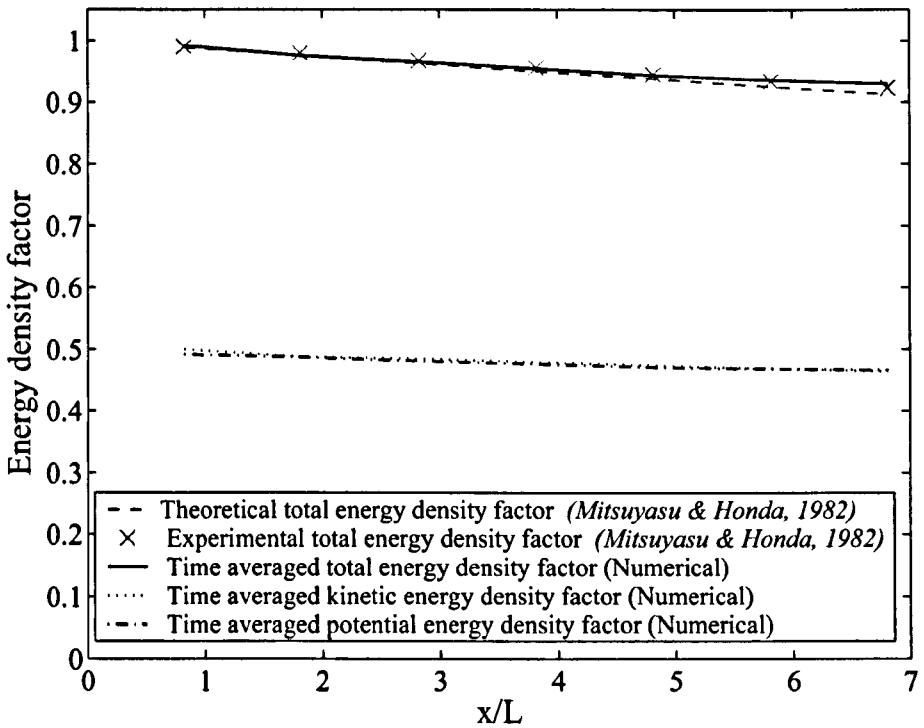

Figure 4.2: Time averaged energy density factor vs x. Case C2.

H/L	T (s)	Δ_{theory}	Δ_{exp}	Δ_{num}
0.06	0.7	1.83×10^{-4}	1.65×10^{-4}	1.727×10^{-4}
0.06	0.6	2.38×10^{-4}	2.10×10^{-4}	1.914×10^{-4}

Table 4.1: Exponential decay rate Δ; $E = E_0 \exp(-\Delta x)$

On comparing the time averaged numerical results for the total, potential and kinetic energy density factors in the intermediate depth water waves (case C1; figure 4.1) and deep water waves (case C2; figure 4.2), we found that the numerical results are in good agreement with theoretical and experimental results described in Mitsuyasu & Honda (1982). The main difference observed is in the wave energy density decay rate in both cases for the same water depth. The deep water wave shows higher decay rate than the intermediate depth water wave over the same distance traveled since the deep water has more waves than the intermediate depth water over the same length of the solution domain. This can be seen in Table 4.1 which shows the decay rate, Δ, calculated from the time averaged total energy density factor, by fitting the relationship

$$\frac{\overline{E}}{\overline{E_0}} = \overline{\alpha}_T = exp(-\Delta x) \tag{4.12}$$

Theoretical and experimental values of Δ; (Δ_{theory} and Δ_{exp}) are from Mitsuyasu & Honda (1982). The decay rate calculated from numerical results (Δ_{num}) show very good agreement with the theoretical and experimental values.

To better understand the physics leading to difference in decay rate, we analyze various aspects of viscous, nonlinear, rotational and transient water waves in the following sections.

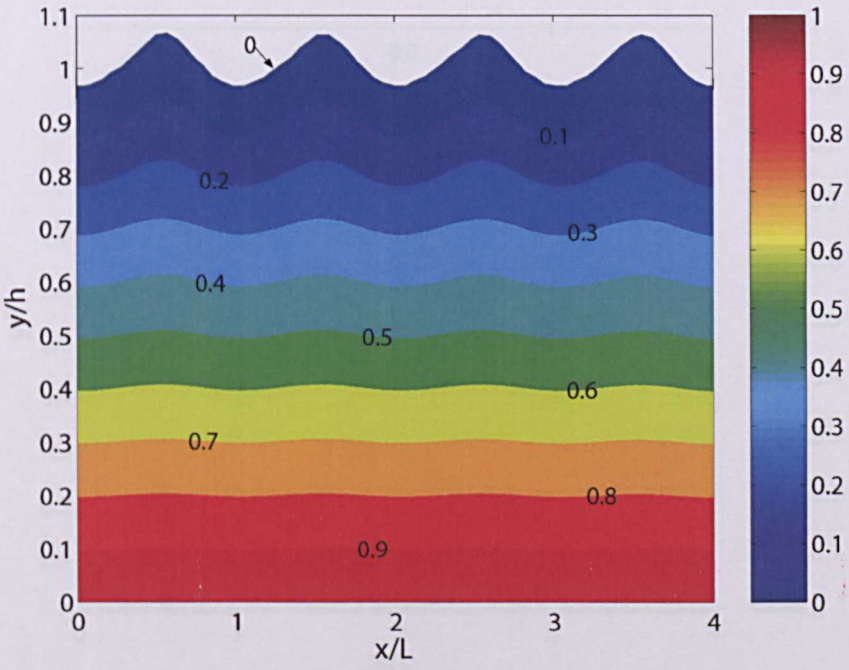

Figure 4.3: Nondimensional pressure in the domain of potential flow in deep water wave; case C2.

4.3 Pressure in the water waves

The pressure inside the water waves include static pressure and dynamic pressure due to presence of wave. The pressure is nondimensionalized as

$$\overline{p} = \frac{p}{\rho_w g h} \tag{4.13}$$

here, ρ_w is density of water, g is acceleration due to gravity and h is mean height of water. Nondimensionalized pressure in the domain of deep water wave case of potential flow and viscous flow are shown in the figure 4.3 and 4.4 respectively. To a large extent in the horizontal direction, the pressure is uniformly distributed while increasing in the vertical direction. The observed change in pressure inside the water is however unnoticeable due to presence of large hydrostatic pressure which exists even without the presence of the waves.

In order to visualize small dynamic pressure changes in the water wave due to

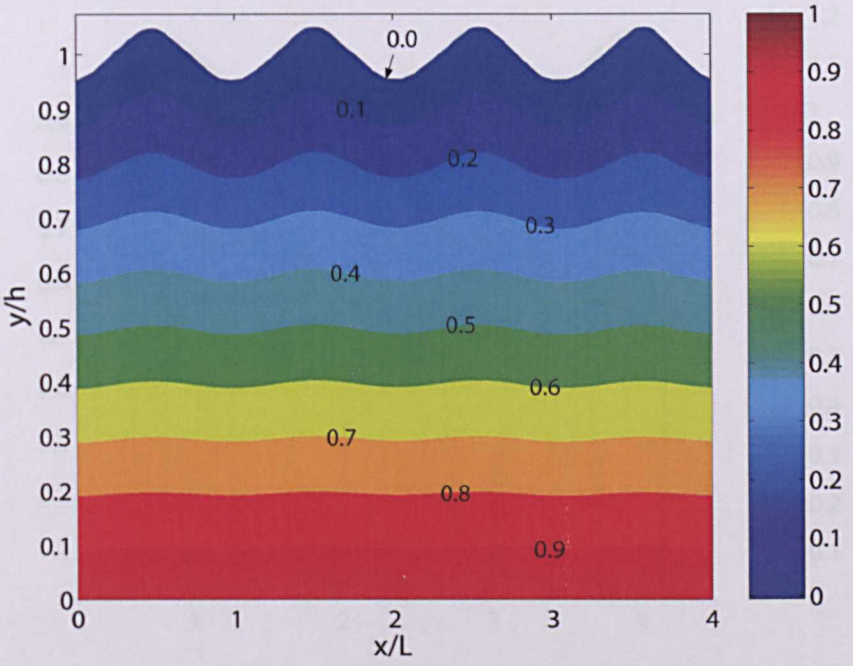

Figure 4.4: Nondimensional pressure in the domain of viscous flow in deep water wave; case C2.

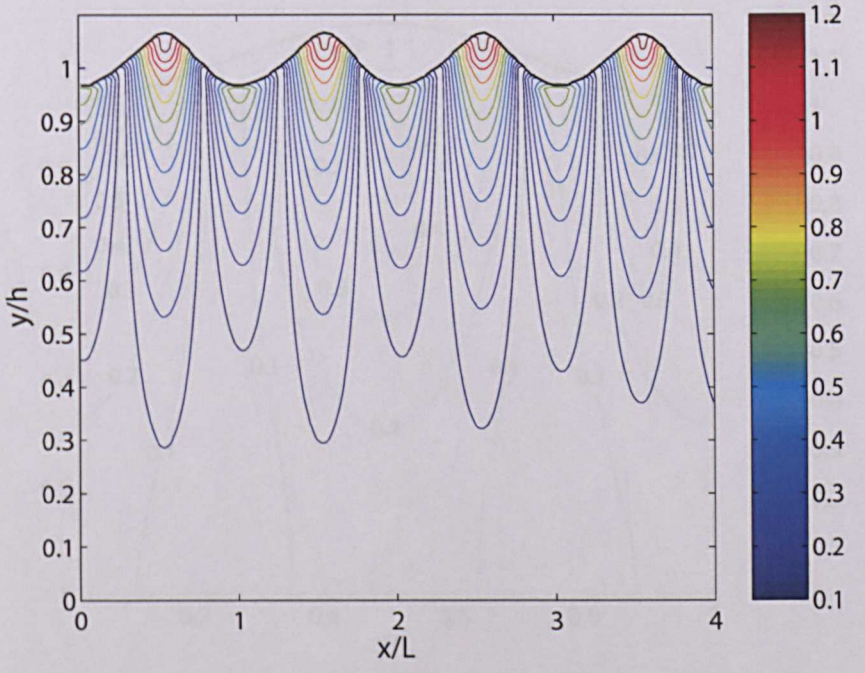

Figure 4.5: Pressure isolines in the domain of potential flow in deep water wave; case C2.

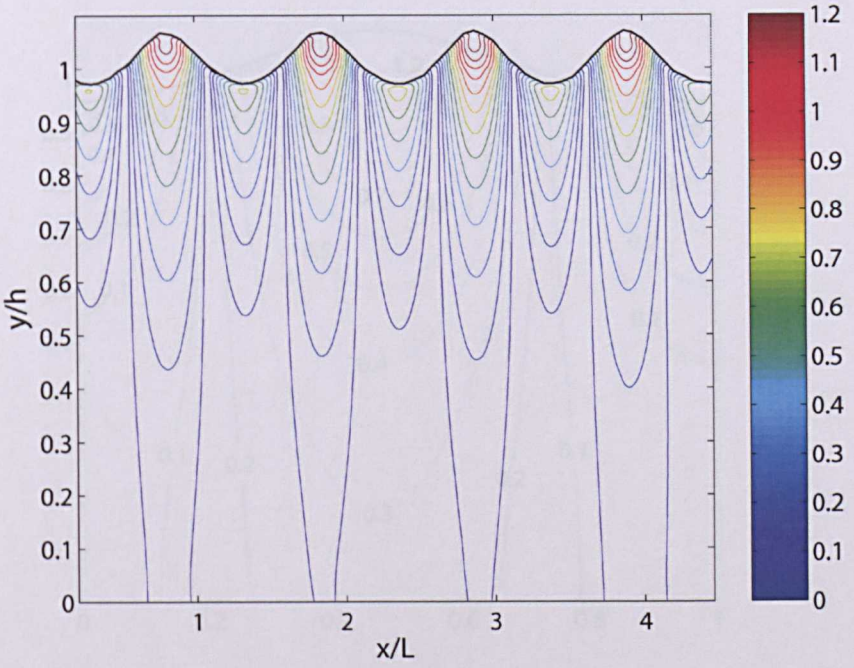

Figure 4.6: Pressure isolines in the domain of viscous flow in deep water wave; case C2.

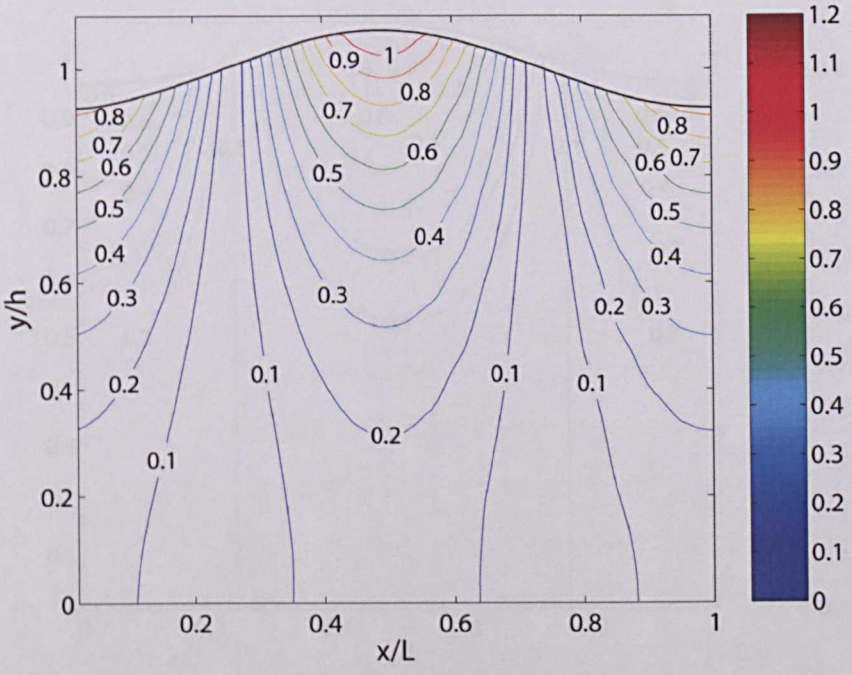

Figure 4.7: Pressure isolines in typical wave of potential flow in intermediate depth water wave; case C1.

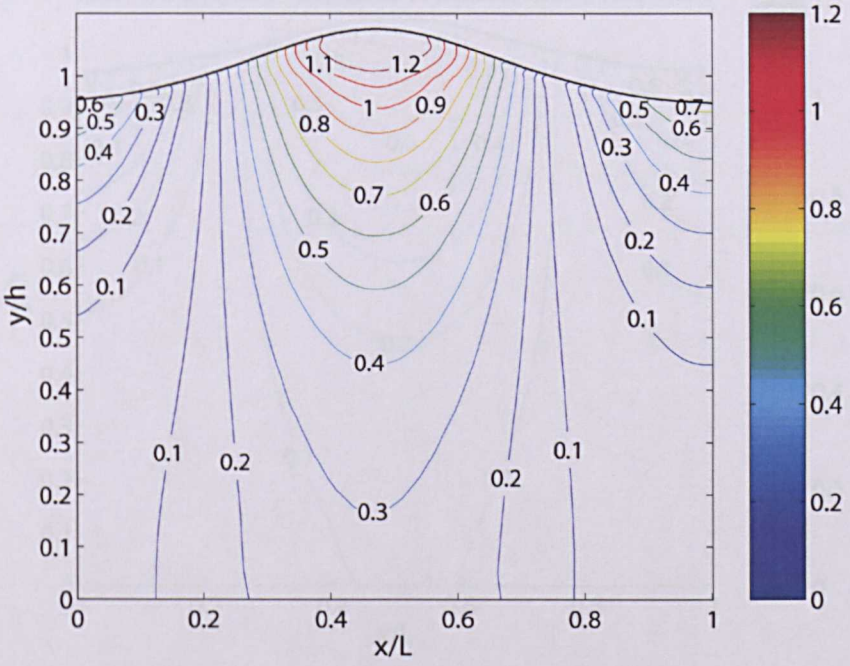

Figure 4.8: Pressure isolines in typical wave of viscous flow in intermediate depth water wave; case C1.

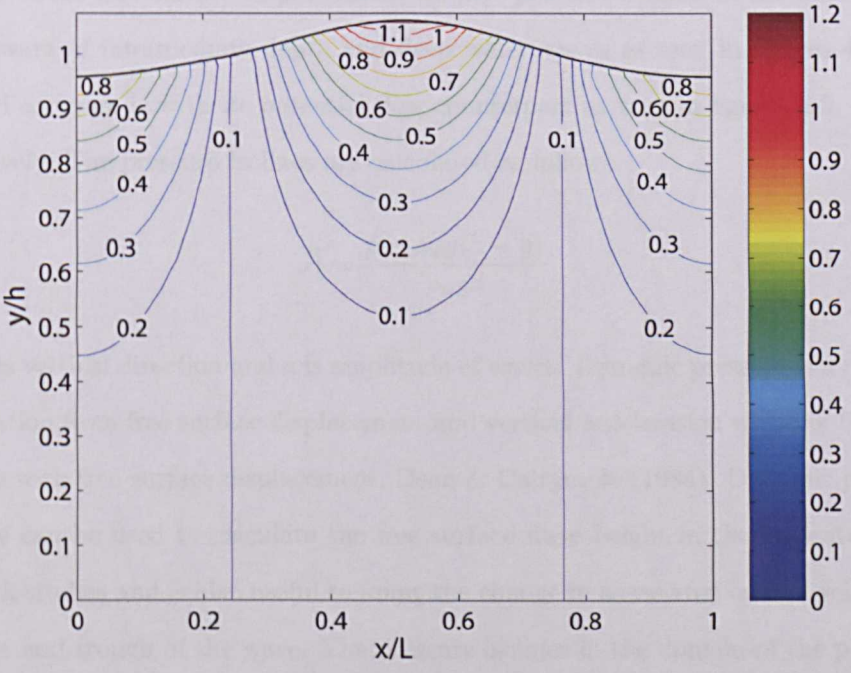

Figure 4.9: Pressure isolines in the domain of potential flow in deep water wave; case C2.

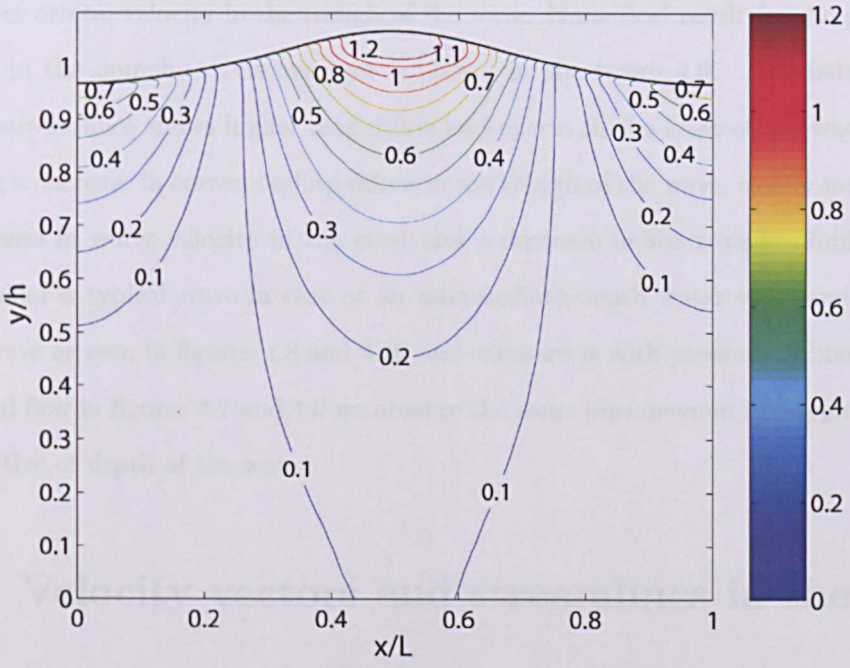

Figure 4.10: Pressure isolines in the domain of viscous flow in deep water wave; case C2.

presence of the free surface displacement, we plot pressure isolines in the domain and typical wave of intermediate depth and deep water waves as seen in figures 4.6, 4.8, 4.10 and compare it with its potential flow counterpart as seen in figures 4.5, 4.7, 4.9 respectively. The pressure isolines are calculated as follows

$$\overline{P_i} = \frac{p - \rho_w g(h - y)}{\rho_w g a} \tag{4.14}$$

here, y is vertical direction and a is amplitude of waves. Dynamic pressure is a result of contribution from free surface displacement and vertical acceleration which is 180 ° out of phase with free surface displacement, Dean & Dalrymple (1984). Dynamic pressure response can be used to calculate the free surface wave height in the laboratory and fieldwork studies and is also useful to know the change in associated orbital velocity in the crest and trough of the wave. The pressure isolines in the domain of the potential flow for the deep water waves is shown in figure 4.5. It shows uniform distribution of the pressure isolines in the crest and trough indicating higher orbital velocity in the crest

and lower orbital velocity in the trough of the wave. Numerical result for the pressure isolines in the domain of viscous flow is shown in the figure 4.6. The distribution of pressure isolines shows higher magnitude and extent in the crest of the wave while showing a decrease in corresponding values in the trough of the wave, clearly indicating an increase in water velocity in the crest and a decrease in the trough. Similarly, if we consider a typical wave in case of an intermediate depth water wave and a deep water wave as seen in figures 4.8 and 4.10 and compare it with pressure isolines in the potential flow in figures 4.7 and 4.9 we observe the same phenomenon in a typical wave irrespective of depth of the water.

4.4 Velocity vectors and streamlines in the water waves

4.4.1 Velocity vectors

The velocity vectors in the water waves are important since its variation shows an increase or decrease in the kinetic energy flux in the water waves. There is an orbital movement of water in the presence of wave and velocity vectors are used to illustrate it. The velocity is nondimensionalized by the wave amplitude a, wave number k and wave speed c and is calculated as

$$\overline{u} = \frac{u}{akc} \tag{4.15}$$

$$\overline{v} = \frac{v}{akc} \tag{4.16}$$

In figure 4.11, the velocity vectors in water shows periodic feature of the wave. To investigate further, velocity distributions in a typical wave in cases C1 and C2 are plotted and compared with the analytical solutions of the corresponding potential flow.

The velocity vectors and contours of velocity magnitude for case C1 and case C2 as per the analytical solutions of the potential flow and the numerical results for the

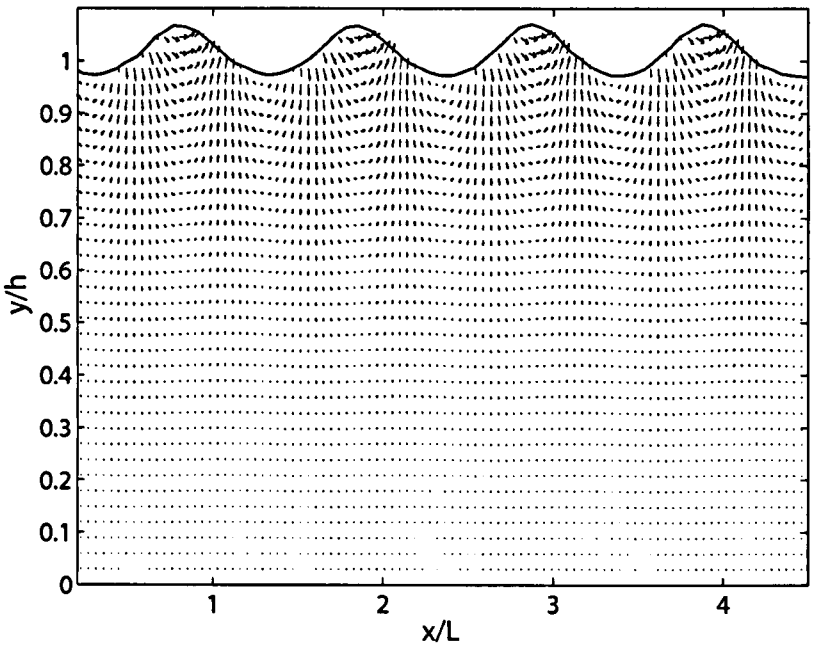

Figure 4.11: Nondimensional velocity vectors in the domain of viscous flow.

viscous flow are shown in figures 4.12, 4.13, 4.14 and 4.15 respectively. On comparing these results we observe that for the viscous flow the velocity contours with the values which are lower than 0.8 move to higher locations, this indicates that in most lower parts of the water wave, the velocity of the viscous flow is lower than the potential flow because of the resistance from the viscosity. We also observe that in the case of the viscous flow the velocity becomes higher in the crest than that in the potential flow because the resistance from the friction in the water decreases from the water into the air and this allows a higher velocity in the crest.

4.4.2 Streamlines

To investigate further we plot streamlines in the water waves. The stream function(ψ) for two dimensional flow in terms of flow velocity can be expressed as:

$$\boldsymbol{u} = \nabla \times \vec{\psi} \tag{4.17}$$

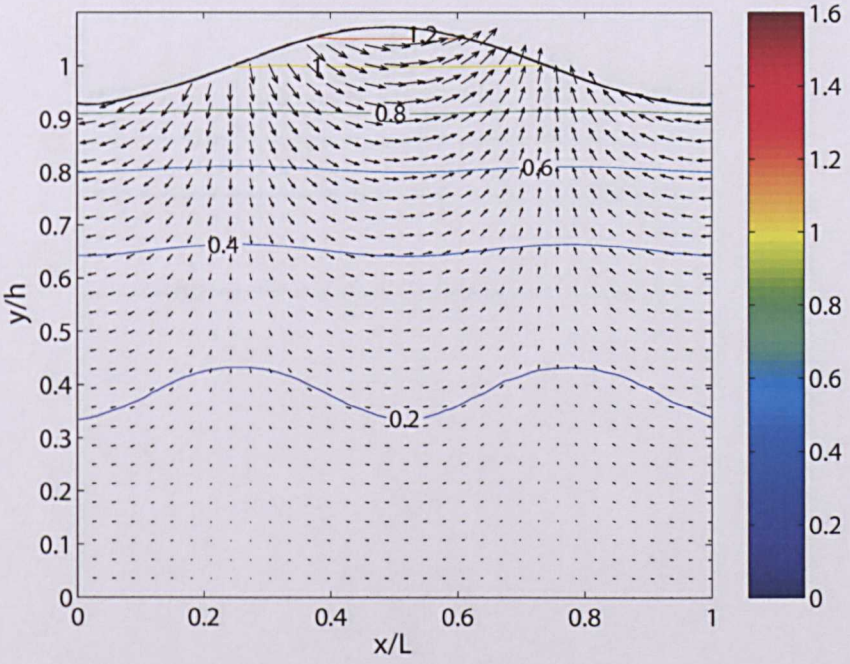

Figure 4.12: Nondimensional velocity vectors in a typical wave of potential flow; case C1.

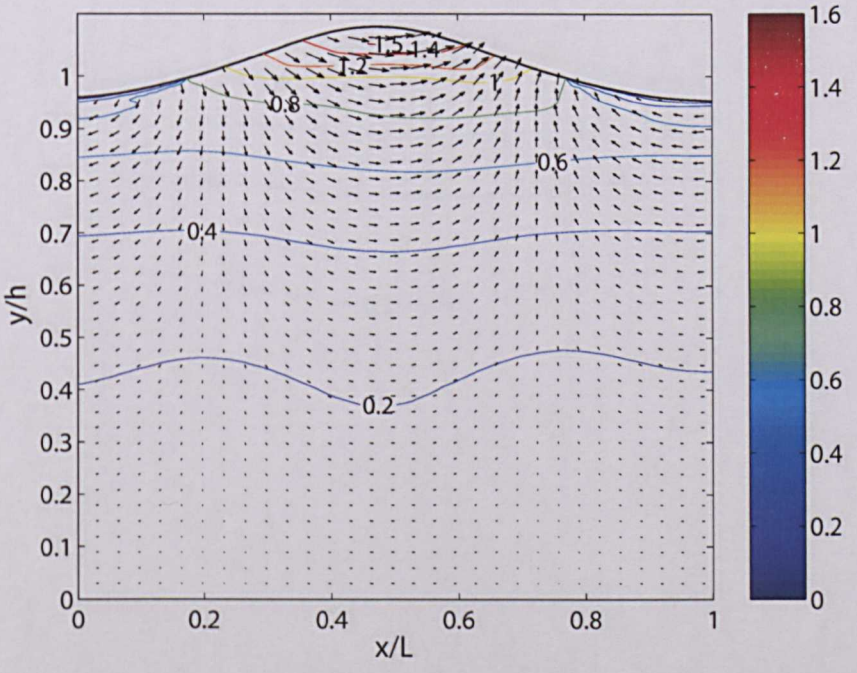

Figure 4.13: Nondimensional velocity vectors in a typical wave of viscous flow; case C1.

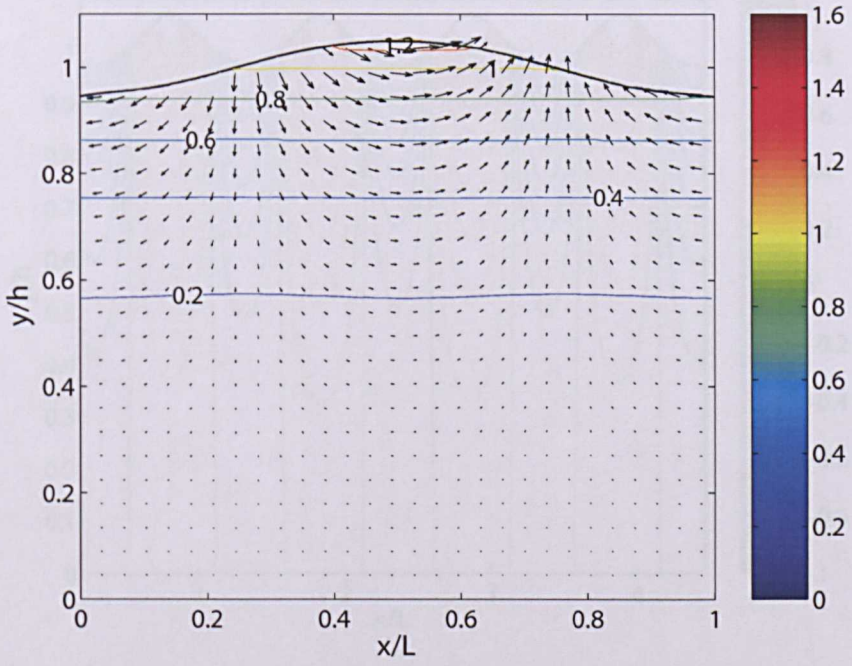

Figure 4.14: Nondimensional velocity vectors in a typical wave of potential flow; case C2.

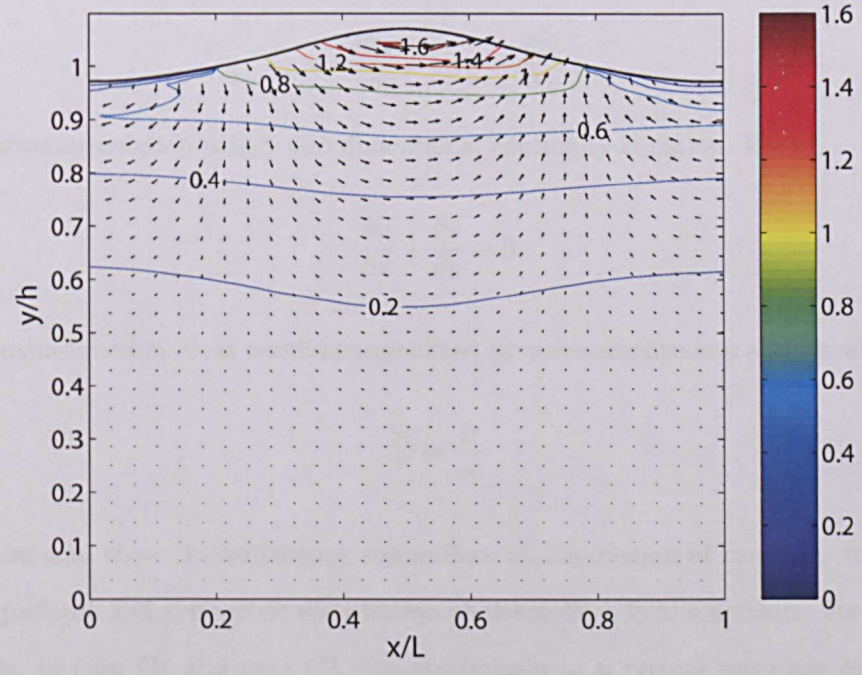

Figure 4.15: Nondimensional velocity vectors in a typical wave of viscous flow; case C2.

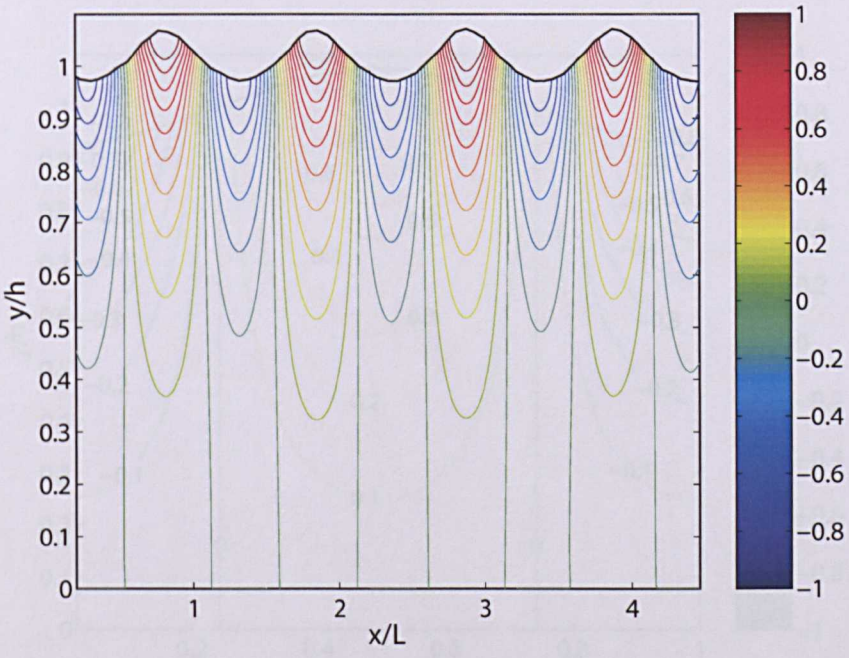

Figure 4.16: Streamlines in the domain of viscous flow.

here, $\vec{\psi} = (0, 0, \psi)$ and $\boldsymbol{u} = (u, v, 0)$. In the cartesian coordinate system it is expressed as,

$$u = \frac{\partial \psi}{\partial y}, \qquad v = -\frac{\partial \psi}{\partial x} \tag{4.18}$$

The above formulation satisfy two dimensional continuity equation. Hence,

$$\frac{\partial u}{\partial x} + \frac{\partial v}{\partial y} = 0 \tag{4.19}$$

The stream function, ψ, is nondimensionalized by wave amplitude a and wave speed c

$$\overline{\psi} = \frac{\psi}{ac} \tag{4.20}$$

Figure 4.16 shows instantaneous streamlines in the domain of case C2. It mostly shows periodic and symmetric distribution of streamlines in the domain. For further analysis, in case C1 and case C2, the streamlines in a typical wave are compared with the analytical solution of the potential flow. Figures 4.17 and 4.19 shows the

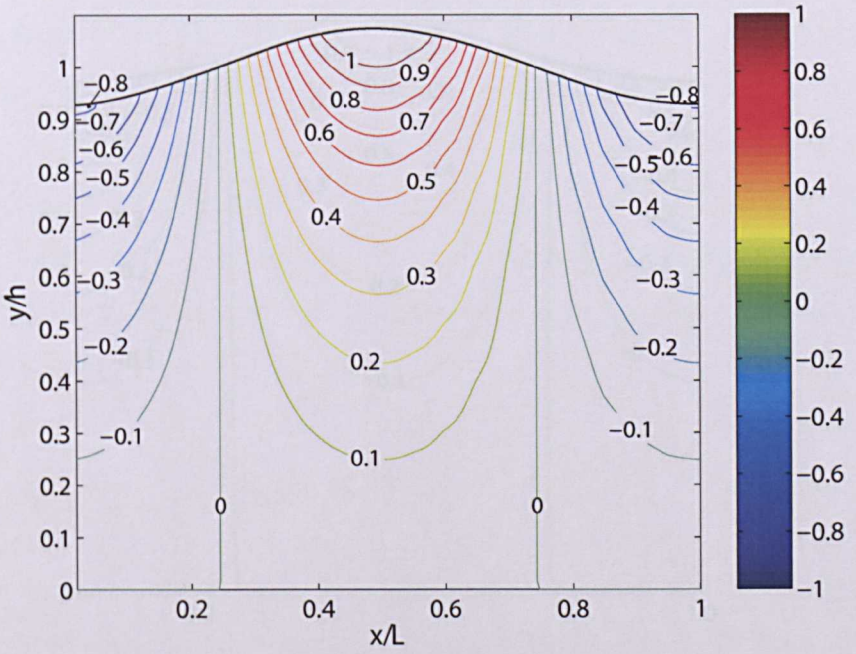

Figure 4.17: Streamlines in a typical wave of potential flow; case C1.

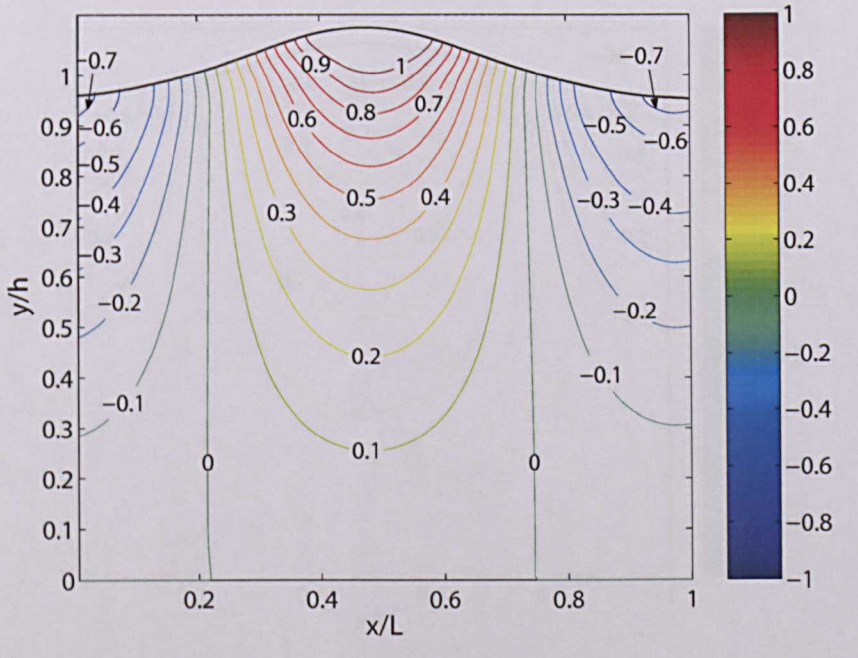

Figure 4.18: Streamlines in a typical wave of viscous flow; case C1.

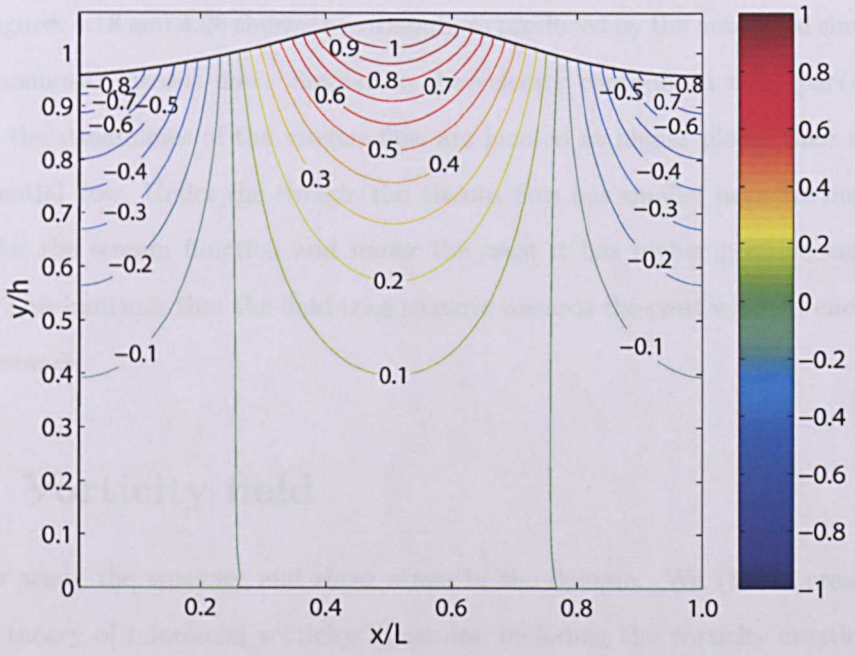

Figure 4.19: Streamlines in a typical wave of potential flow; case C2.

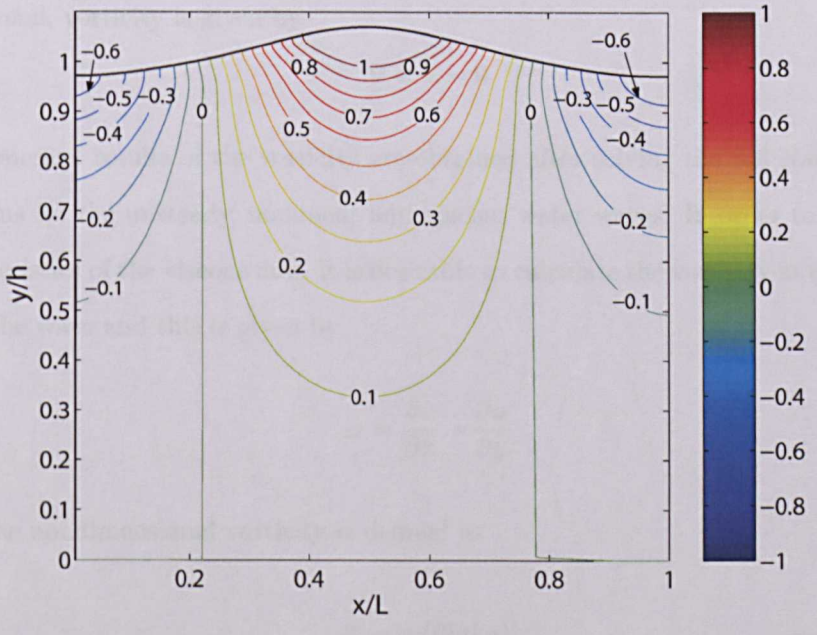

Figure 4.20: Streamlines in a typical wave of viscous flow; case C2.

streamlines in case C1 and case C2 produced by the analytical solution of the potential flow. Figures 4.18 and 4.20 shows the streamlines produced by the numerical simulation of the nonlinear viscous flow. Similar to the velocity contours in most parts of the domain the streamlines of the viscous flow are located at higher places than those of the potential flow. Under the trough, the viscous flow has smaller negative maximum values for the stream function and under the crest it has higher positive maximum values. This indicates that the fluid tries to move towards the crest where it encounters less resistance.

4.5 Vorticity field

We now study the vorticity and shear stress in the domain. Wu (1995) presented a general theory of interfacial vorticity dynamics, including the vorticity creation from interface and mentioned the difference observed in the vorticity creation on a solid wall and an interface. It is impossible to estimate boundary vorticity flux using a potential solution as inviscid terms are self-balanced. In the potential flow, since the flow is irrotational, vorticity is given by,

$$\nabla \times \mathbf{v} = 0 \tag{4.21}$$

The numerical results of the vorticity are obtained after solving the full Navier-Stokes equations for the unsteady, nonlinear and viscous water waves. In order to reveal the characteristics of the viscous flow, it is desirable to calculate the vorticity at every point under the wave and this is given by

$$\omega = \frac{\partial v}{\partial x} - \frac{\partial u}{\partial y} \tag{4.22}$$

while the nondimensional vorticity is defined as

$$\overline{\omega} = \omega/(2ak\sigma) \tag{4.23}$$

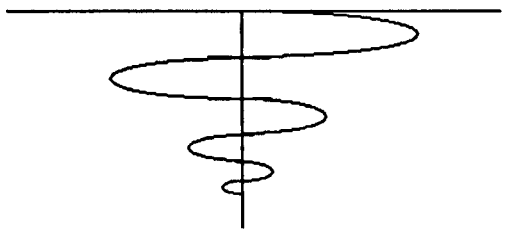

Figure 4.21: A representation of the behavior of the vorticity field with depth

According to Kinsman (1965) and Lamb (1930), for a low Reynolds number flow, the analytical solution for the vorticity in water wave with small amplitude is given by

$$\omega_{an} = -2ak\sigma e^{\left\{\left(\frac{\sigma}{2\nu}\right)^{\frac{1}{2}}z - \frac{2\sigma}{R_w}t\right\}} e^{i\left[kx+\left(\frac{\sigma}{2\nu}\right)^{\frac{1}{2}}z+\sigma t\right]} \tag{4.24}$$

where, ν is the kinematic viscosity of the fluid, z is the depth of water and R_w is the wave Reynolds number, which is defined as

$$R_w \equiv \frac{\sigma}{\nu k^2} \tag{4.25}$$

The behavior of the vorticity field is shown in figure 4.21. From the exponential of real argument we can see that the vorticity is damped to zero exponentially in an oscillatory manner with the increase in water depth z.

The vorticity profile produced by the inviscid rotational Gerstner wave can be found from Lamb (1930)

$$\omega = -\frac{2a^2k^2\sigma e^{2kz_0}}{1 - a^2k^2e^{2kz_0}} \tag{4.26}$$

where z_0 is a parameter given by

$$x = \frac{\theta}{k} + ae^{kz_0}\sin\theta \tag{4.27}$$

$$z = z_0 - ae^{kz_0}\cos\theta \tag{4.28}$$

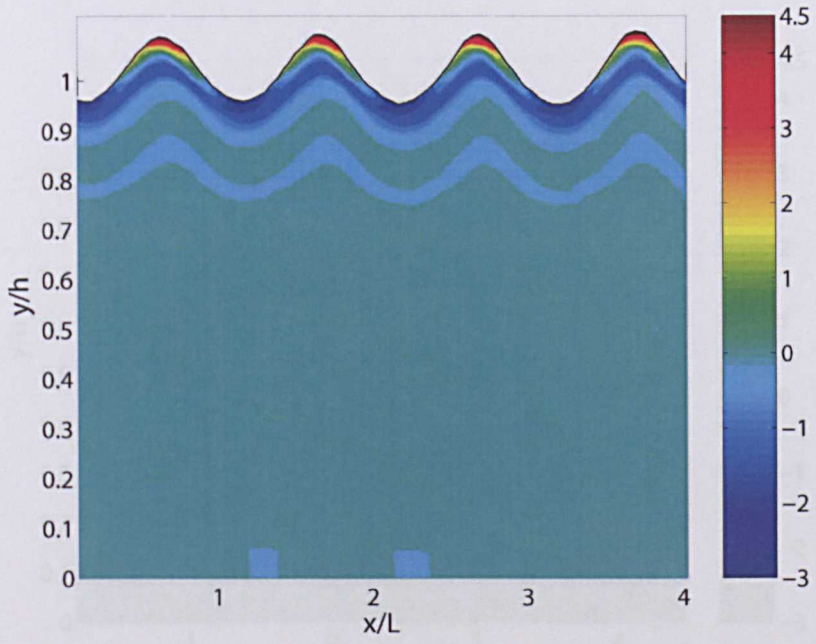

Figure 4.22: Nondimensional vorticity ($\overline{\omega}$) of case C1.

The vorticity is damped in the Gerstner's wave but does not produce oscillations, which indicates that water rotates in the same direction in the whole domain.

The numerical results for the vorticity fields under the water waves for cases C1, C2 and C3 are shown in figures 4.22, 4.23 and 4.24 respectively. They reveal the oscillatory distribution of the vorticity, which indicates that water rotates in different directions in different parts of the domain. In these figures we observe a periodic thick layer of active vorticity near the water surface. The magnitude of the vorticity becomes smaller and reduces to zero with increase in the depth. In all the cases, the values of nondimensional vorticity are almost the same, this indicates that the vorticity ω is proportional to $ak\sigma$. Small variation in the vorticity near the bottom boundary is still clearly visible in the intermediate depth water wave in case C1 as seen in figure 4.22, while for the deep water waves in cases C2 and C3 the vorticity has become too small to be visible.

We now analyze a typical wave to reveal the details of vorticity for the cases C1, C2 and C3. In both cases C1 and C2, referring to intermediate depth water waves and

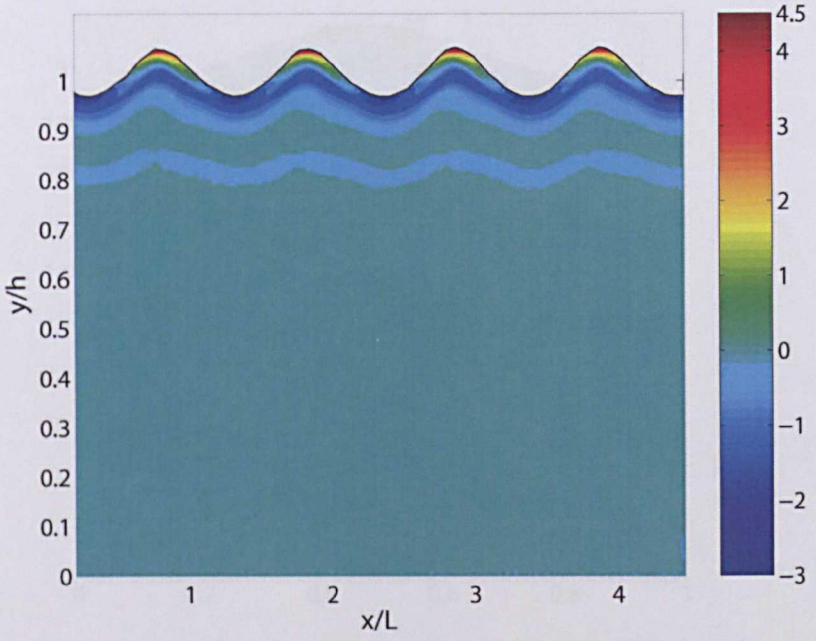

Figure 4.23: Nondimensional vorticity ($\overline{\omega}$) of case C2.

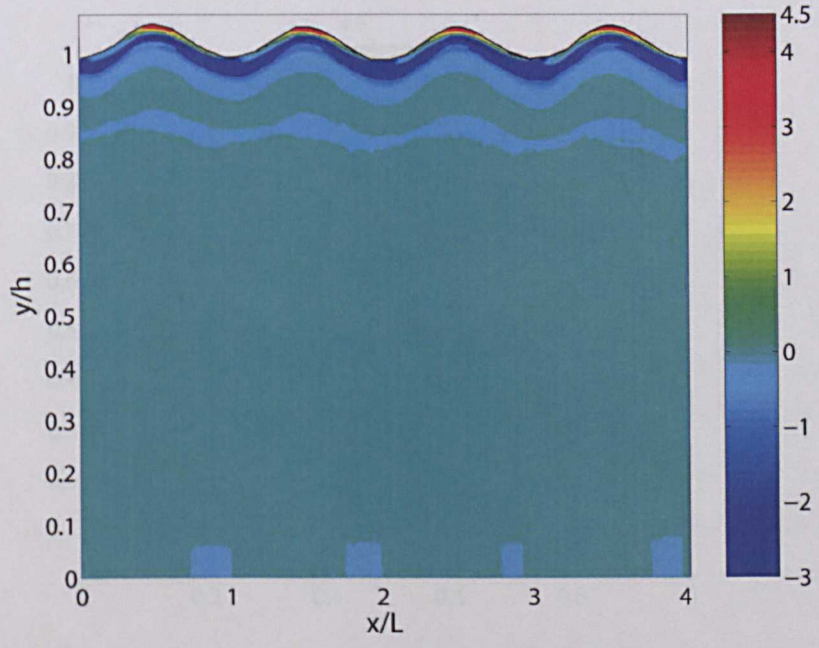

Figure 4.24: Nondimensional vorticity ($\overline{\omega}$) of case C3.

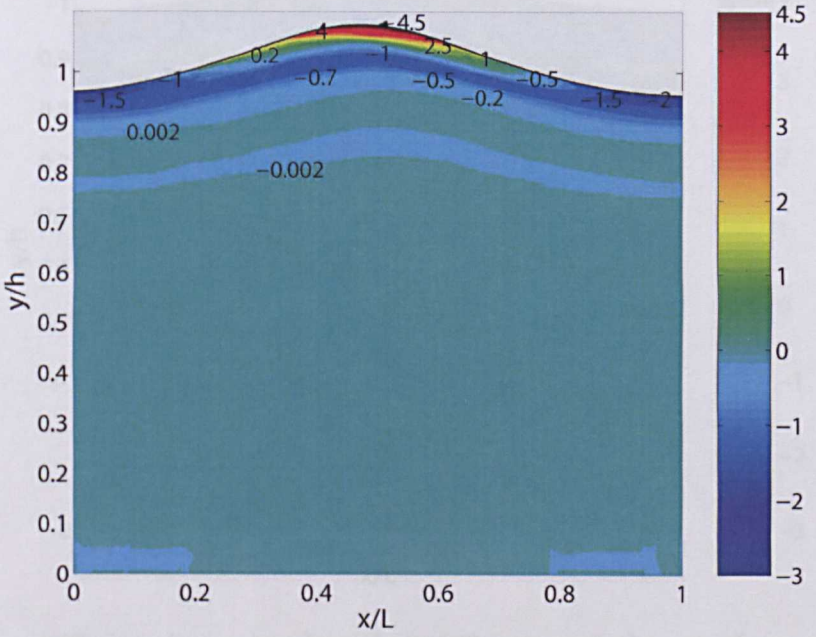

Figure 4.25: Nondimensional vorticity ($\overline{\omega}$) in a typical wave of case C1.

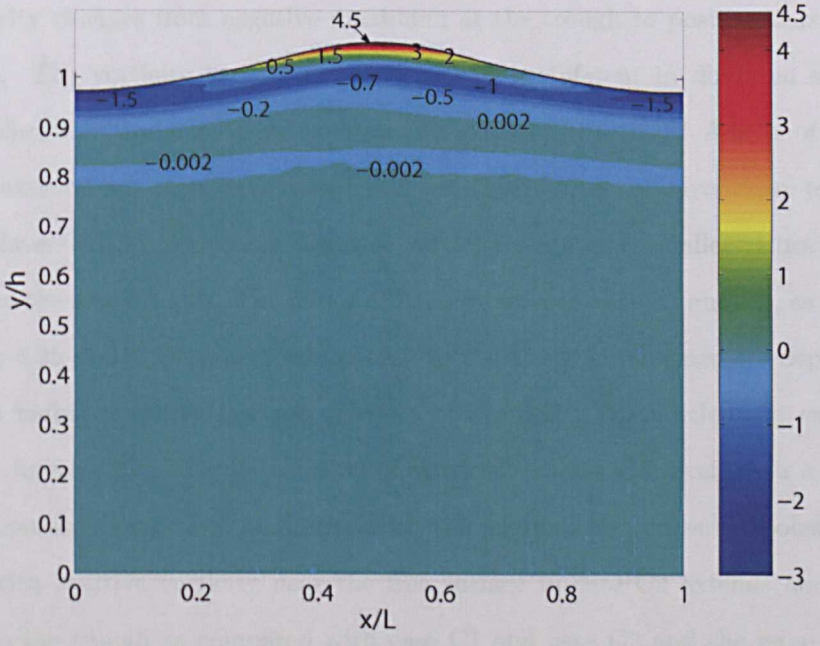

Figure 4.26: Nondimensional vorticity ($\overline{\omega}$) in a typical wave of case C2.

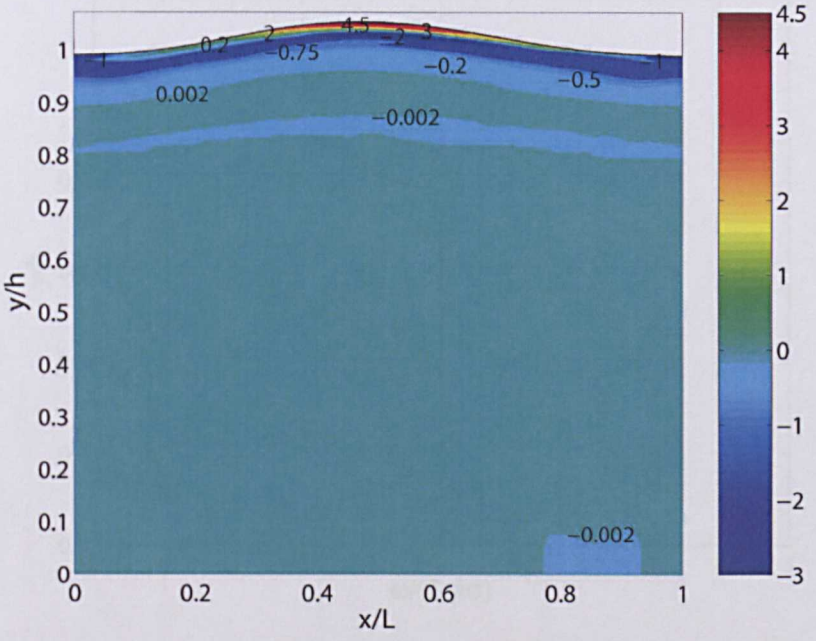

Figure 4.27: Nondimensional vorticity ($\overline{\omega}$) in a typical wave of case C3.

deep water waves as seen in figures 4.25 and 4.26 respectively, the vorticity contours show a similar magnitude of vorticity near the water surface. Along the free surface, the vorticity changes from negative maximum at the trough to positive maximum at the crest. The vorticity in the crest and trough is different in direction signifying the 'anticlockwise' and 'clockwise' rotation of the fluid respectively. A layer of negative vorticity extends from trough to trough and we observe from this layer down to the bed that the layers with positive and negative vorticity reduces to smaller values with the increase in the water depth. The minor difference between case C1 and C2, as observed in figures 4.25 and 4.26 respectively is that in the troughs, intermediate depth water wave has higher vorticity because of effect of the bed. The vorticity in case C3 is shown in figure 4.27. The distribution of vorticity in case C3, even with a different wave steepness, shows much similarity with the previous two cases. We observe that a layer with positive vorticity near the free surface in case C3 extends horizontally further to the trough as compared with case C1 and case C2 and the large vorticity layer is thinner for smaller ak compared with case C1 and case C2.

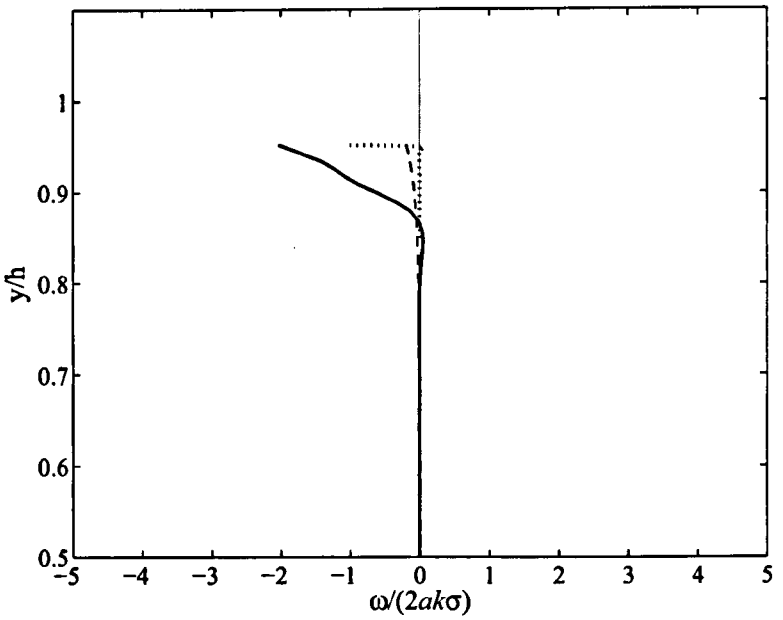

Figure 4.28: In case C1: x/L = 0, thick black line is the current numerical simulation result, dotted line is the analytical solution for Gerstner's wave (Lamb 1930), grey line is the analytical solution of low Reynolds number flow (Kinsman 1965).

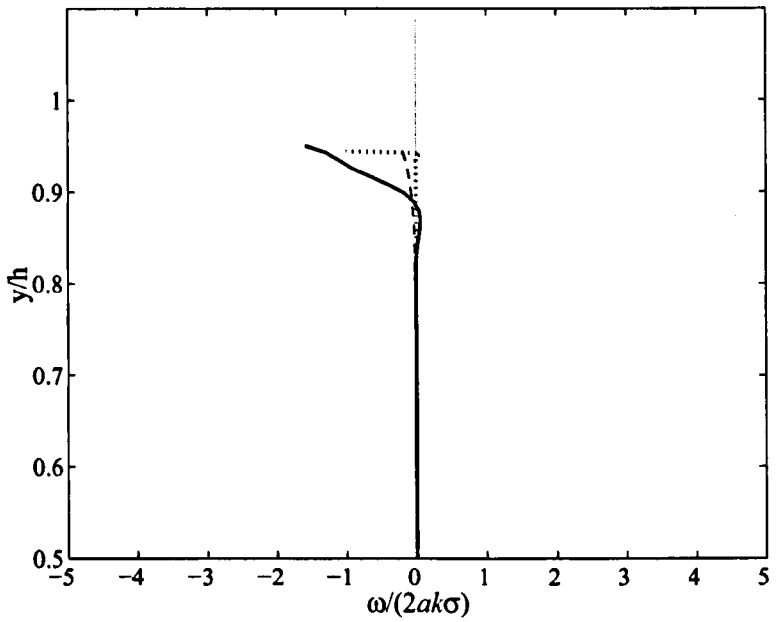

Figure 4.29: In case C2: x/L = 0, thick black line is the current numerical simulation result, dotted line is the analytical solution for Gerstner's wave (Lamb 1930), grey line is the analytical solution of low Reynolds number flow (Kinsman 1965).

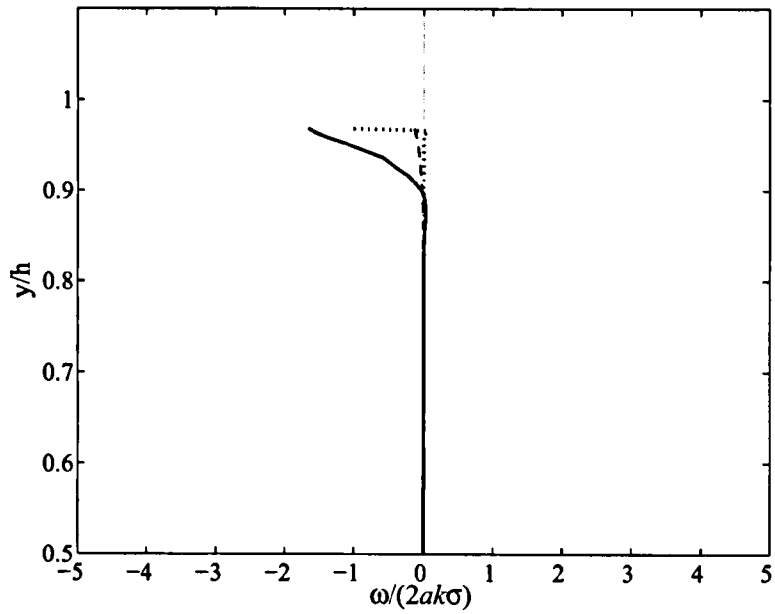

Figure 4.30: In case C3: x/L = 0, thick black line is the current numerical simulation result, dotted line is the analytical solution for Gerstner's wave (Lamb 1930), grey line is the analytical solution of low Reynolds number flow (Kinsman 1965).

To further investigate the behavior of vorticity along the depth, nondimensional vorticity vs nondimensional height is plotted at 5 different locations (x/L = 0, 0.25, 0.5, 0.75, 1) and compared with the analytical solutions given by Lamb (1930) for the Gerstner's trochoidal waves and for the low Reynolds number flow as outlined by Kinsman (1965). The analytical solutions are plotted at locations x/L = 0, 0.5 and 1 as they are the main region of interest. From figures 4.28, 4.29, 4.30, 4.31, 4.32, 4.33, 4.34, 4.35, 4.36, 4.37, 4.38, 4.39, 4.40, 4.41 and 4.42, we can observe a remarkable similarity in vorticity behavior with the depth at various locations. The magnitude of vorticity and thickness of vorticity layer predicted by the numerical solutions of the viscous flow are much larger than the analytical solutions. The solution for the low Reynolds number flow suggests a very thin layer of vorticity just below the water surface and the vorticity generated on the water surface quickly reduces to zero. This is because a low Reynolds number flow is a very viscous flow and viscosity not only prevents the production of large vorticity but also slows down the rotation of the flow

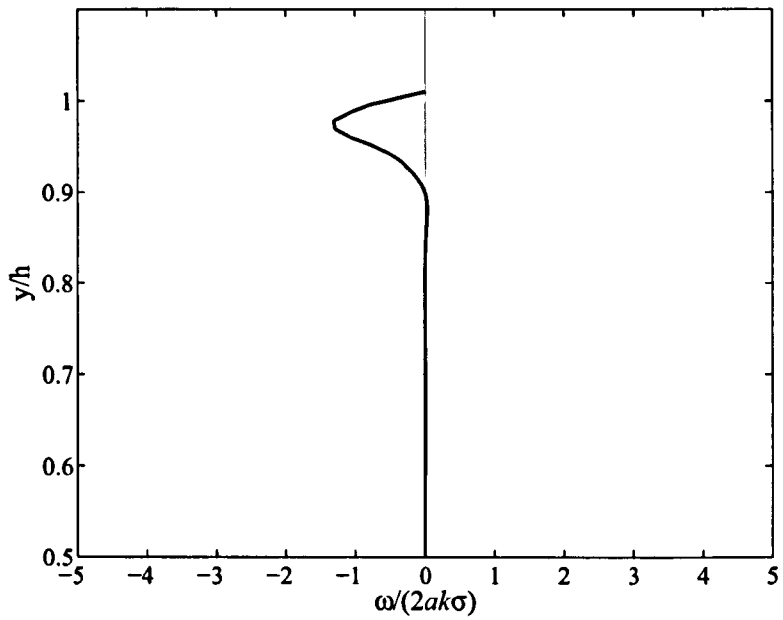

Figure 4.31: In case C1: x/L = 0.25, thick black line is the current numerical simulation result.

very rapidly in a very thin layer. On the other hand, the solution for the Gerstner's wave is damped less quickly with depth but without oscillations. Both these solutions are found inadequate at explaining the magnitude and direction of vorticity in terms of correct understanding.

Figure 4.28, figure 4.29 and figure 4.30 depict the vorticity magnitude varying with depth under the trough of the wave at x/L = 0 in three different cases. On comparing them with analytical vorticity magnitude we observe much higher 'clockwise' rotating vortices of viscous flow in all three cases. Moving further downstream to x/L = 0.25, we observe, from figures 4.31, 4.32 and 4.33, that the magnitude of the vorticity at the free surface is close to zero, but a thick vorticity layer and oscillatory behavior is produced by viscous flow as expected while the magnitude of the vorticity is nearly the same in all cases.

As we move towards the crest at x/L = 0.5, from figures 4.34, 4.35 and 4.36, we observe the 'anticlockwise' rotation of water flow attributed to the positive vorticity in a very thin region of the free surface. The maximum value of positive vorticity

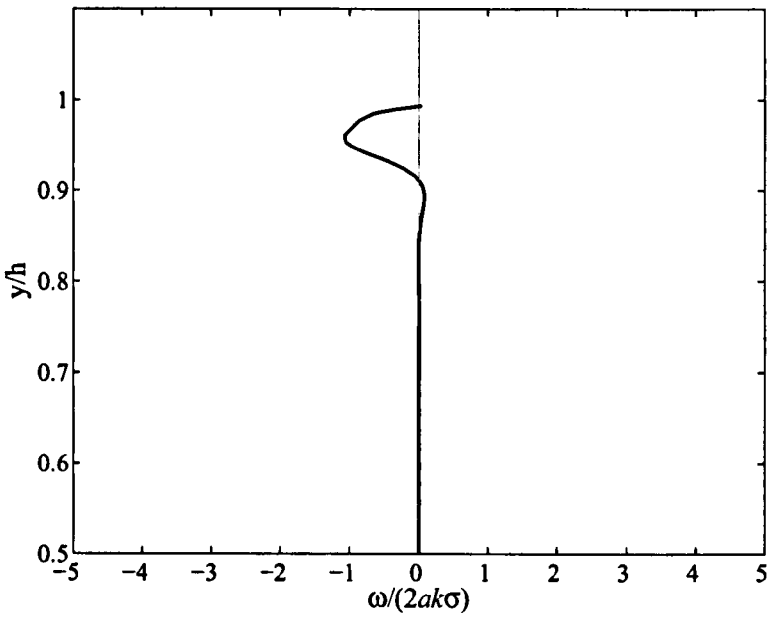

Figure 4.32: In case C2: x/L = 0.25, thick black line is the current numerical simulation result.

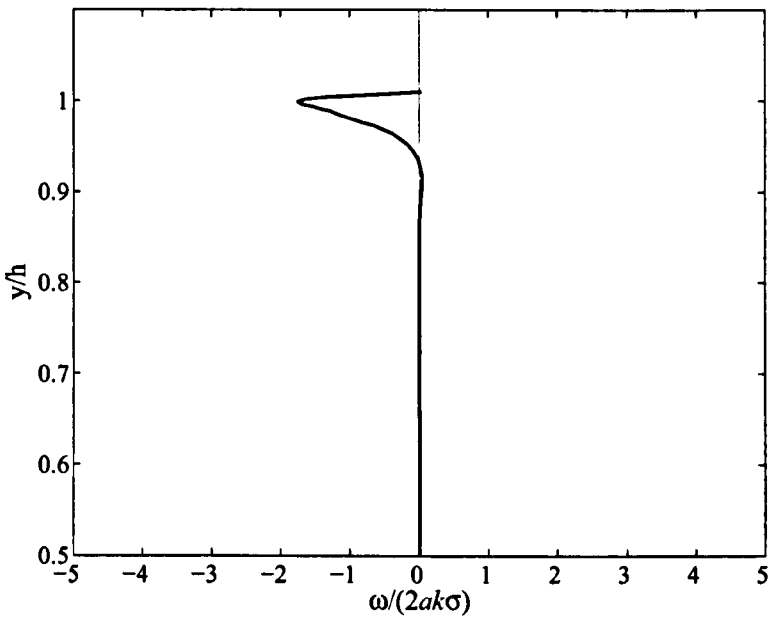

Figure 4.33: In case C3: x/L = 0.25, thick black line is the current numerical simulation result.

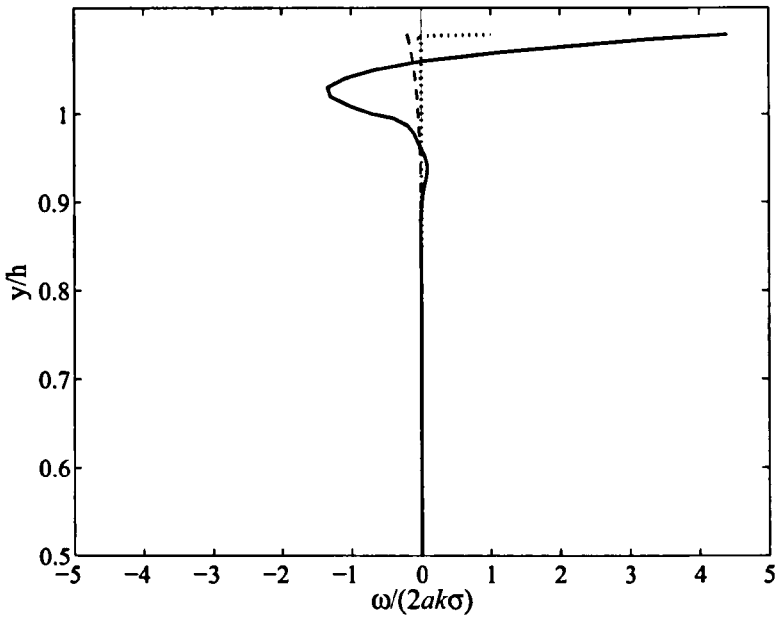

Figure 4.34: In case C1: x/L = 0.5, thick black line is the current numerical simulation result, dotted line is the analytical solution for Gerstner's wave (Lamb 1930), grey line is the analytical solution of low Reynolds number flow (Kinsman 1965).

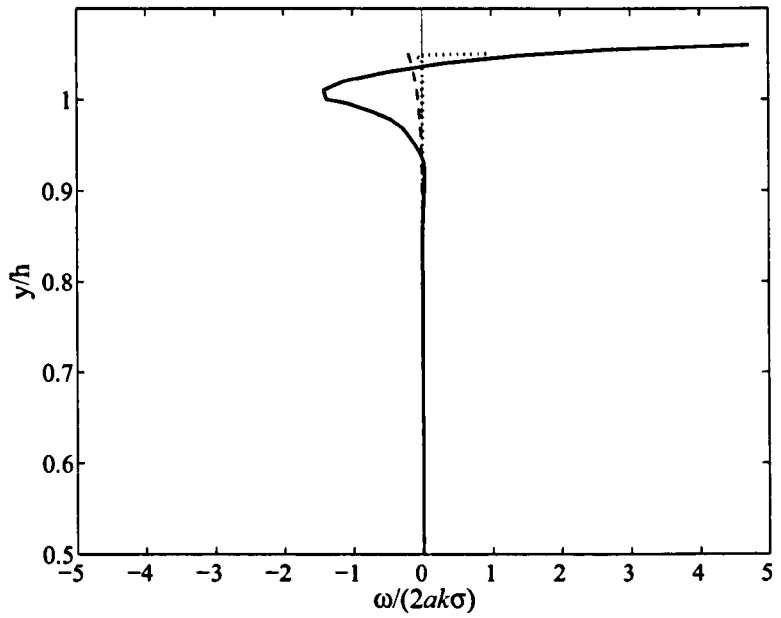

Figure 4.35: In case C2: x/L = 0.5, thick black line is the current numerical simulation result, dotted line is the analytical solution for Gerstner's wave (Lamb 1930), grey line is the analytical solution of low Reynolds number flow (Kinsman 1965).

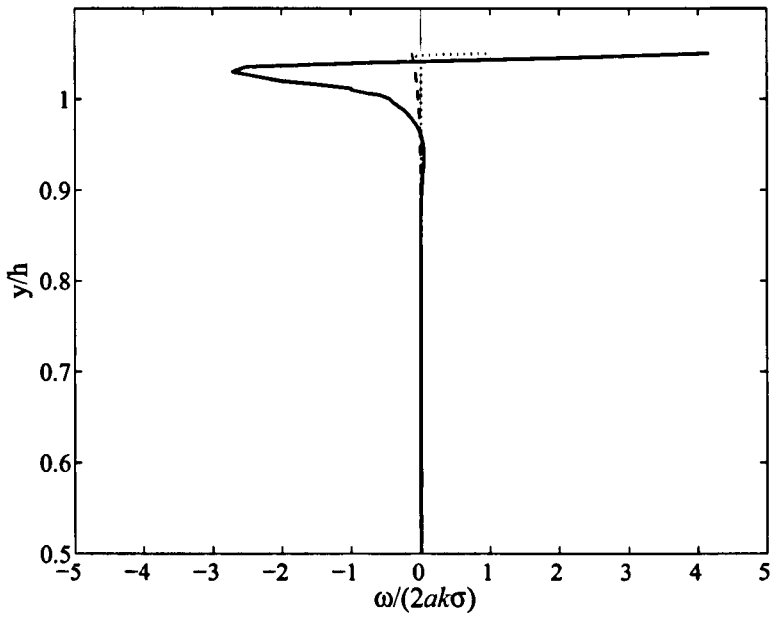

Figure 4.36: In case C3: x/L = 0.5, thick black line is the current numerical simulation result, dotted line is the analytical solution for Gerstner's wave (Lamb 1930), grey line is the analytical solution of low Reynolds number flow (Kinsman 1965).

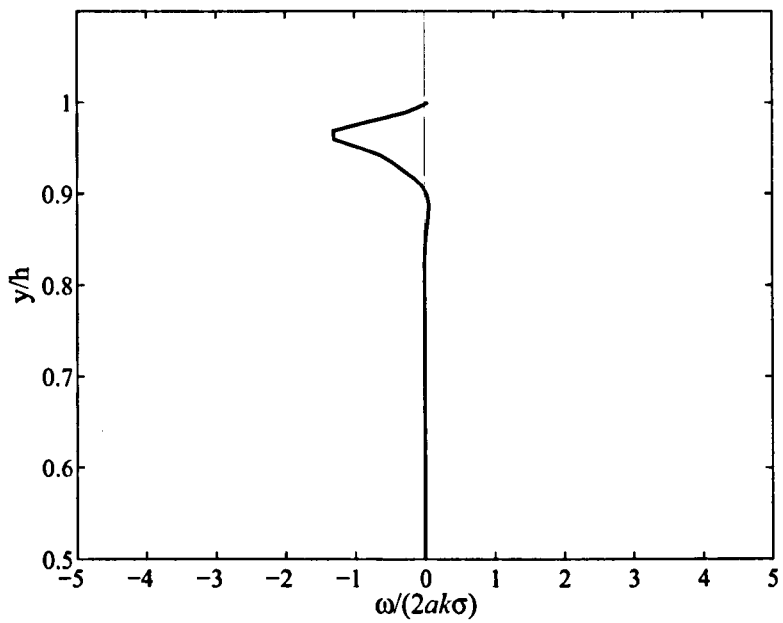

Figure 4.37: In case C1: x/L = 0.75, thick black line is the current numerical simulation result.

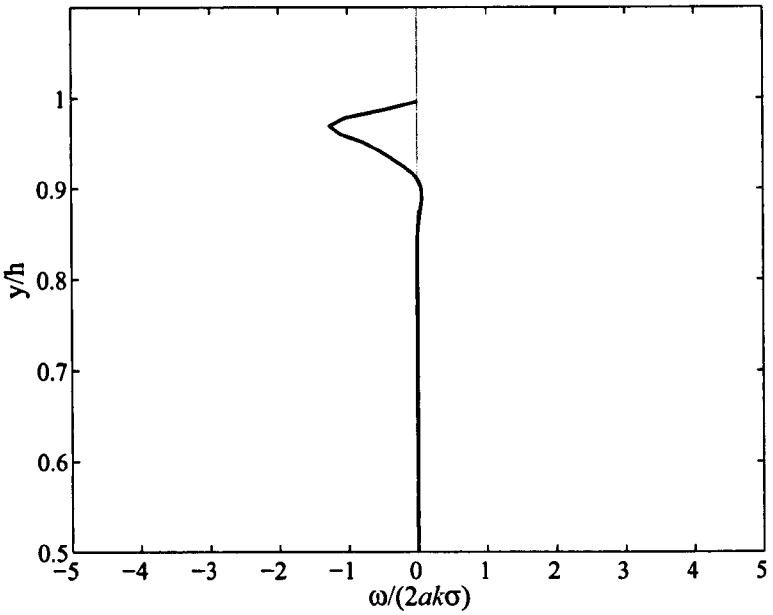

Figure 4.38: In case C2: x/L = 0.75, thick black line is the current numerical simulation result.

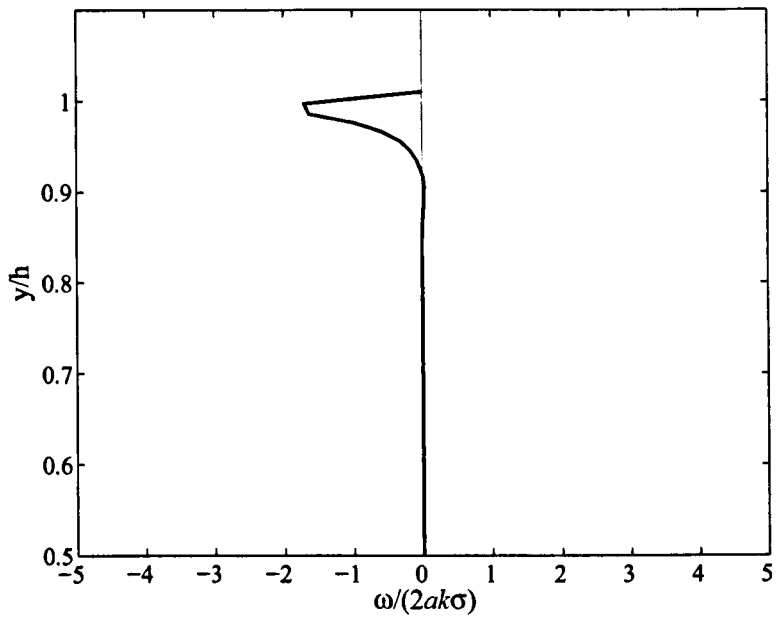

Figure 4.39: In case C3: x/L = 0.75, thick black line is the current numerical simulation result.

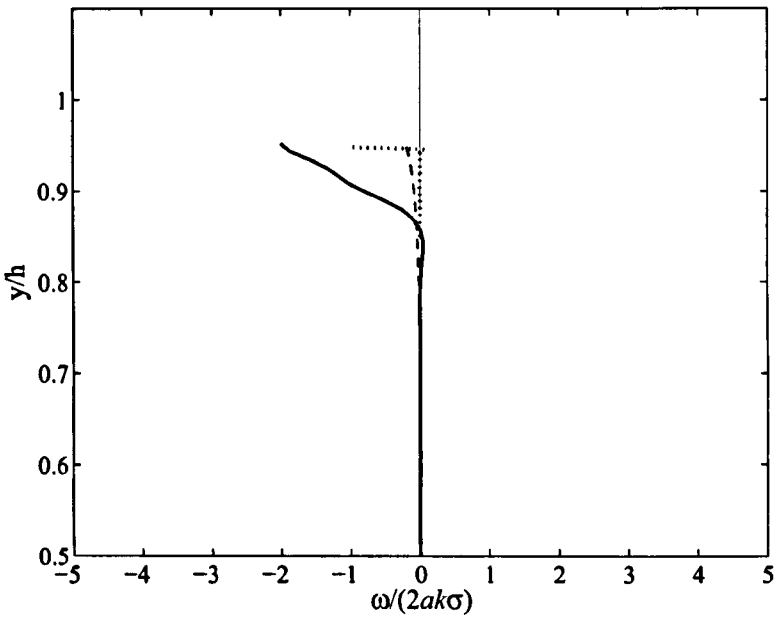

Figure 4.40: In case C1: x/L = 1, thick black line is the current numerical simulation result, dotted line is the analytical solution for Gerstner's wave (Lamb 1930), grey line is the analytical solution of low Reynolds number flow (Kinsman 1965).

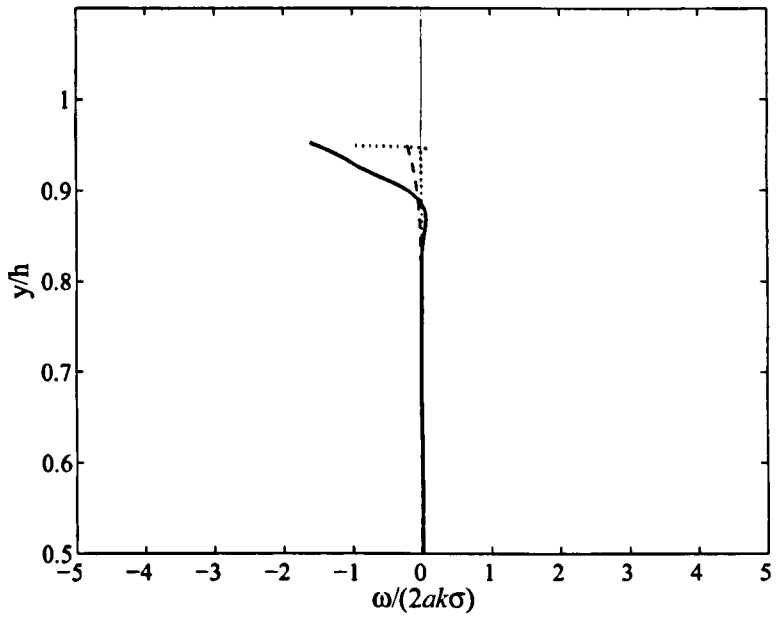

Figure 4.41: In case C2: x/L = 1, thick black line is the current numerical simulation result, dotted line is the analytical solution for Gerstner's wave (Lamb 1930), grey line is the analytical solution of low Reynolds number flow (Kinsman 1965).

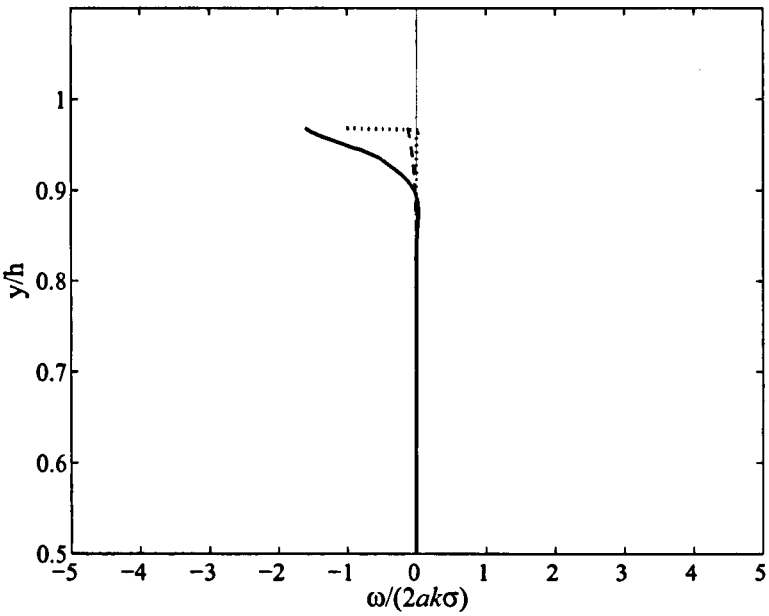

Figure 4.42: In case C3: x/L = 1, thick black line is the current numerical simulation result, dotted line is the analytical solution for Gerstner's wave (Lamb 1930), grey line is the analytical solution of low Reynolds number flow (Kinsman 1965).

is observed on the free surface at the crest, moreover, the maximum positive value observed on the crest is much higher than the maximum negative values at x/L = 0 and x/L = 0.5. Again much higher vorticity magnitude and thickness is observed than predicted by the theories. We observe higher negative vorticity immediately below the positive vorticity region which is very different from the analytical value. We also observe other oscillations as we move along the depth. Moving down to the lee side of the wave at x/L = 0.75 as seen in figures 4.37, 4.38 and 4.39, the vorticity distributions are nearly repeated in magnitude and rotation along the depth and similar to location x/L = 0.25. As we move toward the end of the wave at x/L = 1, we observe in figures 4.40, 4.41 and 4.42 the vorticity pattern being repeated in magnitude and rotation similar to that at x/L = 0.

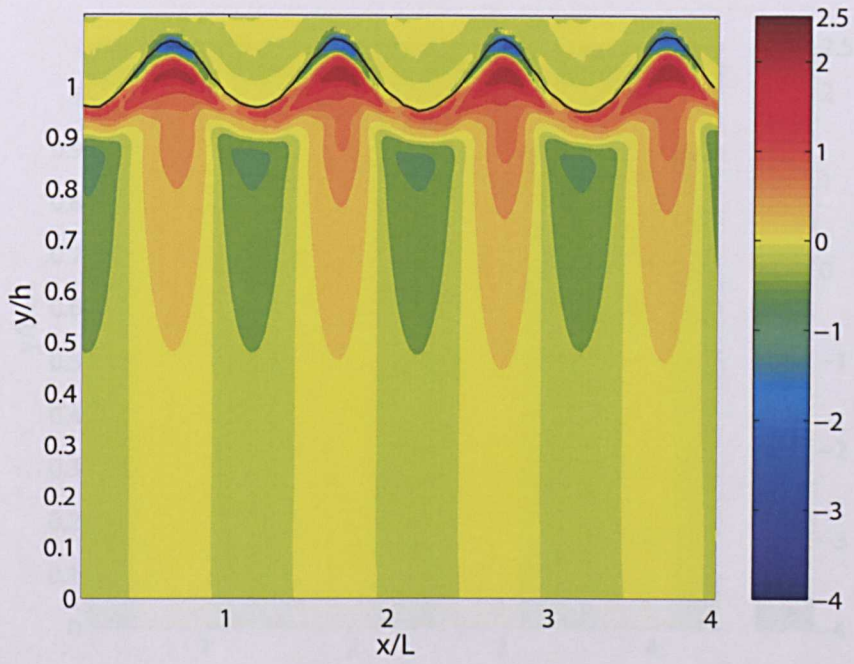

Figure 4.43: Nondimensional shear stress ($\overline{\tau}$) contours of case C1.

4.6 Shear stress

Nondimensionalized shear stress in the flow $\overline{\tau}$ is defined by

$$\overline{\tau} = \tau_m/(2\mu_w ak\sigma) \tag{4.29}$$

where

$$\tau_m = \mu_m \left(\frac{\partial u}{\partial y} + \frac{\partial v}{\partial x}\right) \tag{4.30}$$

The distributions of nondimensionalized shear stress in the domain for cases C1, C2 and C3 are shown in figures 4.43, 4.44 and 4.45 respectively. The shear stress in the air regions above the free surface shows much less variation in all the three cases and is small compared to the water, hence aiding the assumption about the magnitude of shear stress being considered to be zero on the free surface in majority of the theoretical studies. We observe that in all cases the shear stress distributions show high degree of similarity. The most important feature is the existence of a periodic thick layer of shear

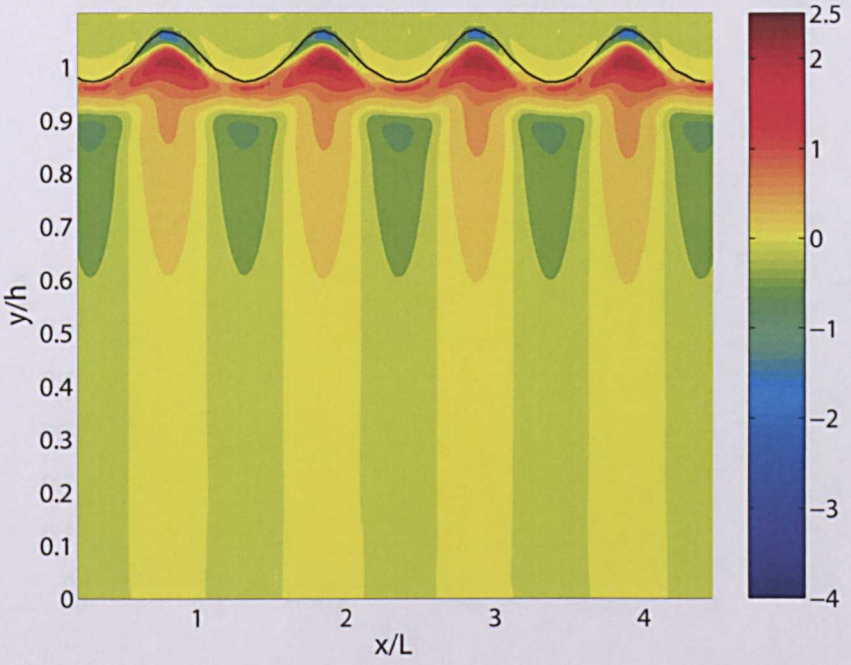

Figure 4.44: Nondimensional shear stress ($\overline{\tau}$) contours of case C2.

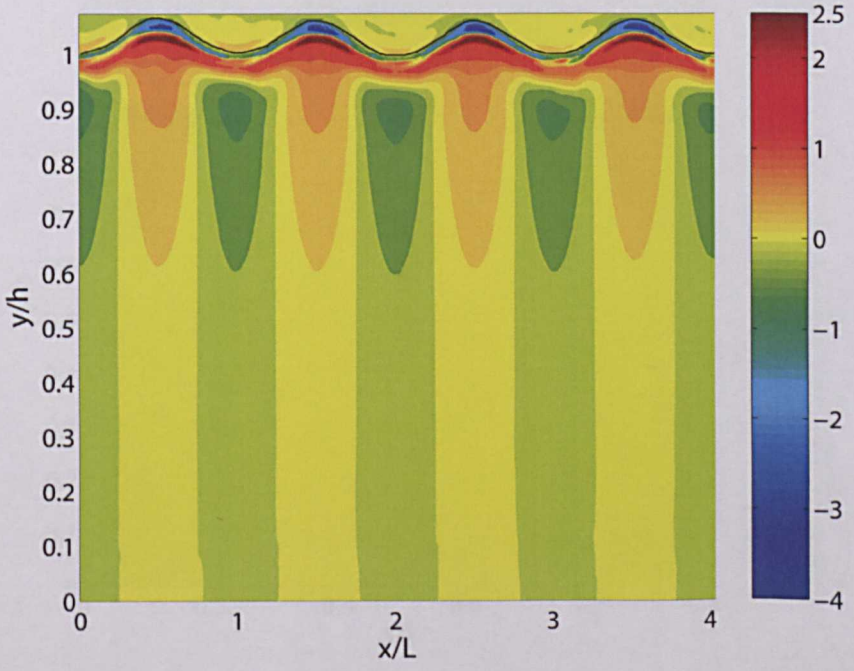

Figure 4.45: Nondimensional shear stress ($\overline{\tau}$) contours of case C3.

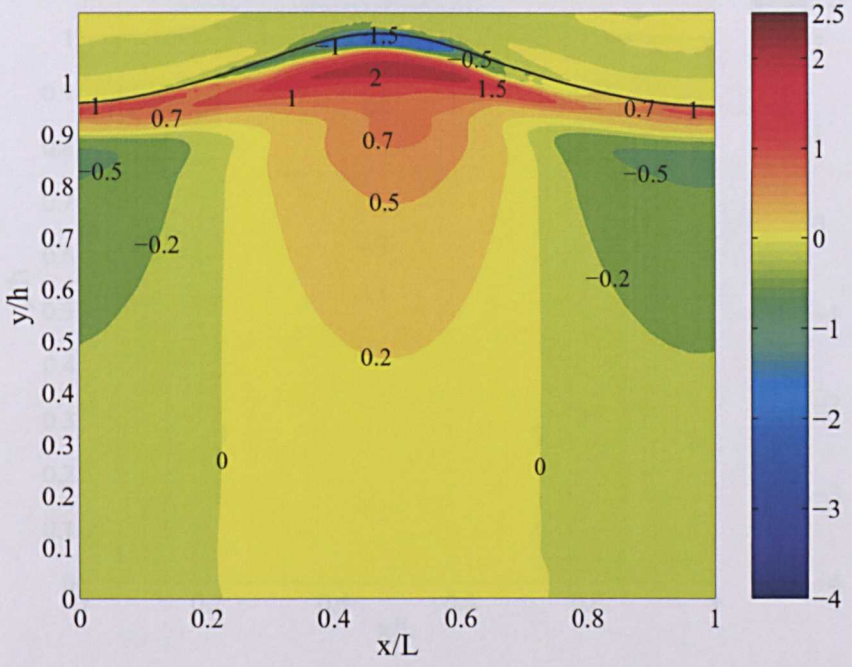

Figure 4.46: Nondimensional shear stress ($\overline{\tau}$) contours in a typical wave in case C1.

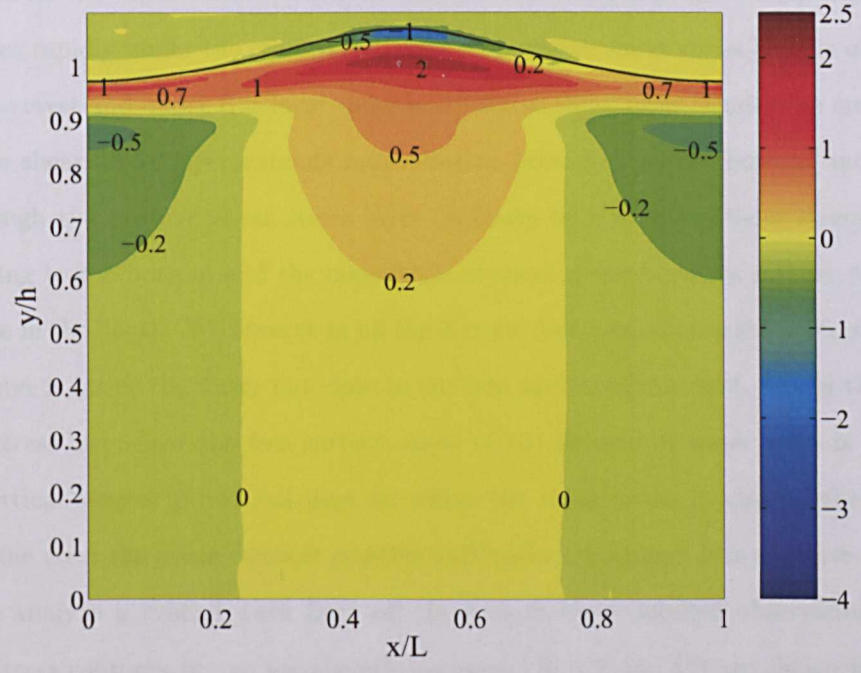

Figure 4.47: Nondimensional shear stress ($\overline{\tau}$) contours in a typical wave in case C2.

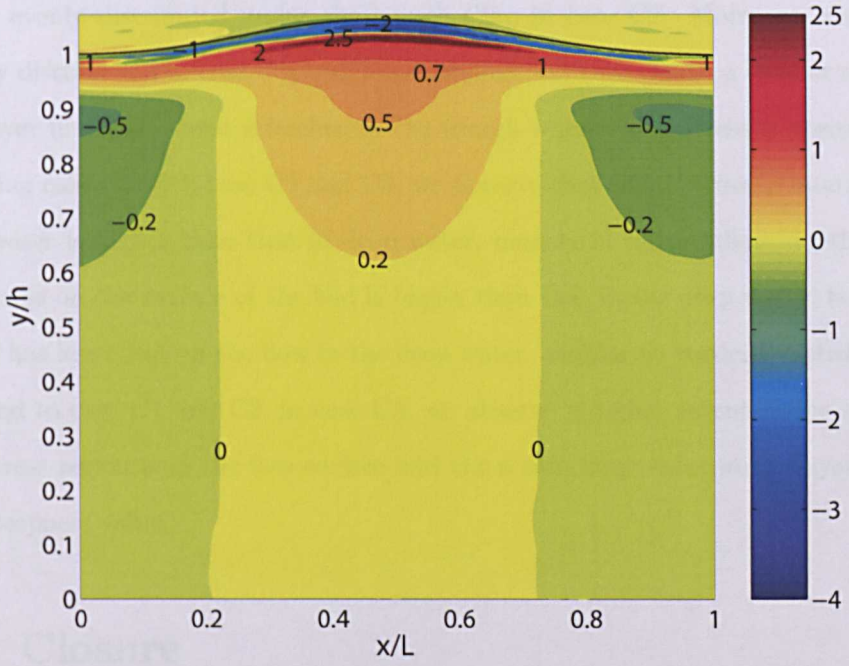

Figure 4.48: Nondimensional shear stress ($\overline{\tau}$) contours in a typical wave in case C3.

stress under the water surface. From the free surface to inside of the water, shear stress increases rapidly under the crest and trough. A negative shear stress layer is observed near the crest and under this layer there is a positive shear layer. Under the crest, this positive shear stress layer extends into a region extending to the bottom and under the trough the positive shear stress layer oscillates to a negative shear stress region extending to the bottom and the magnitude of shear stress becomes smaller with the increase in the depth. We observe in all the 3 cases that a maximum shear stress which is positive is inside the water but close to the free surface of the crest. Under the large shear stress layer near the free surface, most of the domain of water wave is divided into vertical stripes by vertical lines on which the shear stress is zero, in the stripes under the crest the shear stress is positive and under the trough it is negative.

We analyze a typical wave from all three cases by a detailed observation. The shear stress contours in one wavelength for cases C1, C2 and C3 are shown in figure 4.46, 4.47 and 4.48 respectively. In case C1, we observe that positive shear stress layer

is more evenly distributed under the trough than in case C2. Moreover, similar to vorticity distribution in case C3, which has smaller wave steepness, a thinner negative shear layer under the crest stretches to the trough where shear stress is positive. On comparing case C1 with case C2 and C3, we observe that shear stress in intermediate depth water is higher than that in deep water, namely in intermediate depth water, shear stress on the surface of the bed is bigger than that in the deep water, therefore, the bed has less effect on the flow in the deep water. Similar to vorticity distributions, compared to case C1 and C2, in case C3, we observe a higher extent of the negative shear stress region near the free surface and the a thin large shear stress layer due to lower steepness value.

4.7 Closure

In this chapter the analysis of the numerical results obtained for the interactions of water waves with air when the average wind velocity is zero were compared and discussed with available experimental and analytical results. The numerical results of several less studied aspects of water waves such as vorticity and shear stress were presented which will be useful while analyzing the interactions of air with water waves under forced air convection. The volume of fluid developed by Zwart *et al.* (2007) was able to capture the free surface with high accuracy. The level of accuracy for interface capturing was found quite satisfactory for simulating two fluid transient water waves. However we also observed the interface smearing on the beach end where the wave breaks due to relatively coarse mesh. The cases presented in these chapter also illustrated the capability of the solver to accurately predict the water wave interface. We now proceed towards the main area of interest which is simulation of progressive water waves under the action of wind.

Chapter 5

Interaction of deep water waves with air blowing at different velocities

5.1 Introduction

In this chapter we investigate the behaviour of water waves under the effect of air blowing at different velocities in the case of deep water waves. We consider waves of steepness 0.06 similar to the deep water waves studied in the chapter 4. The wind velocities considered here are 1) average wind velocity, $V' = 0$, 2) $V' = u_{max}$, where u_{max} is maximum velocity in water, 3) $V' \approx 0.5c$ and 4) $V' = c$.

In the past, several studies have been carried out to simulate air flow over the water waves and some of these have already been discussed in the chapter 1. Fulgosi *et al.* (2003) carried out DNS study of turbulence with deformable air-water interface in the capillary wave regime. However, this study had a very small domain, small wave slope

and is not applicable to simulate strong topological changes and wave break. Several experimental investigation have been carried out in the past to study the structure of turbulent flow over the progressive waves; a paper by Hsu and Hsu (1983) is one of them. They regarded the surface condition for wind as supersmooth and found that the current supports lower mean turbulent shear stress relative to that supported by a smooth flat plate and that the structure of wave-induced velocity field is sensitive to the height of the critical layer. It was found that, the energy received by the wave is mainly delivered by wave-induced pressure and wind turbulence has little contribution in the direct energy input. We use fixed frame of reference as it is simple and flow motion is relatively easy to visualize than the moving reference frame which may be more difficult for flow visualization if the mean flow does not follow the waveform. The main objective of current study is to improve our understanding on the structure of the mean wind and wave fields. There are several unanswered questions regarding the importance of surface orbital velocity and stokes layer at the interface and its effect on the viscous sub-layer. The inviscid approximation of the potential flow and other works do not provide a solution mechanism for momentum exchange between air and water. Several other questions that we are looking to answer is how the structures of mean flow, streamlines, pressure isolines, vorticity, shear stress change with the space and time and its importance in accurate analysis of air-water exchange in presence of wave. In the earlier chapter, we discussed the behaviour of viscous water waves and analyzed the related flow behaviour in the water side of the domain excluding the analysis of air side of the flow. Here, we will attempt to give a systematic description of mean wind and wave fields in the cases when the average wind velocity is greater than zero. In order to do this, we need to first look at the case of zero average wind speed to explore wave-perturbed flow field and analyze the structure of the Stokes layer under laminar conditions in the deep water waves. Then, the air flow is introduced over the progressive water waves, but the wind speed is still within the range of $V' = c$. At these wind speed, the critical layer does not have any significant role in describing wave-induced flow fields and the waves can be considered *fast waves*. The effect of

mean wind on the wave-induced flow and vice versa in this air-water system can be discussed. At higher wind speeds the turbulent flow is much more complex and affected by varied length scales which requires very high resolution grid than the computational power available. The alternative is to use turbulence closure models which are equally complex to verify and produces different results based on the ability of the model to capture turbulence. Xu *et al.* (1994) used several turbulence closure schemes to predict air flow over sinusoidal terrain and found that different turbulence closure schemes gave different results and also found that higher order turbulence schemes produced better results.

In this chapter, four case studies are discussed to get a detailed view of air-water wave interaction in deep water. All the cases considered are low Froude number cases which can be considered subcritical flow.

5.2 Case study 1: Zero average wind velocity, $V' = 0$

In this case study, the motion in the air above deep water waves when average wind velocity is zero is investigated. All the quantities are nondimensionalized as discussed in the previous chapter. The discussion in this case is largely restricted to the air side of the domain.

5.2.1 Velocity vectors and streamlines in the deep water waves

5.2.1.1 Velocity vectors

The numerical results for velocity vectors in the air and water in the domain and a typical wave are shown in figures 5.1, 5.2 and 5.3. In the case of viscous flow in the deep water wave, along the x-axis, we observe that the movement of air follows

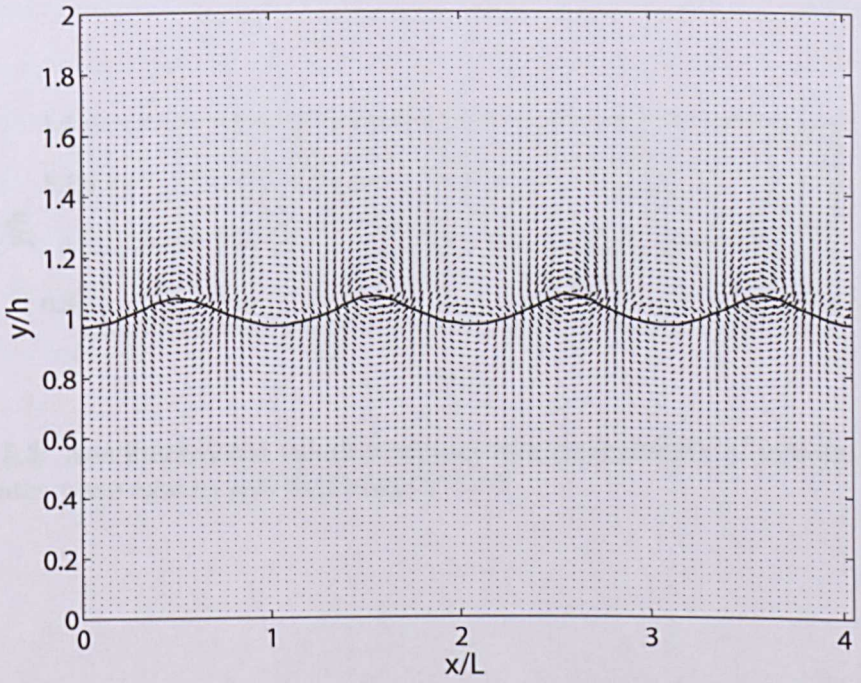

Figure 5.1: Nondimensional velocity vectors in the domain of viscous flow in deep water wave case; $V' = 0$.

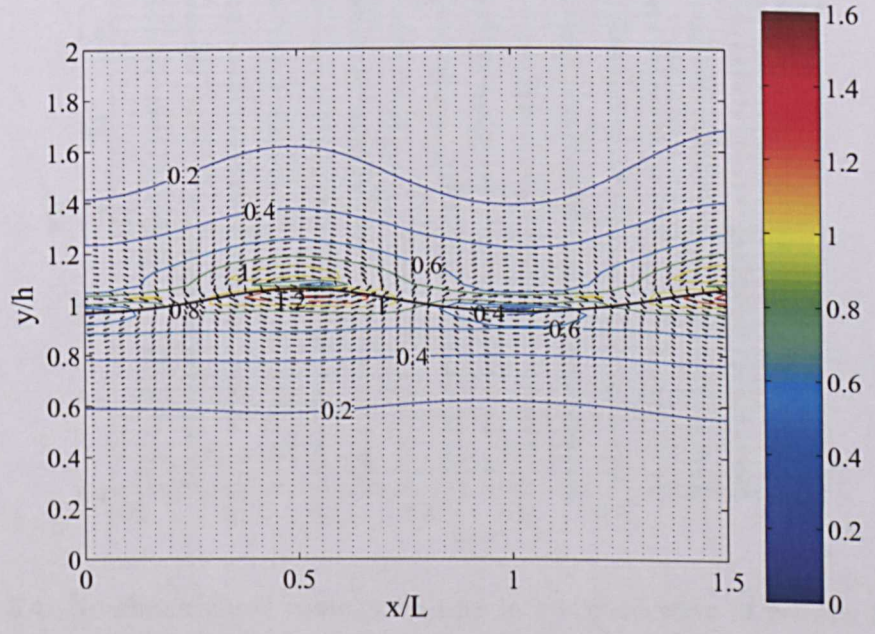

Figure 5.2: Nondimensional velocity vectors in a typical wave of viscous flow in deep water wave case; $V' = 0$, the lines are the contours of magnitude of nondimensional velocity.

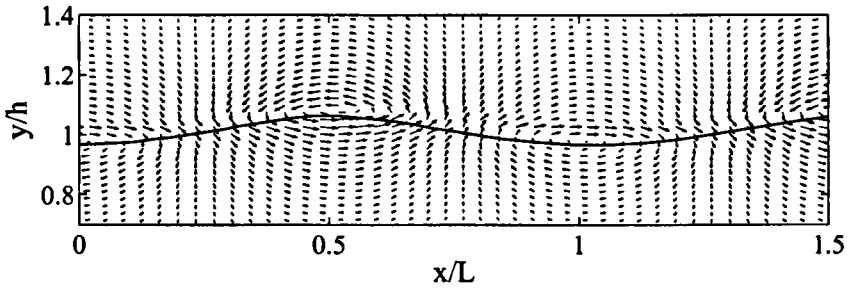

Figure 5.3: Nondimensional velocity vectors in a typical wave of viscous flow in deep water wave case in specified area; $V' = 0$.

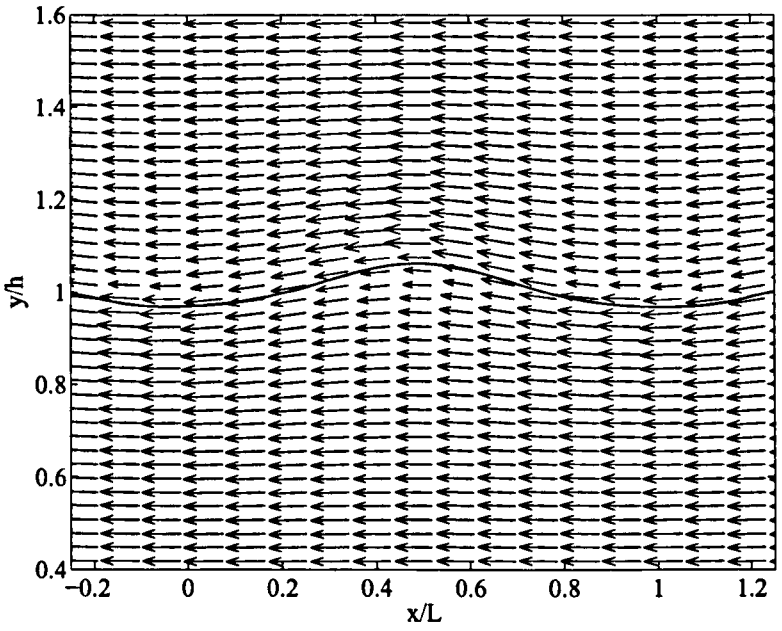

Figure 5.4: Nondimensional velocity vectors in a typical wave of viscous flow in deep water wave case with moving reference frame; $u - c$; $V' = 0$.

the orbital movement of water beneath it. We observe recirculations in the air above the crest and the trough of the wave. These recirculations are mainly due to pressure difference between the windward side and lee side of the wave causing the air to follow the orbital movement in the water. We also observe small acceleration of air above the recirculation in the trough of the wave due to push and pull effect at the front and end of the recirculation zone. Figure 5.2 shows nondimensional velocity vectors and nondimensional RMS (root mean square) velocity contours in a typical wave. Along the y-axis in the air side the velocity progressively decreases as expected. The maximum observed velocity in the air is nearly of same magnitude relative to maximum velocity in the water which is observed near the crest of the wave. These results shows the importance of "wave induced" velocity components. When the wind is moving from left to right these components are opposite in direction to the mean airflow in the crest region and towards the airflow direction in the trough region. Similarly, figure 5.3 shows the specific area of interest in a typical wave. It clearly shows the separation points where air changes its direction to follow the orbital movement in the water. In a moving reference frame, the velocity vectors are as shown in figure 5.4. The flow is seen from right to left as wave velocity is relatively higher compared with mean velocity in the air and water. In the water, we observe higher forward velocity in the crest region.

5.2.1.2 Streamlines

The streamlines in the air and water section of the domain is shown in figures 5.5, 5.6 and 5.7. The streamline topology of mean flow field provides an good overall picture of the flow in the water and air near the progressive wave. The streamlines are uniformly distributed across the domain as expected. The recirculation in the air and orbital movement in the water is also observed and are similar to that predicted by velocity vectors. The analysis of streamlines in a typical wave shows that by locating "zero stream function contour" on the surface we can actually know the precise location where air changes its direction and follows the orbital movement in the water wave. A more detailed area of interest near to the free surface is shown in the figure 5.7.

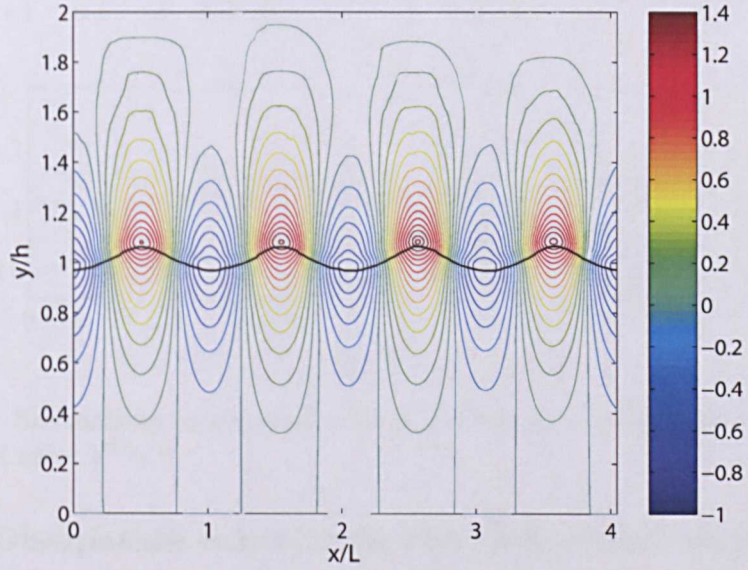

Figure 5.5: Streamlines in the domain of viscous flow in deep water wave case; $V' = 0$.

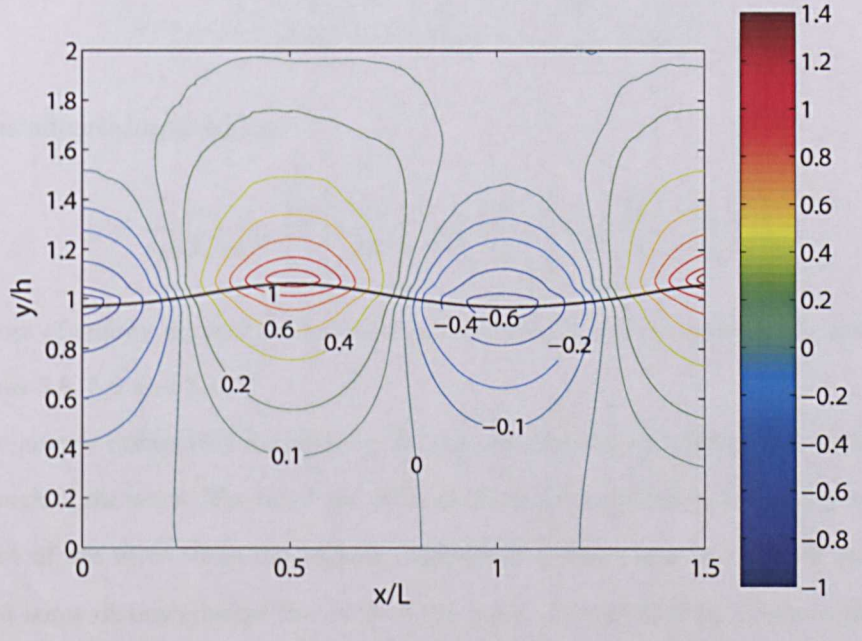

Figure 5.6: Streamlines in a typical wave of viscous flow in deep water wave case; $V' = 0$.

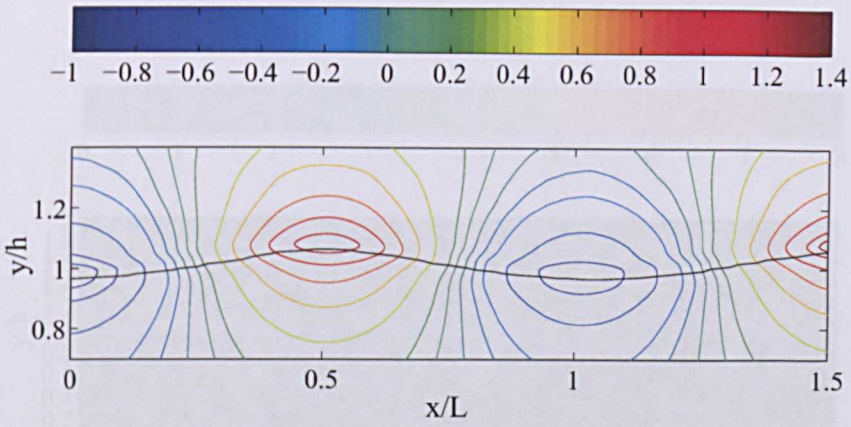

Figure 5.7: Streamlines in a typical wave of viscous flow in deep water wave case in specified area; $V' = 0$.

5.2.2 Dissipation function in the deep water waves

The dissipation of energy in the water wave is primarily due to viscous stresses. The effect due to viscous stresses as a result of deformation of fluid particle in progressive water waves is calculated by dissipation function given by

$$\phi = \mu_m \left\{ 2 \left[\left(\frac{\partial u}{\partial x} \right)^2 + \left(\frac{\partial v}{\partial y} \right)^2 \right] + \left(\frac{\partial u}{\partial y} + \frac{\partial v}{\partial x} \right)^2 \right\} \tag{5.1}$$

and is nondimensionalized by,

$$\phi = \frac{\mu_m}{\mu_w (2ak\sigma)^2} \left\{ 2 \left[\left(\frac{\partial u}{\partial x} \right)^2 + \left(\frac{\partial v}{\partial y} \right)^2 \right] + \left(\frac{\partial u}{\partial y} + \frac{\partial v}{\partial x} \right)^2 \right\} \tag{5.2}$$

The plots of energy dissipation function in the domain and a typical wave are shown in figures 5.8, 5.9 and 5.10.

The energy dissipation function in the domain shows high dissipation in the crest and trough of the wave. The observed value of highest dissipation in the air is just above the crest of the wave while the highest dissipation in the water is observed under the water at some distance below the crest of the wave. The dissipation is also high in the water below the trough of the wave while in the air above the trough the dissipation has lower magnitude. We can attribute this behaviour to relatively higher orbital velocity

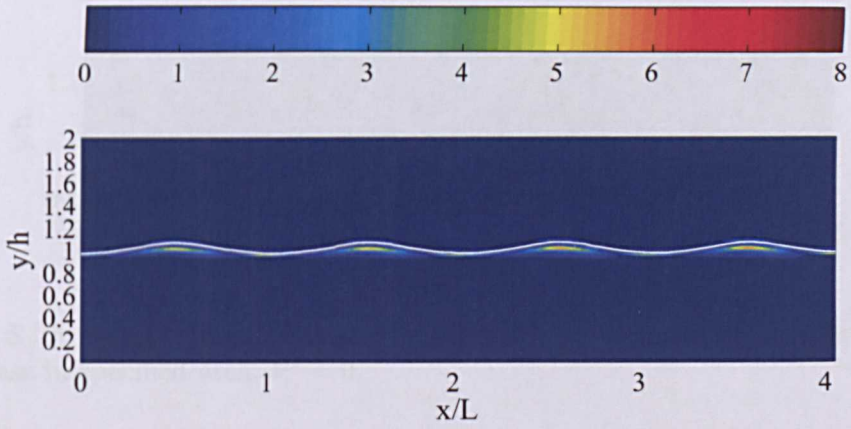

Figure 5.8: Energy dissipation in the domain of viscous flow in deep water wave case; $V' = 0$.

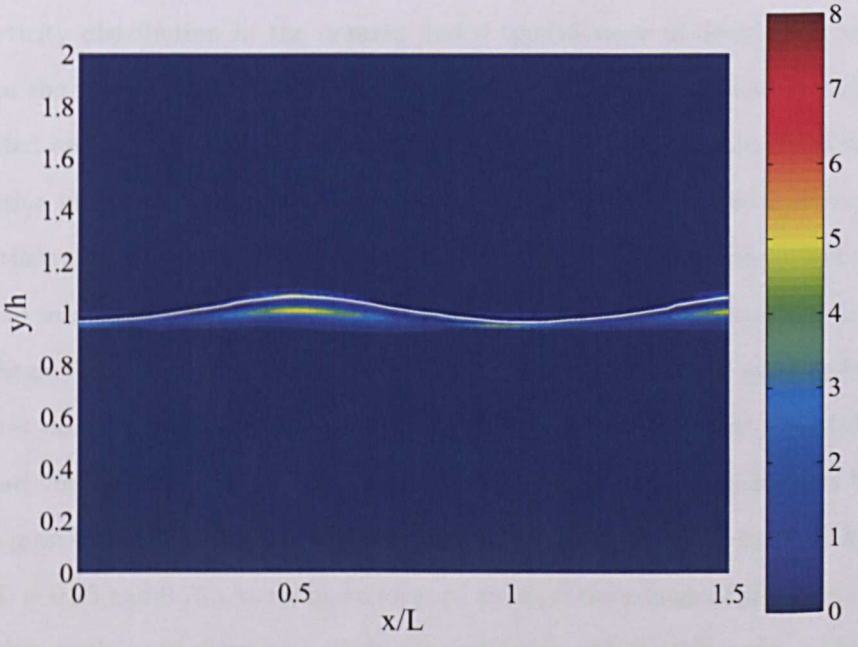

Figure 5.9: Energy dissipation in a typical wave of viscous flow in deep water wave case; $V' = 0$.

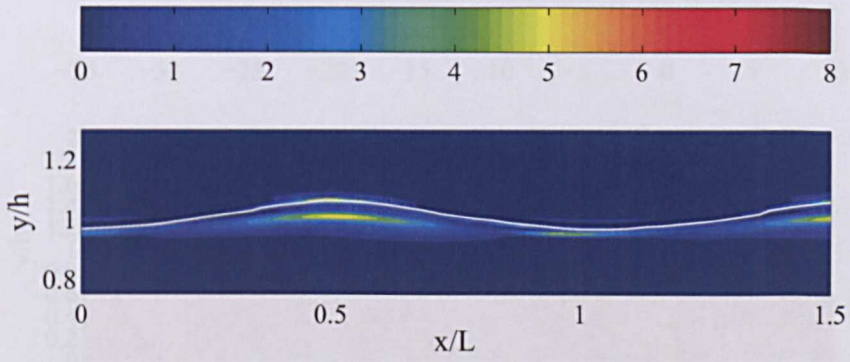

Figure 5.10: Energy dissipation in a typical wave of viscous flow in deep water wave case in specified area; $V' = 0$.

in the water and air near the crest of the wave which leads to higher viscous effects in those regions. A small increase in energy dissipation is also observed along x-axis as the amplitude of the wave reduces due to attenuation.

5.2.3 Vorticity in the deep water waves

The vorticity distribution in the domain and a typical wave of deep water waves is shown in the figures 5.11 and 5.12. As observed in figure 5.11, vorticity is uniformly distributed on each wave along the length of the domain. The magnitude of vorticity distribution in the air is much higher due to higher gradients observed in the air near the interface due to low density and viscosity. The vorticity in the air and water quickly reduces to zero along the depth. In a typical wave, the distribution of vorticity is shown in the figure 5.12. We observe positive vorticity in the crest of the wave in both air and water domain. The vorticity in the air above the crest is more than twice the maximum vorticity observed in the water. A layer of positive vorticity can be seen extending on both sides of wave crest till the air flow changes its direction at location near x/L = 0.25 and 0.75. As we move forward towards the trough of the wave, a layer of negative vorticity is observed both in air and water. Above this layer, a thin layer of positive vorticity is seen which extends on both the trough and crest of the wave. The maximum vorticity in the air above the crest and trough of the wave is more than

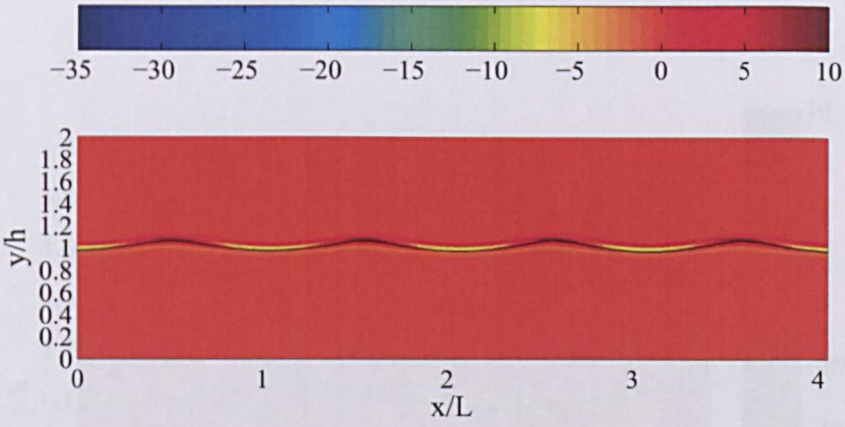

Figure 5.11: Vorticity in the domain of viscous flow in deep water wave case; $V' = 0$.

twice the maximum vorticity observed in the water mainly due to higher gradient in the air about the trough of the wave. We observe both negative and positive vorticity layers in the air above the trough of the wave. A more specific details on the vorticity near the free surface can be seen in figure 5.13.

5.2.4 Shear stress in the deep water waves

The shear stress distribution in the domain and a typical wave of deep water waves is shown in the figures 5.14 and 5.15. As observed in figure 5.14, the shear stress shows uniform distribution on each wave along the length of the domain as expected. Along the x-axis in the air, we observe vertical strips of positive and negative shear stress above the crest and trough of the wave respectively which are similar to those observed in the water below the free surface. Figure 5.15 shows that the magnitude of nondimensional shear stress in the air is nearly zero in crest and trough of the wave corroborating the assumption about shear stress being considered zero on the free surface in major theoretical studies done in the past including Lundgren & Koumoutsakos (1999). A thin positive shear layer is also observed in the trough of the wave above the free surface in the air. A detailed view of near surface shear stress can be observed in figure 5.16.

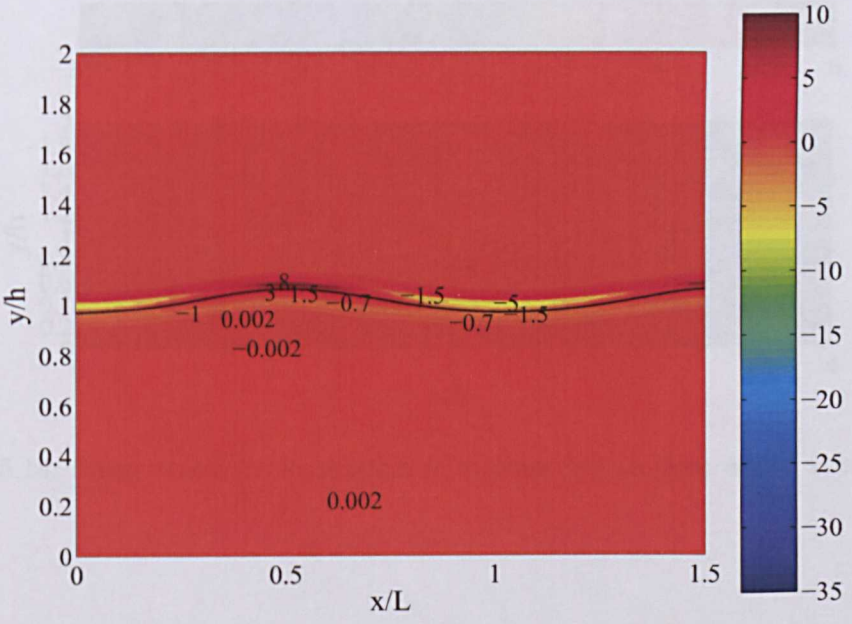

Figure 5.12: Vorticity in a typical wave of viscous flow in deep water wave case; $V' = 0$.

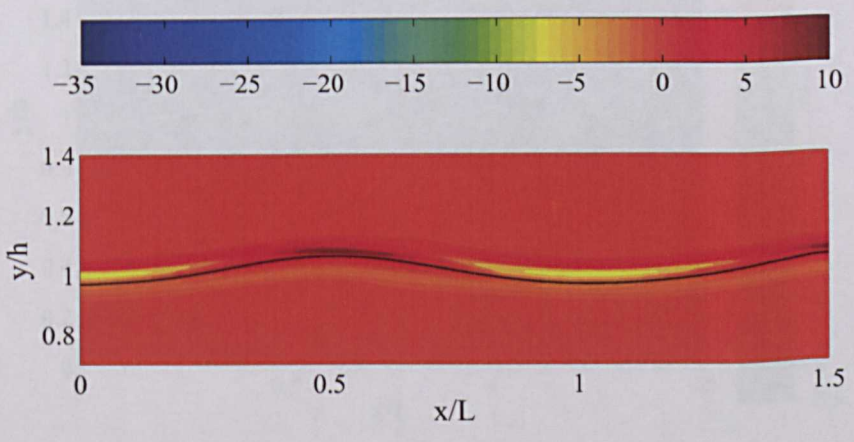

Figure 5.13: Vorticity in a typical wave of viscous flow in deep water wave case in a specified area; $V' = 0$.

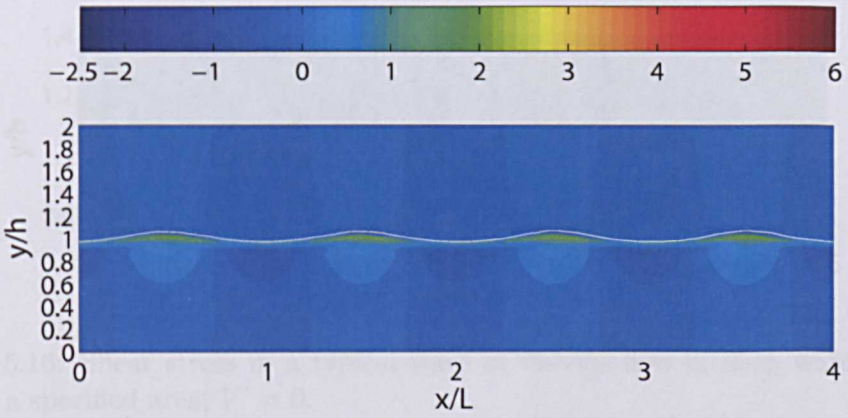

Figure 5.14: Shear stress in the domain of viscous flow in deep water wave case; $V' = 0$.

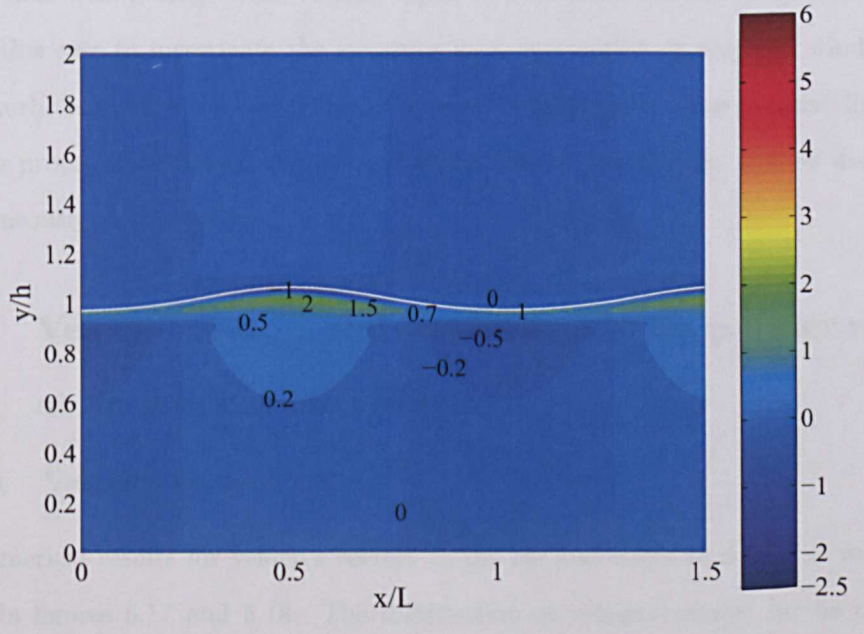

Figure 5.15: Shear stress in a typical wave of viscous flow in deep water wave case; $V' = 0$.

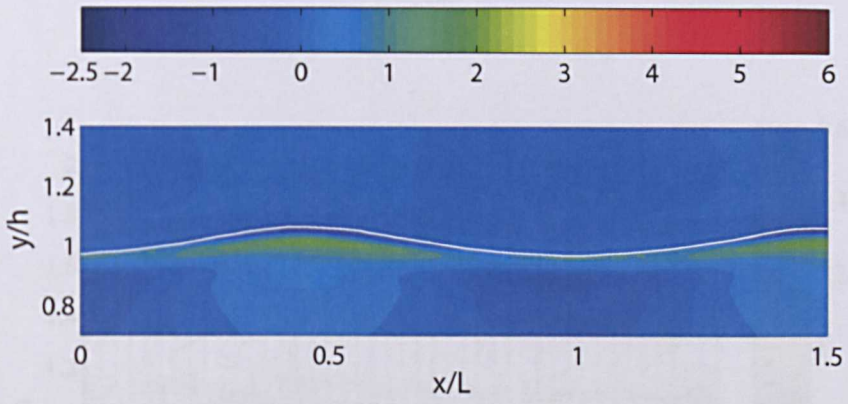

Figure 5.16: Shear stress in a typical wave of viscous flow in deep water wave case in a specified area; $V' = 0$.

5.3 Case study 2: V' = Maximum water velocity $<$ Wave speed, c

In this section, we discuss the numerical results obtained when a wind is forced over the water waves with average wind velocity equal to maximum velocity in the water. We choose this case to investigate the air-water wave interaction at very low wind speed as the turbulence effects are very less. The wind is assumed to blow in same direction as wave propagation. Both the air and water side of the domain will be discussed simultaneously in this section.

5.3.1 Velocity vectors and streamlines in deep water waves at very low wind velocity

5.3.1.1 Velocity vectors

The numerical results for velocity vectors in the air and water in a typical wave are shown in figures 5.17 and 5.18. The distribution of velocity vectors in the domain is excluded as we observe repeated velocity vector pattern throughout the length of the domain. The observation of the contours of velocity magnitude from the figure 5.17 shows an increase in the velocity in the air above the crest and trough of the

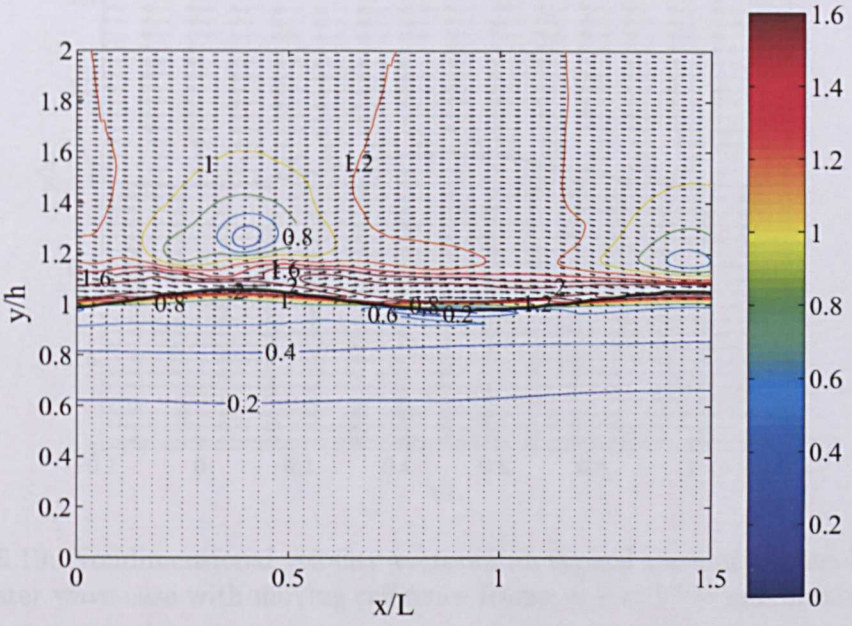

Figure 5.17: Velocity vectors in a typical wave of viscous flow in deep water wave case; V' = maximum water velocity $< c$, the lines are the contours of magnitude of nondimensional velocity.

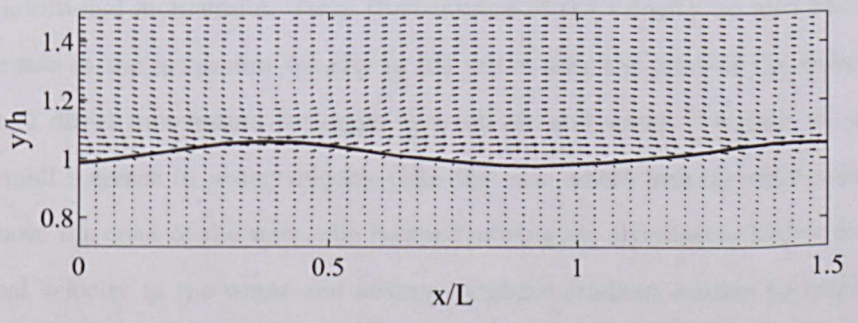

Figure 5.18: Velocity vectors in a typical wave of viscous flow in deep water wave case in specified area; V' = maximum water velocity $< c$.

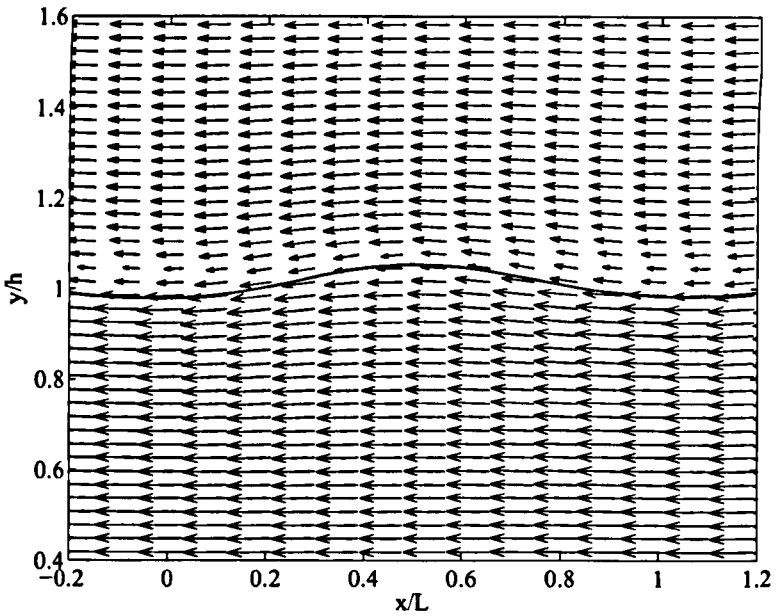

Figure 5.19: Nondimensional velocity vectors in a typical wave of viscous flow in deep water wave case with moving reference frame; $u - c$; V' = maximum water velocity $< c$.

wave. This is due to additional push that air experiences apart from its own u velocity component transferring momentum from the wave crest to the air immediately above it. In the trough on the other hand due to low air velocity the general tendency of air is to remain attached to the water surface but due to presence of wave and recirculation above the trough, the air above the recirculation zone accelerates after gaining additional momentum. From the contours of the velocity we also observe an 15% increase in the maximum velocity in the water near the crest of the wave which is result of direct momentum exchange between air and water. Overall, we observe a very small increase in water velocity than the case where average wind velocity is zero. Above the crest of the wave, the forward moving air experiences higher drag due to vertical velocity in the water and adverse pressure gradient leading to random air movement. A more detailed velocity vectors are shown in the figure 5.18. In a moving reference frame, the velocity vectors are shown in figure 5.19. It shows relatively higher forward moving velocity near the free surface in both air and water.

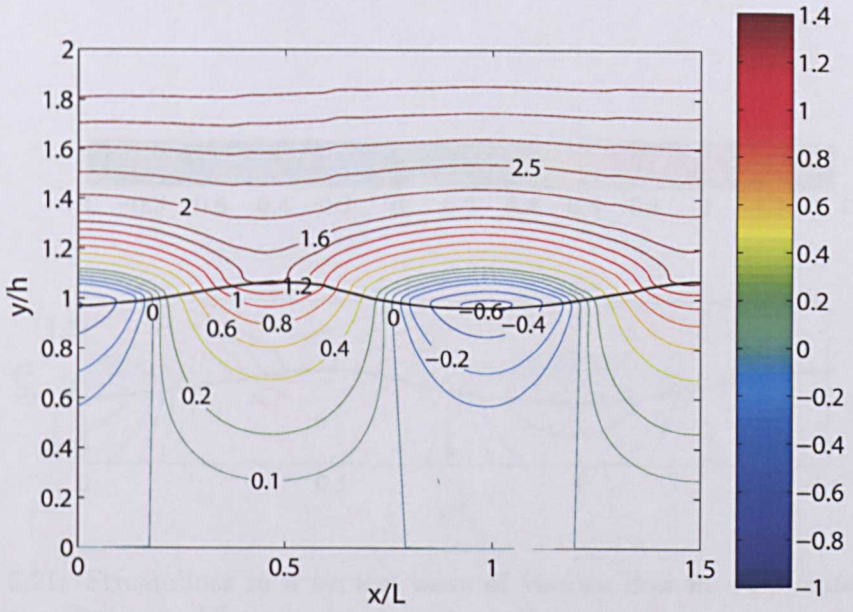

Figure 5.20: Streamlines in a typical wave of viscous flow in deep water wave case; V' = maximum water velocity $< c$.

5.3.1.2 Streamlines

The numerical results for streamlines in the air and water in a typical wave are shown in figures 5.20 and 5.21. The observation of streamlines shows recirculation zone near the trough of the wave similar to velocity vectors discussed earlier. The effect of orbital velocity on the air above the crest and trough is visible. The streamlines shows an increase and decrease in flux in the trough and crest region respectively. Thus at very low wind speed or incase of fast waves we will observe much higher drag than when air is moving at high velocity.

5.3.2 Dynamic pressure isolines in water

The dynamic pressure isolines in the domain and a typical wave are shown in the figures 5.22 and 5.23 respectively. The pressure isolines along the domain shows evenly distributed contours. We can observe the change in the dynamic pressure from the case where average wind velocity was zero (*refer* figure 4.6). The isolines observed in this

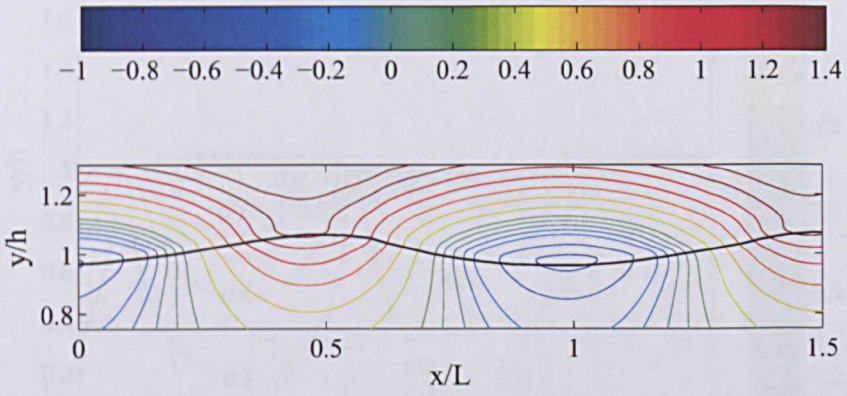

Figure 5.21: Streamlines in a typical wave of viscous flow in deep water wave case in specified area; V' = maximum water velocity $< c$.

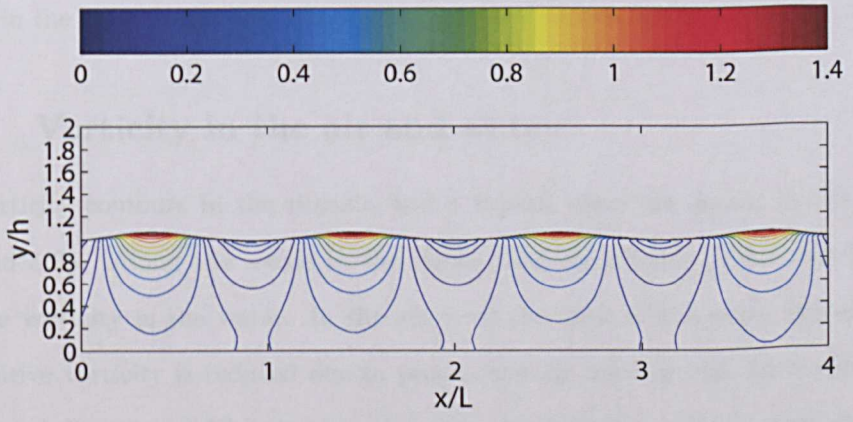

Figure 5.22: Pressure isolines in the domain of viscous flow in deep water wave case; V' = maximum water velocity $< c$.

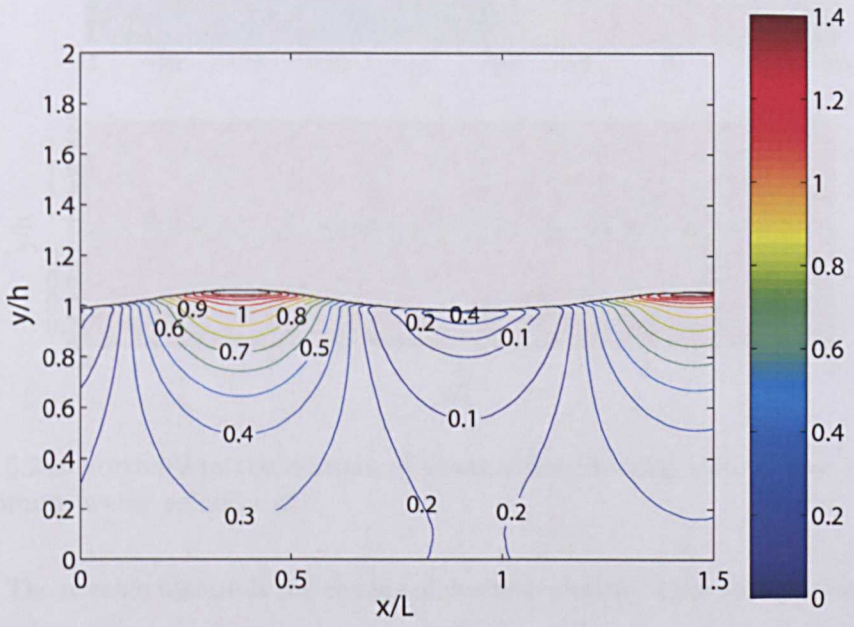

Figure 5.23: Pressure isolines in a typical wave of viscous flow in deep water wave case; V' = maximum water velocity $< c$.

case have increased in the value near the crest of the wave and reduced to a lower value near the trough of the wave indicating reduced velocity in the trough and increased velocity in the crest of the wave. This difference in the isolines is mainly due to small change in the wave profile and velocity in proximity to free surface of the wave.

5.3.3 Vorticity in the air and water

The vorticity contours in the domain and a typical wave are shown in the figures 5.24 and 5.25. Along the x-axis in the figure 5.24, we observe continuous layer of negative vorticity in the water. In the air, near the crest of the wave, the extent of the positive vorticity is reduced due to presence of air moving with finite velocity in the forward direction which helps to reduce the anticlockwise rotation of air above the crest of the wave. In the trough of the wave, we observe an increase in the clockwise rotational movement of the air due to forward movement of air which has increases the extent and magnitude of "negative" vorticity. The contour shown in a typical wave in figure 5.25 shows the magnitude of positive and negative vorticity in the air and water

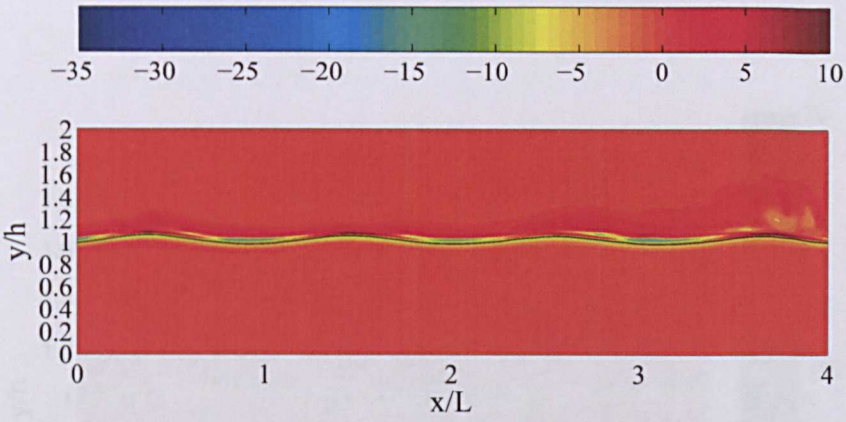

Figure 5.24: Vorticity in the domain of viscous flow in deep water wave case; V' = maximum water velocity $< c$.

region. The notable feature is the change of positive vorticity layer that is observed in the water side of the crest of the wave (when the average wind velocity is zero) to a negative vorticity layer when the air is blowing over the water wave. This is significant observation as a result of air-water interaction and momentum exchange. In the air of the trough of the wave, we observe a two times increase in the maximum value of "negative vorticity" while in the water we observe an 50% increase in the maximum negative value of vorticity as clockwise rotation caused by forward moving air helps the corresponding clockwise rotation in the water. Along the x-axis, inside the water below the negative vorticity layer, we can see a positive vorticity layer with a smaller magnitude. In the air, high above the crest and trough we observe a positive vorticity layer of higher magnitude than earlier case. Further along the depth in both air and water, the vorticity is small. A more detailed view of vorticity can be seen in figure 5.26.

5.3.4 Shear stress in the air and water

The shear stress contours in the domain of a typical wave are shown in the figures 5.27 and 5.28. Along the length of the domain in the figure 5.27, we observe a layer of positive shear stress near the water surface. Below this layer vertical strips of positive

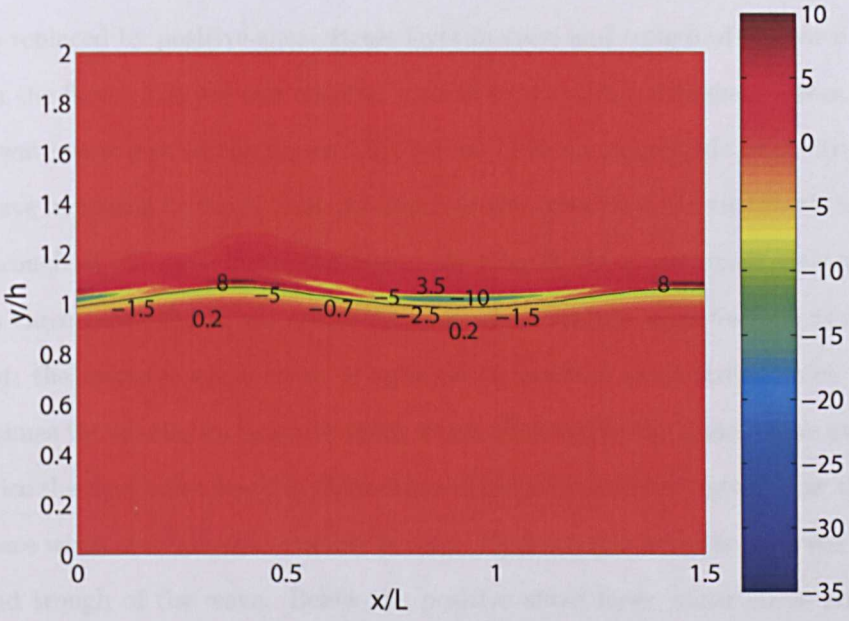

Figure 5.25: Vorticity in a typical wave of viscous flow in deep water wave case; V' = maximum water velocity $< c$.

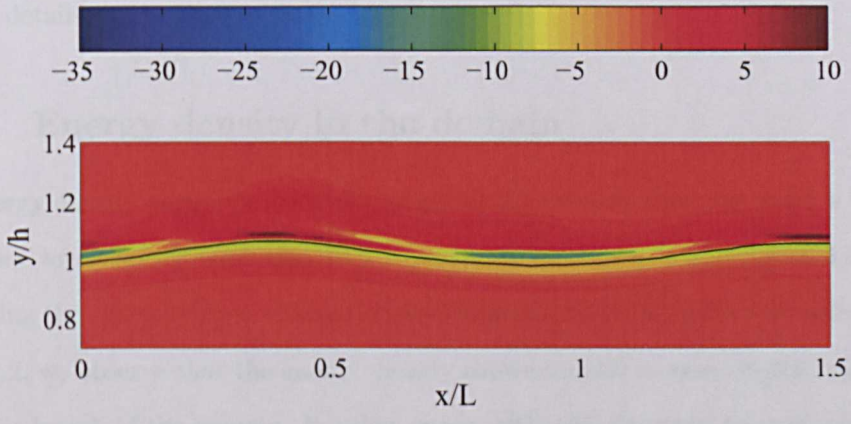

Figure 5.26: Vorticity in a typical wave of viscous flow in deep water wave case in specified area; V' = maximum water velocity $< c$.

and negative shear stresses are observed below crest and trough of the wave respectively. The layer of negative shear stress that was observed in case with zero average wind speed is replaced by positive shear stress layer in crest and trough of the wave. In the air from the figure 5.27 we can observe vertical strips with small shear stress. In the typical wave as shown in the figure 5.28, we see that the magnitude of positive shear stress have increased by more than two times in the crest than the trough of the wave. In the trough of the wave inside the water, the magnitude of maximum positive shear stress is three times that observed in the case when average wind velocity is zero. In the crest, the negative shear stress is replaced by positive shear stress which is more than 4 times the maximum negative shear stress observed in the same region and more than twice the maximum positive shear stress observed inside the water below the wave in the case when average wind velocity is zero. Thus a larger shear is observed in both crest and trough of the wave. Below the positive shear layer, shear stress structure, magnitude and distribution patterns are not significantly different from the earlier case when average wind velocity is zero. In the air, we observe a thin layer with large shear stress just above the trough of the wave as a result of action of wind. This shear layer extends from the leeward side to the windward side of the wave and the magnitude of the shear stress is not large compared to that observed in water below it. A more specific details can be seen in figure 5.29.

5.3.5 Energy density in the domain

The energy density variation along the length of the domain when the wind is blowing with very low velocity over the deep water wave is shown in the figure 5.30. On comparing the time averaged energy density variation shown in figure 5.30 with that in figure 4.2, we observe that the energy density shows a small increase in the magnitude along the length of the domain. In other words, although the wave has not grown but the energy dissipation in the wave is reduced and the water waves have gained energy which is equivalent to 2% of total wave energy from the wind above it. We also observe that this gain of energy is in the form of constant increase in the kinetic energy inside

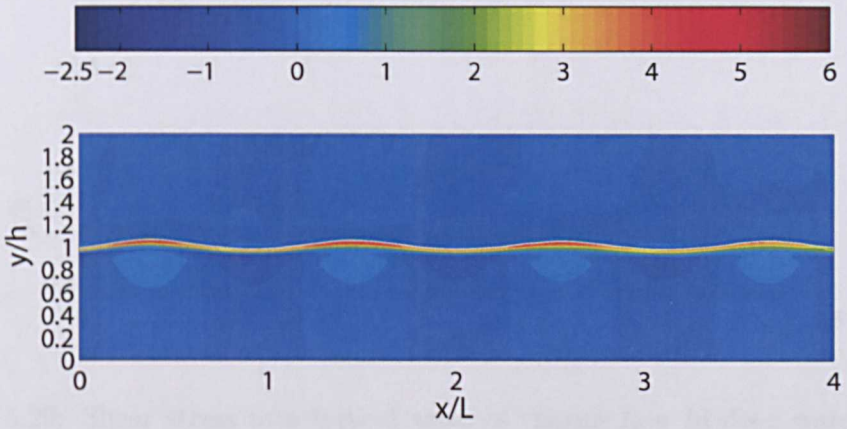

Figure 5.27: Shear stress in the domain of viscous flow in deep water wave case; V' = maximum water velocity $< c$.

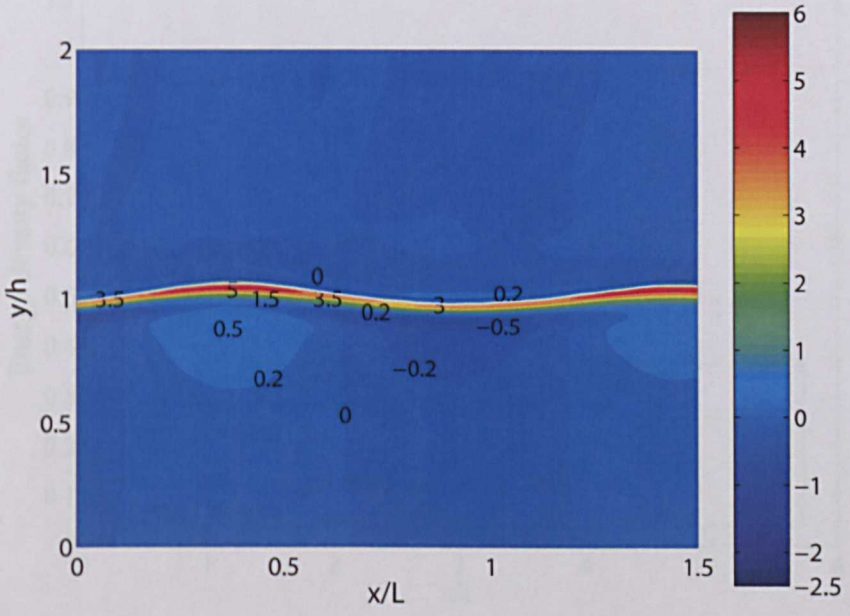

Figure 5.28: Shear stress in a typical wave of viscous flow in deep water wave case; V' = maximum water velocity $< c$.

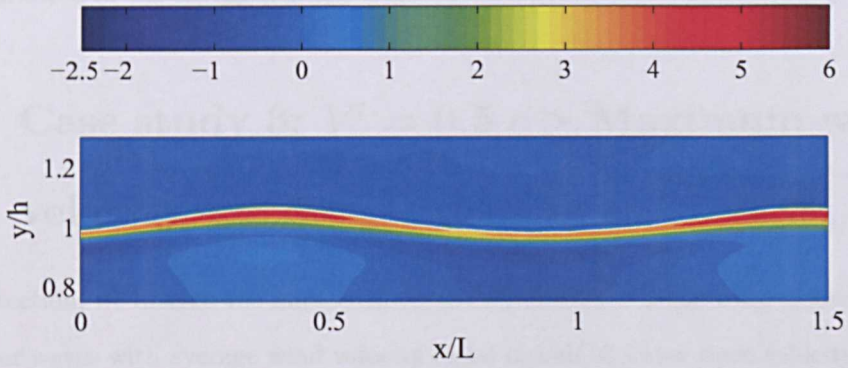

Figure 5.29: Shear stress in a typical wave of viscous flow in deep water wave case in specified area; V' = maximum water velocity $< c$.

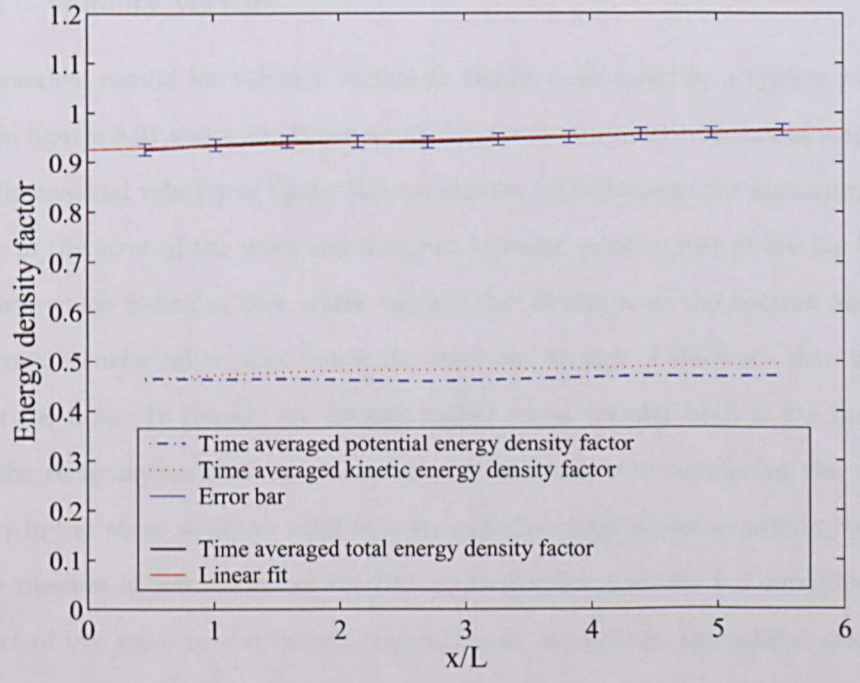

Figure 5.30: Time averaged energy density factor vs x; V' = maximum water velocity $< c$.

the wave which is due to orbital velocity in the water. The potential energy shows very small variation in the energy density.

5.4 Case study 3: $V' = 0.5\ c >$ Maximum water velocity

In this section, we discuss the numerical results obtained when the wind is forced over the water waves with average wind velocity equal to half of water wave velocity, c. We chose this case to investigate the air-water interaction as a logical stepwise increase in wind velocity in order to study the effect of higher wind speed on energy exchange. Both the air and water sides of the domain will be discussed simultaneously in this section.

5.4.0.1 Velocity vectors

The numerical results for velocity vectors in the air and water in a typical wave are shown in figures 5.31 and 5.32. When analyzing the vectors and contours of magnitude of nondimensional velocity in figure 5.31 we observe an increase in the maximum water velocity in the crest of the wave and decrease in water velocity just above the bottom boundary, which indicates that water reduces its velocity near the bottom and more momentum transfer takes place below the crest and trough of the wave than in other parts of the fluid. In the air, we observe higher mean velocity both in the crest and above the recirculation zone in the trough of the wave. On comparing the velocity contours in the water with low wind velocity case discussed earlier as seen in the figure 5.17 we observe higher extent of velocity contours of magnitude 0.6 extending from the crest of the wave to the trough, indicating an increase in the orbital velocity of the water below the crest and trough of the wave. We also observe that the extent of velocity contours with higher magnitude has increased below the crest and trough, which demonstrates the momentum exchange from the air to the water below it. A

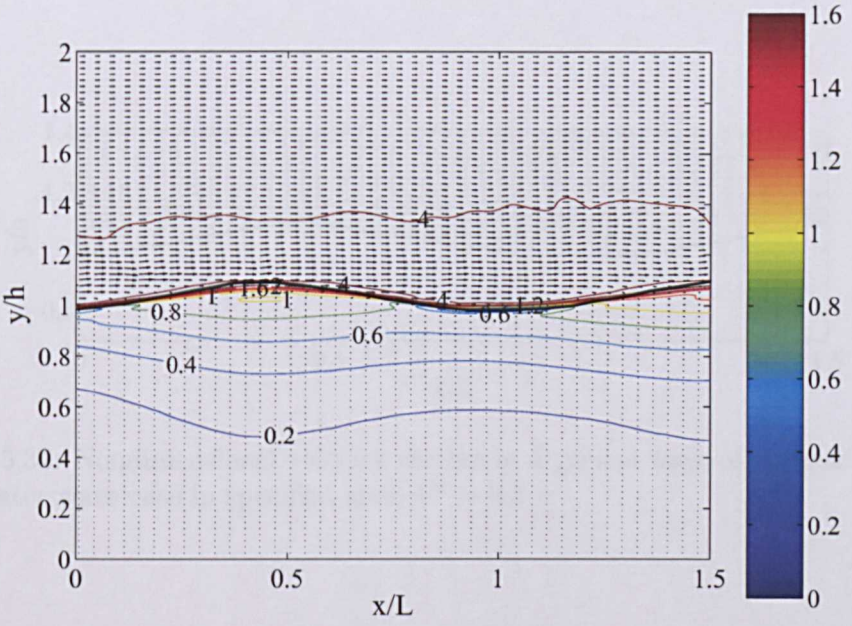

Figure 5.31: Nondimensional velocity vectors in a typical wave of viscous flow in deep water wave case; $V' = 0.5\ c$, the lines are the contours of magnitude of nondimensional velocity.

more detailed view of the velocity vector near the water wave is shown in the figure 5.32. In a moving reference frame the velocity vectors are seen in figure 5.33. It shows recirculation in the crest and trough region of the wave in the air due to higher velocity in the air. The movement of air is also seen more random than that observed in a fixed reference frame.

5.4.0.2 Streamlines

The numerical results for streamlines in the air and water in a typical wave is shown in figures 5.34. It shows all aspects discussed in the earlier subsection of velocity vectors. A more detailed observation in the trough of the wave shows an decrease in the thickness of the recirculation zone in the trough of the wave. This indicates that the tendency in the air with the increase in wind speed is to attach to the water surface and thereby reduce the size of the recirculation zone. The outcome of this phenomenon accelerates the air above the trough faster than the mean wind velocity leading to an increase of

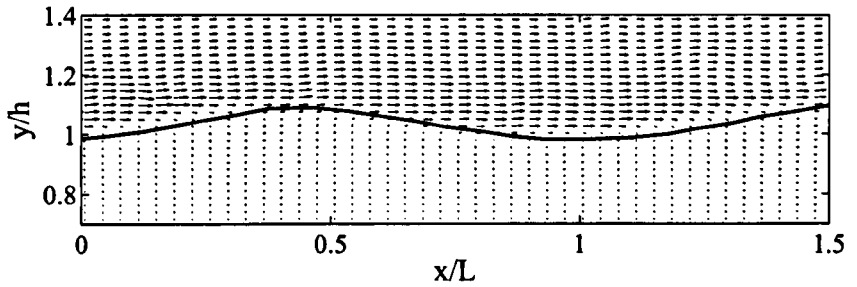

Figure 5.32: Nondimensional velocity vectors in a typical wave of viscous flow in deep water wave case in specified area; $V' = 0.5\ c$.

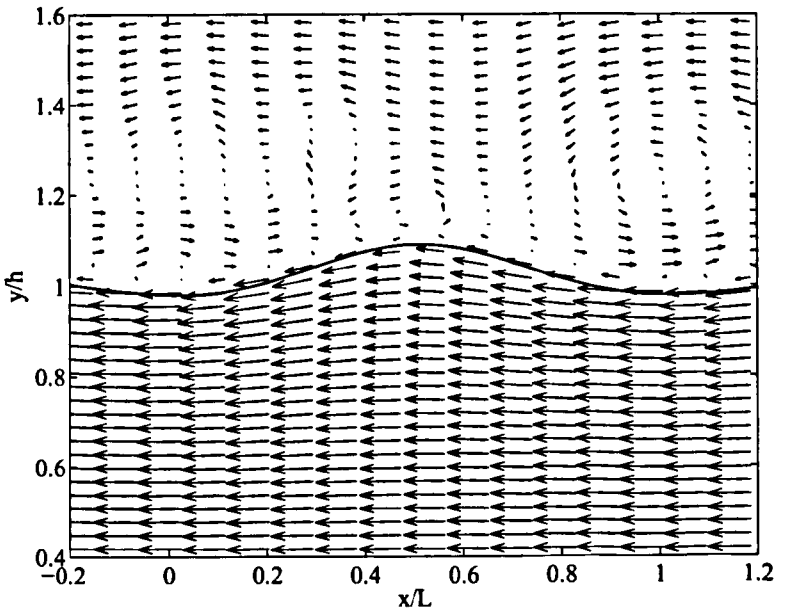

Figure 5.33: Nondimensional velocity vectors in a typical wave of viscous flow in deep water wave case with moving reference frame; $u - c$; $V' = 0.5\ c$.

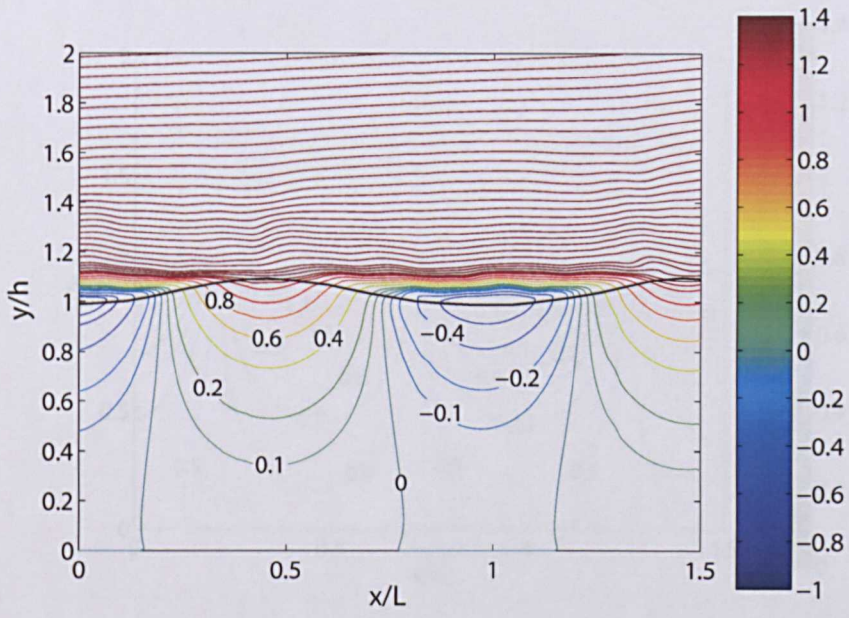

Figure 5.34: Streamlines in a typical wave of viscous flow in deep water wave case; $V' = 0.5$ c.

mass flux in the region which can be observed from figure 5.34. On comparing the streamlines with the earlier cases when average wind velocity is low or zero, above the crest and trough we observe that wind has fully overcome the wave resistance of anti-clockwise moving water particles and is firmly attached to the wave till it encounters a strong pressure gradient in recirculation zone in the trough of the wave.

5.4.1 Dynamic pressure isolines in water

The numerical results for dynamic pressure isolines in the domain and a typical wave are shown in figure 5.35. Along the length of the domain, figure 5.35 shows higher dynamic pressure isolines in the crest of wave than earlier cases corresponding to an increase in effect of dynamic pressure in the crest. This increase is also uniformly distributed along the whole domain in all the crest and trough region. Since, the dynamic pressure isolines are very sensitive to small change in the pressure, we can observe lot of variability in isolines below the wave. The higher dynamic pressure in the crest signifies increased distribution of dynamic pressure below the crest region

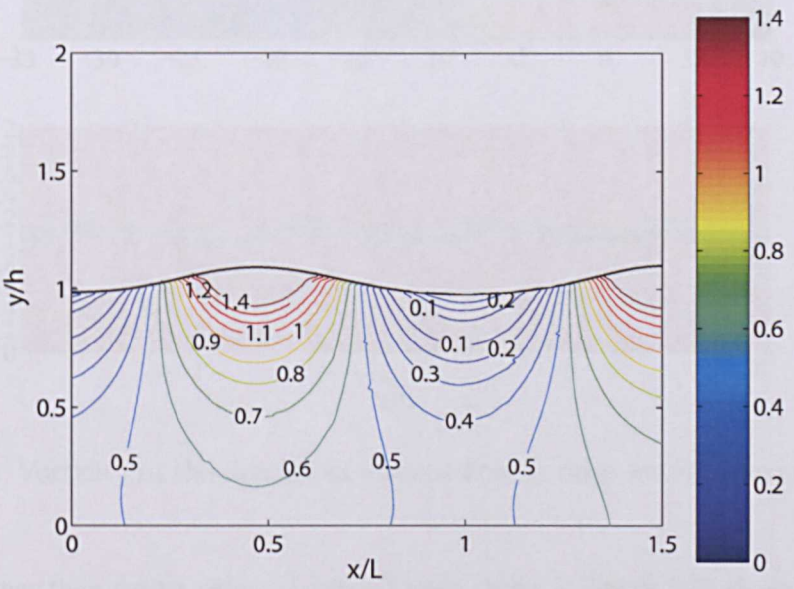

Figure 5.35: Pressure isolines in a typical wave of viscous flow in deep water wave case; $V' = 0.5\ c$.

which also affects the region under the trough. It is worthwhile to study the sensitivity of dynamic pressure as it is often used in the laboratory studies. Figure 5.35 shows lower value of pressure isolines in the trough region indicating reduction in the dynamic pressure in the water below the trough.

5.4.2 Vorticity in the air and water

The numerical results for the vorticity in the air and water in the domain and a typical wave when the average wind velocity is $0.5c$ are shown in figures 5.36 and 5.37 respectively. In the water, we observe a layer of negative vorticity along the water surface. We also observe negative vorticity layer in the air just above the water surface, the magnitude of which is highest in the trough and lowest in the crest of the wave. The negative vorticity is diffused into the air progressively on each waves along the length of the domain while the maximum positive vorticity in the air observed above the trough on the windward side of the slope reduces progressively, indicating a diffusion of vorticity in the air. The depth of diffusion of vorticity in the air is also observed to

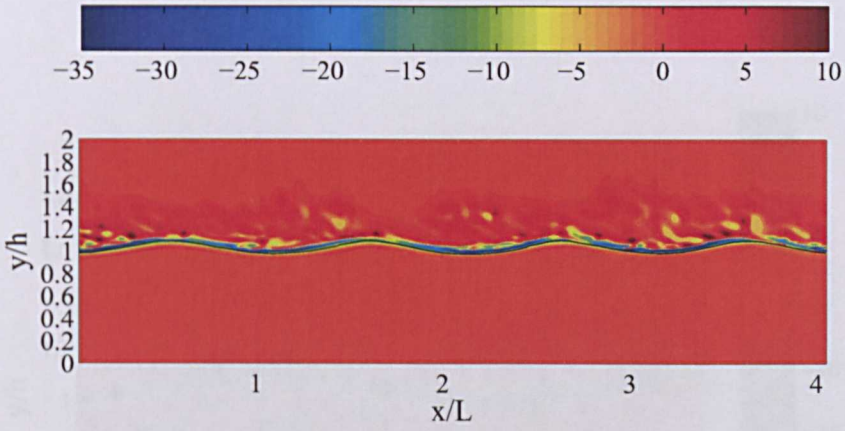

Figure 5.36: Vorticity in the domain of viscous flow in deep water wave case; V' = 0.5 c.

be much higher than earlier cases. A typical wave shown in figure 5.37 shows higher maximum magnitude of vorticity in the trough and on the slope on the windward side indicating a dynamically active air region while in the crest of the wave a negative vorticity is observed due to strong action of wind. This forward moving air flow with negative vorticity moves the positive vorticity in the crest region as observed in earlier cases (*refer* figure 5.25) higher up and forms a negative vorticity layer by forcing the air mass near the free surface to rotate in clockwise direction. The maximum value of negative vorticity observed in this case is 3 times of the maximum value observed in the earlier case with low wind velocity as seen in figure 5.25. In the water side near the free surface, we observe higher negative vorticity in the crest and trough region while positive vorticity in the water is moved inside the water below the negative vorticity layer and reduces in magnitude. In the lower region in the water we observe a very small vorticity. The extent of diffusion of vorticity in the air is much higher than the water. A more specific details on vorticity can be seen in figure 5.38.

5.4.3 Shear stress in the air and water

The numerical results for the shear stress in the air and water when the average wind velocity is 0.5c are shown in figures 5.39 and 5.40. Along the length of the domain

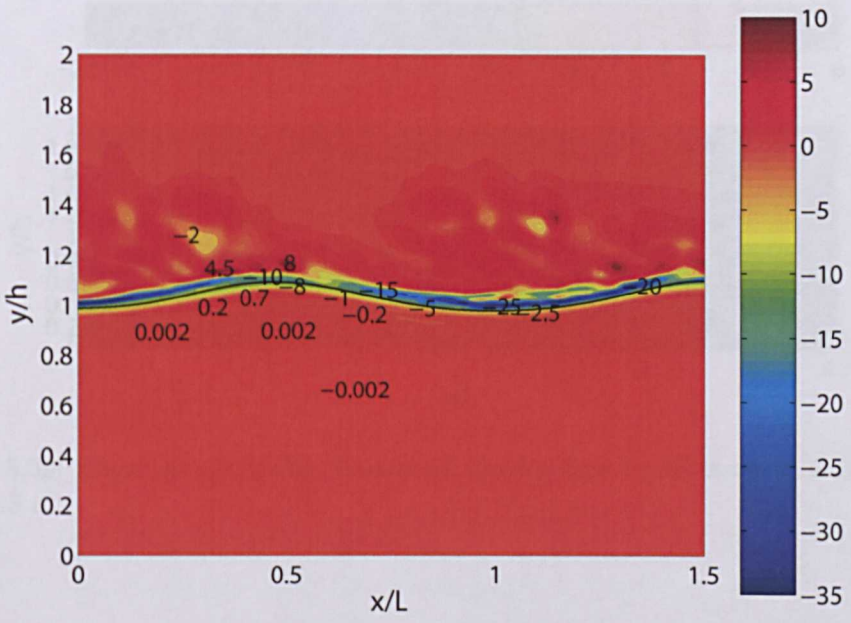

Figure 5.37: Vorticity in a typical wave of viscous flow in deep water wave case; $V' = 0.5\ c$.

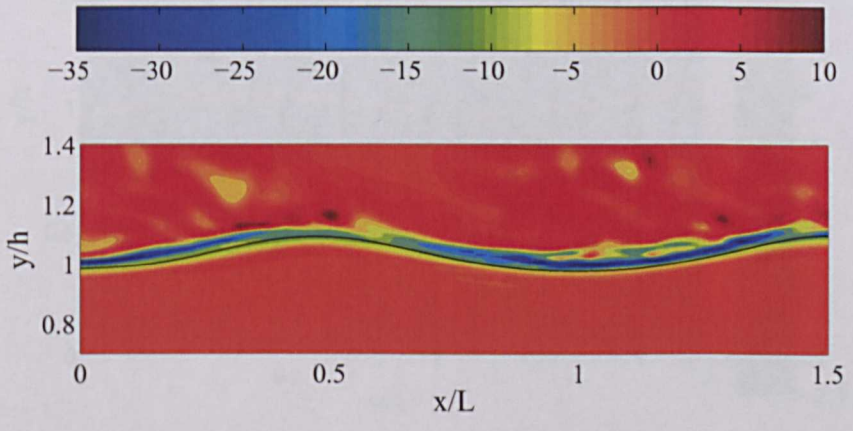

Figure 5.38: Vorticity in a typical wave of viscous flow in deep water wave case in specified area; $V' = 0.5\ c$.

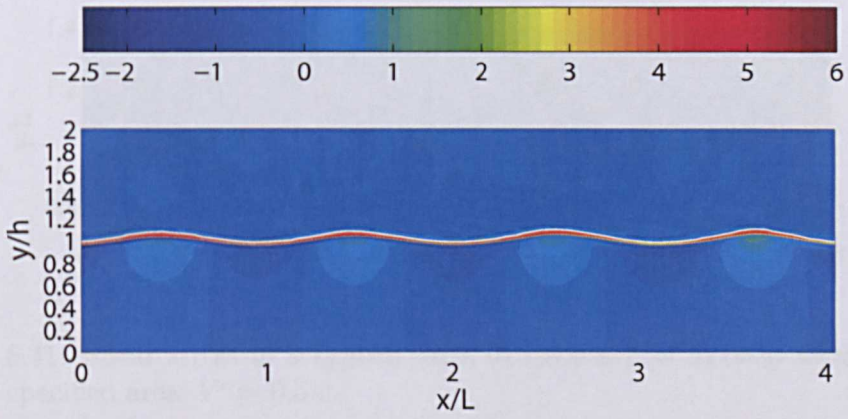

Figure 5.39: Shear stress in the domain of viscous flow in deep water wave case; $V' = 0.5\ c$.

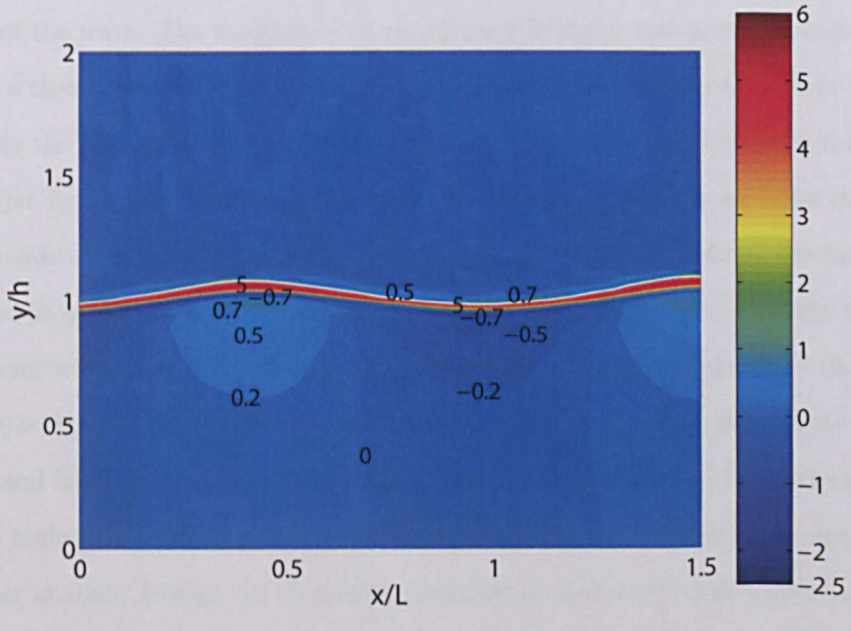

Figure 5.40: Shear stress in a typical wave of viscous flow in deep water wave case; $V' = 0.5\ c$.

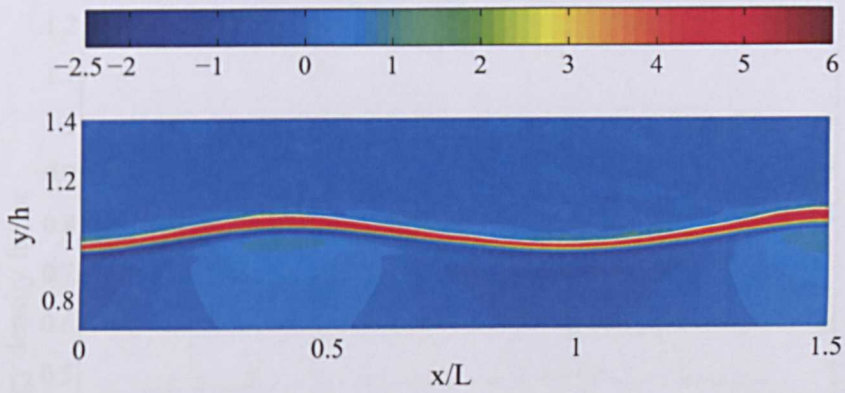

Figure 5.41: Shear stress in a typical wave of viscous flow in deep water wave case in specified area; $V' = 0.5\ c$.

below the free surface, we observe a layer of positive shear stress inside the water in both crest and trough. We also observe a thin layer of negative shear stress of lower magnitude immediately below this positive shear layer. Below this negative shear layer the vertical strips of positive and negative shear stresses below the crest and trough of the wave can be seen. In the air the positive shear stress is observed just above the trough of the wave. The analysis of a typical wave in figure 5.40 shows that in the air there is a three times increase in positive shear stress in the trough of the wave while in the water the positive shear layer which is limited to the crest of the wave in the earlier case (*refer* figure 5.28) now forms a continuous layer to the trough region in the water and extends to the crest of another wave. This positive shear layer is thicker at the crest and progressively becomes thinner as it reaches the trough. Similarly, the negative shear layer which was only observed inside the water below the trough in the earlier case (*refer* figure 5.28) can be seen in the water below the positive shear layer in both trough and crest. This also indicates that the effect of viscosity in the wind wave case is much higher than low or zero average wind velocity case. The maximum shear stress in the air is about 14% of the maximum shear stress observed in the water. Although these magnitude is not very high, it clearly indicates that air cannot be neglected when the wind is blowing at much higher wind speed and may hold key to understanding of coupled wind-wave behaviour. A more specific details can be seen in figure 5.41.

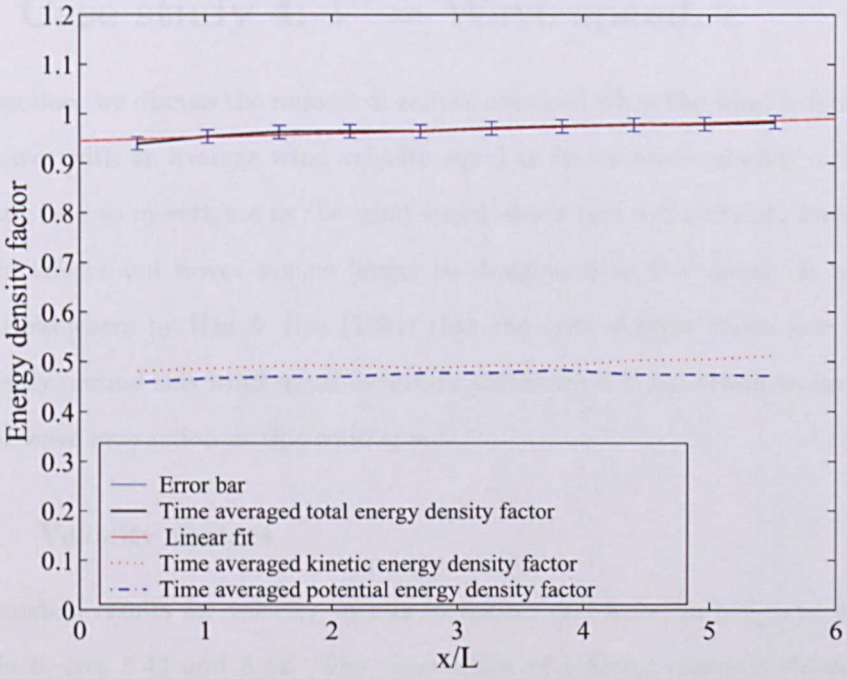

Figure 5.42: Time averaged energy density factor vs x; $V' = 0.5\ c$.

5.4.4 Energy density in the domain

The energy density variation along the length of the domain when the wind is blowing with velocity equal to 0.5 c over the deep water wave is shown in the figure 5.42. On comparing the time averaged energy density variation shown in figure 5.42 with that in figures 5.30 and 4.2, we observe that the energy density of the wave shows increase along the length of the domain. This increase is about 4% more than zero average wind velocity case and about 2% more than low wind velocity case discussed earlier. The potential energy density factor does not show a major increase in the value while kinetic energy in the water wave shows the most increase, which in turn contributes to the total increase observed along the domain. These observations gives the evidence of direct energy exchange between air and water wave. This exchange is mainly by momentum transfer from air to water resulting in increase of orbital velocity of the water and producing the net increase in kinetic energy density of the water wave.

5.5 Case study 4: V' = Wave speed, c

In this section, we discuss the numerical results obtained when the wind is forced over water waves with an average wind velocity equal to water wave velocity, c. It is an important case to investigate as the wind speed above this will certainly have higher turbulent effects and waves can no longer be designated as fast waves. It has been reported elsewhere by Hsu & Hsu (1981) that the critical layer effects can be seen prominently around this wind speed condition and hence it is important to investigate the wind-wave interaction at this wind speed.

5.5.0.1 Velocity vectors

The numerical results for velocity vectors in the air and water in a typical wave are shown in figures 5.43 and 5.44. The observation of velocity contours shows higher velocity in the air region and extremely small recirculation zone in the trough region of the wave. The extent and magnitude of velocity in the water near the crest is higher than earlier cases. We also observe higher velocity from the velocity contour in the region of windward side of the water wave, indicating influx of momentum from air which increases the orbital movement in the water leading to an increase in kinetic energy inside the water wave. The observation of velocity vectors in figure 5.44 shows that flow in the air remains attached to the free surface in most part of the wave due to higher velocity in the air except in the small part near the trough. It also indicates that after reaching a critical speed the air starts to dominate the flow leading to an increase in air-water wave interaction and momentum exchange. The boundary layer region near the free surface is more significant than other cases as the difference in the velocity in the air and water waves is higher and wave surface acts as super smooth wall to the airflow above it. In a moving reference frame as seen in figure 5.45, we observe the velocity vectors with very small velocity indicating forward moving air with higher velocity. Near the free surface we observe lower velocity in the air near the crest and trough due to lower mean velocity under the water. Since the difference in velocity in

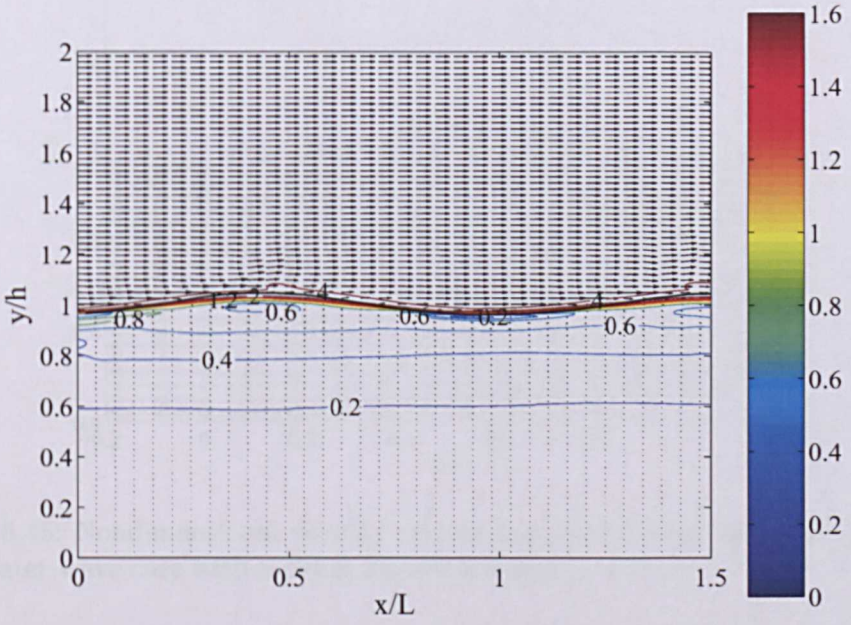

Figure 5.43: Nondimensional velocity vectors in a typical wave of viscous flow in deep water wave case; $V' = c$.

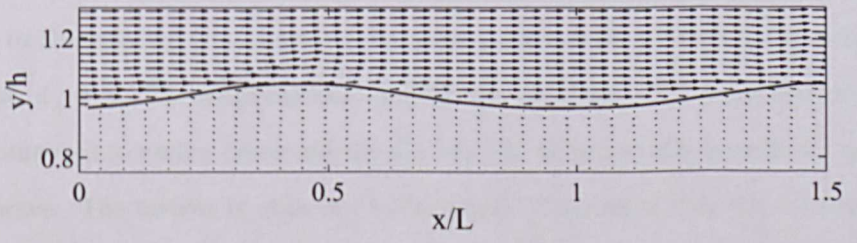

Figure 5.44: Nondimensional velocity vectors in a typical wave of viscous flow in deep water wave case in specified area; $V' = c$.

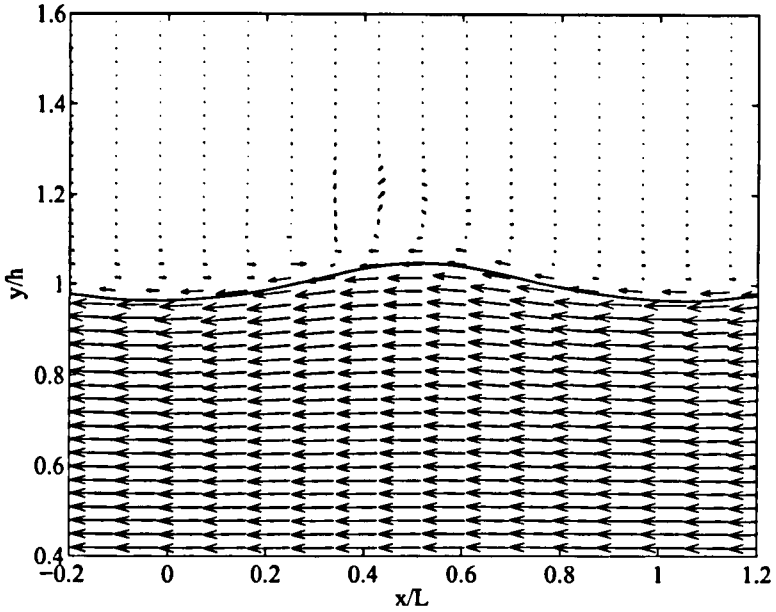

Figure 5.45: Nondimensional velocity vectors in a typical wave of viscous flow in deep water wave case with moving reference frame; $u - c$; $V' = c$.

the air and water is higher in this case, we observe higher shear stress at higher wind speed than earlier cases.

5.5.0.2 Streamlines

The numerical results for streamlines in the air and water in a typical wave is shown in the figure 5.46. The streamlines shows much lower effect of orbital velocity of water on the airflow. It shows an increase in the velocity in both trough and crest of the wave. Similar to the velocity vectors inside the water, it shows an increase in the velocity in the crest of wave. The recirculation observed in the trough of the wave is extremely small compared to earlier cases and the air flow can be practically considered attached to the wave. The airflow is observed to be evenly distributed over the crest and the trough of the wave.

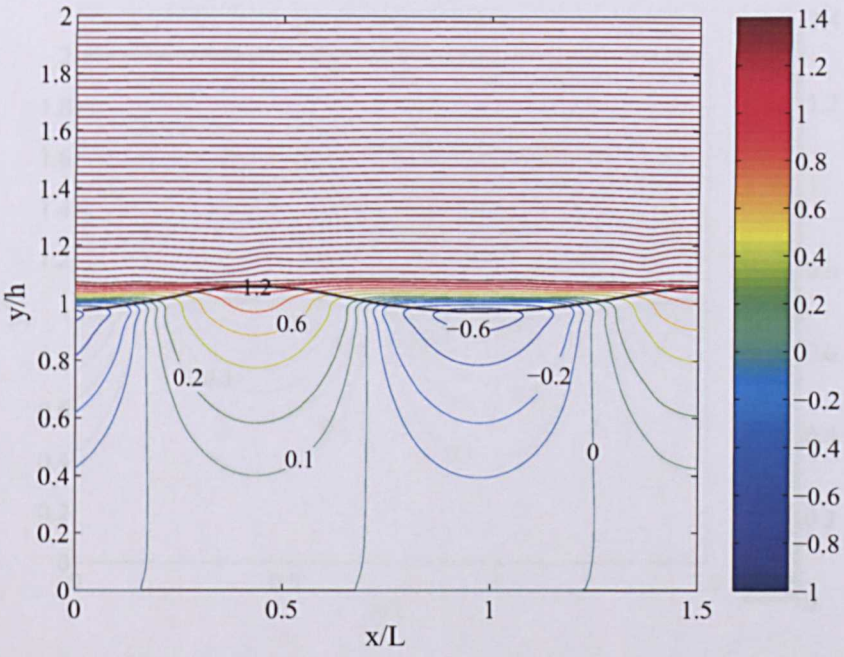

Figure 5.46: Streamlines in a typical wave of viscous flow in deep water wave case; $V' = c$.

5.5.1 Dynamic pressure isolines in water

The numerical results for pressure isolines in a typical wave is shown in the figure 5.47. Along the length of the domain we observe the distribution of pressure isolines. The dynamic pressure isolines as observed in a typical wave shows maximum value in the peak of the wave. An increase in the magnitude of pressure isolines indicates an increase in dynamic pressure in both crest and trough region of the wave. The isolines in this case has even distribution of dynamic pressure in both the crest and trough region of the wave as compared to earlier cases.

5.5.2 Vorticity in the air and water

The numerical results for vorticity in the domain of the water wave and a typical wave are shown in figures 5.48 and 5.49. Along the length of the domain we observe an increase in thickness of the negative vorticity layer in the water due to an increase in velocity of the wind. We also observe in the air, a region of positive vorticity above

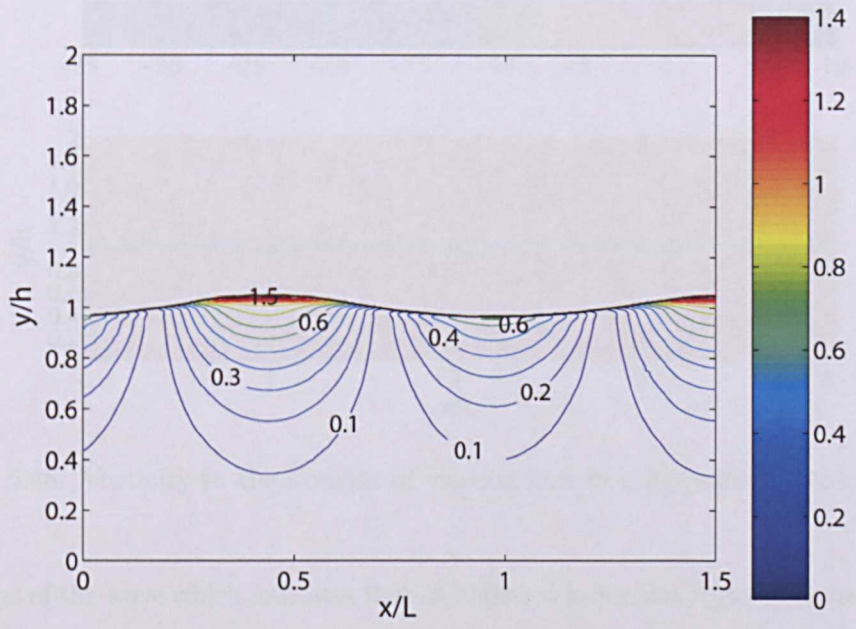

Figure 5.47: Pressure isolines in a typical wave of viscous flow in deep water wave case; $V' = c$.

the negative vorticity layer above the trough of the wave. The magnitude of this positive vorticity reduces along the length of the domain. We also observe diffusion of vorticity in the air in the form of vorticity bubbles moving up above the slope on the windward side of the wave near the crest of the wave into the air region above and moving further up along the length. These vortex bubbles are evolved from the vortex sheet near the interface and after breaking it forms a distinct vorticity structure by rolling. The diffusion of this vorticity is mainly due to the effect of viscosity. These vortex structures are formed from the negative vorticity layer found over the trough of the wave. When the wind velocity increases progressively the negative vorticity layer thickens as seen from earlier cases and there is a reduction in resistance to movement of air which helps to reduce the drag on the free surface. Inside the water below the water surface, we observe thicker negative vorticity layer along the length of the domain while the magnitude of vorticity quickly reduces to zero along the depth of the water. The magnitude of vorticity in a typical wave is shown in figure 5.49. It shows shift of negative vorticity layer just above the trough region towards the windward side on

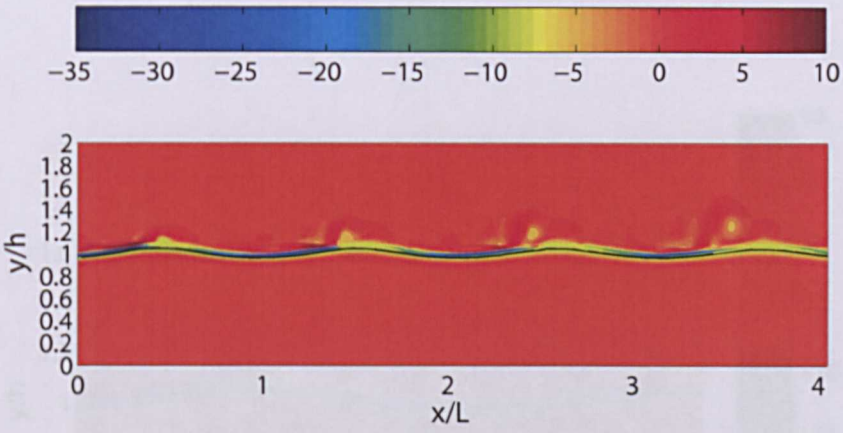

Figure 5.48: Vorticity in the domain of viscous flow in deep water wave case; $V' = c$.

the slope of the wave which indicates that at higher velocity this region is dynamically important for momentum transfer between air and water. On comparing the case with earlier cases (*refer* figure 5.37), we observe a 20% increase in negative vorticity inside the water in both crest and trough of the wave. In the bottom we observe very small vorticity as earlier cases. The positive vorticity seen near the top of the crest in the water in the case of zero average wind velocity is clearly seen to be pushed down into the water by the negative vorticity generated due to air-water interaction and is redistributed as the thick positive vorticity layer which extends along the length of the wave. A more detailed view is presented in figure 5.50.

5.5.3 Shear stress in the air and water

The numerical results for the shear stress in the domain of the water wave and a typical wave are shown in figures 5.51 and 5.52. In the air, a thicker shear stress layer with large magnitude is observed in the trough of the wave as compared to earlier cases and is seen to extend to the crest region on the windward side of the wave. Above this shear layer, the magnitude is small in the air. Near the crest, the shear stress in the air is small in magnitude. We observe a thicker positive shear stress layer along the length of the domain below the water wave on comparing it with earlier cases (*refer*

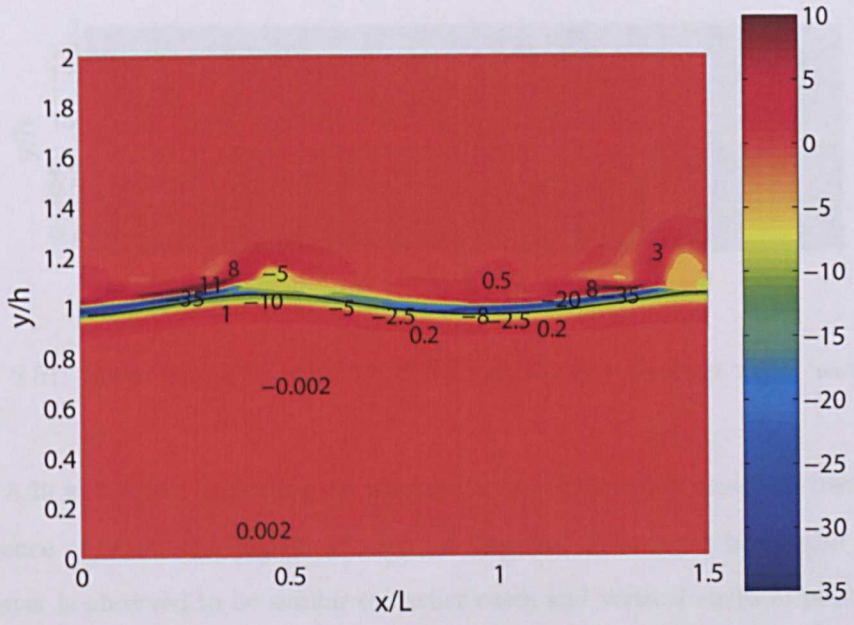

Figure 5.49: Vorticity in a typical wave of viscous flow in deep water wave case; $V' = c$.

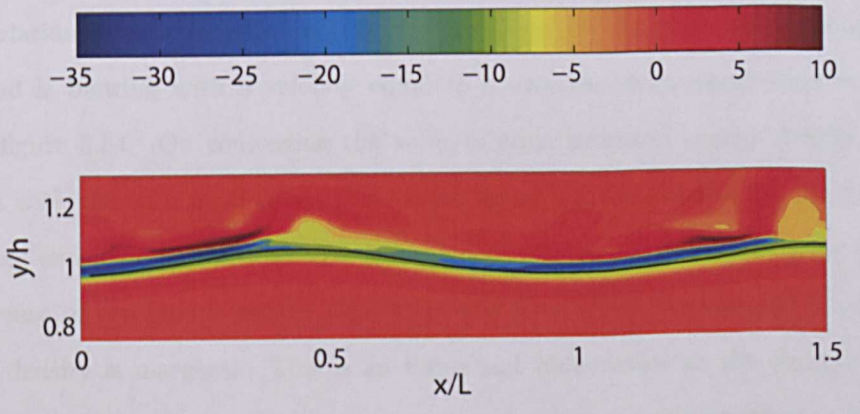

Figure 5.50: Vorticity in a typical wave of viscous flow in deep water wave case in specified area; $V' = c$.

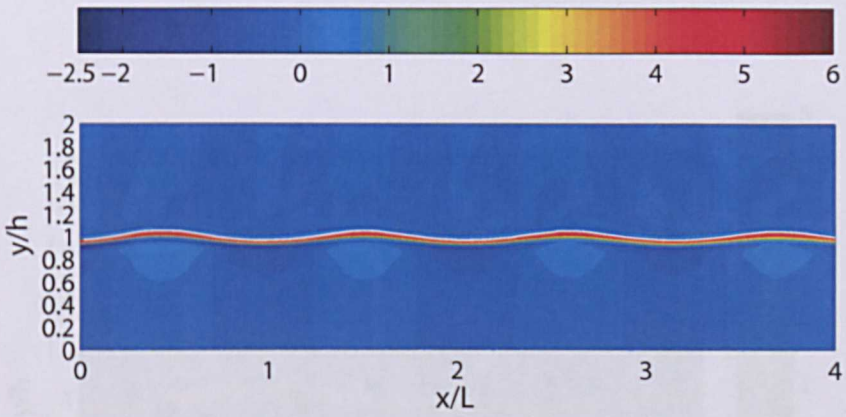

Figure 5.51: Shear stress in the domain of viscous flow in deep water wave case; $V' = c$.

figures 5.39 and 5.27), indicating an increase in the shear effect near the free surface in presence of wind with higher velocity. A negative shear layer below the positive shear layer is observed to be similar to earlier cases and vertical strips of positive and negative shear stresses are observed below the crest and trough. The majority of shear stress in both air and water is found to be concentrated near the free surface of wave. A more detailed view is presented in figure 5.53.

5.5.4 Energy density in the domain

The variation of time averaged energy density along the length of the domain when the wind is blowing with a velocity equal to c over the deep water wave is shown in the figure 5.54. On comparing the value of time averaged energy density in the domain with the zero wind speed case (*refer* figure 4.2, we observe 6% increase due to energy exchange between air and water wave. Similar to earlier cases, we observe an increase in the kinetic energy density in the wave while the increase of potential energy density is marginal. This is an important observation as the energy density calculated in laboratory and field measurements is potential energy density. It is also worth mentioning that it is possible that the kinetic energy inside the wave takes longer time to make full transition to potential energy which requires very long domain to be modeled in order to observe it. We also observe internal energy exchange between

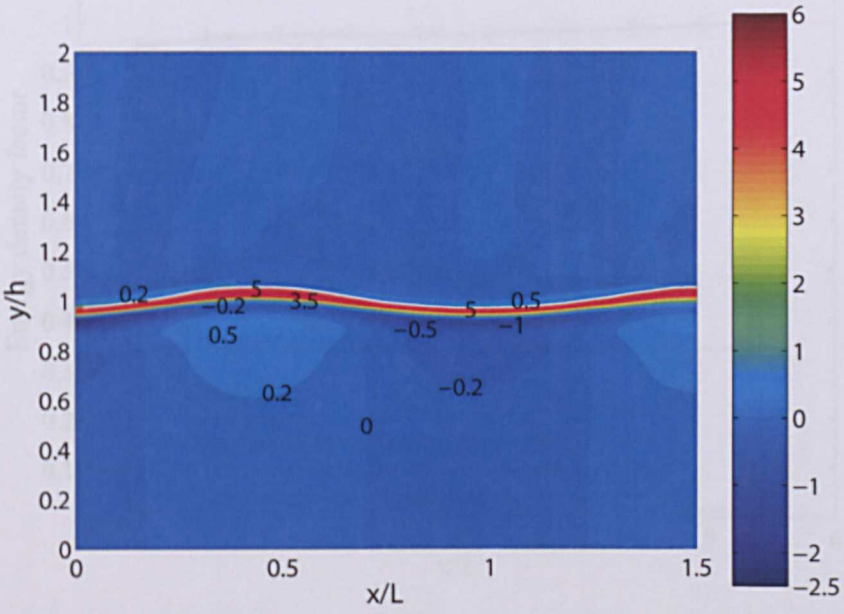

Figure 5.52: Shear stress in a typical wave of viscous flow in deep water wave case; $V' = c$.

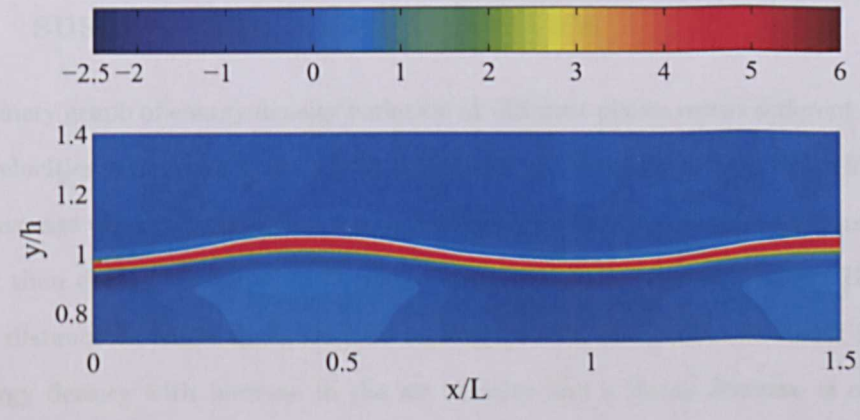

Figure 5.53: Shear stress in a typical wave of viscous flow in deep water wave case in specified area; $V' = c$.

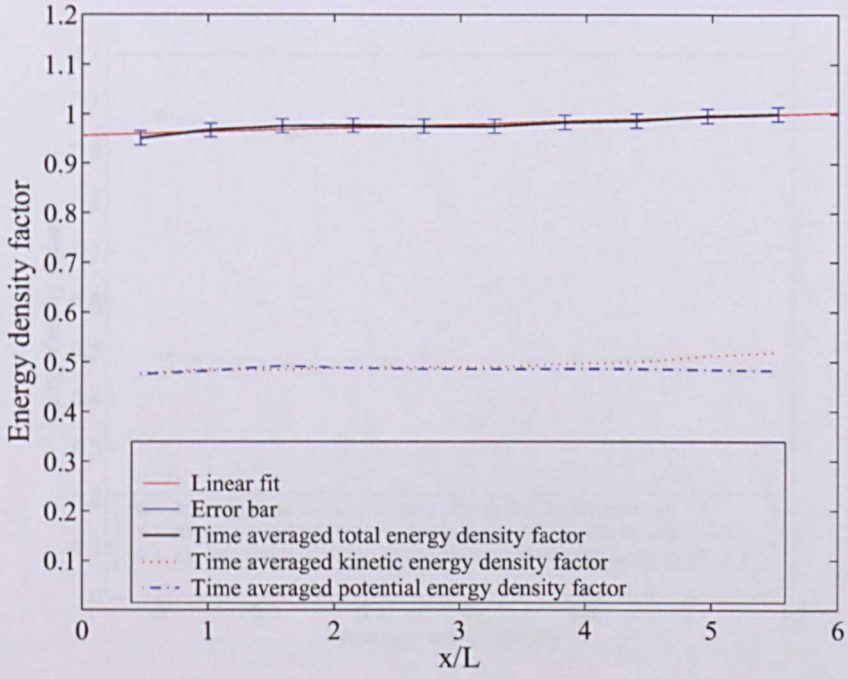

Figure 5.54: Time averaged energy density factor vs x; $V' = c$.

kinetic and potential energy in the water wave along the domain.

5.6 Summery graph of energy density factor versus average wind velocities

A summery graph of energy density variation at different places versus different average wind velocities is shown in figure's 5.55, 5.56 and 5.57. We observe from figure 5.55 that when average wind velocity is zero the wave relatively nearer to the inlet contains higher energy than energy contained in the wave when the air is blowing over it. However, as the distance increases in figure 5.56 and figure 5.57 we observe an linear increase in energy density with increase in the air velocity and a linear decrease is observed in the case when average wind velocity is zero. At all wind speed the major change in total energy density is mainly due to change in kinetic energy density in the wave. This proves that energy exchange phenomenon between air and water wave has both

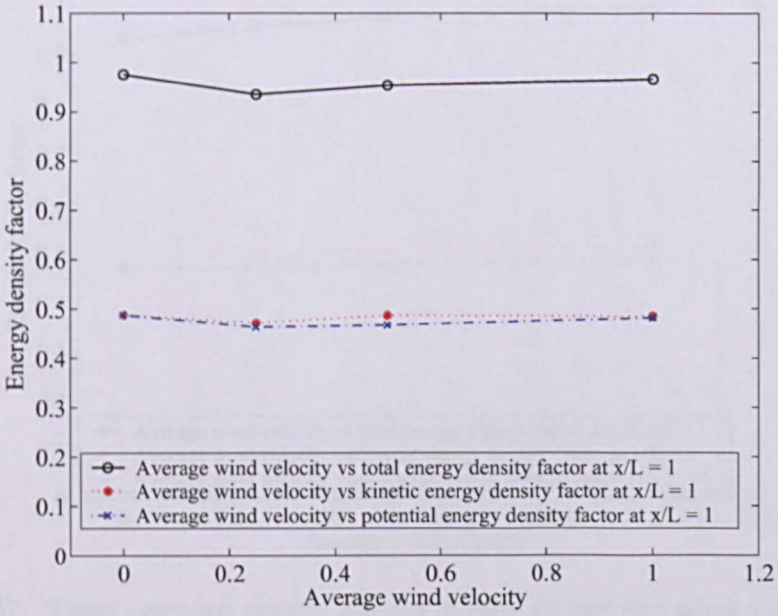

Figure 5.55: Time averaged energy density factor vs average wind velocities at x/L = 1.

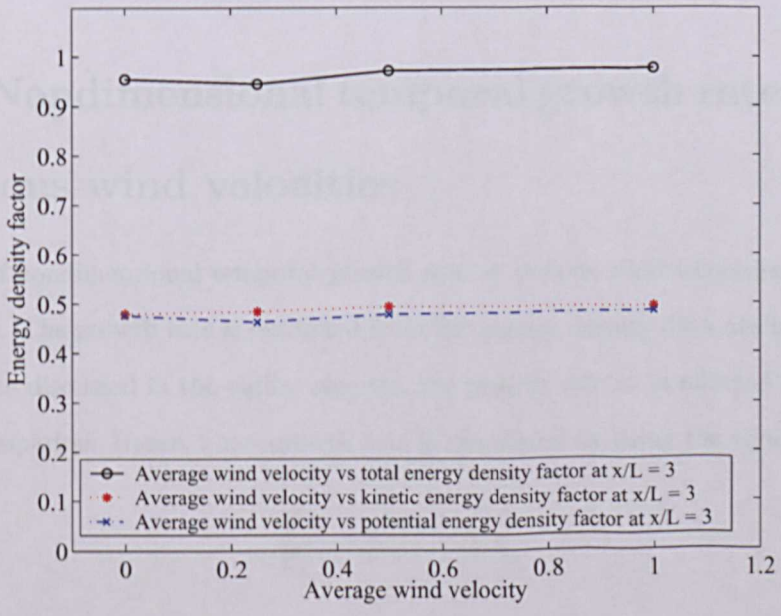

Figure 5.56: Time averaged energy density factor vs average wind velocities at x/L = 3.

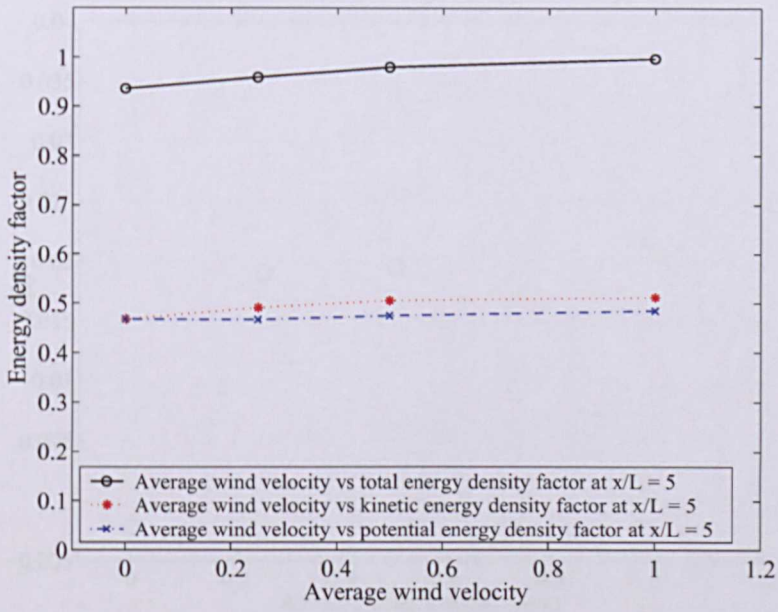

Figure 5.57: Time averaged energy density factor vs average wind velocities at x/L = 5.

spatial as well as time dependence. The results can be compared to similar laboratory experiments and provide valuable input into the study of energy exchange in *fast waves.*

5.7 Nondimensional temporal growth rate at various wind velocities

A graph of nondimensional temporal growth rate at various wind velocities is seen in figure 5.58. The growth rate is extracted from the energy density data available in the domain. As discussed in the earlier chapter, the growth rate $\alpha^{'}$ is affected by viscous energy dissipation. Hence, a net growth rate is calculated by using the equation

$$\frac{\overline{E}}{\overline{E_0}} = exp(\overline{\alpha^{'}} - \Delta)x \tag{5.3}$$

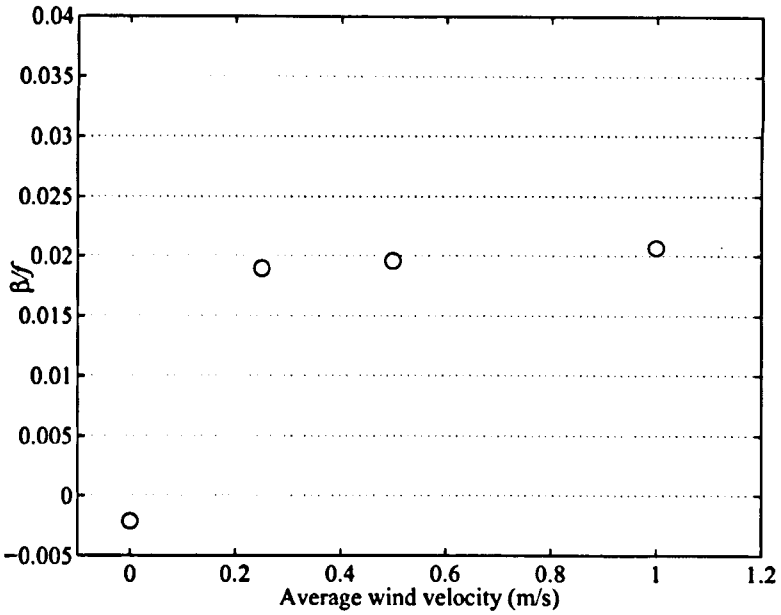

Figure 5.58: Plot of β/f versus average wind velocities in the domain; deep wind-water waves.

where, Δ is the decay rate calculated in §4.2. The spatial growth rate $\overline{\alpha}'$ is converted to the temporal growth rate β through the relation

$$\beta = c\,\overline{\alpha}' \tag{5.4}$$

where c is wave speed. The relation between nondimensional growth rate β/f and average wind velocity is plotted in figure 5.58, where f is the frequency of the wave. The growth rate shows linear increase with an increase in the wind velocity. The growth rate term is negative when the wind velocity is zero due to the fact that the energy is dissipated continuously from the start of the wave till the end of the test section. While in the cases when average wind velocity is higher the growth rate term is increasing in the domain with an increase in the wind speed. Along with wind speed the other factor which can affect the temporal growth rate is the wave steepness. However, it is not discussed in this work.

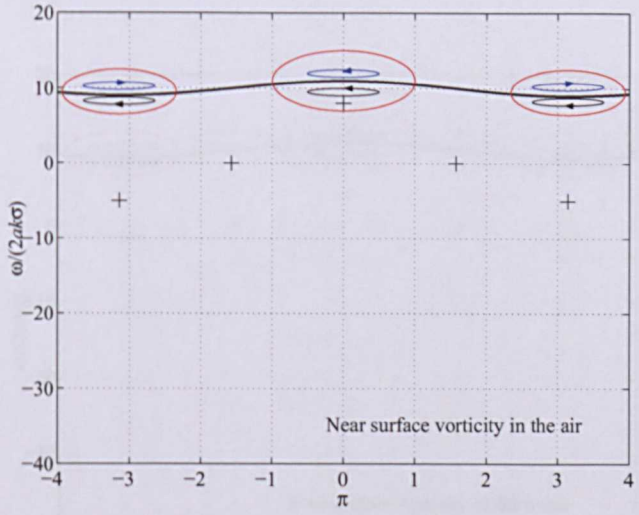

Figure 5.59: A schematic of maximum near surface vorticity in the air at $-\pi$ (trough), $-\pi/2$, 0 (crest), $\pi/2$, π ; 1)+, case 1, $V' = 0$; — represents fluid rotation in the air, —, fluid rotation in the water .

5.8 Schematic of maximum near surface vorticity in the air and water

The schematics of near surface vorticity in the air and water when the average wind velocity is zero in deep water waves is shown in figures 5.59 and 5.62 respectively. Both figures show a positive vorticity in the air and water near the crest owing to anticlockwise movement of water particles. While in the trough we observe clockwise rotation of water particles. In the crest, the rotation of air at zero wind velocity is in anticlockwise direction following the rotation of water. Hence, we can observe positive vorticity in the air and water. As the wind speed is increased as seen in figures 5.61 and 5.63, the air starts interacting with the water primarily in the windward side and crest of the wave as wind experiences the push due to convection as well as pull by the clockwise moving water in the trough of the wave. These effect creates higher gradients in the windward side of the wave resulting in more convection and diffusion of air on the windward side producing more vorticity on the windward side of the wave at higher wind speed. On the other hand on the leeward side, the forward moving air experiences

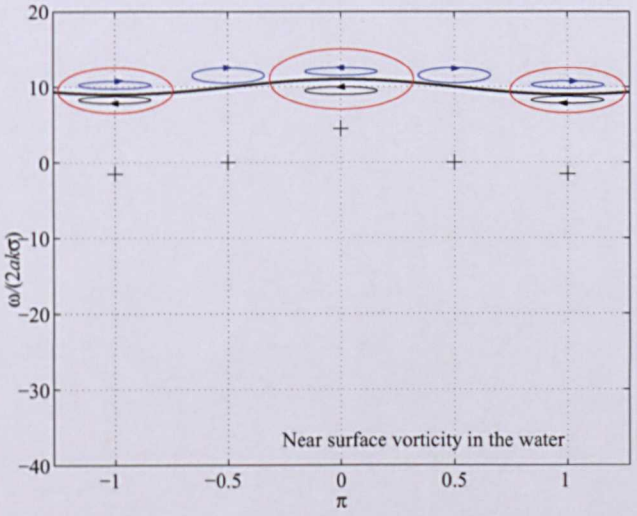

Figure 5.60: A schematic of maximum near surface vorticity in the water at $-\pi$ (trough), $-\pi/2$, 0 (crest), $\pi/2$, π ; 1)+, case 1, $V' = 0$; — represents fluid rotation in the air, —, fluid rotation in the water .

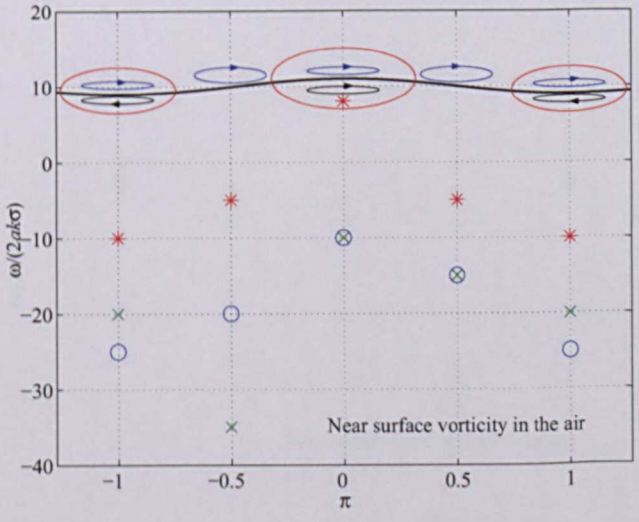

Figure 5.61: A schematic of maximum near surface vorticity in the air at $-\pi$ (trough), $-\pi/2$, 0 (crest), $\pi/2$, π ; 1) $*$, case 2, $V' = u_{max}$, 2) $\circ$, case 3, $V' = 0.5c$, 3) $\times$, case 4, $V' = c$; — represents fluid rotation in the air, —, fluid rotation in the water .

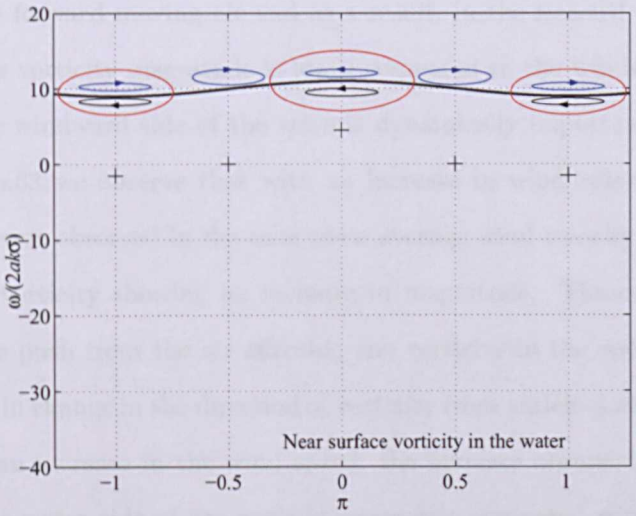

Figure 5.62: A schematic of maximum near surface vorticity in the water at $-\pi$ (trough), $-\pi/2$, 0 (crest), $\pi/2$, π ; 1)+, case 1, $V' = 0$; — represents fluid rotation in the air, —, fluid rotation in the water .

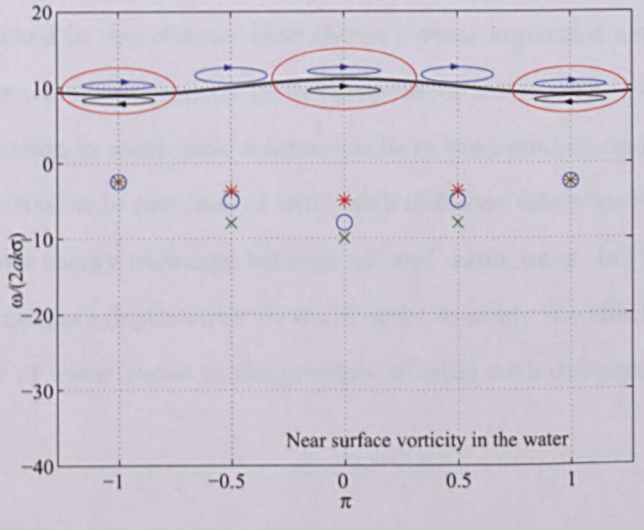

Figure 5.63: A schematic of maximum near surface vorticity in the water at $-\pi$ (trough), $-\pi/2$, 0 (crest), $\pi/2$, π ; 1) $*$, case 2, $V' = u_{max}$, 2) $\circ$, case 3, $V' = 0.5c$, 3) $\times$, case 4, $V' = c$; — represents fluid rotation in the air, —, fluid rotation in the water .

a push from the upward moving water in the opposite direction reducing the clockwise movement of the forward moving air and as a result, in the leeward side, we observe that the negative vorticity magnitude is lower compared to the windward side, which signifies that the windward side of the wave is dynamically important region. In the water in figure 5.63 we observe that with an increase in wind velocity, the positive vorticity in the crest observed in the case when average wind velocity is zero, changes to the negative vorticity showing an increase in magnitude. These increase can be attributed to the push from the air affecting the vorticity in the water near the free surface resulting in change in the direction of vorticity from anticlockwise to a clockwise rotation. With an increase in the wind speed, the increase observed in the vorticity magnitude in the water side of the wave is symmetric compared with the air side of the wave. We also observe the diffusion of vorticity in both the air and water side of the domain due to both spatial and temporal vorticity transport.

5.9 Closure

The results discussed in this chapter have shown several important aspects to be considered in the air water interactions in the deep water waves. The effect of viscosity and rotational motion in wind wave interaction have been studied and discussed. The energy density variation in presence of wind with different velocities is calculated and discussed. It shows energy exchange between air and water wave. In the next chapter, we move to intermediate depth water waves in order to study the effect of water depth on the behaviour of water waves in the presence of wind with different velocities.

Chapter 6

Interaction of intermediate depth water waves with air blowing at different velocities

---

6.1 Introduction

In this chapter we investigate the behaviour of water waves under the effect of air blowing at different velocities in the case of intermediate depth water waves. In order to draw comparison, we consider the waves of steepness 0.06 which are similar to the deep water waves studied in Chapter: 4 and 5. The ratio h/L is similar to intermediate depth water waves in Chapter: 4. The average wind velocities considered here are 1) $V' = 0ms^{-1}$, 2) $V' = u_{max}$, where u_{max} is the maximum velocity in water, 3)$V'(\approx 0.5c)$ and 4) $V' = c$. The study of interaction of intermediate depth water wave with wind is essential to study how the change in the depth of water affects the behaviour of water waves.

6.2 Case study 1: Zero average wind velocity, $V' = 0$

In the previous chapter, we analyzed the air-water interaction in deep water wave system with air blowing at different velocities. In this case, we investigate the motion in the air above the intermediate depth water waves when the average wind velocity is zero. All the quantities are nondimensionalized as discussed in the chapter 4. We restrict the discussion here to the air side of the domain as the water side of the domain is already discussed in chapter 4.

6.2.1 Velocity vectors and streamlines in the intermediate depth water waves

6.2.1.1 Velocity vectors

The numerical results for velocity vectors in the air and water in the domain and a typical wave are shown in figures 6.1, 6.2 and 6.3. In the domain of viscous flow along the length, we observe a periodic motion in the air following the orbital movement of water beneath it. We also observe recirculation of air above the crest and the trough of the wave. This movement of the air is similar to the one observed in deep water waves as plotted in figure 5.1. The maximum velocity in the air near the free surface is of same magnitude as maximum velocity in the water beneath the wave. A typical wave in figure 6.2 shows the nondimensional velocity contours in the air and water. The fluid motion in the air mirrors that in the water and a gradual reduction in the velocity of air is observed when the distance to the water surface increases. In the trough region, in the air we see higher velocity than the maximum velocity in the water which is expected in the most boundary layer phenomenon. A more detailed view of velocity vectors is seen in figure 6.3. In a moving reference frame, the velocity vectors are shown in figure 6.4. Here, the relative velocity in the air and water are nearly similar in magnitude which results in relatively lower shear stress on the free surface in both

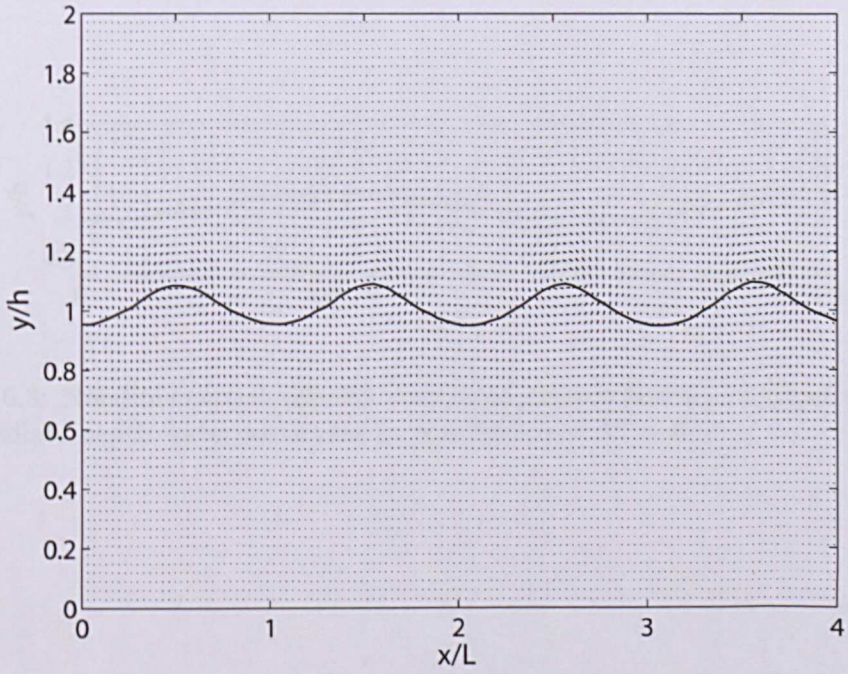

Figure 6.1: Nondimensional velocity vectors of viscous flow in the domain of intermediate depth water wave case; $V' = 0$.

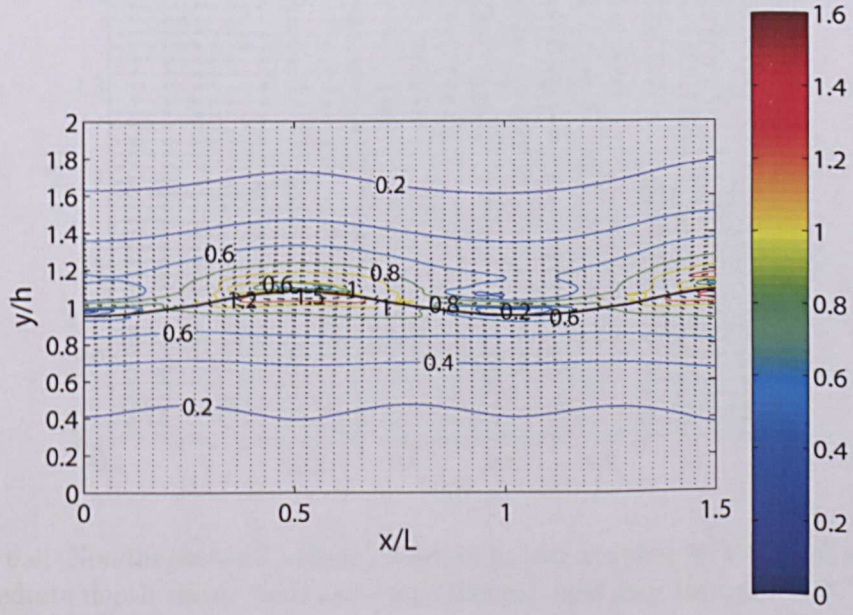

Figure 6.2: Nondimensional velocity vectors of viscous flow in a typical wave of intermediate depth water wave case; $V' = 0$.

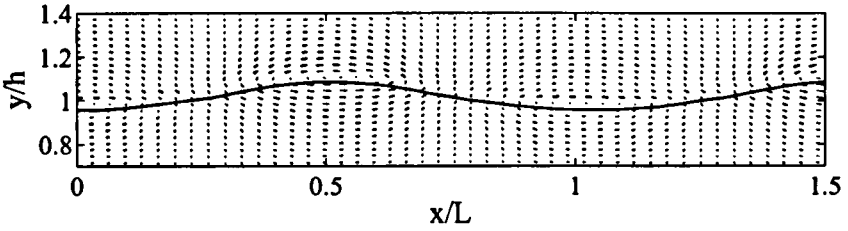

Figure 6.3: Nondimensional velocity vectors of viscous flow in a typical wave of intermediate depth water wave case in specified area; $V' = 0$.

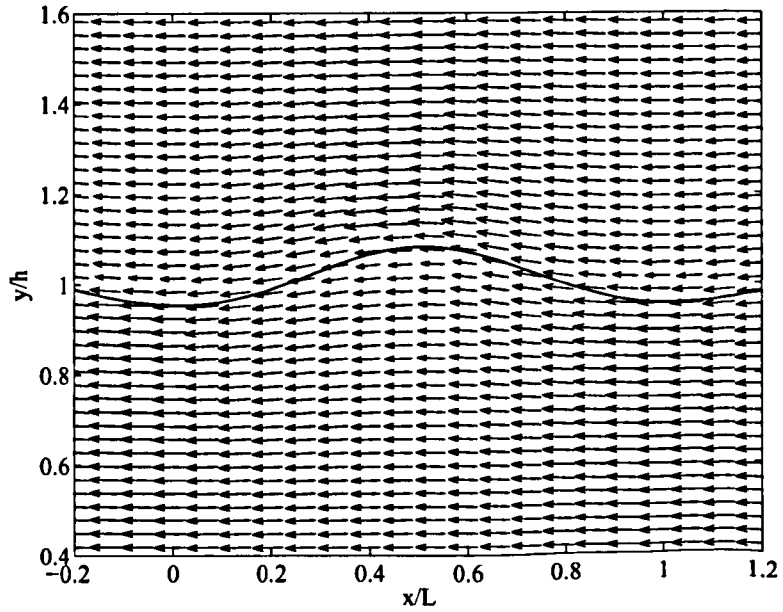

Figure 6.4: Nondimensional velocity vectors of viscous flow in a typical wave of intermediate depth water wave case with moving reference frame; $u - c$; $V' = 0$.

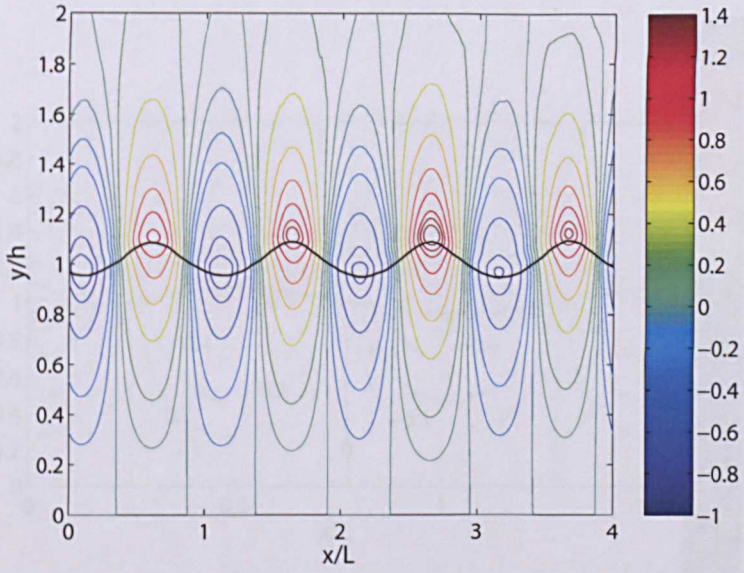

Figure 6.5: Streamlines in the domain of viscous flow in intermediate depth water wave case; $V' = 0$.

the air and water. The smaller velocity vectors in the crest inside the water indicates higher velocity in this region.

6.2.1.2 Streamlines

The streamlines in the air and water section are shown in figures 6.5 and 6.6. The streamlines along the length of the domain are periodically distributed similar to deep water wave case (*refer* 5.5). The streamlines in the air are also periodic on each wave and the follows the orbital motion in the water. The examination of a typical wave in figure 6.6 shows the location in the air where air changes its direction to follow the orbital motion in the water below. The extent of movement in the air along the depth is higher than deep water waves since the longer wavelength of the intermediate depth disturbs the air at greater height above the water surface.

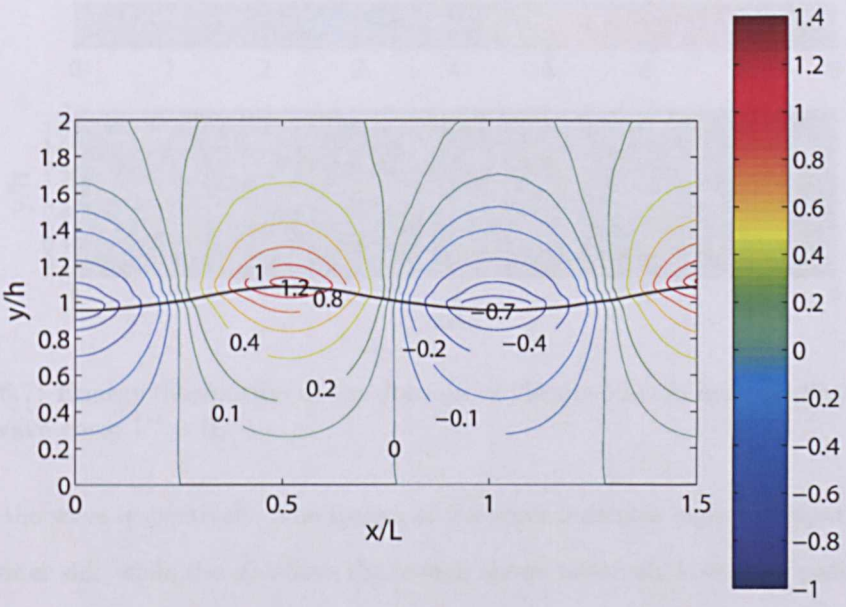

Figure 6.6: Streamlines in a typical wave of viscous flow in intermediate depth water wave case; $V' = 0$.

6.2.2 Dissipation function in the intermediate depth water waves

The plots of energy dissipation function in the domain and a typical wave are shown in figures 6.7 and 6.8. The dissipation function along the length of the domain shows much higher dissipation rate in the crest of the wave which signifies the effect of viscous stresses in the region. We also observe higher dissipation rate in the air above the crest and trough of the wave as compared to deep water waves. The dissipation rate in the air is quickly reduced to lower values while we observe higher dissipation rate inside the water. This is mainly due to duel effects of longer wave length of intermediate depth water wave affecting more area under water surface by orbital motion resulting in higher viscous dissipation and secondly, higher bottom boundary effects as the bottom wall boundary is nearer to the wave which results in higher viscous effects on the orbital motion in the water. The dissipation function of a typical wave is shown in figure 6.8. It shows the magnitude of the dissipation function in a typical wave and overlying air region. We observe high magnitude in both water and air region above and below the

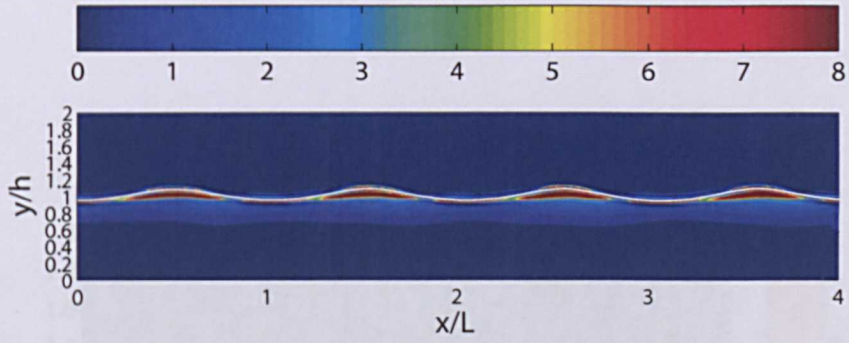

Figure 6.7: Energy dissipation in the domain of viscous flow in intermediate depth water wave case; $V' = 0$.

crest of the wave respectively. The trough of the wave indicates higher dissipation rate in the water side while the air above the trough shows relatively lower dissipation rate. Along the depth of the wave in the water below the crest, we observe linear reduction in the dissipation rate while in the trough region below the higher dissipation layer, we observe a small layer where the dissipation rate is lower which again increases along the depth and reduces linearly along the depth afterwards. A more detailed view of energy dissipation is presented in figure 6.9.

6.2.3 Vorticity in the intermediate depth water waves

The vorticity distribution in the domain and a typical wave of the intermediate depth water waves are shown in the figures 6.10 and 6.11. In the air and water, along the length of the domain we observe the contours with both positive and negative vorticity in the crest and trough. Along the depth in both air and water the vorticity quickly reduces to a small value. The maximum vorticity near the free surface in the air as seen in the figure 6.11 is more than twice the maximum vorticity observed in the water. In the air, the positive and negative vorticity layers are observed immediately above the negative vorticity layer in the trough of the wave. The magnitude of the negative vorticity observed above the positive vorticity layer in the trough is much higher than that observed in the deep water wave in figure 5.12. In the crest, the vorticity quickly reduces to a lower value along the depth of the air. The basic structure of vorticity

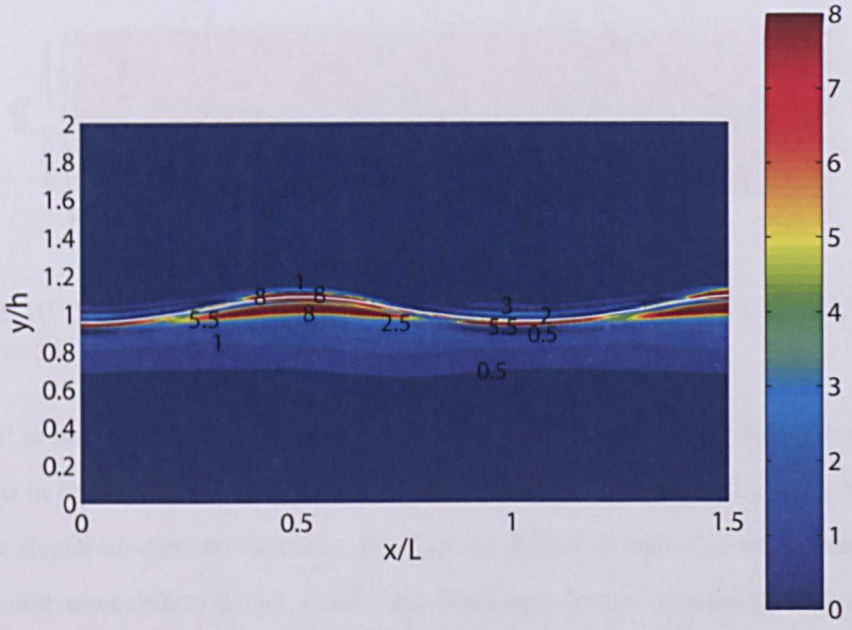

Figure 6.8: Energy dissipation in a typical wave of viscous flow in intermediate depth water wave case; $V' = 0$.

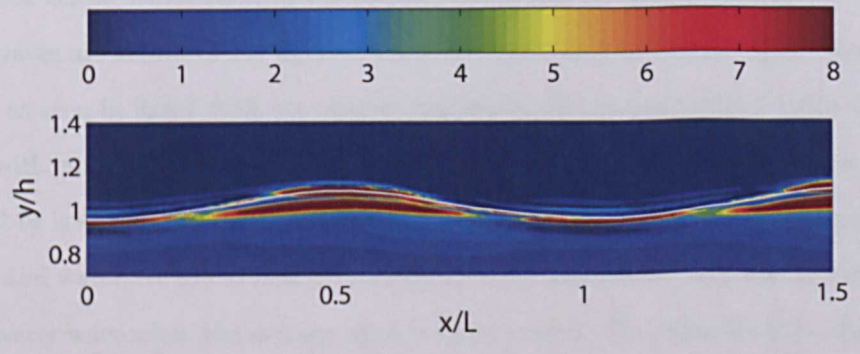

Figure 6.9: Energy dissipation in a typical wave of viscous flow in intermediate depth water wave case in specified area; $V' = 0$.

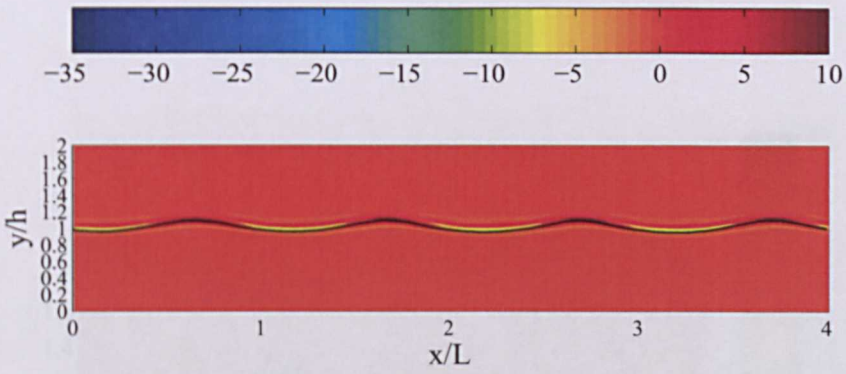

Figure 6.10: Vorticity in the domain of viscous flow in intermediated depth water wave case; $V' = 0$.

observed in both the air and water as shown in figure 6.11 and for the deep water waves as shown in figure 5.12 shows similarities. The difference between both types of waves is in the depth of vorticity distributed in the air which is higher in the intermediate depth water wave due to longer wavelength leading to higher velocity gradients in the air. The vorticity near the bottom boundary is very small as compared to the vorticity near to the surface which shows higher magnitude than that observed in deep water waves.

6.2.4 Shear stress in the air and water

The shear stress distribution in the domain and a typical wave of intermediate depth water waves are shown in the figures 6.13 and 6.14. Along the length of the domain in the air as seen in figure 6.13, we observe uniformly distributed vertical strips of shear stress with small magnitude. In the air, the magnitude of this shear stress as seen in figure 6.14 is small compared with that in the water. The structures of shear stress in the air and water are found nearly identical in both deep water wave and intermediate depth water wave when the average wind velocity is zero. The vertical strips of positive and negative shear stress are identical to those found inside the water mainly due to the fact that air is following the orbital velocity in the water. A more detailed view of shear stress is seen in figure 6.15.

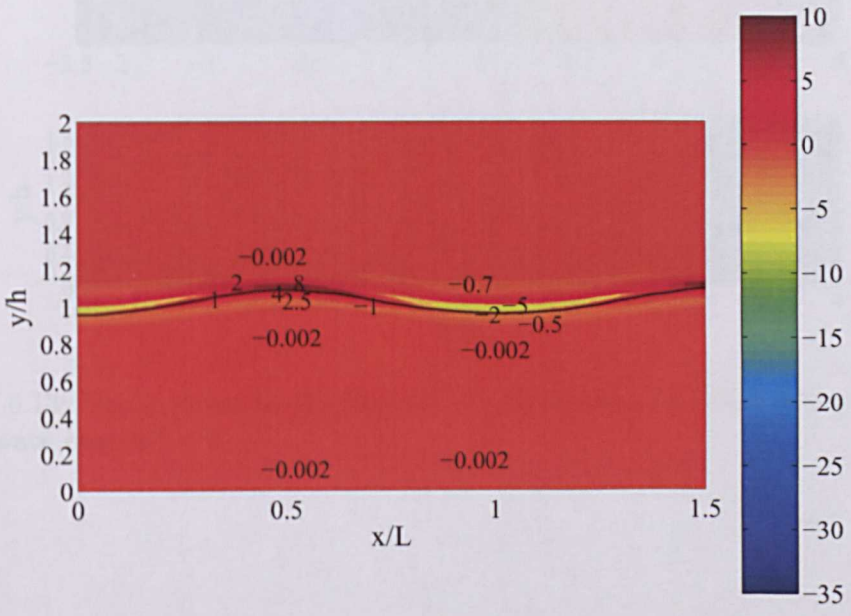

Figure 6.11: Vorticity in a typical wave of viscous flow in intermediate depth water wave case; $V' = 0$.

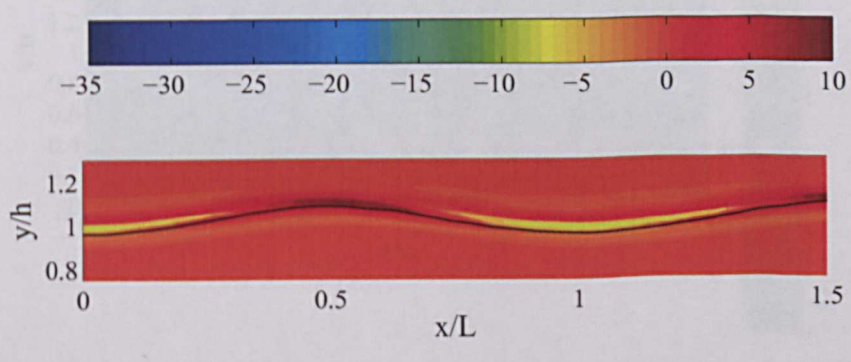

Figure 6.12: Vorticity in a typical wave of viscous flow in intermediate depth water wave case in specified area; $V' = 0$.

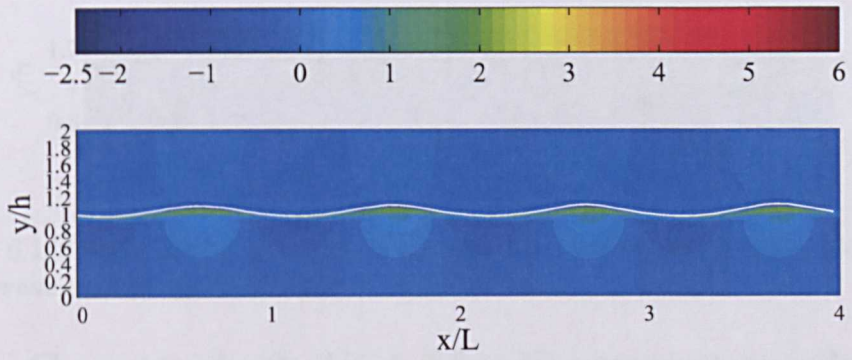

Figure 6.13: Shear stress in the domain of viscous flow in intermediate depth water wave case; $V' = 0$.

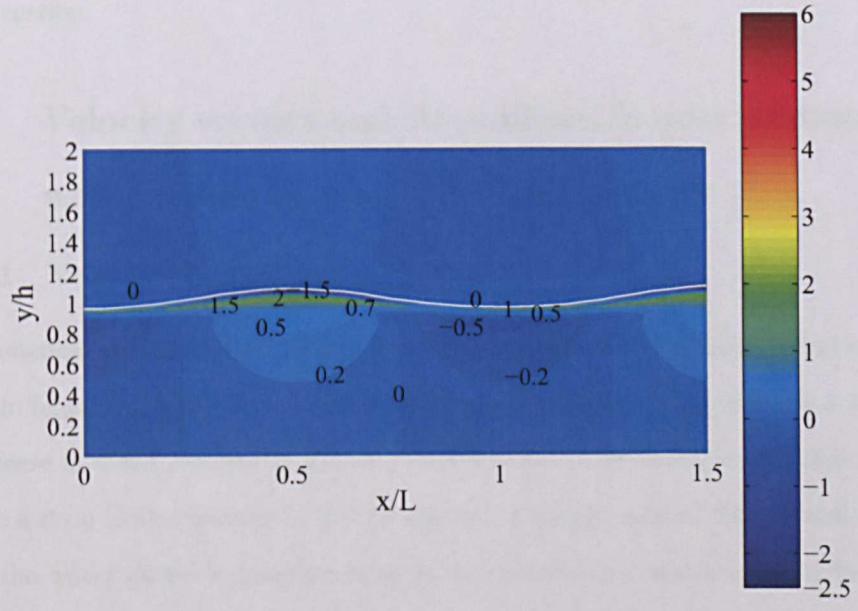

Figure 6.14: Shear stress in a typical wave of viscous flow in intermediate depth water wave case; $V' = 0$.

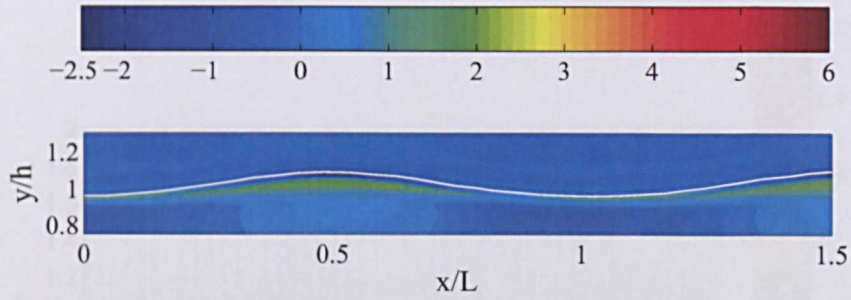

Figure 6.15: Shear stress in a typical wave of viscous flow in intermediate depth water wave case in specified area; $V' = 0$.

6.3 Case study 2: V' = Maximum water velocity $<$ Wave speed, c

In this section, we discuss the numerical results obtained when the air is forced over the intermediate depth water wave with an average velocity equal to maximum velocity in the water. The domains of both the air and water side will be discussed simultaneously in this section.

6.3.1 Velocity vectors and streamlines in intermediate depth water waves at very low wind velocity

6.3.1.1 Velocity vectors

The numerical results for the velocity vectors in the air and water in a typical wave are shown in figures 6.16 and 6.17. The contours of velocity magnitude in figure 6.16 shows an increase in mean velocity in the air just above the crest of the wave, while we also observe a drop in the velocity in the air above the trough region. The orbital velocity inside the water shows a small increase in the crest region and a small reduction in the trough region of the wave. The velocity vectors distribution in the air is more chaotic due to longer wave length and higher velocity in the crest of the wave, thereby producing a greater resistance to the forward moving air leading to disarray in velocity distribution near the crest and the windward side of slope of the wave. The interaction

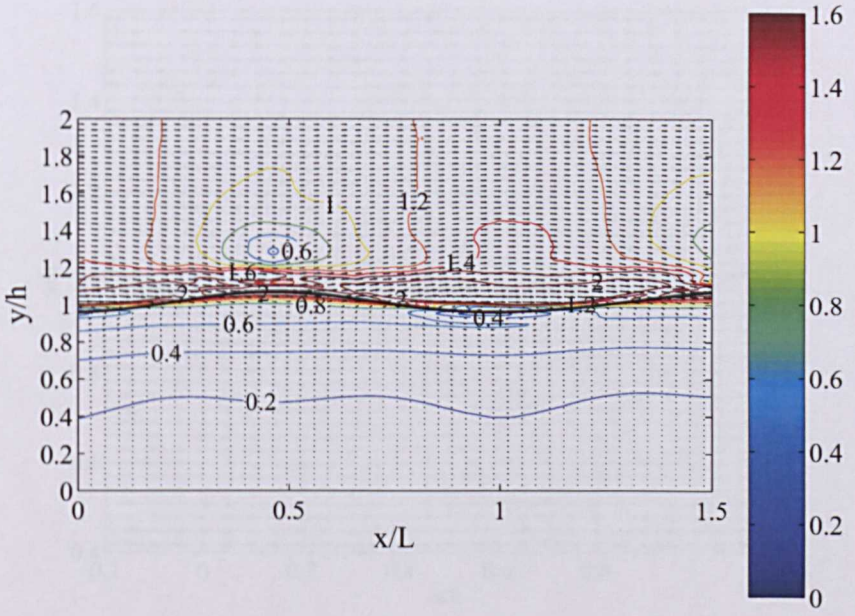

Figure 6.16: Velocity vectors with velocity contours in a typical wave of viscous flow in intermediate depth water wave case; V' = maximum water velocity $< c$.

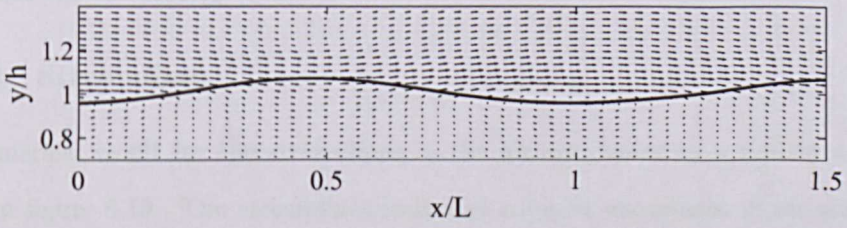

Figure 6.17: Velocity vectors in a typical wave of viscous flow in intermediate depth water wave case in specified area; V' = maximum water velocity $< c$.

at low wind speed is much more complex as both wind and wave tries to dominate the fluid motion. A more detailed view of velocity vectors is seen in figure 6.17. In general, the velocity vector distribution observed is not significantly different than deep water waves. In a moving reference frame, the velocity vectors are seen in figure 6.18. In the air above the crest and trough, it shows relatively smaller size due to higher velocity observed in these region. The highest velocity in the air is observed above the trough of the wave.

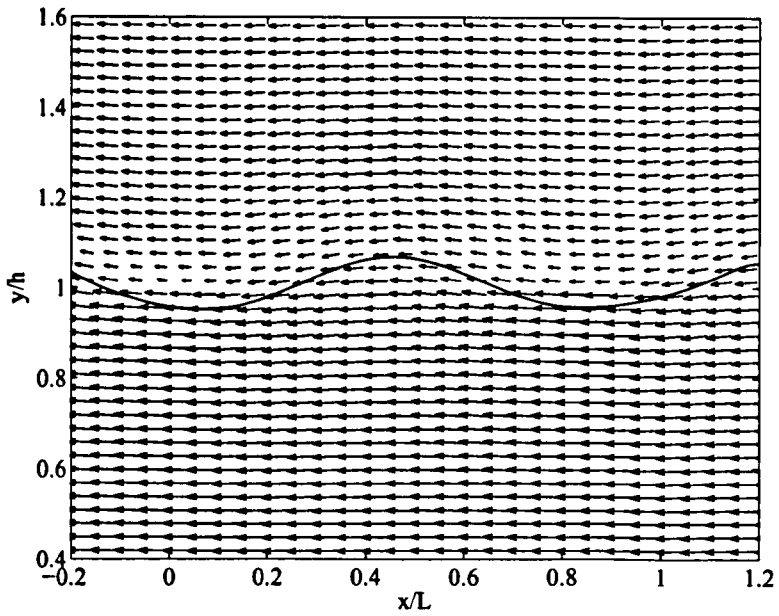

Figure 6.18: Nondimensional velocity vectors of viscous flow in a typical wave of intermediate depth water wave case with moving reference frame; $u - c$; V'= maximum water velocity $< c$.

6.3.1.2 Streamlines

The numerical result for the streamlines in the air and water in a typical wave are shown in figure 6.19. The streamlines indicates complex movement of air above the wave. In the trough of the wave, the orbital motion in the water dominates the fluid motion and forces the air above it to follow its path. The streamlines in the air are very similar to those observed in deep water waves in figure 5.20. The velocity distribution in the water near the crest of the wave in the intermediate depth water wave case is very similar to deep water wave case. The differences between both the cases is observed above the crest of the wave in the air. The streamlines in the air in the deep water waves are more uniformly distributed than in the intermediate depth water wave. In the intermediate depth waves, we observe an increased flux above the crest of the wave. Similar to deep water waves, we observe the recirculation zone above the trough of the wave.

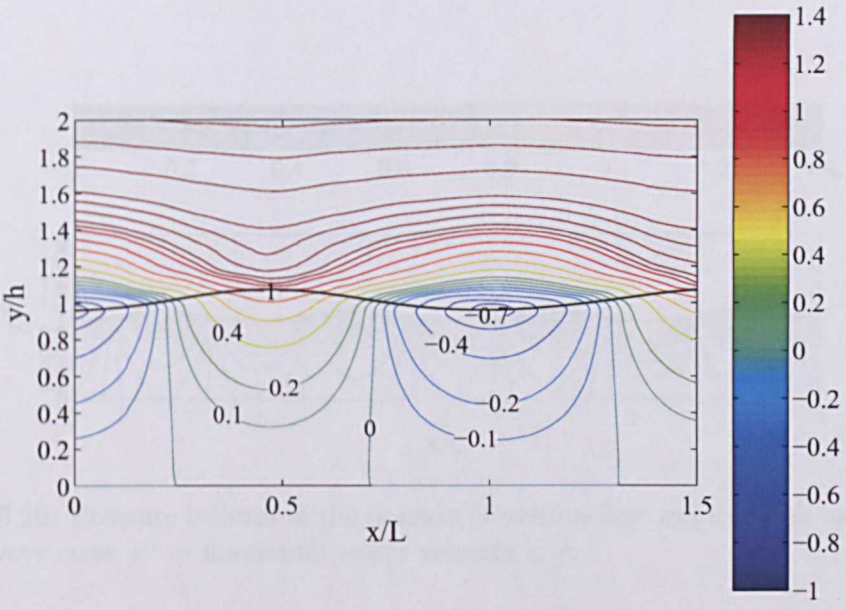

Figure 6.19: Streamlines in a typical wave of viscous flow in intermediate depth water wave case; V' = maximum water velocity $< c$.

6.3.2 Dynamic pressure isolines in water

The dynamic pressure isolines in the domain and a typical wave are shown in the figures 6.20 and 6.21 respectively. The pressure isolines along the length of the domain shows periodic distribution in the water. On comparing a typical wave shown in figure 6.21 with the case when the average wind velocity is zero (*refer* figure 4.8) for the intermediate depth water, we observe higher magnitude of dynamic pressure in the trough of the water, this may be due to the effect of bottom boundary. Since the dynamic pressure is very sensitive to a small change in the total pressure it is possible to observe large variation in its magnitude and its structure inside the waves.

6.3.3 Vorticity in the air and water

The vorticity contours in the domain and a typical wave are shown in the figures 6.22 and 6.23. Along the length of the domain in figure 6.22 we observe high positive and negative vorticity contours diffused in the air side of the domain due to longer wavelength and increased effect of viscosity. We also observe high negative vorticity

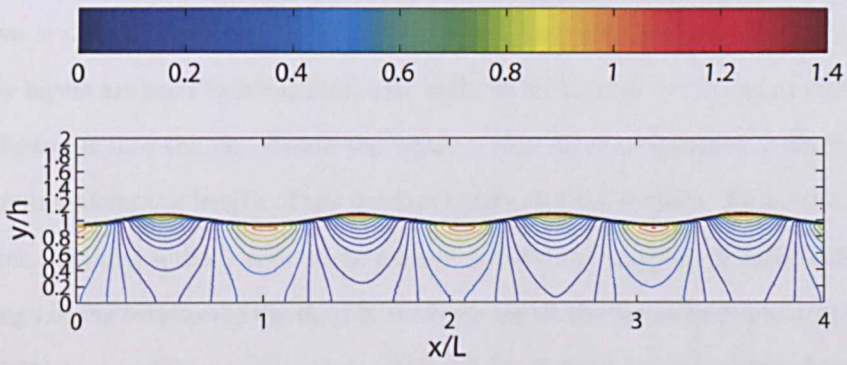

Figure 6.20: Pressure isolines in the domain of viscous flow in intermediate depth water wave case; V' = maximum water velocity $< c$.

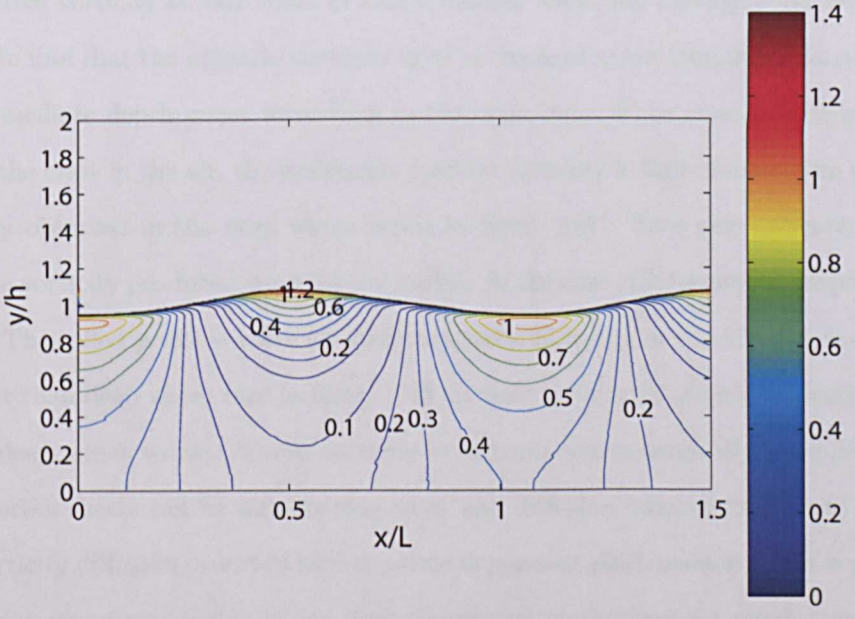

Figure 6.21: Pressure isolines in a typical wave of viscous flow in intermediate depth water wave case; V' = maximum water velocity $< c$.

layer in the trough of the wave and in the crest of the wave, on the air side, we observe positive and negative vorticity layers. The vorticity produced near the free surface of the wave is diffused into the air along the depth and both the positive and negative vorticity layers are seen forming a circular bulbous structures by rolling of vortex sheet and diffusing it into the air. Inside the water a thin layer of negative vorticity can be seen running along the length of the domain below the free surface. Along the depth in the water, vorticity quickly reduces to a lower value. The analysis of figure 6.23, shows the change in the rotation of the fluid in the crest inside the water from positive vorticity (*refer* 6.11) to negative vorticity due to the effect of wind forcing in the thin layer of the free surface. This is similar to that observed in the deep water waves. Along the depth below the crest, the vorticity magnitude quickly reduces while fluctuating from positive vorticity to negative vorticity. In the air above the crest, the strong positive vorticity in figure 6.11 is reduced to small positive vorticity showing a reduction of 50% in the magnitude, while in the air in the trough region, we observe that the magnitude of negative vorticity is four times of that observed when the average wind velocity is zero. We find that the negative vorticity layer is stronger in the trough region in the air of intermediate depth water wave than in the deep water wave as seen in figure 5.25. Above the crest in the air, the maximum positive vorticity is half of maximum positive vorticity observed in the deep water waves in figure 5.25. This also indicates higher negative vorticity produced near the free surface in the case of intermediate depth water waves. The rolled positive vorticity structures seen diffusing in the air in this case are different than deep water case in figure 5.25 as these structures are not strongly visible in the deep water waves. These vorticity structures which originally produced from same vortex sheets can be seen moving away and diffusing independently into the air. The vorticity diffusion observed here is a time dependent phenomenon and it is possible that these structures could change if the numerical model runs for much longer time which is computationally very expensive. A detailed view of vorticity is seen in figure 6.24.

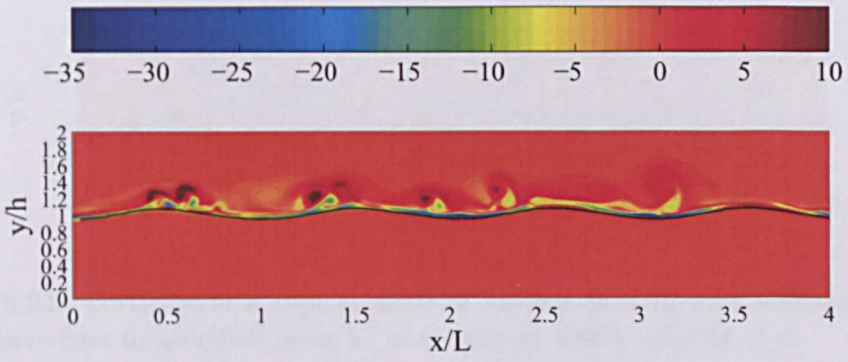

Figure 6.22: Vorticity in the domain of viscous flow in intermediate depth water wave case; V' = maximum water velocity $< c$.

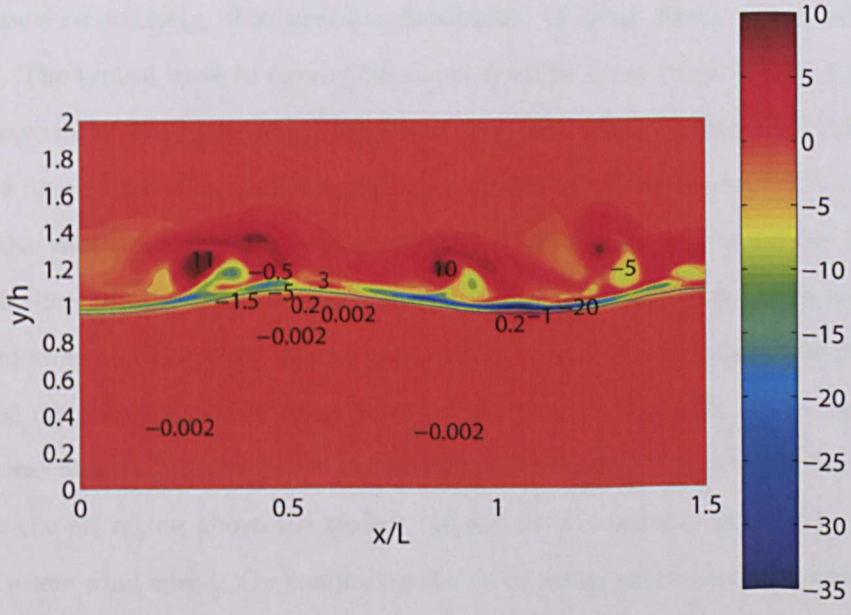

Figure 6.23: Vorticity in a typical wave of viscous flow in intermediate depth water wave case; V' = maximum water velocity $< c$.

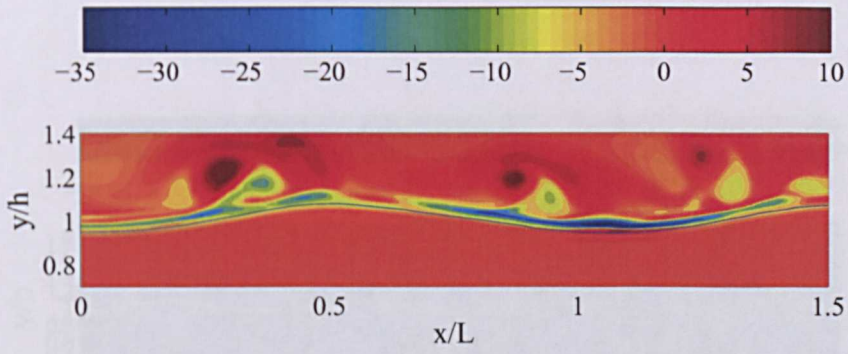

Figure 6.24: Vorticity in a typical wave of viscous flow in intermediate depth water wave case in specified area; V' = maximum water velocity $< c$.

6.3.4 Shear stress in the air and water

The shear stress contours in the domain and a typical wave are shown in the figures 6.25 and 6.26. Along the length of the domain in figure 6.25, we observe very small shear stress in the air side of the domain, while in the water below the free surface the vertical strips of positive and negative shear stress are observed below crest and trough of the wave respectively. The periodic distribution of shear stress is seen along the domain. The typical wave in figure 6.26 shows positive shear stress layer in the crest of the wave inside the water unlike negative shear layer when average wind velocity is zero; see figure 6.14. The positive shear layer in the trough in figure 6.14 is changed to negative shear layer due to the effect of wind in the thin layer near the free surface. Along the depth in the water we observe a linear decrease in the shear stress below the crest and trough of the wave. In the air, the shear stress is very small near the crest while the magnitude of shear stress near the trough is equal to 5% of the maximum shear stress observed inside the water. It indicates a small but non negligible viscous effect in the air region above the trough. Hence the viscous effects can be observed even at a low wind speed. On comparing the shear stress with the deep water waves in figure 5.28 we observe that the magnitude and distribution of shear stress is similar to the intermediate depth water waves. A detailed view of shear stress is seen in figure 6.27.

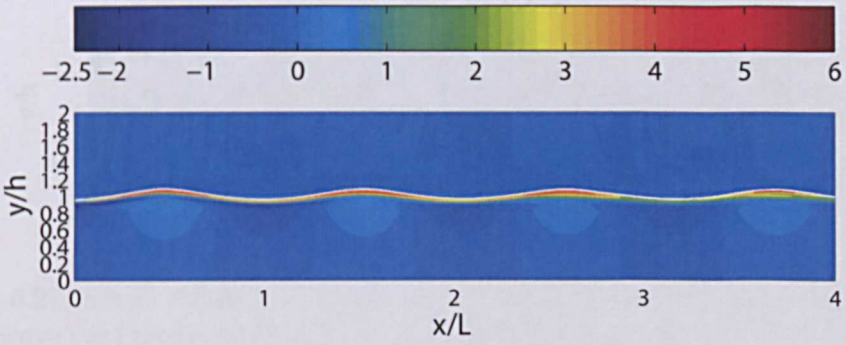

Figure 6.25: Shear stress in the domain of viscous flow in intermediate depth water wave case; V' = maximum water velocity $< c$.

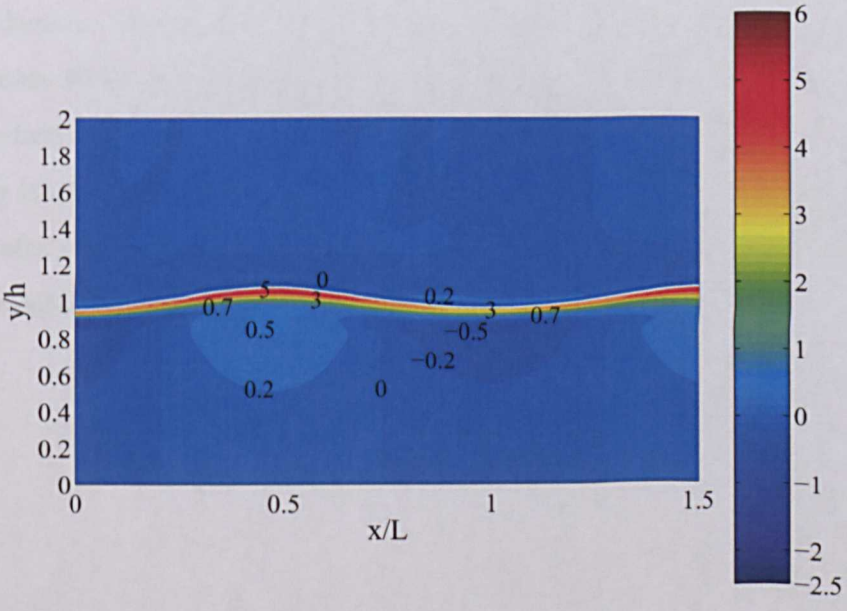

Figure 6.26: Shear stress in a typical wave of viscous flow in intermediate depth water wave case; V' = maximum water velocity $< c$.

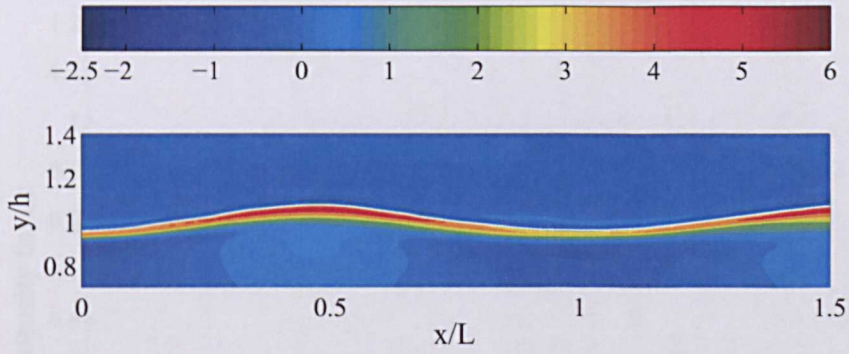

Figure 6.27: Shear stress in a typical wave of viscous flow in intermediate depth water wave case in specified area; V' = maximum water velocity $< c$.

6.3.5 Energy density in the domain

The energy density variation along the length of the domain when the air is blowing with very low velocity over the intermediate water wave is shown in the figure 6.28. On comparing the time averaged energy density variation with that in figure 4.1, we observe that the energy density of the wave shows an small increase along the length of the domain. The majority of this increase is observed in the kinetic energy of the water wave while the increase in the potential energy is negligible. The total energy density factor increases by about 2.5% as compared with case when the average wind velocity is zero. These results are very similar to the energy exchange observed in the deep water wave case strengthening the idea of direct input of momentum from the air to the orbital motion of the water.

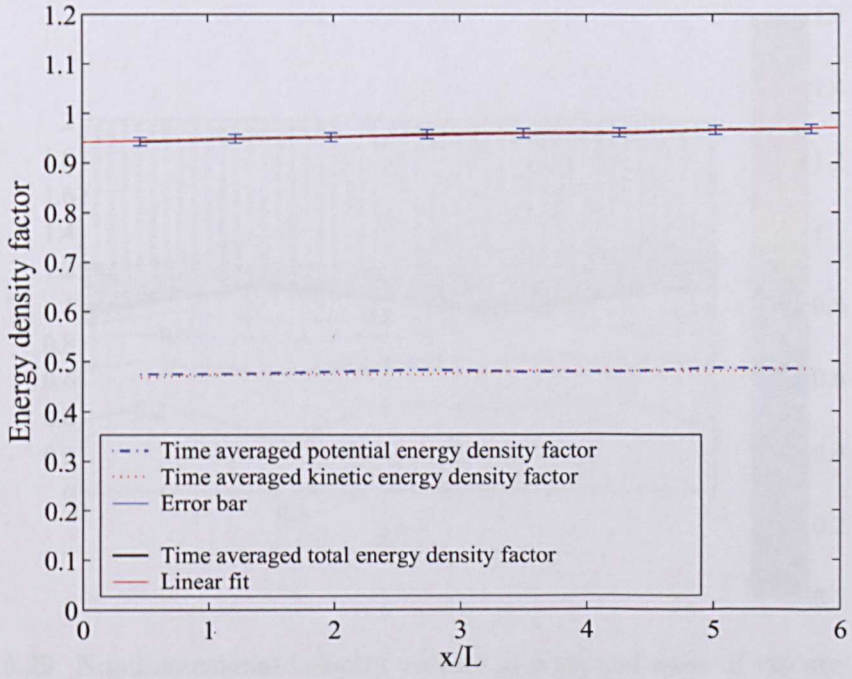

Figure 6.28: Time averaged energy density factor vs x; V' = maximum water velocity $< c$.

6.4 Case study 3: $V' = 0.5\ c$

In this section, we discuss the numerical results obtained when the average wind velocity is equal to half of wave velocity, c. The choice of the cases is based upon the idea of consistency in cases in both deep and intermediate depth water waves.

6.4.0.1 Velocity vectors

The numerical results for the velocity vectors in the air and water in a typical wave are shown in figures 6.29 and 6.30 respectively. The contours shows an overall increase in the velocity of fluid in the crest and trough of the wave, this is confirmed by downward movement of the contour with a value of 0.2 to a lower location below the crest and trough of the wave. We also observe an increase in the maximum velocity in the crest region inside the wave and the velocity contour with a value of 0.8 now extends from the crest to the trough in the whole region of wave. In the air, we observe an increase in

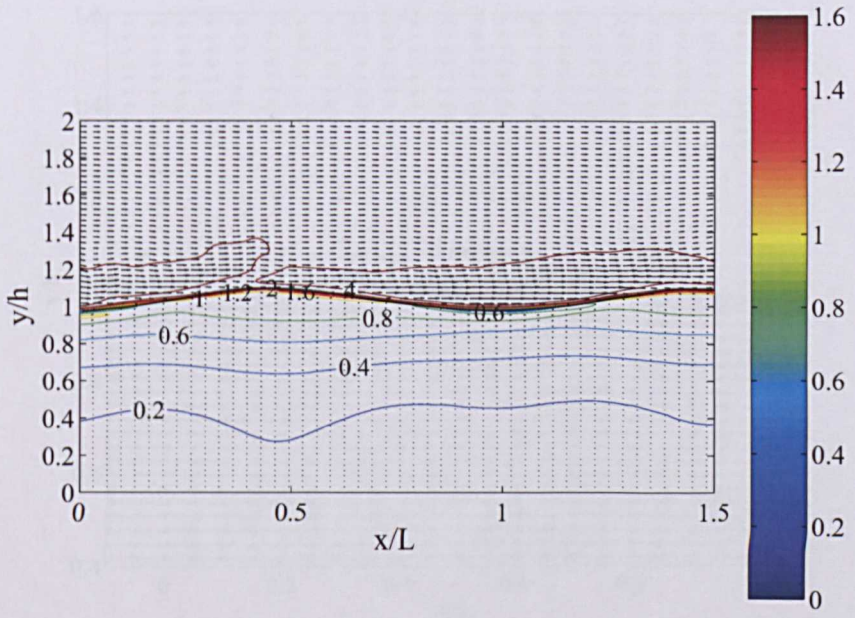

Figure 6.29: Nondimensional velocity vectors in a typical wave of viscous flow in intermediate depth water wave case; $V' = 0.5\ c$.

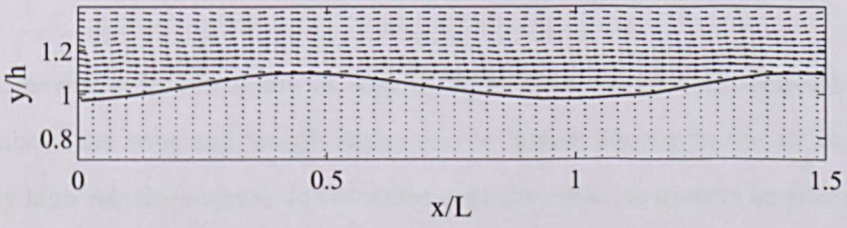

Figure 6.30: Nondimensional velocity vectors in a typical wave of viscous flow in intermediate depth water wave case in specified area; $V' = 0.5\ c$.

the velocity above the trough region and the air accelerates on passing over the slope on the lee side of the wave, this is due to higher pressure gradient in the air coupled with the free surface movement providing additional momentum to the flow in the trough region. The mean wind velocity in the trough region is higher as a result of additional momentum it receives from fast moving wave alongside the forward moving air. The bursts of random moving air that are observed when the wind velocity was lower in the earlier case is not observed in this case and the airflow movement is similar to that in deep water waves as expected. A thin recirculation zone can be observed near to the free surface in figure 6.30.

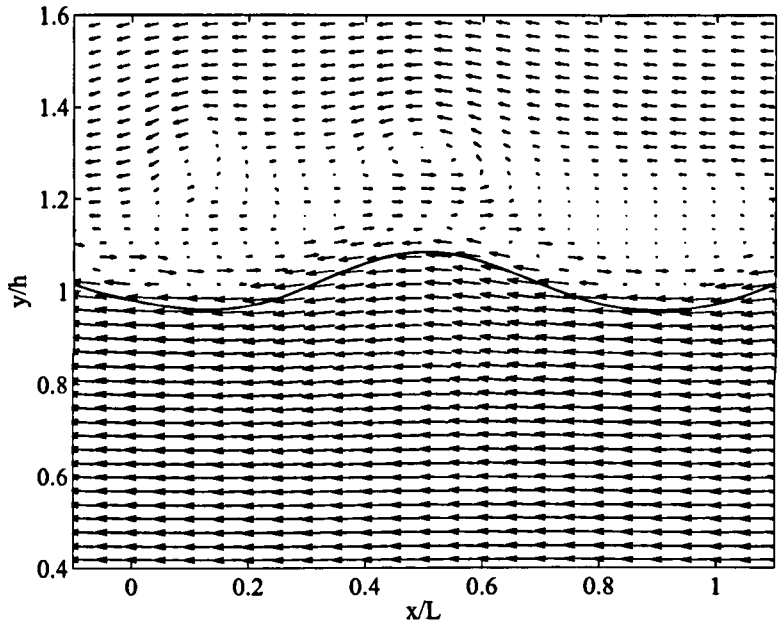

Figure 6.31: Nondimensional velocity vectors of viscous flow in a typical wave of intermediate depth water wave case with moving reference frame; $u - c$; $V' = 0.5$ c.

In a moving reference frame as seen in figure 6.31, we observe recirculations in the air above the crest and trough region due to higher velocity in the air indicating relatively high velocity regions. In the water near the crest, we observe smaller velocity vectors due to increased momentum exchange between the air and water. This also leads to a higher shear stress in the region compared with earlier cases.

6.4.0.2 Streamlines

The numerical result for streamlines in the air and water in a typical wave is shown in figure 6.32. It shows an increase in the velocity in the water below crest and trough and in the air, we observe that the air dominates the flow above the crest and the effect of orbital movement of water on the airflow above is smaller compared to low wind velocity case discussed in the earlier section. The thickness of the recirculation zone is reduced more than the earlier case as air tries to remain attached to the surface of the wave. In the water near the trough we observe streamlines of higher magnitude

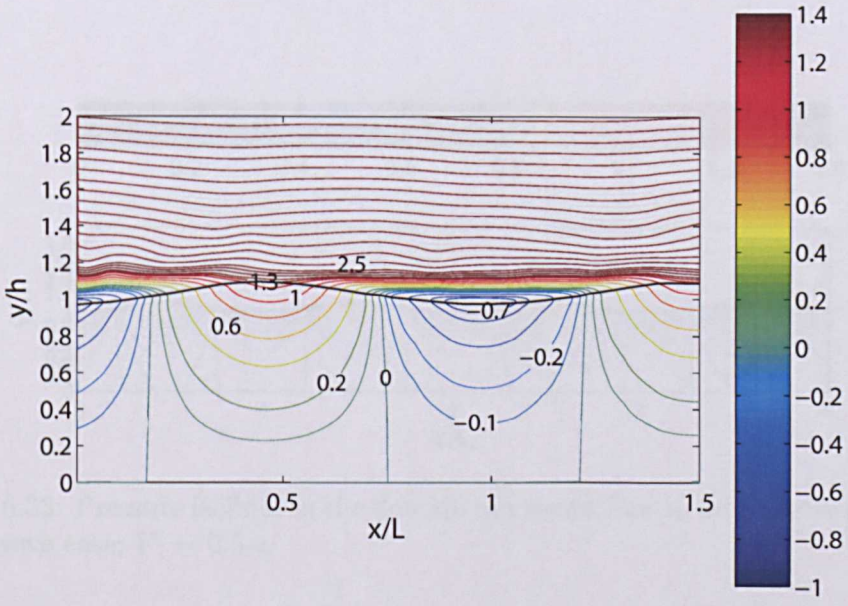

Figure 6.32: Streamlines in a typical wave of viscous flow in intermediate depth water wave case; $V' = 0.5\ c$.

indicating less decrease in the water velocity in the trough region than the earlier cases.

6.4.1 Dynamic pressure isolines in water

The numerical results for dynamic pressure isolines in the air and water in the domain and a typical wave are shown in figures 6.33 and 6.34 respectively. Along the length of the domain as seen in figure 6.33, we observe a periodic distribution of dynamic pressure isolines in the crest and trough of the wave. The dynamic pressure isolines in the trough have lower magnitude than earlier cases. A typical wave in figure 6.34 shows an increase in the magnitude of isolines in the crest and decrease in the trough of the wave. This increased difference in the dynamic pressure between crest and trough of the wave indicates larger effect of wave on the underlying water. On comparing it with the earlier case 6.21 we observe an increase in the magnitude by 20% in the crest and reduction of 50% in the trough. Thus with a progressive increase in the wind speed we observe an increase in the magnitude of pressure isolines in the crest and a decrease in

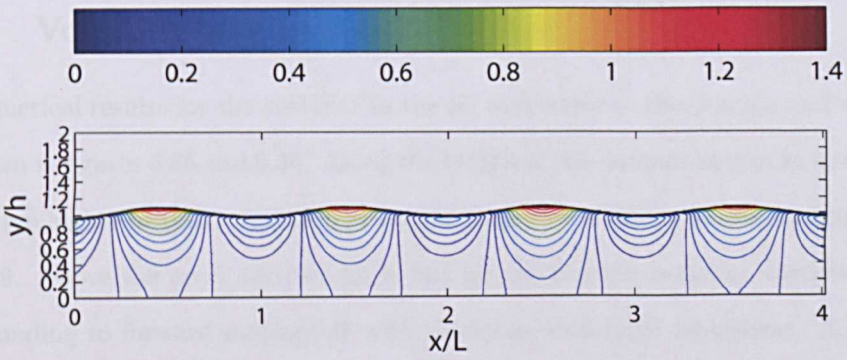

Figure 6.33: Pressure isolines in the domain of viscous flow in intermediate depth water wave case; $V' = 0.5\ c$.

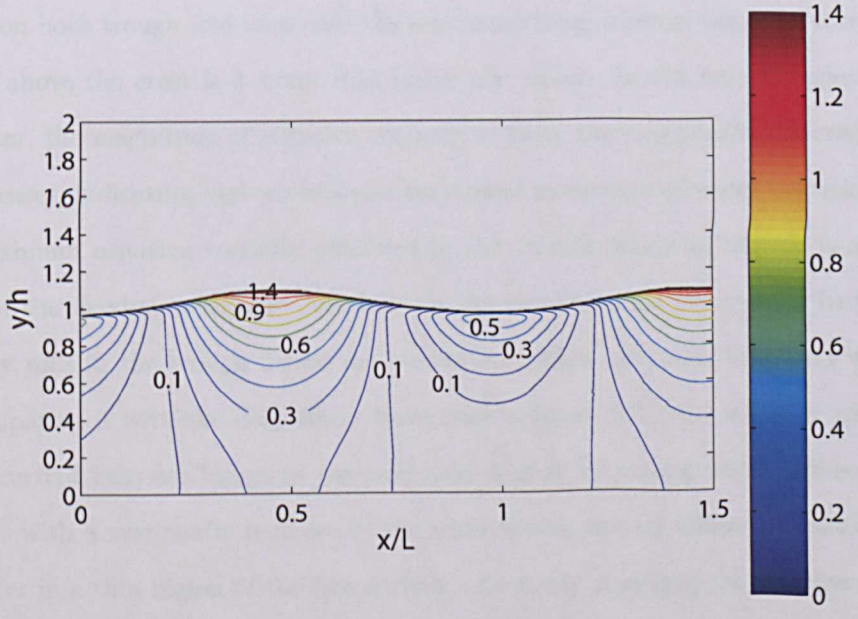

Figure 6.34: Pressure isolines in a typical wave of viscous flow in intermediate depth water wave case; $V' = 0.5\ c$.

the trough of the wave.

6.4.2 Vorticity in the air and water

The numerical results for the vorticity in the air and water in the domain and a typical are shown in figures 6.35 and 6.36. Along the length of the domain as seen in figure 6.35, we observe higher negative vorticity in the air than earlier cases as seen in figures 6.22 and 6.10. Above the crest and trough in the air, we observe negative vorticity layers corresponding to forward moving air with clockwise rotational movement. A positive vorticity found immediately above the crest in the two earlier cases is visible higher up in the crest with an increase in wind velocity and near the free surface of the water only negative vorticity is visible. The diffusion of vorticity in the air is higher up along its depth and inside the water there is a very thin layer of negative vorticity. A typical wave in figure 6.36 shows a thicker high vorticity region in the trough of the air and water as compared with previous case in figure 6.23. The distribution of negative vorticity is seen on both trough and crest and the maximum magnitude of negative vorticity in the air above the crest is 3 times that inside the water. In the trough region inside the water, the magnitude of negative vorticity is twice the magnitude observed in the earlier cases, indicating higher clockwise rotational movement of water particles while the maximum negative vorticity observed in the trough region in the air is about 8 times of the maximum negative vorticity in the trough inside the water. In the air, vorticity rolls in the trough region are similar to earlier case with low wind velocity. On comparing it with the deep water wave case in figure 5.37, the vorticity rolls seen in the current case are bigger in size and have higher maximum value. Thus we can see that with a systematic increase in the wind speed, the air starts interacting with the water in a thin region of the free surface, effectively changing the rotation of fluid and exchanging the momentum and energy in this process with the underlying water. Inside the water a thin layer of negative vorticity is seen along the length followed by the layers of positive and negative vorticity quickly reducing to a very small value along the depth. A detailed view of vorticity can be seen in figure 6.37.

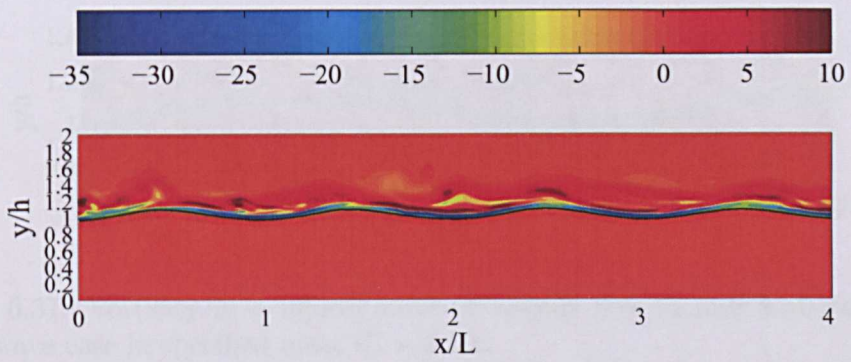

Figure 6.35: Vorticity in the domain of viscous flow in intermediate depth water wave case; $V' = 0.5\ c$.

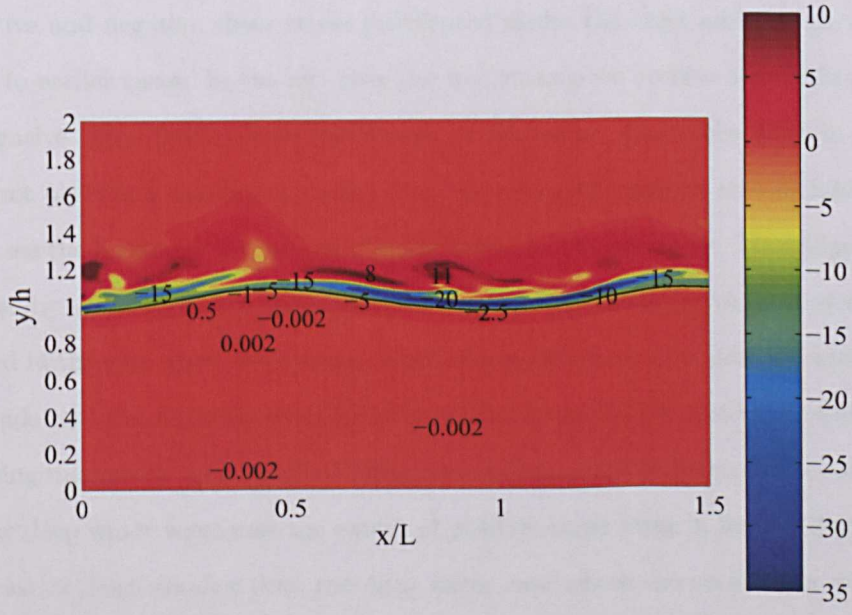

Figure 6.36: Vorticity in a typical wave of viscous flow in intermediate depth water wave case; $V' = 0.5\ c$.

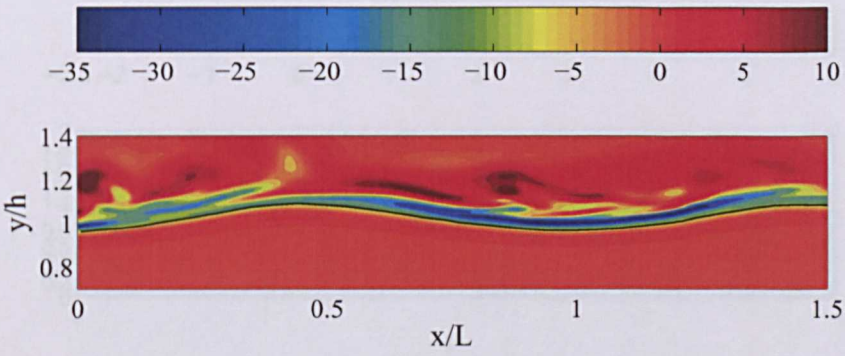

Figure 6.37: Vorticity in a typical wave of viscous flow in intermediate depth water wave case in specified area; $V' = 0.5$ c.

6.4.3 Shear stress in the air and water

The numerical results for the shear stress in the air and water in the domain of the intermediate depth water wave and a typical wave are shown in figures 6.38 and 6.39. Along the length of the domain in figure 6.38, below the water surface we observe positive and negative shear layers. Below these layers, we can see the vertical layers of positive and negative shear stress distributed under the crest and trough which is similar to earlier cases. In the air, near the free surface we observe very thin positive and negative shear layers above the trough of the wave. Above the crest in the air, we do not observe a significant shear stress. In a typical wave as seen in figure 6.39, we can see the increased magnitude of shear stress inside the water. The magnitude is increased by about 15% than the earlier case. In the crest the negative shear stress layer observed in the case when the average wind velocity is zero is now positive with higher magnitude and the negative shear layer is pushed down deeper inside the water with decreasing magnitude as a result of interaction between air and water. On comparing with the deep water wave case the extent of positive shear layer in intermediate depth water case is much smaller than the deep water case where the shear layer with high magnitude is extended till the trough of the wave. This is mainly due to stronger vertical velocity gradient in the intermediate depth water case which has a stronger effect near the trough as the bottom boundary is nearer than that in the deep water

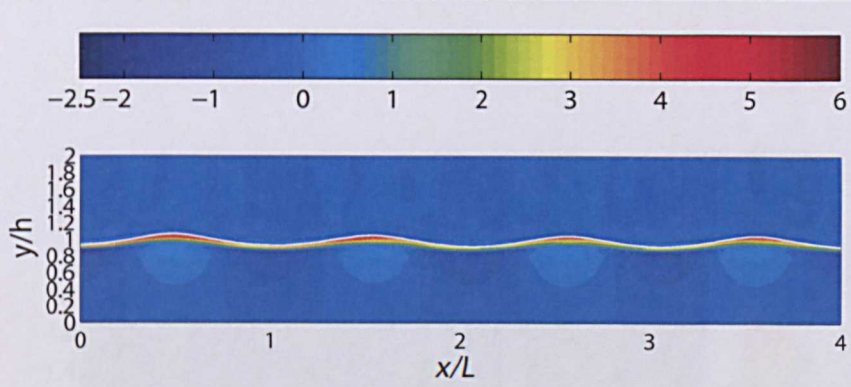

Figure 6.38: Shear stress in the domain of viscous flow in intermediate depth water wave case; $V' = 0.5\ c$.

wave. A thin negative shear layer which was observed immediately below the positive shear layer in the crest is not observed in intermediate depth case. A detailed view of shear stress is seen in figure 6.40.

6.4.4 Energy density in the domain

The energy density variation along the length of the domain when the wind is blowing with velocity equal to $0.5c$ over the intermediate depth water wave is shown in the figure 6.41. On comparing the time averaged energy density shown in figure 6.41 with that in figures 6.28 and 4.1, we observe that the energy density of the wave shows increase in the value along the length of the domain. This increase is about 5% more than zero average wind velocity case as seen in figure 4.1 and about 2.5% more than low wind velocity case shown in figure 6.28. In this case, we observe an increase in both kinetic and potential energy density factors contributing to an overall increase in total energy density in the water. The increase in the intermediate depth water case is higher since the number of waves interacting with the air is smaller which reduces the rate of attenuation of waves and improves energy exchange from air to water.

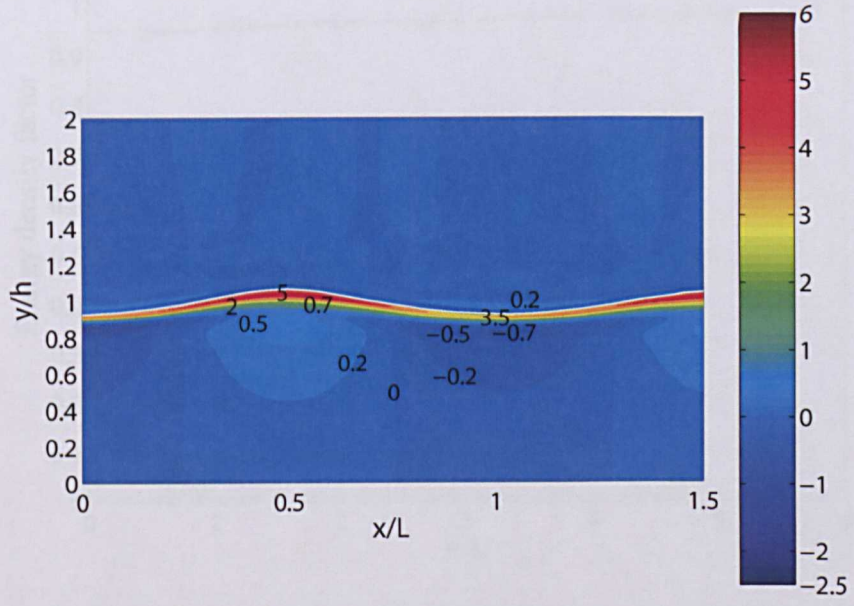

Figure 6.39: Shear stress in a typical wave of viscous flow in intermediate depth water wave case; $V' = 0.5\ c$.

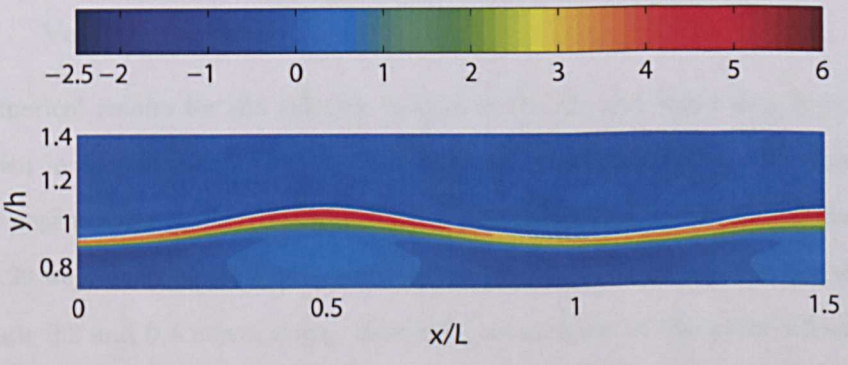

Figure 6.40: Shear stress in a typical wave of viscous flow in intermediate depth water wave case in specified area; $V' = 0.5$ c.

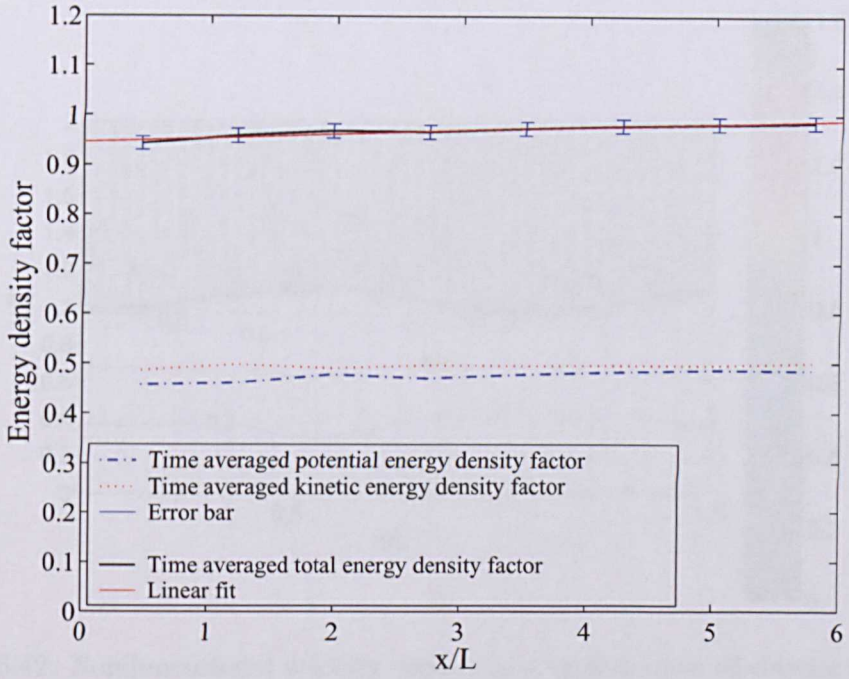

Figure 6.41: Time averaged energy density factor vs x; average wind velocity = 0.5 c.

6.5 Case study 4: V' = Wave speed, c

In this section, we discuss the numerical results obtained when the average wind velocity is equal to wave velocity, c.

6.5.0.1 Velocity vectors

The numerical results for the velocity vectors in the air and water in a typical wave are shown in figures 6.42 and 6.43. The velocity contours shows an increase in the velocity near the free surface inside the water. On comparing it with the earlier case in figure 6.29 we observe an overall increase in the velocity of the water as the contours of magnitude 0.2 and 0.4 moves down, indicating an increase in the water velocity. The velocity vectors in the figure 6.43 shows an increase in the air velocity near the crest of the wave, this is mainly due to high velocity in the air which overcomes the wave resistance and distributes itself over the trough region. The bursts of velocity in the air are observed in the crest which are similar to earlier cases. The air near the trough has

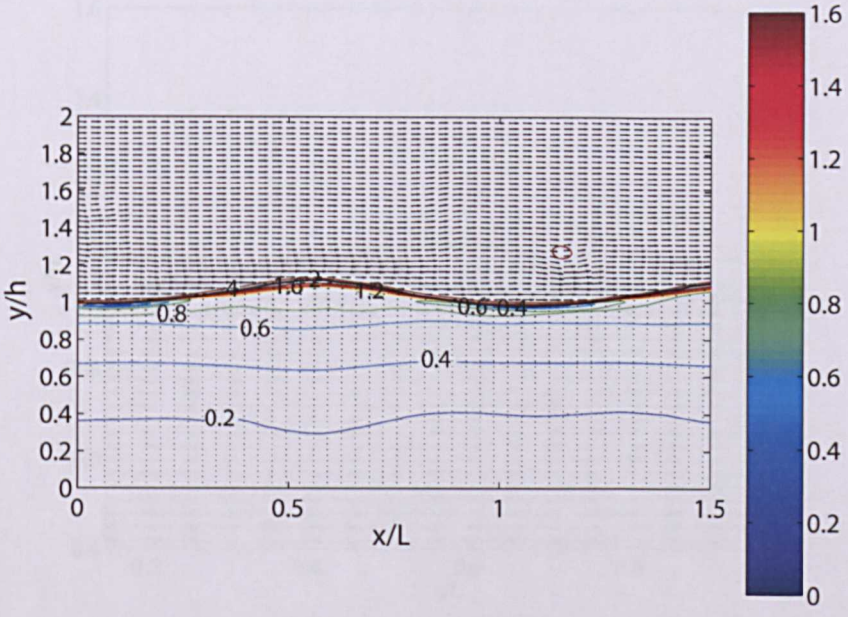

Figure 6.42: Nondimensional velocity vectors in a typical wave of viscous flow in intermediate depth water wave case; $V' = c$.

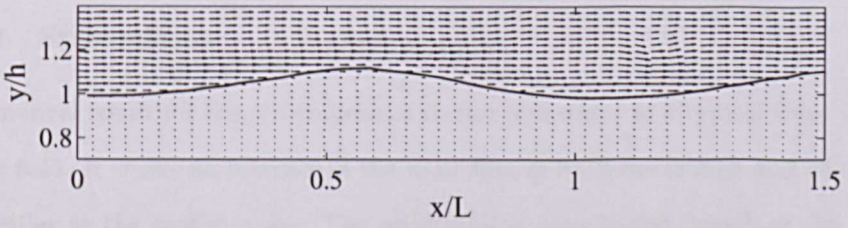

Figure 6.43: Nondimensional velocity vectors in a typical wave of viscous flow in intermediate depth water wave case in specified area; $V' = c$.

higher velocity similar to the crest region. In the water we observe higher velocity in a thin layer in the crest region due to momentum input from the air above it. This high velocity layer is thicker compared to the earlier cases. In a moving reference frame as seen in figure 6.44, we observe that the air has higher relative velocity compared to both wave and mean water velocity. Hence, we observe forward moving vectors in the air while near the free surface due to low mean water velocity, the velocity in the air quickly reduces near the free surface. This results in much higher shear stress in both air and water. We also observe smaller velocity vectors in the crest region indicating increase in the velocity in the water compared with earlier cases.

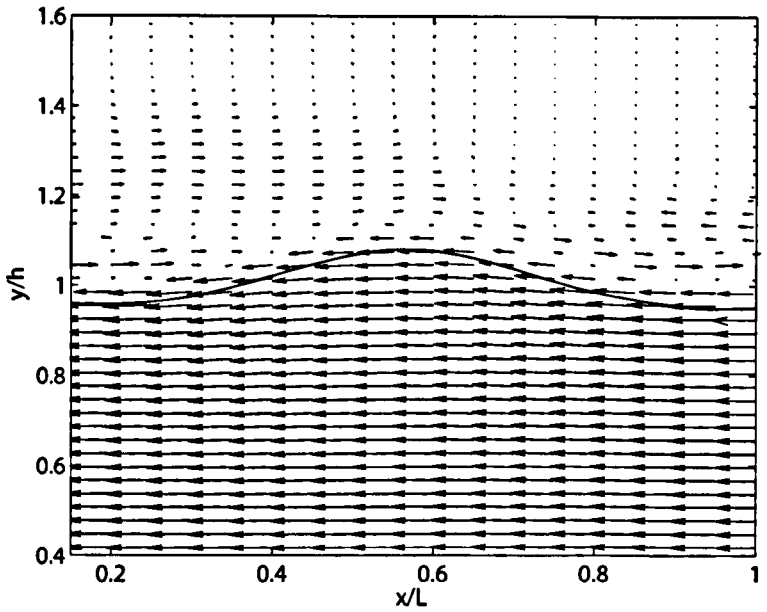

Figure 6.44: Nondimensional velocity vectors of viscous flow in a typical wave of intermediate depth water wave case with moving reference frame; $u - c$; $V' = c$.

6.5.0.2 Streamlines

The numerical result for the streamlines in the air and water in a typical wave is shown in figure 6.45. It shows an increase in the mass flux in both the trough and crest of the wave similar to the earlier cases. The recirculation seen in the trough of the wave is very small as compared with earlier cases. The streamline value near the crest in the water is higher than earlier cases indicating greater velocity of fluid in the region. The orbital movement of water have smaller effect on the air moving over the wave when the air is blowing at the speed of the wave.

6.5.1 Dynamic pressure isolines in water

The numerical results for pressure isolines in the domain of the water wave and a typical wave are shown in figures 6.46 and 6.47 respectively. Along the length of the domain we observe a periodic distribution of pressure isolines. We observe an increase in the dynamic pressure in the crest and reduction in the trough of the wave which is similar to earlier cases where we observe a stepwise increase in the dynamic pressure in the

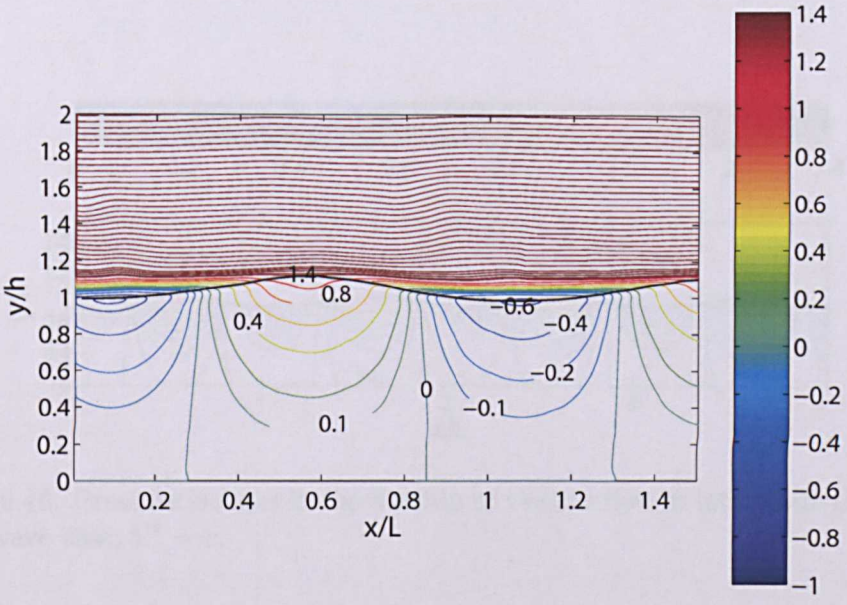

Figure 6.45: Streamlines in a typical wave of viscous flow in intermediate depth water wave case; $V' = c$.

wave in the crest region and a reduction in the trough region with an increase in the wind speed. The deep water wave cases also show similar behaviour. These isolines also indicate that the dynamic pressure under the wave is very sensitive to small change in surface profile and needs to be highly accurate to measure correct pressure fluctuations in the crest and trough region of the water.

6.5.2 Vorticity in the air and water

The numerical results for vorticity in the domain of the water wave and a typical wave are shown in figures 6.48 and 6.49. Along the length of the domain as seen in figure 6.48, the effect of vorticity is very prominent and diffused at much higher level in the air above the wave. A layer of negative vorticity as a result of forward moving air is thicker than the earlier cases and is distributed along the length in the air and water region near the wave. We also observe a positive vorticity layer above this negative vorticity layer. This positive vorticity is diffused in the air above in form of rolls in the slope region of windward side of the wave. From the figure 6.49 we also observe

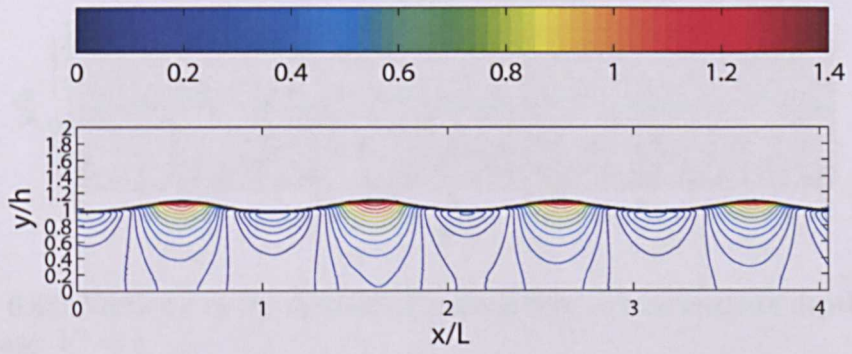

Figure 6.46: Pressure isolines in the domain of viscous flow in intermediate depth water wave case; $V' = c$.

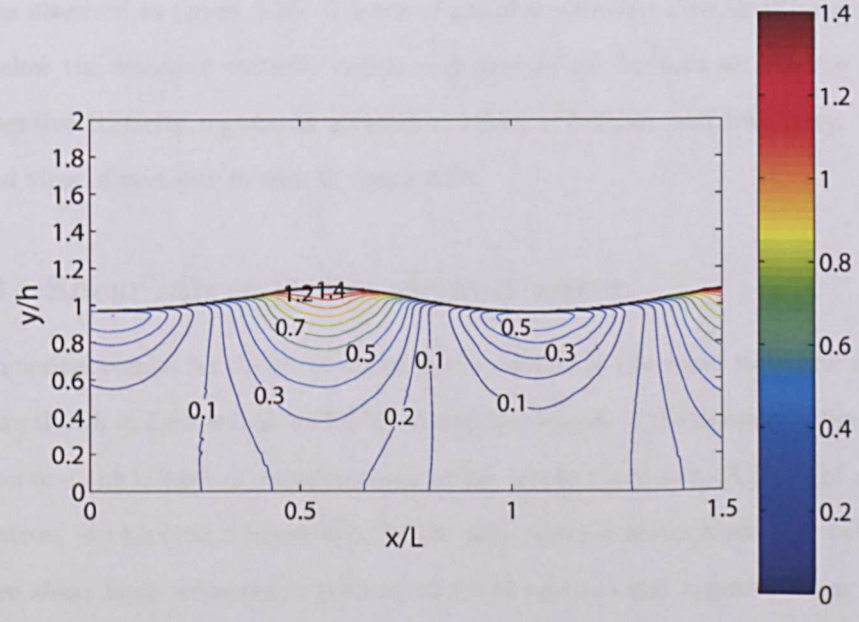

Figure 6.47: Pressure isolines in a typical wave of viscous flow in intermediate depth water wave case; $V' = c$.

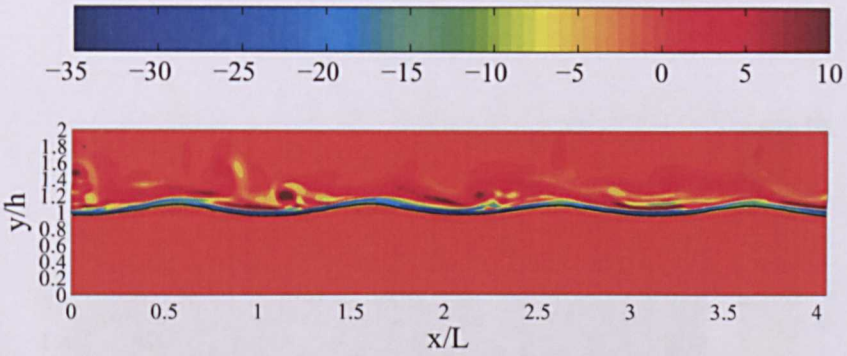

Figure 6.48: Vorticity in the domain of viscous flow in intermediate depth water wave case; $V' = c$.

negative vorticity rolls being diffused in the air alongside the positive vorticity rolls. In a typical wave as seen in figure 6.49, we see that the magnitude of maximum negative vorticity is about 50% more than that observed in figure 6.36. The negative vorticity region above the crest and the trough region is much thicker than earlier cases. In the water, the increase in the negative vorticity in both the crest and trough region is twice as observed in figure 6.36. A layer of positive vorticity with small magnitude is seen below the negative vorticity region and near to the bottom we observe positive and negative vorticity regions as a result of effect of bottom wall boundary. A more detailed view of vorticity is seen in figure 6.50.

6.5.3 Shear stress in the air and water

The numerical results for the shear stress in the domain of the water wave and a typical wave are shown in figures 6.51 and 6.52. Along the length of the domain in figure 6.51, we observe a thick layer of positive shear stress inside the water. A layer of negative shear stress is observed immediately below this positive shear layer and below this negative shear layer we observe vertical strips of positive and negative shear stresses along the depth under the crest and trough respectively which are similar in structure to earlier cases while differing in the magnitude and extent. In the air, we observe the layers of positive and negative shear stresses in the trough. The magnitude of shear

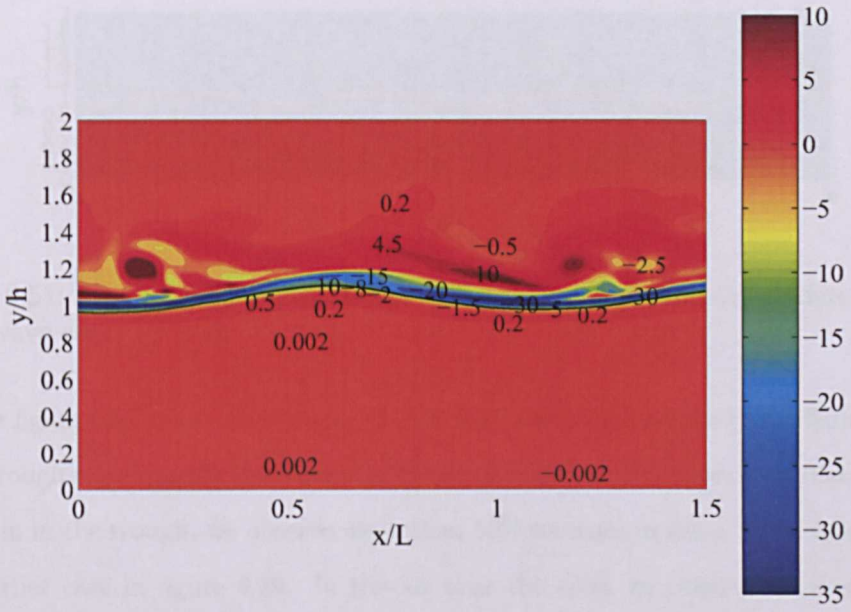

Figure 6.49: Vorticity in a typical wave of viscous flow in intermediate depth water wave case; $V' = c$.

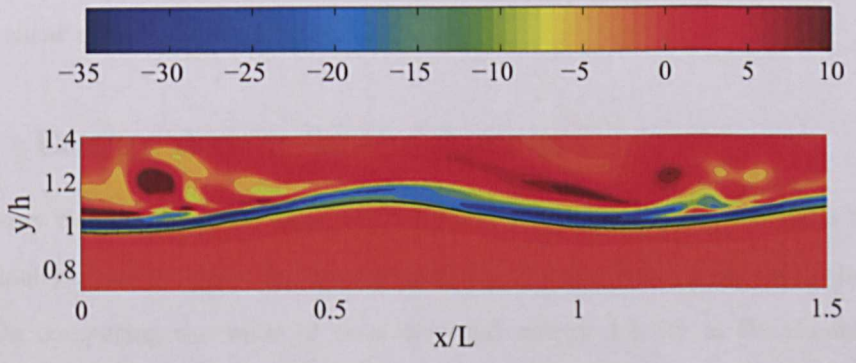

Figure 6.50: Vorticity in a typical wave of viscous flow in intermediate depth water wave case in specified area; $V' = c$.

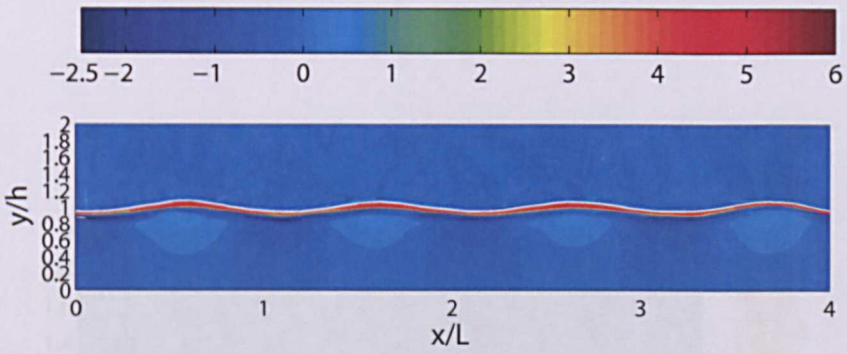

Figure 6.51: Shear stress in the domain of viscous flow in intermediate depth water wave case; $V' = c$.

stress in figure 6.52 shows an increase of 30% than the previous case (*refer* figure 6.39) in the trough region inside the water. In the crest region the increase is smaller. In the air region in the trough, we observe more than 50% increase in shear stress magnitude than earlier case in figure 6.39. In the air near the crest we observe an increase in shear stress although the magnitude observed is smaller. As seen in the figures, the viscous effects acting in the air in the trough are not negligible in magnitude even when the wind velocity is not very high. With an increase in the wind velocity these shear stresses increase to an order of that observed in the water and can have substantial effect on the fluid flow near the interface. This shows that the shear stresses play a very important role in air-water interaction at higher wind speeds. A more detailed view of shear stress is seen in figure 6.53.

6.5.4 Energy density in the domain

The energy density variation along the length of the domain when the air is blowing with velocity equal to c over the intermediate depth water wave is shown in the figure 6.54. On comparing the value of time averaged energy density in the domain with the zero average wind velocity case (*refer* figure 4.2), we observe 7% increase due to energy exchange between air and water wave. The net gain in the energy is observed with an linear increase in the energy density in the water mainly due to increase in kinetic energy of the water. The results shown here is an important proof of direct

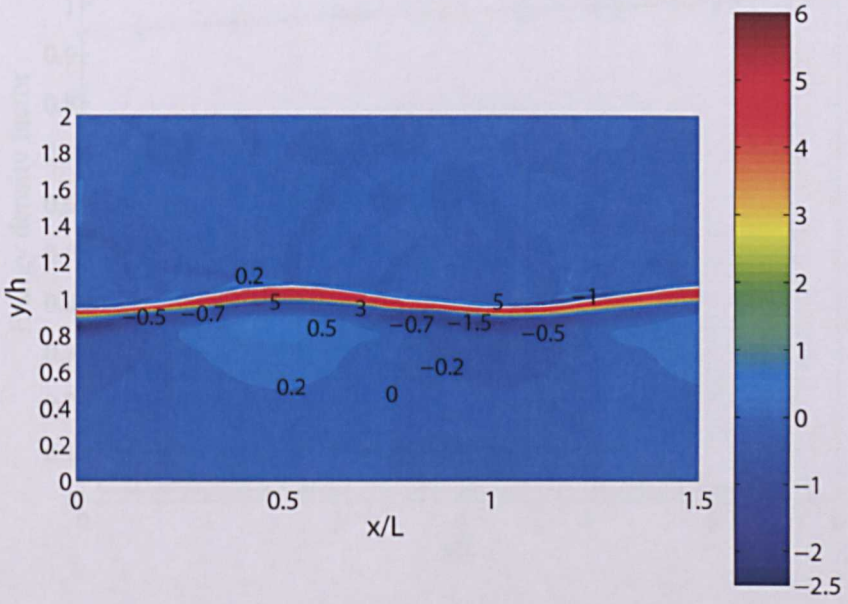

Figure 6.52: Shear stress in a typical wave of viscous flow in intermediate depth water wave case; $V' = c$.

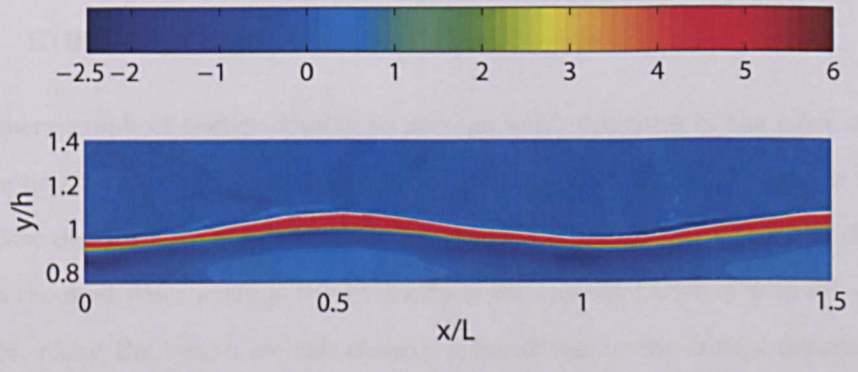

Figure 6.53: Shear stress in a typical wave of viscous flow in intermediate depth water wave case in specified area; average wind velocity = c.

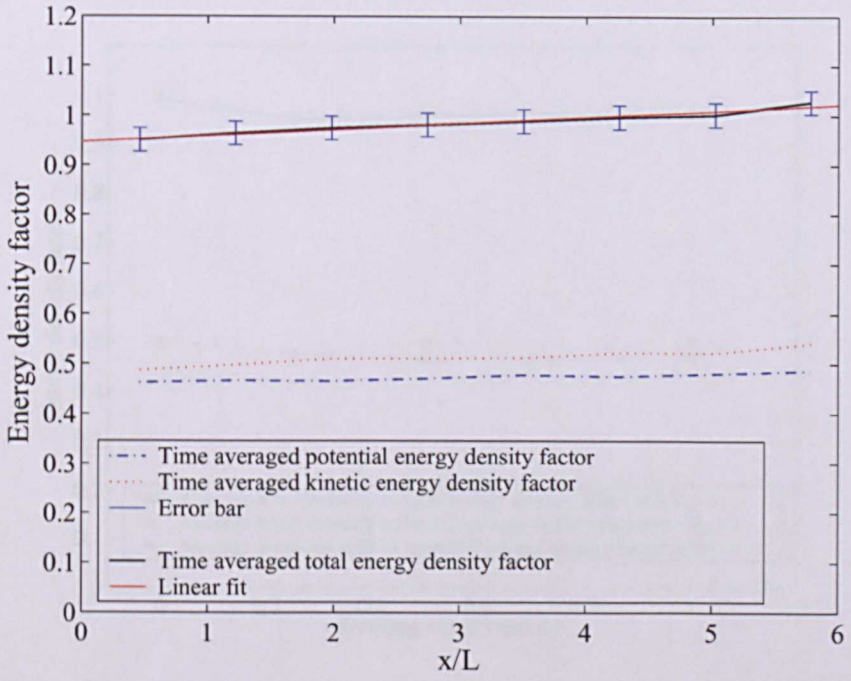

Figure 6.54: Time averaged energy density factor vs x; $V' = c$.

energy exchange between air and water wave in the problem pertaining to air-water wave interaction.

6.6 Summery graph of energy density factor versus average wind velocities

A summery graph of energy density vs average wind velocities in the cases of intermediate depth water wave are shown in figures 6.55, 6.56 and 6.57. Similar to deep water case discussed in earlier chapter, we observe higher energy density in the wave close to the inlet when average wind velocity is zero on comparing it with other cases. However, along the length we can observe a linear rise in the energy density of the fluid at various wind velocities. The rise in energy density in intermediate depth case is slightly higher than deep water cases because of lower number of waves reducing the total dissipation in the domain. In general we found that this phenomenon is both time

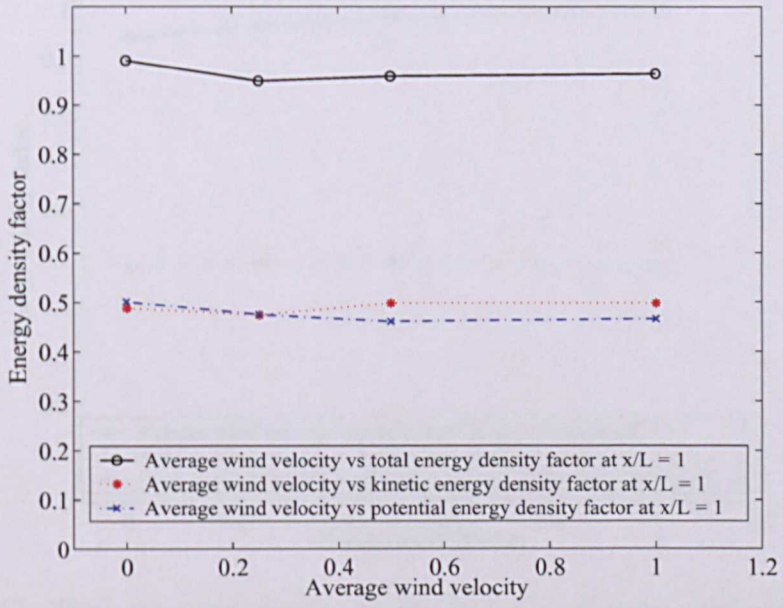

Figure 6.55: Time averaged energy density factor vs average wind velocities at x/L = 1.

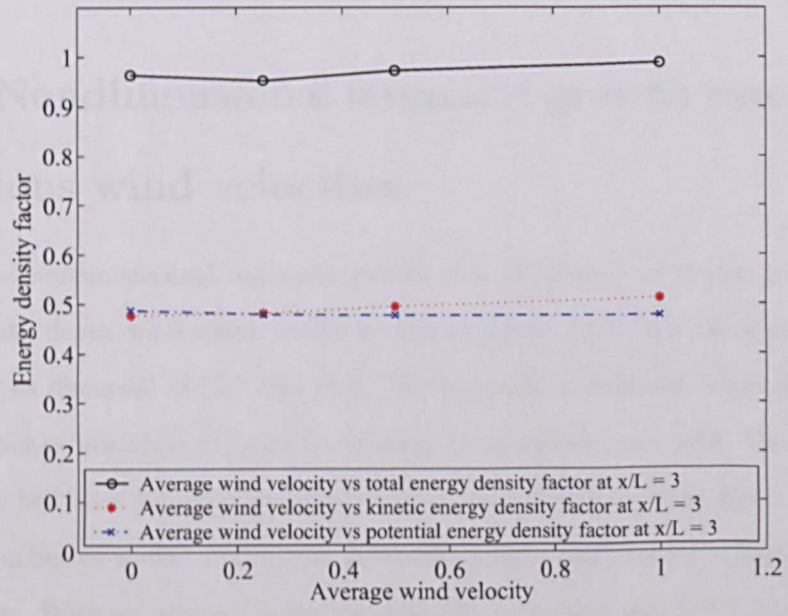

Figure 6.56: Time averaged energy density factor vs average wind velocities at x/L = 3.

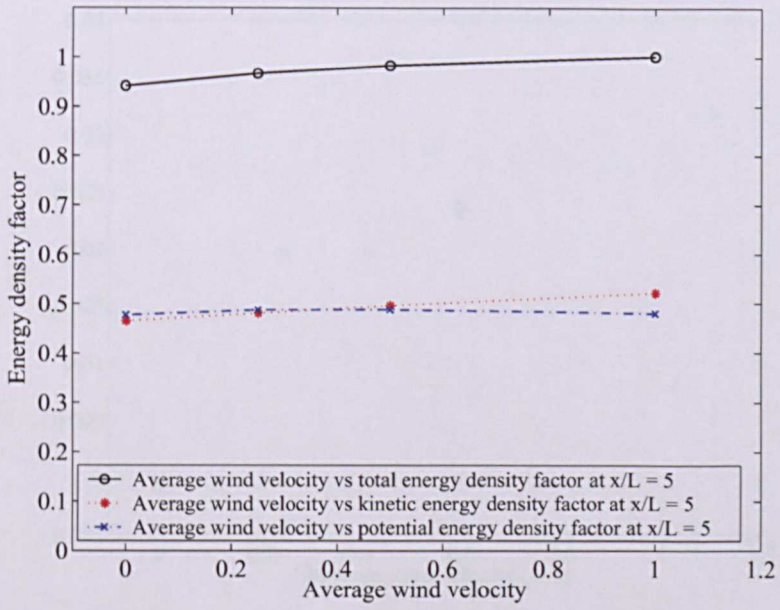

Figure 6.57: Time averaged energy density factor vs average wind velocities at x/L = 5.

and space dependent and could serve as an important comparison point for laboratory measurements as well as simulation using other numerical technique.

6.7 Nondimensional temporal growth rate at various wind velocities

A graph of nondimensional temporal growth rate at various wind velocities for the intermediate depth wind-water waves is seen in figure 6.58. All the quantities are calculated as discussed in §5.7 and §4.2. The temporal growth rate term in this case shows higher values when compared with deep water waves; figure 5.58. This is mainly due to the fact that for same length of the domain the intermediate depth waves has smaller number of waves resulting in lower dissipation and thereby a higher relative growth rate. With an increase in the wind speed, the growth rate term shows a linear increase which is comparable with deep water waves. Hence, we can conclude that both deep and intermediate depth waves shows much similarity in characteristics of

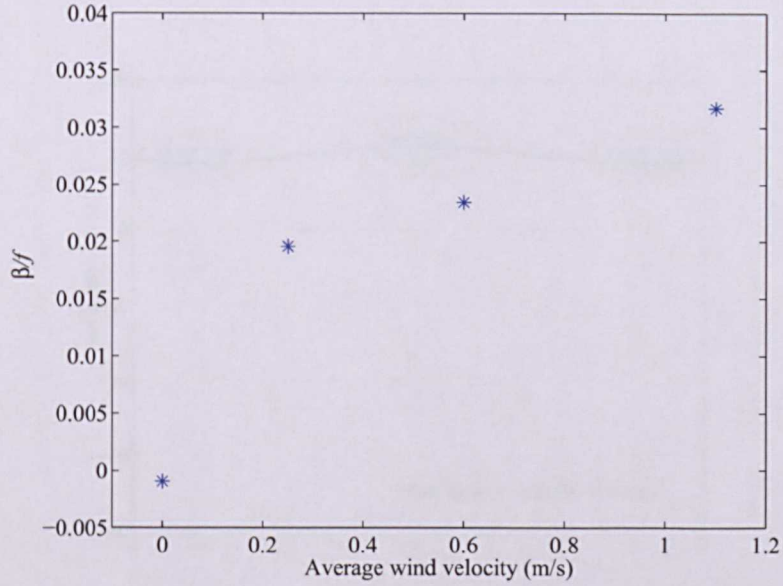

Figure 6.58: Plot of β/f versus vs average wind velocities in the domain; intermediate depth wind-water waves.

wave growth rate term in the cases studied here. The cases studied here are limited in steepness value and hence in order to extract a more generalized value for the wave growth rate, more comprehensive simulations are an important requirement.

6.8 Schematic of maximum near surface vorticity in the air and water

The schematic of near surface vorticity in the air and water when the average wind velocity is zero is shown in figures 6.59 and 6.60 respectively. We observe similar to deep water waves that the rotation of fluid in the air and water both is in anti-clockwise direction owing to movement of the fluid in the air and water. The rotation of fluid changes at locations $-\pi/2$ and $\pi/2$ shown in the figures where the vorticity magnitude is zero in the air and water. The plot of near surface vorticity in the air and water when the air is blowing over intermediate depth water waves is shown in figures 6.61 and 6.62 respectively. Figure 6.61 shows near surface distribution of maximum vorticity observed

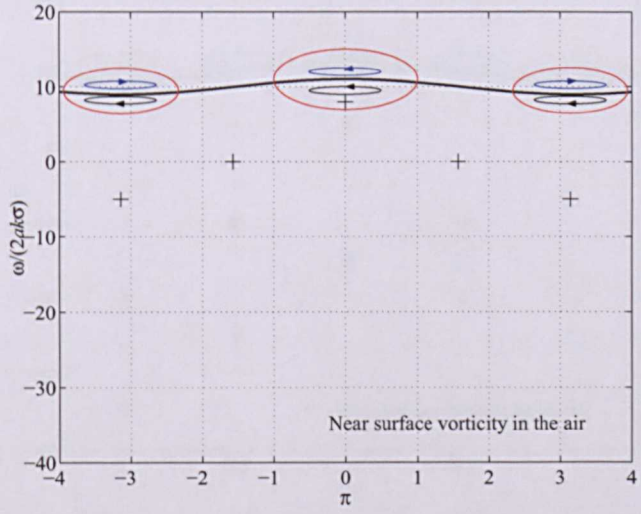

Figure 6.59: A schematic of maximum near surface vorticity in the air at $-\pi$ (trough), $-\pi/2$, 0 (crest), $\pi/2$, π ; 1)+, case 1, $V' = 0$; — represents fluid rotation in the air, —, fluid rotation in the water .

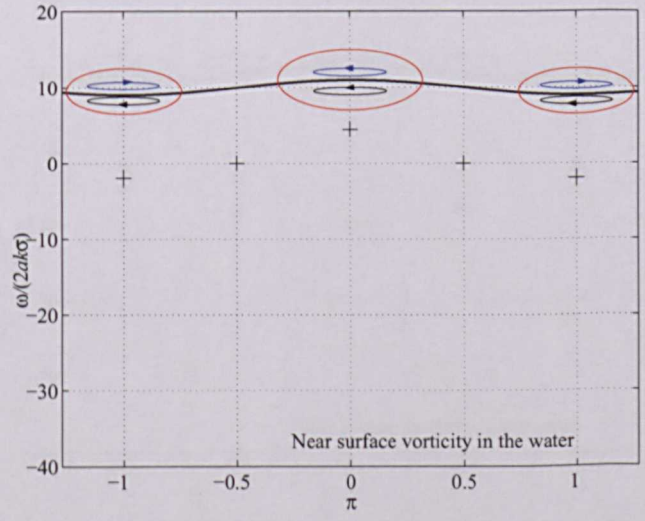

Figure 6.60: A schematic of maximum near surface vorticity in the water at $-\pi$ (trough), $-\pi/2$, 0 (crest), $\pi/2$, π ; 1)+, case 1, $V' = 0$; — represents fluid rotation in the air, —, fluid rotation in the water .

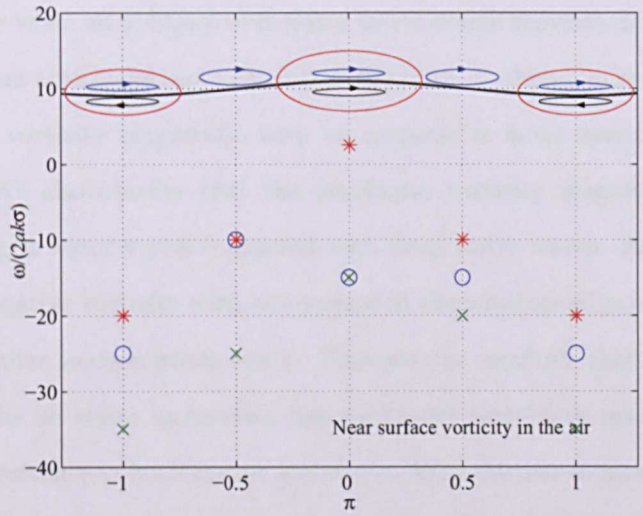

Figure 6.61: A schematic of maximum near surface vorticity in the air at $-\pi$ (trough), $-\pi/2$, 0 (crest), $\pi/2$, π ; 1) $*$, case 2, $V' = u_{max}$, 2) $\circ$, case 3, $V' = 0.5c$, 3) $\times$, case 4, $V' = c$; — represents fluid rotation in the air, —, fluid rotation in the water .

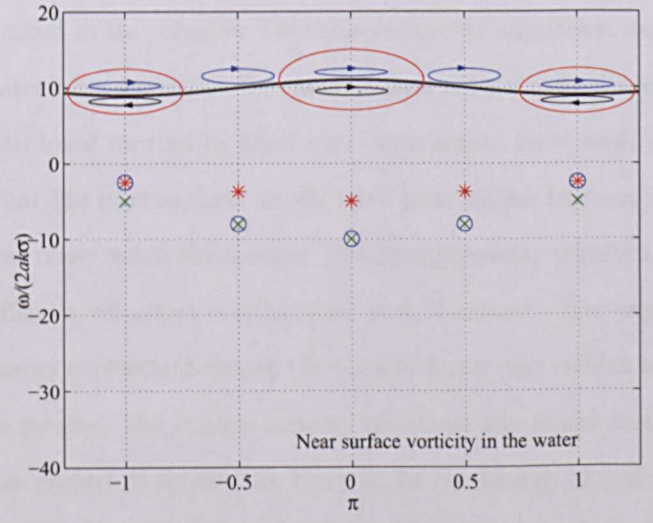

Figure 6.62: A schematic of maximum near surface vorticity in the water at $-\pi$ (trough), $-\pi/2$, 0 (crest), $\pi/2$, π ; 1) $*$, case 2, $V' = u_{max}$, 2) $\circ$, case 3, $V' = 0.5c$, 3) $\times$, case 4, $V' = c$; — represents fluid rotation in the air, —, fluid rotation in the water .

in the air. Similar to deep water waves, a change in vorticity sign is observed in the crest of the wave when air is blown over water waves which signifies that the rotation of fluid changes from anticlockwise to clockwise direction. It shows an sequential increase in the negative vorticity magnitude with an increase in wind speed similar to deep water waves. We also observe that the maximum vorticity magnitude is higher in intermediate depth water waves compared with deep water waves. An increase in the magnitude of negative vorticity with an increase in the wind speed is observed in figure 6.62. This is similar to deep water waves. Thus we can conclude that with an increase in wind speed the air-water interaction becomes more prominent resulting in increase in the negative vorticity in both the air and water. With further increase in wind speed, higher magnitude of vorticity might be observable. These higher magnitude vortices in the water and air can have significant impact on the air-water interaction at longer time periods.

6.9 Closure

The results discussed in this chapter have shown several important aspects to be considered in air water interactions in the intermediate depth water waves. The effect of viscosity and rotational motion in wind wave interaction have been studied and the analysis found that the intermediate depth wave have higher bottom boundary effects on the shear stress observed in the trough. The energy density variation in the presence of wind with different velocities is calculated and discussed. The variation of energy density shows energy exchange between the air and water wave which is similar to deep water waves. In general, the energy density variation was found similar in line with deep water waves except it showed an increase in the energy density mainly due to lower number of waves dissipating energy for the same length of domain. In the next chapter, we discuss short summery and conclusion derived from the current research.

Chapter 7

Conclusions and future work

7.1 Summery of numerical results

This section summarizes the numerical results obtained by solving the Navier-Stokes equations for the water-wind waves using CFD technique. The numerical results agree well with experimental and theoretical results of Mitsuyasu & Honda (1982). The numerical model can be utilized for waves with different steepnesses, frequency or depth of water. Several interesting features related to dynamics of the wave are presented and its importance is highlighted. There are some significant observations regarding the change in the magnitude and direction of near surface vorticity and shear stress observed when we compare the case when average wind velocity zero with the cases when average wind velocity is equal to or higher than maximum water velocity. We observed that both vorticity and shear stress layers thickens with an increase in wind speed and can significantly alter the near surface flow field at longer time periods. The results are significant in terms of overall understanding of energy exchange taking place between surface wave and air blowing over it as so far, potential flow approach has been unable to quantify or effectively model, both near surface and near bottom boundary

flow conditions. The research in this thesis has achieved its aim of understanding and visualizing near surface physical and energy exchange processes taking place in wind-wave environment. In terms of overall understanding of the wave dynamics, it has provided a new and better understanding of vorticity, shear stress and energy exchange and has increased our understanding of certain aspects in wind-water wave interaction. The model presented in the thesis can be further developed to solve variety of wind-wave conditions.

In Chapter 2, a mathematical formulation that describes the wave as an interface between two different density fluids using potential flow approach and theory of complex potential as described by Milne-Thomson (1994) is presented and elaborated to derive the initial and boundary conditions to be used in solution of full Navier-Stokes equations. These initial and boundary conditions are later applied to a variety of water wave and wind wave interaction flow conditions, the results of which are analyzed and presented in later chapters. The elaborate discussion on the topic is avoided as the potential flow solution is very well established and long studied. The general transport equation used in the solution of N-S equations along with the governing equations for the fluid flow is presented. The physical definition of various boundary conditions to be used in the problem formulation are also presented.

In Chapter 3, the numerical method for the solution of full Navier-Stokes equations to simulate wind-water wave interaction is explained. The discretization of mass and momentum conservation equations solved in the coupled finite element control volume algorithm is presented. The algorithm combines the geometric flexibility offered by finite-element formulation and strict conservation properties of finite volume formulation. It uses a vertex-centered method to define the control volume in the mesh which has slightly higher storage requirements compared to cell-centered method. A single cell, co-located grid arrangement is utilized for control volume discretization to overcome decoupling of pressure and/or velocity. The problem of "checker-board" oscillations is handled by using the method similar to Rhie & Chow (1983). In order to track the water wave interface the method developed by Zwart *et al* (2007) is used.

The advection term is discretized using an upwind biased scheme and the transient term is discretized using second-order backward Euler scheme which is considered very robust and accurate. A coupled solver solves the equations for velocities u, v, w and pressure p as a single system using a fully implicit discretization of the equation at any given time step. This method has been found accurate and satisfactory when applied to many other industrial problems related to interface tracking and is used here to track the wind/water wave.

Chapter 4 presented the analysis of numerical results obtained from the solution of Navier Stokes equations for intermediate depth and deep water waves with viscosity when the average wind velocity is zero. On comparing the numerical results for time averaged kinetic, potential and total energy density in the domain with the experimental and theoretical calculations presented in Mitsuyasu & Honda (1982), the results agree well. Thus the accuracy of numerical model to predict the water surface and velocity fields in the air and water is verified and found satisfactory. The numerical results for velocity vectors, velocity contours, streamlines, pressure isolines, pressure, energy dissipation are studied and compared with the potential flow in several cases. The study of dynamic pressure isolines is carried out since the variation in pressure due to presence of wave is mostly dynamic in nature and is difficult to grasp by studying the combined pressure which consist of large static pressure due to depth of water and dynamic pressure due to presence of wave. Other previously less studied aspects in water waves such as shear stress and vorticity under the water wave are presented and compared with the analytical solutions available. Several questions related to the presence of vorticity and shear stress in the progressive water waves are answered. For example, what is the maximum value of the vorticity and shear stress in the water waves ? Are they symmetrical under the crest and trough ? How does the structure and the behavior of vorticity and shear stress change with varying water depth and how does it affect our understanding of wave dynamics ? The results found that the past analytical theories to predict the vorticity in the water waves under predict its magnitude by the factor of 4. However the analytical theory does predict the oscillatory

nature of the vorticity along the depth correctly which is similar to that predicted by the numerical results. The study of vorticity is found to be very attractive to describe high Reynolds number flow of water/wind waves. The effect of viscosity is observed with the study of shear stress in the wave domain.

Chapter 5 considers another class of problem pertaining to air-sea interaction which deals with the study of air flow over transient, nonlinear and progressive water waves in deep water and examines the energy and momentum exchange between air and water. The numerical results for velocity vectors, free surface, dynamic pressure isolines, energy dissipation, shear stress, vorticity and time averaged energy density variation along the domain are discussed. The numerical results found that the presence of wind alters the direction and magnitude of vorticity near the free surface in the crest of the wave both in air and water and increase the magnitude of vorticity in air and water near the trough of the wave. An increase in the magnitude of vorticity is also observed with an increase in wind speed. This is a significant observation from the numerical results and can play a major role in enhancing the knowledge about near interface processes governing the fluid flow behaviour in air-sea interaction. The results of shear stress show the appearance of positive shear layer in crest of the wave which becomes stronger, thicker and extends to the trough of the wave with the increase in the wind speed. The study of energy density variation along the domain shows a reduction in the energy dissipation of water waves on comparing with case when the average with velocity was kept zero. When the average wind velocity equals the wave phase speed, the wave is found to significantly reduce the loss of energy. Physically this means that if the wind velocity is further increased than the wave phase speed it is possible to see the wave growth over certain period of time. It however, transforms into turbulent flow which is very difficult to verify. An alternative to this is to further reduce the mesh size to very small value to capture the eddies with varied length scale including the smaller ones which is computationally very expensive with the resources available.

In Chapter 6, we study another problem dealing with the interaction of transient, nonlinear and progressive waves in an intermediate depth water with air blowing at

various wind speeds in order to reveal energy and momentum exchange between air and water. The wind velocity and wave steepness are defined in same manner as in chapter 5 in order to help draw comparison between two cases when there is change is depth of the water. The numerical results for velocity vectors, profile of free surface, dynamic pressure isolines, energy dissipation, shear stress, vorticity and time averaged energy density variation along the domain are discussed. The numerical results reveal an increase in the velocity in the crest of the wave resulting in increase in the kinetic energy density in the water. The analysis of vorticity showed the presence of vorticity rolls which are formed from rolling of vortex sheet in the trough region and subsequently diffused higher up in the air along the domain. These rolls also have negative vorticity which are formed from the negative vorticity layer in the trough region and are diffused in the air. These vorticity structures over the time period of testing produce nearly same structures when time averaged over the wave period, however it may change over the length and depth if we run the simulation for much longer time period which is computationally very expensive exercise with the resources available. The maximum shear stress observed in the trough of the intermediate depth water case is different in magnitude for the case when the average wind velocity is low and the case when the average wind velocity is $0.5c$ which is mainly due to higher vertical velocity gradient in the intermediate depth case due to effect of bottom boundary. The increase observed in the shear stress in the water and air is sequential depending upon the wind speed. When the average wind velocity is equal to c the maximum value of shear stress in the air is about 10% of the maximum observed in the water and is not negligible. With an increase in the wind speed the magnitude of shear stress can be of order similar to the one in the water and can have substantially alter the flow structure near the free surface. The energy density in the water in the domain shows an increase in net energy gain as the attenuation due to dissipation is reduced and when the average wind velocity is equal to the wave phase speed the total energy density shows an net gain of 7% over the case when the average wind velocity is zero. This results show the presence of direct energy and momentum exchange between air and water. In general

many physical quantities show differences in magnitude with the change in the depth of water. The measurable physical quantities like velocity, pressure etc show very small difference in structure and magnitude while some hard to measure quantities such as vorticity, shear stress etc highlight the subtle difference observed in the flow over the deep water wave and intermediate depth water wave.

7.2 Concluding remarks

This thesis is concerned with the modeling of air-water wave interaction using Navier-Stokes equations with the main aim of developing a numerical model to study the hard to measure and difficult to visualize physical quantities that governs wind-wave interaction for viscous, transient and nonlinear fast waves. In general, the real wind-wave interaction problem is modelled with assumption that waves are either steady, linear and inviscid which is contrary to the observed flow in nature. The work presented in this thesis can be extended to be applied to water wave with different wave height, steepness, water depth and varying air flow conditions as long as the turbulence is not the major factor affecting the flow conditions. The application to other flow conditions will require small modifications in size of the domain and location of high resolution mesh to capture free surface accurately. These model although applicable to shallow water waves cannot guarantee accuracy and stability for shallow water conditions as the flow conditions are complicated due to large effect of viscosity and bottom boundary and may require the use of turbulence closure model to capture range of fluctuations produced in the flow field. The solution to full Navier-Stokes is the most accurate way to study the problem of wind-wave interaction. However, at higher wind velocities it will be necessary to employ the turbulence closure models. The VOF tracking scheme employed in the solver is found accurate and is able to effectively capture the free surface and produces mesh independent results when twelve nodes are included along the wave height.

The quality of numerical results also depends upon the type of initial and boundary

conditions provided as it could take longer time to solve if the initial conditions are far away from the actual conditions. The other aspect of this thesis deals with study of subtle physical quantities affecting the near-surface flow in wind-wave interaction. I have found that the vorticity and shear stress quantities have higher magnitude than previously analytical studies that the vorticity and shear stress should be considered important when considering the problem of wind-wave interaction. These quantities hold the key to understanding of the higher observed growth rate in laboratory and field measurements. The other aspect dealing with study of energy exchange has revealed that wind wave stops loosing the energy through dissipation when the wind velocity is equal to wave speed and the major increase in the energy density is observed in the form of increased momentum inside the water while the wave amplitude still does not show an major increase. This could be mainly due to shorter computational domain and may require much larger computational domain to report a significant change in wave amplitude. These indicates that at low wind speeds initially the exchange between air and water results in net increase in the kinetic energy of the water. At higher wind speed the momentum exchange rate can be much higher and these increased kinetic energy gets converted into potential energy via internal energy exchange and could result in increase in wave amplitude. However, the role of turbulence is an important factor to be considered while studying any energy exchange between wind and wave.

The results presented for vorticity and shear stress suffers from the lack of direct experimental or fieldwork observations. A few experimental works are often concentrated on the study of vorticity observed in the breaking wave which may be very high as compared with observed values in the non-breaking wave and hence un-comparable with current numerical results. The limited theoretical work regarding the vorticity behaviour with the depth is compared with the numerical results in Chapter 4. The current development in use of PIV can capture the instantaneous flow field with high resolution in a limited area. These velocity field data can be used to calculate the velocity gradient in the air and water giving shear stress and vorticity in the air and water. The accurate measurements of near surface velocity and pressure fields in both air and

water are required for effective comparison between numerical results and laboratory field data for surface velocity, shear stress and vorticity as these quantities are important in the boundary layer region which may affect the near surface flow field. The numerical model presented here is very effective for studying the near surface processes.

This thesis presents a application of full Navier-Stokes equations to study the physical quantities governing the fluid flow in wind-wave interaction with high accuracy. The results presented here shows that stable and accurate numerical results can be obtained to study near surface physical processes for wind-wave conditions when turbulent field is not very strong. The results show convergence with respect to the number of mesh points and was found stable with increase and decrease in time step size within the prescribed range. Therefore, it can be concluded that the numerical model presented here for studying the wind-wave interaction problem is both efficient and sufficiently accurate.

7.3 Future work

The possible future work related to the studies carried out in the current thesis could present some interesting comparison for experimental and theoretical study for pressure and shear drag in the wind waves. An accurate experimental future work related to measurement of both pressure and shear drag is needed in order to compare the results of pressure and shear drag obtained from numerical study. The numerical results for pressure and velocity of this study can be further used to study the coefficient of drag on the free surface for range of wind conditions presented in this study. To accurately model the drag coefficient from experimental data an accurate velocity and pressure measurements are required which can then be compared with the numerical results. Several other possible directions of extending the work presented in this thesis include blowing the wind from the opposite direction and blowing the wind obliquely at an angle to observe the change in physical quantities presented in the current thesis. It is also possible to look at a much longer domain to observe how these flow quantities

change along the length in a longer domain. Another very interesting aspect to study could be full 3D modeling of the flow field, however it is worthwhile to note that it is computationally expensive. The future work should also include an accurate experimental investigation of near surface velocity and pressure field which can be compared with the numerical model results to reveal many other interesting aspects related to wind waves and wave drag. Moreover, the numerical model should also be compared with more accurate and comprehensive experimental and theoretical investigations for wind-waves.

Bibliography

Airy, G. B. (1841), 'Tides and waves.', *Encyclopaedia Metropolitana (1817 1845), Mixed Sciences* **3**, 396.

Airy, G. B. (1845), 'On the laws of the tides on the coasts of Ireland, as inferred from an extensive series of observations made in connexion with the Ordnance Survey of Ireland.', *Philos. Trans. R. Soc. London* pp. 1–124.

Al-Zanaidi, M. A. & Hui, W. H. (1984), 'Turbulent airflow over water waves - a numerical study.', *J. Fluid Mech.* **148**, 225–246.

Angelis, D., Lombardi, P. & Banerjee, S. (1997), 'Direct numerical simulation of turbulent flow over a wavy wall.', *Physics of Fluids* **9**, 2429–2442.

Apel, J. R. (1994), 'An improved model of the ocean surface wave vector spectrum and its effects on radar backscatter.', *J. Geophysical Research* **99**, 16269–16291.

Ashgriz, N. & Poo, J. Y. (1991), 'FLAIRflux line-segment model for advection and interface reconstruction.', *Journal of Computational Physics* **92**, 449–68.

Aulisa, E., Manservisi, S. & Scardovelli, R. (2004), 'A surface marker algorithm coupled to an area-preserving marker redistribution method for three-dimensional interface tracking.', *Journal of Computational Physics* **197**, 5555846.

Baker, G. R. & Burger, K. M. (2001), 'Numerical studies of the nonlinear interaction between turbulent air flow and sea surface waves, with application to ocean surface wave turbulence.', *ITR/AP Proposal*.

Baliga, B. & Patankar, S. V. (1983), 'A control volume finite element method for two-dimensional fluid flow and heat transfer.', *Numerical Heat Transfer* **6**, 245–261.

Banner, M. L. & Peirson, W. L. (1998), 'Tangential stress beneath wind-driven air-water interfaces.', *J. Fluid Mech.* **364**, 115145.

Barnettt, P. & Wilkerson, C. (1967), 'On the generation of wind waves as inferred from airborne radar measurements of fetch-limited spectra.', *J. Mar. Res.* **25**, 292–328.

Barr, P. K. & Ashurst, W. T. (1984), An interface scheme for turbulent flame propagation, Technical report SAND82-8773, Sandia National Laboratories.

Barth, T. J. & Jesperson, D. C. (1989), 'The design and application of upwind schemes on unstructured meshes.', *AIAA Paper - Aerospace Sciences Meeting, 27th, Reno, NV* p. 0366.

Basset, A. B. (1888), Treatise on hydrodynamics., Cambridge: Deighton, Bell.

Belcher, S. E. & Hunt, J. C. R. (1993), 'Turbulent shear flow over slowly moving waves.', *J. Fluid Mech.* **251**, 109–147.

Belcher, S. E. & Hunt, J. C. R. (1998), 'Turbulent flow over hills and waves.', *Annual Review of Fluid Mech.* **30**, 507–538.

Belcher, S. E., J. A. H. & Street, R. L. (1994), 'Linear dynamics of wind waves in coupled turbulent air-water flow.', *J. Fluid Mech.* **271**, 119–151.

Bole, J. B. & Hsu, Y. E. (1969), 'Response of gravity water waves to wind excitation.', *J. Fluid Mech* **35**, 657–675.

Bossut, C. (1786), Trait Thorique et Exprimental d'Hydrodynamique. 2 Vols., l'Imprimerie Royale, Paris.

Boussinesq, J. (1895), 'Lois de lextinction de la houle en haute mer.', *C. R. Ac. Sc. Paris* **121**, 15–20.

Cherukat, P., Na, Y., Hanratty, T. J. & Mclaughlin, J. B. (1998), 'Direct numerical simulation of a fully developed turbulent flow over a wavy wall', *Theoretical Fluid Dynamics* **11**, 109–134.

Cheung, T. & Street, R. (1988), 'Turbulence layers in the water at an air-water interface, Part A.', *J. Fluid Mech.* **194**, 133–151.

Choi, H., Moin, P. & Kim, J. (1992), 'Direct numerical simulation of turbulent flow over riblets.', *Center for Turbulence Research Stanford University, CTR manuscript* **137**.

Chorin, A. J. (1980), 'Flame advection and propagation algorithms.', *Journal of Computational Physics* **35**, 1–11.

Cohen, J. E. & Belcher, S. E. (1999), 'Turbulent shear flow over fast moving waves.', *J. Fluid Mech.* **386**, 345–371.

Constantin, A. (2001), 'On the deep water wave motion', *Journal of Physics A: Mathematical and general.* **34**, 1405–1417.

Constantin, A., S. D. & Strauss, W. (2006), 'Variational formulations for steady water waves with vorticity.', *J. Fluid Mech.* **548**, 151–163.

Craik, D. D. A. (2004), 'The Origins of Water Wave Theory.', *Annual Review of Fluid Mech.* **36**, 1–28.

Dalmedico, A. D. (1988), *In the history of Modern Mathematics.*, London, Academic Press.

Dalrymple, R. & Rogers, B. (2005), 'Numerical modeling of water waves with the SPH method.', *Journal of Coastal Engineering* **53**, 141–147.

Dean, R. & Dalrymple, R. (1984), *Water Wave Mechanics for Engineers and Scientists.*, New Jersey, Prentice-Hall Inc.

DeBar, R. (1974), Fundamentals of the kraken code, Technical report UCIR-760, LLNL.

Dimas A. A., Triantafyllou, G. S. (1994), 'Nonlinear interaction of shear flow with a free surface.', *J. Fluid Mech.* **260**, 211–46.

Dobson, F. W. (1971), 'Measurements of atmospheric pressure on wind-generated sea waves.', *J. Fluid Mech.* **48**, 91–127.

Dommermuth, D. G. & Yue, D. K. P. (1987*a*), 'A high order spectral method for the study of nonlinear gravity waves.', *J. Fluid Mech* **184**, 267–88.

Dommermuth, D. G. & Yue, D. K. P. (1987*b*), 'Numerical simulations of nonlinear axisymmetric flows with a free surface.', *J. Fluid Mech* **178**, 195–219.

Donelan, M. A. (1999), *Wind-induced growth and attenuation of laboratory waves. Wind-over-Wave Couplings. Perspective and Prospects*, Clarendon Press, chapter Wind-Induced Growth and Attenuation of Laboratory Waves, pp. 183–194.

Donelan, M. A., Babanin, A. V., Young, I. R. & Banner, M. L. (2006), 'Wave-Follower Field Measurements of the Wind-Input Spectral Function. Part II: Parameterization of the Wind Input.', *Journal of Physical Oceanography* **36**, 1672–1689.

Donelan, M. A. & Pierson, W. (1987), 'Radar scattering and equilibrium ranges in wind generated waves with application to scatterometry.', *J. Geophysical Research* **92**, 4971–5029.

Durden, S. L. & Vesecky, J. F. (1985), 'A physical radar cross-section model for a wind driven sea with swell.', *IEEE J. Oceanic Eng.* **10**, 445–451.

Earnshaw, S. (1847), 'The mathematical theory of the two great solitary waves of the first order.', *Trans. Camb. Philos. Soc.* **8**, 326–341.

Elfouhaily, T., Chapron, B., Katsaros, K. & Vandemark, D. (1997), 'A unified directional spectrum for long and short wind-driven waves.', *J. Geophysical Research* **102**, 15780–15796.

Elliott, J. A. (1972), 'Microscale pressure fluctuations measured within the lower atmospheric boundary layer.', *J. Fluid Mech.* **53**, 351–383.

Euler, L. (1757*a*), 'Continuation des recherches sur la thorie du movement des fluides.', *Mm. Acad. Sci. Berlin* .

Euler, L. (1757*b*), 'Principes gneraux du mouvement des fluides.', *Mm. Acad. Sci. Berlin, ed. CA Truesdell* .

Euler, L. (1761), 'Principia motus fluidorum', *Novi Commentarii Acad. Sci. Petropolitanae.* **6**, 271–311.

Fulgosi, M., L. D. B. S. & Angelis, V. D. (2003), 'Direct numerical simulation of turbulence in a sheared air-water flow with a deformable interface.', *J. Fluid Mech.* **482**, 319–345.

Gent, P. R. (1977), 'A numerical model of the air flow above water waves: Part 2.', *J. Fluid Mech.* **82**, 349–369.

Gent, P. R. & Taylor, P. A. (1976), 'A numerical model of the air flow above water waves.', *J. Fluid Mech.* **77**, 105–128.

Gerstner, F. J. (1802), *Theorie der Wellen.*, Prague, Abhand. Kn. Bhmischen Gesel. Wiss.

Gingold, R. & Monaghan, J. (1977), 'Smoothed Particle Hydrodynamics: theory and application to non-spherical stars.', *Mon. Not. R. Astron. Soc.* **181**, 375–389.

Glimm, J., Grove, J. W., Li, X. L., Oh, W. & Sharp, D. H. (2001), 'A critical analysis of RayleighTaylor growth rates.', *J. Comput. Phys.* **169**, 652.

Gong, W., Taylor, P. A. & Dornbrack., A. (1996), 'Turbulent boundary-layer flow over fixed aerodynamically rough two-dimensional sinusoidal waves.', *J. Fluid Mech.* **312**, 1–37.

Gravesande, W. J. (1721), *An Introduction to Sir Isaac Newton's Philosophy. Engl. transl. JT Desaguliers.*, London, Senex and Taylor, 2nd ed.

Grosenbaugh, M. A. & Yeung, R. W. (1989), 'Nonlinear free-surface flow at a two-dimensional bow.', *J. Fluid Mech.* **209**, 57–75.

Hara, T. & Plant, W. J. (1994), 'Hydrodynamic modulation of short wind-wave spectra by long waves and its measurement using microwave backscatter.', *J. Geophysical Research* **99**, 9767–9784.

Harlow, F. & Welch, J. (1965), 'Numerical calculation of time-dependent viscous incompressible flow of fluid with free surface.', *Phys. Fluids* **8**, 2182–2189.

Harris, J. A., S. E. B. & Street, R. L. (1996), 'Linear dynamics of wind waves in coupled turbulent air-water flow. Part 2. Numerical model.', *J. Fluid Mech.* **308**, 219–254.

Hasselmann, D. & Bosenberg, J. (1991), 'Field measurements of wave-induced pressure over wind-sea and swell.', *J. Fluid Mech.* **230**, 391–428.

Hasselmann, K., Barnett, T. P., Bouws, E., Carlson, H., Cartwright, D. E., Enke, K., Ewing, J. A., Gienapp, H., Hasselmann, D. E., Kruseman, P., Meerburg, A., Müller, P., Olbers, D. J., Richter, K., Sell, W. & Walden, H. (1973), 'Measurements of wind-wave growth and swell decay during the Joint North Sea Wave Project (JONSWAP)', *Dt. Hydrogr. Z., A8 (Suppl.)* **12**, 95.

Hatori, M. & Toba, Y. (1983), 'Transition of mechanically generated regular waves to wind waves under the action of wind.', *J. Fluid Mech.* **130**, 397–409.

Henn, D. & Sykes, R. I. (1999), 'Large-eddy simulation of flow over wavy surfaces.', *J. Fluid Mech.* **383**, 75–112.

Hirt, C. & Nicholas, B. (1981), 'Volume of Fluid (VOF) method for the dynamics of free boundaries.', *J. Comput. Phys* **39**, 201–225.

Hsu, C. T. & Hsu, E. Y. (1983), 'On the structure of turbulent flow over a progressive wat,er wave : theory and experiment in a transformed, wave-following coordinate system. Part 2', *J. Fluid Mech.* **131**, 123–153.

Hsu, C. T., Hsu, E. Y. & Street, R. L. (1981), 'On the structure of turbulent flow over a progressive wat,er wave : theory and experiment in a transformed, wave-following coordinate system.', *J. Fluid Mech.* **105**, 87–117.

Hu, H. H. (1996), 'Direct simulations of flows of solidliquid mixtures.', *Int. J. Multiphase Flow* **22**, 335.

Hutchinson, B. R. & Raithby, G. (1986), 'A multigrid method based on the additive correction strategy.', *Numerical Heat Transfer* **9**, 511–537.

J. E. Pilliod, J. & Puckett, E. G. (2004), 'Second-order accurate volume-of-fluid algorithms for tracking material interfaces.', *Journal of Computational Physics* **199**, 465–502.

J. Feng, H. H. H. & Joseph, D. D. (1994), 'Direct simulation of initial value problems for the motion of solid bodies in a Newtonian fluid. 1. Sedimation', *J. Fluid Mech.* **261**, 95.

J. Feng, H. H. H. & Joseph, D. D. (1995), 'Direct simulation of initial value problems for the motion of solid bodies in a Newtonian fluid. 2. Couette and Poiseuilli flows.', *J. Fluid Mech.* **277**, 271.

Jacqmin, D. (1999), 'Calculation of Two-Phase Navier-Stokes Flows Using Phase-Field Modeling.', *J. Comput. Phys.* **155**, 96–127.

Jamet, D., Lebaigue, O., Coutris, N. & Delhaye, J. M. (2001), 'The Second Gradient Method for the Direct Numerical Simulation of Liquid-Vapor Flows With Phase Change.', *Int. J. Multiphase Flow* **169**, 624–651.

Jeffreys, H. (1924*a*), 'On the formation of waves by wind.', *Proc. Roy. Soc.* **107A**, 189206.

Jeffreys, H. (1924*b*), *The earth.*, Cambridge, Cambirdge University Press, 1st edition.

Jeffreys, H. (1925), 'On the formation of waves by wind. II.', *Proc. Roy. Soc.* **110A**, 341347.

Jones, I. S. F. & Toba, Y. (2001), *Wind stress over the ocean.*, Cambridge, Cambirdge University Press, 1st edition.

Joseph, D. & Wang, J. (2004), 'The dissipation approximation and viscous potential flow.', *J. Fluid Mech.* **505**, 365–377.

Kawai, S. (1977), 'On the generation of wind waves relating to the shear flow in water-A preliminary study. ', *Sci. Rep. Tohoku Univ.* (5), *Geophys.* **24**, 1–17.

Kawai, S. (1979), 'Generation of initial wavelets by instability of a coupled shear flow and their evolution to wind waves ', *J . Fluid Mech.* **93**, 661–703.

Kelland, P. (1844), 'On the theory of waves, Part 2.', *Trans. R. Soc. Edinburgh* **15**, 101–44.

Kinsman, B. (1965), *WIND WAVES their generation and propagation on the ocean surface.*, Newjersey, Prentice Hall Inc.

Kitaigorodskii, S. A. & Donelan, M. (1984), '$Wind-waveeffectsongastransfer$, Gas Transfer at Water Surfaces', *ed. W. Brutsaert and G. H. Jirka, Reidel* .

Komen, G., Cavaleri, L., Donelan, M., Hasselmann, K., Hasselmann, S. & Janssen, P. (1994), *Dynamics and Modelling of Ocean Waves.*, Cambridge, Cambridge University Press.

Lagrange, J. L. (1781), 'Mmoire sur la thorie du mouvement des fluides.', *Nouv. Mm. Acad. Berlin* **196**.

Lagrange, J. L. (1786), 'Sur la manire de rectifier deux entroits des Principes de Newton relatifs la propagation du son et au mouvement des ondes.', *Nouv. Mm. Acad. Berlin* .

Lamb, H. (1930), *Hydrodynamics.*, Cambridge, Cambridge University Press.

Laplace, M. (1776), 'Suite des rcherches sur plusieurs points du systme du monde.', *Mm. Prsents Divers Savans Acad. R. Sci. Inst. France* **XXVXXVII**, 525–552.

Laplace, M. (1799), *Trait de Mcanique CelesteVol. 1, 2.*, Paris, Duprat.

Li, J. (1995), 'Calcul d'interface affine par morceaux (piecewise linear interface calculation)', *CR Acad. Sci. Paris, Sér. IIb* **320**, 391–396.

Li, P. Y., Xu, D. & Taylor, P. A. (2000), 'Numerical modeling of turbulent airflow over water waves.', *Boundary Layer Met.* **95**, 397–425.

Longuet-Higgins, M. S. (1992), ' Theory of weakly damped Stokes waves: a new formulation and its physical interpretation.', *J. Fluid Mech.* **235**, 319–24.

Longuet-Higgins, M. S. & Cokelet, E. D. (1976), 'The deformation of steep surface waves on water. I. A numerical method of computation.', *Proc. R. Soc. London Sec A* **95**, 1–26.

Lopez, J., Hernandez, J., Gomez, P. & Faura, F. (2004), 'A volume of fluid method based on multidimensional advection and spline interface reconstruction.', *J. Comput. Phys.* **195**, 718–742.

Lopez, J., Hernandez, J., Gomez, P. & Faura, F. (2005), 'An improved PLIC-VOF method for tracking thin fluid structures in incompressible two-phase flows', *J. Comput. Phys.* **208**, 51–74.

Losasso, F., Fedkiw, R. & Osher, S. (2006), 'Spatially adaptive techniques for level set methods and incompressible flow.', *Computers and Fluids* **35**, 9951010.

Lucy, L. (1977), ' A numerical approach to the testing of fusion process.', *Astronomical J.* **88**, 1013–1024.

Lundgren, T. & Koumoutsakos, P. (1999), 'On the generation of vorticity at a free surface.', *J. Fluid Mech.* **382**, 351366.

Maass, C. & Schumann, U. (1994), 'Numerical simulation of turbulent flow over a wavy boundary.', *Proc. First ERCOFTAC Workshop on Direct and Large-Eddy Simulation* pp. 287–2973.

Maat, N. & Makin, V. K. (1992), 'Numerical simulation of air flow over breaking wave.', *Boundary Layer Met.* **60**, 77–93.

Mastenbroek, C., Makin, V. K., Garat, M. H. & Giovanangeli, J. P. (1996), 'Experimental evidence of the rapid distortion of turbulence in the air flow over water waves.', *J. Fluid Mech.* **318**, 273–302.

Mei, C. C. (1989), *The Applied Dynamics of Ocean Surface Waves.*, World Scientific.

Meirink, J. F. & Makin, V. K. (2000), 'Modeling low Reynolds number effects in the turbulent airflow over water waves.', *J. Fluid Mech.* **415**, 155–174.

Miles, J. W. (1957), 'On the generation of surface waves by shear flows.', *J. Fluid Mech.* **3**, 185–204.

Miles, J. W. (1993), 'Surface wave generation revisited.', *J. Fluid Mech.* **256**, 427–441.

Miles, J. W. (1996), 'Surface wave generation: a viscoelastic model.', *J. Fluid Mech.* **322**, 131–1451.

Milne-Thomson, L. M. (1994), *Theoretical Hydrodynamics.*, NewYork, Dover Publications Inc.

Mitsuyasu, H. & Honda, T. (1982), 'Wind-induced growth of water waves.', *J. Fluid Mech.* **123**, 425–442.

Monaghan, J. (1994), 'Simulating free surface flows with SPH.', *Journal of Computational Physics.* **110**, 399–406.

Monaghan, J. & Kos, A. (1999), 'Solitary waves on a Cretan beach.', *Journal of Waterway Port, Coastal and Ocean Engineering.* **125(3)**, 145–154.

Newton, I. (1687), *Philosophiae Naturalis Principia Mathematica.*, London: Jussu Societatis Regiae ac Typis J. Streater. Engl. transl. N Motte.

Nielsen, K. B. (2003), Numerical Prediction of Green Water Loads on Ships, PhD thesis, Technical University of Denmark.

Noh, W. & Woodward, P. (1976), 'SLIC (simple line interface calculation).', In *Proc. 5th Int. Conf. Fluid Dyn. Lec. Notes Phys.* ed. A vande Vooren, P Zandbergen. Berlin: Springer-Verlag **59**, 330–40.

Oran, E. S. & Boris, J. P. (1987), *Numerical Simulation of Reactive Flow*, Elsevier, New York.

Osher, O. & Sethian, J. A. (1988), 'Fronts propagating with curvature-dependent-speed: algorithms based on HamiltonJacobi formulations.', *Journal of Computational Physics.* **79**, 1249.

Papadimitrakis, Y. A., Hsu, E. Y. & Street, R. L. (1986), 'The role of wave-induced pressure fluctuations in the transfer processes across an air-water interface.', *J. Fluid Mech.* **170**, 113137.

Parker, B. J. & Youngs, D. L. (1992), 'Two and Three dimensional Eulerial simulation and fluid flow with material interfaces. Tech Rep. UK Atomic Weapons Establ.'.

Patankar, S. V. (1980), *Numerical Heat Transfer and Fluid Flow.*, Taylor & Francis,USA.

Peirson, W. L., Garcia, A. W. & Pells, S. E. (2003), 'Water wave attenuation due to opposing wind.', *J. Fluid Mech.* **487**, 345–365.

Phillips, O. M. (1957), 'On the generation of waves by turbulent wind.', *J. Fluid Mech.* **2**, 417–445.

Plant, W. J. (1982), 'A relationship between wind stress and wave slope.', *J. Geophysical Research.* **87**, 1961–1967.

Prakash, C. (1986), 'An improved control volume finite-element method for heat and mass transfer and for fluid flow using equal-order velocity-pressure interpolation.', *Numerical Heat Transfer* **9**, 253–276.

Pratt, J. H. (1836), *The Mathematical Principles of Mechanical Philosophy and their application to the Theory of Universal Gravitation.*, Cambridge, University press.

Price, W. G. & Chen, Y. G. (2006), 'A simulation of free surface waves for incompressible two-phase flows using a curvilinear level set formulation', *International Journal for Numerical Methods in Fluids* **51**, 305330.

Priestley, J. T. (1965), 'Correlation studies of pressure fluctuations on the ground beneath a turbulent boundary layer.', *U.S. Nat. Bureau Standards Rep. 8942* .

Raw, M. (1996), 'Robustness of coupled algebraic multigrid for the Navier-Stokes equations', *AIAA Paper* p. 0297.

Raw, M. J. (1985), A new control-volume based finite element procedure for the numerical solution of the fluid flow and scalar transport equations, PhD thesis, University of Waterloo, Ontario, Canada.

Rayleigh, B. (1876), 'On waves.', *Philos. Mag.* **5**, 257–279.

Rhie, C. & Chow, W. (1983), 'Numerical study of the turbulent flow past an airfoil with trailing edge separation.', *AIAA Journal* **21**, 1525–1532.

Rider, W. J. & Kothe, D. B. (1995), 'Stretching and tearing interface tracking methods', *The 12th AIAA CFD Conference, San Diego, June 20, 1995* AIAA - 95 - 1717 .

Rider, W. J. & Kothe, D. B. (1998), 'Reconstructing Volume Tracking', *Journal of Computational Physics* **141**, 112–152.

Rudman, M. (1997), 'Volume-tracking methods for interfacial flow calculations.', *Int. J. Numer. Meth. Fluids* **24**, 671–91.

Rudman, M. (1998), 'A volume-tracking method for incompressible multifluid flows with large density variations.', *Int. J. Numer. Meth. Fluids* **284**, 357–378.

Ruvinsky, K., Feldstein, F. & G.I., F. (1991), 'Numerical simulation of the quasi-stationary stage of ripple exitation by steep gravity-capillary waves.', *J. Fluid Mech.* **230**, 339–353.

Saffman, P. G. (1981), 'Dynamics of vorticity.', *J. Fluid Mech.* **106**, 49–58.

Scardovelli, R., Z. S. (1999), 'Direct Numerical Simulation of Free-Surface and Interfacial Flow.', *Annu. Rev. Fluid Mech.* **31**, 567–603.

Schlottke, J. & Weigand, B. (2008), 'Direct numerical simulation of evaporating droplets.', *Journal of Computational Physics* **227**, 52155237.

Schneider, G. E. & Raw, M. (1985*a*), 'A skewed, positive influence coefficient upwinding procedure for control-volume -based finite-element convection-diffusion computation .', *Numerical Heat Transfer* **9**, 1–26.

Schneider, G. E. & Raw, M. (1985*b*), A new control-volume-based finite element procedure for the numerical solution of the fluid flow and scalar transport equations, Final report, Atomic Energy of Canada Ltd., Chalk river, Ontario.

Schneider, G. E. & Raw, M. (1987*a*), 'Control Volume finite-element method for heat transfer and fluid flow using collocated variables -1. Computational procedure.', *Numerical Heat Transfer* **26**, 363–390.

Schneider, G. E. & Raw, M. (1987*b*), 'Control Volume finite-element method for heat transfer and fluid flow using collocated variables -2. Application and Validation', *Numerical Heat Transfer* **26**, 391–400.

Sethian, J. A. (1999), *Level Set Methods and Fast Marching Methods: Evolving Interfaces in Computational Geometry, Fluid Mechanics, Computer Vision, and Materials Science.*, Cambridge University Press, Cambridge, England.

Shanks S. P., Thompson, J. F. (1977), 'Numerical solution of the Navier-Stokes equations for 2D hydrofoils in or below a free surface.', *In Proc. 2nd Int. Conf. Numer. Ship Hydrodyn, Berkeley, CA*. pp. 202–20.

Shopov, P. J., Minev, P. D., Bazhekov, I. B. & Zapryanov, Z. D. (1990), 'Interaction of a deformable bubble with a rigid wall at moderate Reynolds numbers.', *J. Fluid Mech.* **219**, 241.

Snyder, L. & Cox, C. S. (1966), 'A field study of the wind generation of ocean waves.', *J. Mar. Res.* **24**, 141–78.

Snyder, L. & Cox, C. S. (1981), 'Array measurements of atmospheric pressure fluctuations above surface gravity waves.', *J. Fluid Mech.* **102**, 1–59.

Sullivan, P. P., McWilliams, J. & Moeng, C. H. (2000), 'Simulation of turbulent flow over idealizaed water waves.', *J. Fluid Mech.* **404**, 47–85.

Sussman, M., Fatemi, E., Smereka, P. & Osher, S. (1994), 'A level set approach for computing solutions to incompressible two-phase flow.', *J. Comput. Phys.* **114**, 146.

Teles da silva, A. F. & Peregrine, D. (1988), 'Steep, steady surface waves on water of finite depth with constant vorticity.', *J. Fluid Mech.* **195**, 281–302.

Thais, L. & Magnaudet, J. (1995*a*), 'A triple decomposition of the fluctuation motion below laboratory wind water waves.', *Journal of Geophysical Research. C1* **100**, 741–755.

Thais, L. & Magnaudet, J. (1995*b*), 'Orbital rotational motion and turbulence below laboratory.', *Journal of Geophysical Research. C1* **100**, 757–771.

Tryggvason, G., Bunner, B., Esmaeeli, A., Juric, D., Al-Rawahi, N., Tauber, W., Han, J., Nas, S. & Janz, Y.-J. (2001), 'A Front-Tracking Method for the Computations of Multiphase Flow.', *Journal of Computational Physics* **169**, 708759.

Tsai, W. T. & Yue, D. K. P. (1995), 'Effects of soluble and insoluble surfactant on laminar interactions of vortical flows with a free surface.', *J. Fluid Mech.* **289**, 315–49.

Ubbink, O. & Issa, R. I. (1999), 'A method for capturing sharp fluid interfaces on arbitary meshes.', *Journal of Computational Physics* **153**, 26–50.

Ulaby, F. T., Moore, R. K. & Fung., A. K. (1982), *Microwave Remote Sensing: Active and Passive, Vol. II - Radar Remote Sensing and Surface Scattering and Emission Theory.*, Addison-Wesley.

Unverdi, S. O. & Tryggvason, G. (1992), 'A front-tracking method for viscous, incompressible, multi-fluid flows.', *J. Comput. Phys.* **100**, 25.

Ursell, F. (1956), 'Wave Generation by Wind.', *Surveys in Mechanics,Eds. G. K. Batchelor and R. M. Davies* pp. 216–249.

Uz, B. M., Donelan, M. A., Hara, T. & Bock, E. J. (2002), 'Laboratory studies of wind stress over surface waves.', *Bound.- Layer Meteor.* **102**, 301–331.

Vanden-broeck, J. M. (1996), 'Periodic waves with constant vorticity in water of infinite depth.', *IMA Journal of Applied Mathematics* **56**, 207–217.

Versteeg, H. & ., W. M. (2007), *An Introduction to Computational Fluid Dynamics: The Finite Volume Method.*, Pearson Education, USA .

Vince, S. (1798), *The Principles of Hydrostatics.*, Cambridge, University Press.

Wang, J. & Joseph, D. D. (2006), 'Purely irrotational theories of the effect of the viscosity on the decay of free gravity waves.', *J. Fluid Mech.* **559**, 461–72.

West, B., Brueckner, K. A., Janda, R. S., Milder, M. & Milton, R. L. (1987), 'A new numerical method for surface hydrodynamics.', *J. Geophys. Res.* **92:11**, 803–24.

Wu, Z, J. (1995), 'A theory of three-dimensional interfacial vorticity dynamics.', *Phys. Fluids* **7**, 2375.

Xu, D., Ayotte, K. W. & Taylor, P. (1994), 'Development of a non-linear mixed spectral finite difference model for turbulent boundary layer flow over topography.', *Boundary-Layer Meteorology* **70**, 341–367.

Xu, H. & Yue, D. K. P. (1992), 'Computations of fully nonlinear three-dimensional water waves.', *Proc. 19th Symp. on Naval Hydrodyn., Seoul, Korea* pp. 177–201.

Yeung, R.W., A. P. (1992), 'Oscillation of floating body in a viscous fluid.', *J. Eng. Math.* **26**, 211–30.

Young, T. (1821), *Elementary Illustrations of the Celestial Mechanics of Laplace., Book 1*, London, Murray.

Zhang, X., Khooa, B. & Lou, J. (2006), 'Wave propagation in a fully nonlinear numerical wave tank: A desingularized method.', *Elsevier Ocean Engineering* **33**, 2310–31.

Zwart, P. J., Burns, A. & Galpin, P. F. (2007), 'Coupled algebraic multigrid for free surface flow simulations.', *In Proceedings of OMAE 2007 26th International Conference on Offshore Mechanics and Arctic Engineering.* .

Zwart, P. J., Burns, A., Phillipson, S. & Gobby, D. (2002), 'Finite volume simulation of an airlift loop reactor with coupled algebraic multigrd.', *In Proceedings of ASME FEDSM'02.* .